

**Design and Evaluation of Façade-Integrated Solar Technologies Suitable for
High-Latitude Applications**

Yichao Chen

A Thesis

In the Department

of

Building, Civil and Environmental Engineering

Presented in Partial Fulfillment of the Requirements
for the Degree of Master of Applied Science (Building Engineering) at

Concordia University

Montreal, Quebec, Canada

August 2012

©Yichao Chen, 2012

CONCORDIA UNIVERSITY
School of Graduate Studies

This is to certify that the thesis prepared

By: Yichao Chen

Entitled: Design and Evaluation of Façade-Integrated Solar Technologies Suitable for High-Latitude Applications

and submitted in partial fulfillment of the requirements for the degree of

M.A.Sc. Building Engineering

complies with the regulations of the University and meets the accepted standards with respect to originality and quality.

Signed by the final examining committee:

Dr. Sheldon Williamson

Chair

Dr. Ted Stathopoulos

Examiner

Dr. Radu Zmeureanu

Examiner

Dr. Andreas Athienitis; Dr. Paul Fazio

Supervisor

Approved by _____
Chair of Department or Graduate Program Director

Dean of Faculty

Date August 10, 2012

Abstract

Design and Evaluation of Façade-Integrated Solar Technologies Suitable for High-Latitude Applications

Yichao Chen

This thesis investigates the design and evaluation of façade-integrated solar technologies optimized for high latitude locations. To address the climatic and socio-economic challenges pertaining to Northern housing, a pre-fabricated active envelope system is designed to generate energy from renewable sources while functioning effectively as a passive building enclosure.

An experimental prototype is developed using high-performance structural insulated panel (SIP) wall with the capacity to accommodate several modular solar components including unglazed transpired collector (UTC), transpired glazing (TG), and photovoltaic/thermal (PV/T) systems. Ten collector configurations based on the experimental prototype have been evaluated at the state-of-the-art Solar Simulator and Environmental Chamber (SSEC) laboratory, which allows for a compressed timeline and repeatable results compared to outdoor experiments.

Custom thermal network models for the different collector configurations are developed for steady state and annual analyses. Simulation results are compared to and validated by experimental data from the SSEC laboratory. The potential of energy conservation and renewable generation by the proposed solar facades is estimated using typical meteorological year weather data of three northern Canadian cities.

Two case studies, involving existing façade-integrated solar technologies at high

latitudes, are presented in the Appendix. Field inspections were conducted for a 17-year-old photovoltaic façade in Nunavut, and six Unglazed Transpired Collector (UTC) façade installations in Northwest Territories. In an effort to connect with reality and to investigate the suitability of building integrated solar technologies, the fieldwork examined and discussed the current state of performance and operation issues for the existing solar installations at high latitudes.

Acknowledgement

I want to thank my co-supervisors, Dr. Andreas K. Athienitis and Dr. Paul Fazio, for their unwavering guidance, support and encouragement during my Master's studies at Concordia. Thank you for your trust and the opportunity to work in this exciting field. Thank you for sharing your technical expertise and exposing me to various projects and research groups. I am very grateful for the opportunities to attend appropriate conferences and conduct relevant field projects during the course of my studies.

I would like to express my appreciation for the financial support of the Natural Sciences and Engineering Research Council of Canada (NSERC) through the Smart Net-zero Energy Buildings Strategic Research Network and through the Discovery grants of my supervisors. I also wish to thank Concordia University for granting me financial assistance such as the tuition remission, international partial scholarship, travel support award, and graduate student mobility award.

I would like to thank all the current and past members of the Solar Lab and Building Envelope Lab, as well as the graduate students who inhabit EV 16th and 15th at Concordia University. I owe them for their constant support, technical assistance, and the invaluable idea-bouncing discussions that make research truly enjoyable.

A special thanks to Jacques Payer, Joseph Hrib, Luc Demers, Jaime Yeargans, Sylvain Bélanger, Dr. Jiwu Rao and all the personnel in the BCEE Department for their strong technical support. A special note to Lyne Dee, our project coordinator of the network, for all her hard work and patience dealing with the logistics and planning. I also would like to thank Frank Luginsland, Jan Steinmetz, and other technical personnel in

Germany for being extremely accessible and prompt for remote trouble-shooting. I would also like to thank Josef Ayoub, Yves Poissant and the researchers at NRCan for their kind support that facilitated the knowledge transfer for my research.

I would like to acknowledge the in-kind support from KOTT Group (DAC International). In particular, I am grateful for support and dedication of Jeff Armstrong, for following my research closely and enabling the field project to Iqaluit. The wonderful folks at the Nunavut Research Institute, Arctic Energy Alliance, and Aurora Research Institute deserve a special thanks. I have learnt a great deal from them and am touched by their kindness and hospitality.

Finally, I cannot understate the support of my beloved friends and family, who have helped me through the many ups-and-downs during the course of my studies and for years to come.

Table of Contents

List of Figures	X
List of Tables	xviii
Nomenclature	xx
1. Introduction	1
1.1 Context and Motivation	1
1.1.1 Northern Housing Challenges	1
1.1.2 Opportunities for Housing in High-Latitude	3
1.2 Research Scope	5
1.2.1 Passive and Active Design Principles	5
1.2.2 Scope and Limitations	6
1.3 Research Objectives	7
1.4 Thesis Overview	8
2 Literature Review	10
2.1 Best Practice of Nordic Low Energy Building Design	10
2.1.1 Survey of Nordic Low Energy Buildings Outside Canada	10
2.1.2 Survey of Low Energy Building Practices in Northern Canada	13
2.2 Design Principles for Low Energy Houses in Cold Climate	16
2.2.1 Low Energy Building Practices in Northern Europe and Canada	16
2.2.2 Suitability of Air Based or Liquid Based Solar Thermal Collectors	19
2.2.3 Suitability of Roof or Façade Integration	20
2.3 Transpired Solar Collector Technology in Northern Canada	21
2.3.1 Unglazed Transpired Collector.....	21
2.3.2 Potential Improvements for Unglazed Transpired Collectors.....	23
2.4 Building Integrated Photovoltaic Technology for Cold Climate	26
2.4.1 Flat Plate Photovoltaic Panels.....	26
2.4.2 Concentrator-type Photovoltaic for Northern Applications.....	28
2.4.3 Suitability of Photovoltaic Technology in the High North	30
2.5 Building Integrated Photovoltaic/Thermal (BIPV/T) for Cold Climate	31
2.6 Auxiliary Systems	34
3 Design Methodology of Façade-Integrated Solar Prototypes	37
3.1 Design Considerations	37
3.1.1 Prototype Design Guidelines	37
3.1.2 Configuration Design and Features	37
3.1.3 System-Level Design and Optimization	39
3.2 Components and Configurations	41
3.2.1 Experimental Assembly and Components.....	41
3.2.2 Possible Configurations and Testing Capacity	43
3.3 Instrumentation	44
4 Experimental Evaluation	48
4.1 Solar Simulator / Environmental Chamber (SSEC) Laboratory	48
4.1.1 Introduction to the Laboratory Facility.....	48
4.1.2 Solar Simulator	48
4.1.3 Environmental Chamber	51

4.2 Test Sequence under the Solar Simulator	53
4.3 Results and Discussion – Solar Simulator Experiments	59
4.3.1 Benchmarking Commercially-Available Collectors’ Performance (A1 and B1)....	59
4.3.2 Effects of Fins, Transpired Glazing, and Transpired Absorber (A1, A2 and B1)...	62
4.3.3 Effects of Corrugation Orientation in Transpired Absorber (B1 and B4)	64
4.3.4 Effects of Adding Glazing on Transpired Absorber (B1, B3, B4, and B6).....	65
4.3.5 Effects of Adding Transpired Glazing to Transpired Absorber (B1, B2, B4, B5) ...	67
4.3.6 Effects of Adding PV and Transpired Glazing to Transpired Absorber (C1,C2)....	69
4.3.7 Detailed Temperature Profiles (B1 and B2)	74
4.4 Testing Sequence for the Environmental Chamber	76
4.5 Results and Discussion – Environmental Chamber Experiments	82
4.5.1 Discrepancy in Results between Solar Simulator and Environmental Chamber ..	82
4.5.2 Effects of Air Leakage in Environmental Chamber	83
5 Simulation and Model Validation	88
5.1 Steady State Models of Two Transpired Collectors	88
5.1.1 Model Assumptions.....	88
5.1.2 Heat Transfer Theory	89
5.1.3 Thermal Network Models	94
5.2 Steady State Thermal Network Model for PV/T	97
5.3 Steady-State Simulation Results compared with Experimental Data	101
5.3.1 Uncertainty Analyses of Experimental Results	101
5.3.2 Convective Heat Transfer Coefficients.....	103
5.3.3 Temperature Profiles	106
5.3.4 Collector Effectiveness and Efficiency.....	108
5.4 Applying Numerical Corrections to compare Experimental Results from Solar Simulator and from Environmental Chamber	112
5.4.1 Introduction.....	112
5.4.2 Surface Radiant Gain Correction for the Environmental Chamber Results.....	113
5.4.3 Back Loss Correction for the Solar Simulator Results.....	116
5.4.4 Wind Loss Correction for the Environmental Chamber Results.....	117
5.4.5 Corrected Efficiency Results.....	120
5.5 Annual Analyses	123
5.5.1 Model Description.....	123
5.5.2 Annual Potential for Three Northern Cities.....	125
6 Conclusions and Recommendations	130
6.1 Conclusions	130
6.2 Recommendations for Solar Integration on SIP Envelope	132
6.3 Future Work	134
References	137
Appendix A. Experimental Set Up	146
Appendix B. Experimental Results	158
Appendix C. Uncertainty Analysis	178
Appendix D. Steady-State Simulation and Results	181
Appendix E. Annual Results	192

Appendix F. Field Evaluation of PV Façade at Nunavut Arctic College, Iqaluit
..... 195

**Appendix G. Field Survey of Façade Integrated Unglazed Transpired Collectors
in the Northwest Territories** 206

List of Figures

Figure 1.1 Three Northern Territories (left) and Climate Zones of Canada (right), (NRCan, 2011).....	1
Figure 1.2 Photovoltaic Potential kWh/kW of Canada at Latitude tilt (left) and Vertical tilt (right), (NRCan, 2007)	4
Figure 2.1 Left: Low energy house in Sisimiut, Greenland, 67°N, 2005 (Norling et al. 2006); Right: IEA5 Solar House in Pietarsaari, Finland, 62°N, 1994 (IEA, 1997).....	11
Figure 2.2 Left: PV-Vent facade in Skovlunde, Denmark, 56°N, 2001 (Jensen, 2001); Right: Rønnebækhave house in Næstved, Denmark, 55°N, 2005 (Andresen et al., 2008);.....	12
Figure 2.3 Left: Riverdale NetZero House, Edmonton, 53.5°N, 2008 (Howell, 2008); Right: Northern Sustainable House, Inuvik, 68°N, 2011 (Photo taken by author).....	14
Figure 2.4 Structural Insulated Panel House (left) and SIP cross-section (right). (Armstrong, 2011).....	15
Figure 2.5 Left: Dark UTC façade, product name SolarWall, Rankin Inlet, Nunavut, 67°N; Right: Schematics of how SolarWall works (Conserval Engineering, 2009).....	21
Figure 2.6 Schematic drawings of four different PV/Tair Models (Hegazy, 2000).....	32
Figure 2.7 A BIPV/T demonstration project using UTC and PV/T solar facade in Montreal, Canada (Athienitis et al., 2011).....	34
Figure 3.1 Design of façade collector configurations.....	38
Figure 3.2 Utilization of solar pre-heated air, System-Level Schematics; Route 1: Solar heated air > 25°C; Route 2: Solar heated air <0°C; Route 3: 0°C <Solar heated air<25°C;.....	39
Figure 3.3 BIPV/T-SIP Prototype Experimental Assembly.....	41
Figure 3.4 Schematic of the Experimental Assembly (SIP not shown).....	42
Figure 3.5. Test Configurations: A1. Collector with Transpired Glazing (TG) and flat absorber; A2. TG and finned absorber; B1. UTC with corrugation along flow (UTC-v); B2. UTC-v + TG; B3. UTC-v with top glazing; B4. UTC with corrugation against flow (UTC-h); B5. UTC-h + TG; B6. UTC-h with top glazing; C1. UTC-h + PV/T (PV coverage 50%); C2. UTC-h +PV/T+TG;.....	43
Figure 3.6 Left: BIPV/T prototype integrated with SIP façade; Right: BIPV/T-SIP facade mounted on a Test Room.....	44
Figure 3.7 Thermocouple locations for the layer of Transpired Glazing (TG).....	45

Figure 3.8 Thermocouple Names for the layer of SolarWall (UTC).....	46
Figure 4.1 Spectral Intensity Distribution of MHG lamps compared to Natural Sun Light, (PSE AG, 2011).....	49
Figure 4.2 Solar Simulator in Operation: Main Lamp Field and Test Platform at 0° (left) and 45° (right) tilt angles.....	49
Figure 4.3 Custom Solar Air Collector Test Stand.....	51
Figure 4.4 Left: Mobile Lamp Fields and Environmental Chamber (main façade with glazed apertures); Right: Portal Test Hut inside the Environmental Chamber.....	52
Figure 4.5 Experiments in progress under the Solar Simulator.....	54
Figure 4.6 Irradiance Distribution on the Collector Surface (Solar Simulator), average 838 W/m ²	58
Figure 4.7 Standard deviation of solar distribution at Collector Surface (Solar Simulator), 5% maximum.....	58
Figure 4.8 Collector B1 (SWv) Performance: SolarWall manufacturer’s data (wind speed unknown) compared to Experimental data (0.8m/s surface flow).....	60
Figure 4.9 Collector A1 (TG) Performance: LubiWall Manufacturer’s data (wind speed unknown) compared to Experimental data (0.9 m/s surface flow).....	60
Figure 4.10 Collector B1 (SWv) temperature rise at different irradiance with five mass flow rates, tested at 3.5m/s surface parallel flow condition.....	62
Figure 4.11 Collector A1 (TG no Fins), A2 (TG with Fins) and B1 (SW-v): Efficiency at high (top) and low (bottom) surface flows, steady state at five mass flow rates.....	63
Figure 4.12 Collector A1 (TG no Fins) and B1 (SW-v): Efficiency at high and low surface parallel flows (wind), steady state at five mass flow rates.....	64
Figure 4.13 Collector B1 (SW-v) and B4 (SW-h): Efficiency at high and low surface parallel flows (wind), steady state at five mass flow rates.....	64
Figure 4.14 Collector B4 (SWh) and B6 (SWh+G): Efficiency at high and low surface parallel flows (wind), steady state at five mass flow rates.....	66
Figure 4.15 Infrared evaluation of SWv (B1), SWh (B4), SWv+G (B3), SWh+G (B6) and SWh+TG (B5) at 1148 W/m ² and 1m/s surface parallel flow, with mass flow rate of 50 kg/hr/m ²	67
Figure 4.16 Collector B4 (SWh) and B5 (SWh+TG): Efficiency at high and low surface parallel flows (wind),	67
Figure 4.17 Collector B5 (SWh+TG) & A1 (TG no Fins): Efficiency at high and low surface parallel flows (wind).....	68

Figure 4.18 Infrared evaluation of C1 (SW _h +PV) and C2 (SW _h +PV+TG) at 1148 W/m ² and 0.9m/s surface parallel flow (wind), with mass flow rate of 50 kg/hr/m ²	71
Figure 4.19 Collector C1 (SW _h +PV) and C2 (SW _h +PV+TG): Efficiency at high and low surface parallel flows (wind); Outdoor Data for SW _h +70%PV spring efficiency (Athienitis et al., 2011).....	73
Figure 4.20 Thermal Equivalent Efficiency: Collector C1 (SW _h +PV) and C2 (SW _h +PV+TG); Outdoor Data for SW _h +70%PV (Athienitis et al., 2011);.....	73
Figure 4.21 Temperature Rise at each layer: Collector B1 (SW _v) and B2 (SW _v +TG), 0.9m/s surface parallel flow condition (low wind).....	75
Figure 4.22 Temperature Rise at each layer: Collector B1 (SW _v) and B2 (SW _v +TG), 3.5m/s surface parallel flow condition (high wind)	75
Figure 4.23 Collectors tested in the Environmental Chamber: B4: SolarWall (SW _h); B5: SolarWall covered with transpired glazing (SW _h +TG); C1: SW _h +PV; C2: SW _h +PV+TG.....	77
Figure 4.24 Schematic Drawing of experimental set up in the Environmental Chamber.....	78
Figure 4.25 Photo of experimental set up in the Environmental Chamber, showing Mobile Lamp Field, Test Hut with active façade, and Duct exiting the Chamber.....	78
Figure 4.26 Photos of experiments in progress in the Environmental Chamber; Left: Lamps in action; Right: details of Test Hut assembly.....	80
Figure 4.27 Irradiance Distribution at Collector surface (inside Chamber), average 824 W/m ²	81
Figure 4.28 Standard deviation of solar distribution at Collector Surface (inside Chamber), 10% maximum.....	81
Figure 4.29 Duct Air Leakage Test results and extrapolated flow loss for Experimental Mass flow Rates.....	83
Figure 4.30 Duct Air Leakage Correction for Collector B4 (SW _h).....	85
Figure 4.31 Duct Air Leakage Correction for Collector B5 (SW _h +TG)	85
Figure 4.32 Duct Air Leakage Correction for Collector C1 (SW _h +PV).....	86
Figure 4.33 Duct Air Leakage Correction for Collector C2 (SW _h +PV+TG).....	86
Figure 5.1 Energy Balance and Thermal Network models of conventional Unglazed Transpired Collector (Collector B4: SW _h); Plenum exaggerated.....	90
Figure 5.2 Energy Balance and Thermal Network models of improved UTC with Transpired Glazing (Collector B2: SW _v +TG) Plenum exaggerated.....	90

Figure 5.3. Original (a) and Simplified (b) Thermal Network Models for PV mounted on UTC cladding (Athienitis et al., 2011).....	98
Figure 5.4 Simplified Thermal Network Model for a PV/T system.....	98
Figure 5.5 Collector SW _v : Modelled (equation5.45) and Experimental results for convective heat transfer coefficient (h _{conv}).....	105
Figure 5.6 Collector SW _v +TG: Modelled (equation5.46) and Experimental results for convective heat transfer coefficient (h _{conv}).....	106
Figure 5.7 Surface and Absorber temperature rise of SW _v and SW _v +TG (838 W/m ²); Above: Low Wind (0.9m/s); Below: High Wind (3.5m/s);.....	107
Figure 5.8 Effectiveness of Transpired Collector (SW _v) at Low Gain (838 W/m ²) and Low Wind (0.9m/s).....	109
Figure 5.9 Collector SW _v +TG: Steady-state efficiency at different flow rates.....	110
Figure 5.10 Collector SW _v : Steady-state efficiency at different flow rates.....	110
Figure 5.11 Collector SW _h +PV/T and PV/T model: Steady-state efficiency.....	111
Figure 5.12 Collector SW _h +PV+TG compared to PV/T model + SW+TG model: Steady-state efficiency.....	112
Figure 5.13 Heat Transfer Diagram comparing Experiments under Solar Simulator (left) and Environmental Chamber (right).....	113
Figure 5.14 Measured Temperatures during Environmental Chamber experiments....	114
Figure 5.15 Collector SW _h and SW _h +TG: Efficiency in Chamber corrected for radiant gain to account for heated Chamber façade surface.....	116
Figure 5.16 Collector SW _h : Efficiency in Solar Simulator corrected from 0.9 m/s surface parallel flow (parallel wind) to zero-wind condition.....	120
Figure 5.17 Collector B4 (SW _h): Efficiency in Solar Simulator and in Environmental Chamber, before and after corrections.....	121
Figure 5.18 Collector B5 (SW _h +TG): Efficiency in Solar Simulator and in Environmental Chamber, before and after corrections.....	121
Figure 5.19 Collector C1 (SW _h +PV): Efficiency in Solar Simulator and in Environmental Chamber, before and after corrections.....	122
Figure 5.20 Collector C2 (SW _h +PV+TG): Efficiency in Solar Simulator and in Environmental Chamber, before and after corrections.....	122
Figure 5.21 Useful power (W/m ²) collected by SW+TG (green), and SW+PV (red), and total irradiance on Facade (black). MFR=150kg/hr/m ² ; Whitehorse;.....	125

Figure 5.22 Collector Outlet temperatures of SW+TG (green), and SW+PV (red), and outdoor temperature (black). MFR=150kg/hr/m ² ; Whitehorse;.....	128
Figure 5.23 Collector Outlet temperatures of SW+TG (green), and SW+PV (red), and outdoor temperature (black). MFR=50kg/hr/m ² ; Whitehorse;.....	129
Figure A.1 Custom sized PV panel dimensions.....	146
Figure A.2 Components of the Experimental Assembly (CAD drawing, to scale).....	147
Figure A.3 Instrumentation Diagram of SolarWall Layer.....	148
Figure A.4 Instrumentation Diagram of Transpired Glazing/Glazing Layer.....	149
Figure A.5 Instrumentation Diagram of Back Plate Layer.....	149
Figure A.6 Instrumentation Diagram of PV modules Layer.....	150
Figure A.7 SolarWall Corrugation Dimensions (Conserval Engineering, 2010).....	150
Figure A.8 LabVIEW DAQ Interface (above) and Block Diagram (below).....	152
Figure A.9 Construction Photo: Collector base with instrumentation.....	153
Figure A.10 Construction Photo: Transpired Glazing top with instrumentation.....	153
Figure A.11 Construction Photo: Instrumentation seen from duct outlet.....	153
Figure A.12 Construction Photo: Assembled collector A1 mounted on test stand.....	154
Figure A.13 Construction Photo: Collector A1 at vertical tilt with duct connected.....	154
Figure A.14 Schematics of BIPV/T-SIP system for Environmental Chamber tests.....	155
Figure A.15 Construction photo: SIP shipment in three pieces (left) and Test Hut with hollow façade (right)	156
Figure A.16 Construction photo: Sensor feeding into the test hut before insulation and sealing (left); Duct installation from outside (top right) and inside (bottom right) Test Hut.....	156
Figure A.17 Construction photo: Complete Integration of Collector onto SIP without scanner (left), with scanner (right).....	157
Figure A.18 National Instrumentation, Data Acquisition modules and chassis.....	157
Figure B.1 Irradiance Distribution at Collector surface (Solar Simulator).....	159
Figure B.2 Standard deviation of irradiance at Collector Surface (Solar Simulator)....	159

Figure B.3 Transmittance results for UV-resistant high-performance polycarbonate sheet, tested by the Agilent Spectrophotometer.....	160
Figure B.4 I-V tracer results for two 60W PV modules at 838 W/m ²	160
Figure B.5 I-V tracer results for two 60W PV modules at 1148 W/m ²	161
Figure B.6 Collector (B1: SW _v) outlet temperature rise at 3.5m/s surface parallel flow and under different solar irradiance and different mass flow rates.....	161
Figure B.7 Temperature readings across collector height (B2: SW _v +TG) at 1148 W/m ² , 1m/s surface parallel wind, and constant mass flow rate of 50kg/hr/m ²	162
Figure B.8 All Collectors Performance at 1148W/m ² , 3.5m/s.....	173
Figure B.9 All Collectors Performance at 1148W/m ² , 0.9m/s.....	173
Figure B.10 All Collectors Performance at 838W/m ² , 3.5m/s.....	174
Figure B.11 All Collectors Performance at 838W/m ² , 0.9m/s.....	174
Figure B.12 Duct Air Leakage Correction for B4 (SW _h) and B5 (SW _h +TG).....	177
Figure B.13 Duct Air Leakage Correction for C1 (SW _h +PV), C2 (SW _h +PV+TG)....	177
Figure D.1 Results of finite element analysis after all results converge.....	184
Figure D.2 Level-1 Block diagram of SW or SW+TG models: climatic loads matching 4 sets of experimental tests at five mass flow rates.....	185
Figure D.3 Close up section of one SW or SW+TG model, showing input and output variables for one flow rate and one set of environmental conditions.....	185
Figure D.4 Thermal network model detail: Complete View.....	186
Figure D.5 Details of the “Air Properties” Block.....	187
Figure D.6 Details of the “UTC Properties” block: preparation block for performance calculation of a transpired collector (SW or SW+TG).....	187
Figure D.7 Detail of the “UTC_cal” block.....	188
Figure D.8 Convective heat loss coefficients in relation with V _{wind} /V _s ratio, for Collector B4 (SW _v).....	189
Figure D.9 Convective heat loss coefficients in relation with V _{wind} /V _s ratio, for collector B5 (SW+TG).....	189
Figure D.10 View Factor for two parallel finite surfaces.....	190
Figure D.11 Collector SW _h +PV and SW _h +PV+TG: Efficiency in Chamber corrected for radiant gain to account for heated Chamber façade surface.....	191

Figure E.1 Collector Outlet temperatures of SW+TG (green), and SW+PV (red), and outdoor temperature (black). MFR=50kg/hr/m ² ; Fort Smith.....	192
Figure E.2 Collector Outlet temperatures of SW+TG (green), and SW+PV (red), and outdoor temperature (black). MFR=150kg/hr/m ² ; Fort Smith.....	192
Figure E.3 Useful power (W/m ²) collected by SW+TG (green), and SW+PV (red), and total irradiance on Facade (black). MFR=150kg/hr/m ² ; Fort Smith.....	193
Figure E.4 Useful power (W/m ²) collected by SW+TG (green), and SW+PV (red), and total irradiance on Facade (black). MFR=50kg/hr/m ² ; Iqaluit.....	193
Figure E.5 Useful power (W/m ²) collected by SW+TG (green), and SW+PV (red), and total irradiance on Facade (black). MFR=150kg/hr/m ² ; Iqaluit.....	194
Figure E.6 Useful power (W/m ²) collected by SW+TG (green), and SW+PV (red), and total irradiance on Facade (black). MFR=150kg/hr/m ² ; Iqaluit.....	194
Figure F.1 Façade PV system, Iqaluit. Left: Picture 1995 (Sunny day); Right: Picture 2012 (Snowy day);.....	195
Figure F.2 Eppley pyranometer used for measuring solar irradiance.....	197
Figure F.3 Experimental PV Module Testing.....	199
Figure F.4 I-V curves of sample experimental modules under Sunny and Snowy weather.....	201
Figure F.5 Solar Array Testing: DC wiring in mechanical room for Siemens (L1) and Solec (L2) array.....	202
Figure F.6 I-V curves of the Solar Array (L1 Siemens, L2 Solec), snowy day.....	204
Figure G.1 SolarWall at the GeoScience Building, Yellowknife, 62.4°N.....	210
Figure G.2 SolarWall façade on a private house, Yellowknife, 62.4°N.....	210
Figure G.3 SolarWall at Fort Smith Recreation Center, Fort Smith 60°N, Picture from Conserva Engineering (2010c).....	211
Figure G.4 Left: SolarWall at Female Young Offenders Correctional Facility, Inuvik 68°N; Right: Honeywell Building Control System Interface showing SolarWall controls.....	212
Figure G.5 Interior Structural Failures at Female Young Offenders Correctional Facility.....	212
Figure G.6 Left: SolarWall at Weledeh Catholic School, Yellowknife 62.4°N; Right: Honeywell Building Control System Interface showing SolarWall controls.....	214

Figure G.7 Locations of New Sensors implemented for the Weledeh SolarWall system..... 215

Figure G.8 Aurora Research Institute, Inuvik 68°N; Left: Back of building with SolarWall on the Penthouse; Right: Front of building;..... 216

Figure G.9 Sensors Installation at SolarWall air intake inside mechanical room..... 217

List of Tables

Table 2.1 Summary of Nordic Low Energy Buildings outside Canada.....	10
Table 2.2 Summary of Solar Technologies used in Buildings in Northern Canada.....	16
Table 4.1 Test Stage A (Transpired Glazing/Glazing).....	55
Table 4.2 Test Stage B (SolarWall, Transpired Glazing/Glazing).....	55
Table 4.3 Test Stage C (SolarWall, Transpired Glazing/Glazing, PV Panels).....	56
Table 4.4 Steady-State Testing Conditions (Solar Simulator Testing).....	57
Table 4.5 Photovoltaic Module Electric Characterizations.....	70
Table 4.6 Steady-State Testing Conditions (Environmental Chamber Testing).....	77
Table 4.7 Summary of reasons contributing to different efficiency results between tests under Solar Simulator and test in the Environmental Chamber.....	82
Table 5.1 Summary of sample uncertainty values for calculated variables.....	102
Table 5.2 Summary: Sources that explain differences between Solar Simulator and Environmental Chamber results.....	113
Table 5.3 Summary of Weather Data for Iqaluit, Whitehorse and Fort Smith.....	124
Table 5.4 Annual Simulation results for three Northern locations.....	126
Table A.1 List of Materials needed for prototype construction.....	146
Table A.2 Thermocouple Master List.....	151
Table B.1 Scan results of parallel wind speed across collector height.....	158
Table B.2 Collector A1 (TG) Performance under Solar Simulator.....	163
Table B.3 Collector A2 (TG with fins) Performance under Solar Simulator.....	164
Table B.4 Collector B1 (SWv) Performance under Solar Simulator.....	165
Table B.5 Collector B2 (SWv+TG) Performance under Solar Simulator.....	166
Table B.6 Collector B3 (SWv+G) Performance under Solar Simulator.....	167
Table B.7 Collector B4 (SWh) Performance under Solar Simulator.....	168
Table B.8 Collector B5 (SWh+TG) Performance under Solar Simulator.....	169

Table B.9 Collector B6 (SWh+G) Performance under Solar Simulator.....	170
Table B.10 Collector C1 (SWh+PV) Performance under Solar Simulator.....	171
Table B.11 Collector C2 (SWh+PV+TG) Performance under Solar Simulator.....	172
Table B.12 Collector B4 (SWh) and B5 (SWh+TG) Performance at Environmental Chamber, no wind, irradiance 824 W/m ² (Raw data, uncorrected).....	193
Table B.13 Collector C1 (SWh+PV) and C2 (SWh+PV+TG) Performance at Environmental Chamber, no wind, irradiance 824 W/m ² (Raw data, uncorrected).....	175
Table B.14 Duct leakage Testing Data using a calibrated fan.....	176
Table C.1 Example values of measured variables used in this uncertainty analysis....	178
Table D.1 View Factor for two parallel finite surfaces.....	190
Table F.1 Specifications of the two types of PV modules used in the original installation.....	196
Table F.2 Eppley PSP Readings.....	198
Table F.3 Experimental PV modules Testing Results.....	200
Table F.4 Open-circuit Voltage of PV Array on April 23rd and 25th, 2012;.....	202
Table F.5 Results of Solar Array Performance (snowy day).....	203
Table G.1 Inventory of SolarWall projects in NWT.....	207
Table G.2 Summary of operational details for SolarWall installations in NWT.....	208

Nomenclature

Symbols

A	Area, m^2
A_{col}	Total collector area, m^2
A_{PV}	Collector area covered by PV modules, m^2
c_p	Specific heat of the air, $J/(kg \cdot K)$
D	Pore diameters for the perforation of transpired collectors, m
e	Surface long-wave emissivity
$F_{facade-surface}$	View factor from the Chamber façade to the collector surface; calculated for two finite parallel plates
F_R	Heat removal factor
G	Total incident solar radiation on the plane of the collector per unit area, W/m^2
h_b	Convective heat transfer coefficient from the back of collector per unit area, $W/(m^2K)$
h_C	Convective heat transfer coefficients of the interior surfaces in the air plenum, $W/(m^2K)$
h_{conv}	Convective heat transfer coefficient for the top surface per unit area, $W/(m^2K)$
h_R	Radiative heat transfer coefficient between two long parallel surfaces per unit area, $W/(m^2K)$
h_{wind}	Exterior convective heat transfer coefficient only due to surface parallel flow (wind), per unit area, $W/(m^2K)$
H	Total height of the PV module, m
I	Irradiance incident on surface, W/m^2
I_{peak}	PV current at maximum power point, A
I_{sc}	PV short circuit current, A
k	Thermal conductivity of air, $W/(mK)$
L	Collector characteristic length, m

N	Day of the year, e.g. January 1 st = $n = 1$
Nu	Nusselt number
P	Distance between pores (pitch) of transpired collectors, m
Pr	Prandtl number, calculated at average velocity in the plenum
Q_b	Collector heat loss from the back into the building, W
Q_{RO}	Collector surface radiant heat loss to the outside, W
Q_s	Absorbed solar radiation, W
Q_{wind}	Collector surface convective heat loss due to wind, W
Q_u	Useful heat captured by the collector, W
Re	Reynolds number, calculated at average velocity in the plenum
T_{plm}	Temperature at collector plenum outlet, K
T_{amb}	Temperature of the immediate ambient air, measured near the collector surface, K
T_b	Temperature at collector backplate, K
T_{dp}	Dew point temperature of ambient air, K
T_{ma}	Equivalent temperature that gives the mean air temperature at mid-plenum (K)
T_{mid}	Temperature at the middle layer, i.e. transpired absorber
T_{PV}	Temperature at photovoltaic module surface, K
T_{room}	Temperature inside the test hut, simulating room condition, K
T_{sky}	Sky Temperature, K
T_{STC}	PV cell temperature at Standard Testing Conditions, 25°C
T_{surf}	Temperature at collector surface, K
V_{oc}	PV open circuit voltage, V
V_{peak}	PV voltage at maximum power point, V
V_{plm}	Average velocity of air in the collector plenum, m/s
V_s	Suction velocity at transpired collector surface, m/s
V_{wind}	Wind speed at collector surface, m/s
y	Distance from the bottom of the PV module (from 0 to 0.36m);

Abbreviations and Acronyms

AHU	Air Handling Unit
BIPV	Building Integrated Photovoltaic
BIPV/T	Building Integrated Photovoltaic/Thermal
CDD	Cooling Degree Day, °C-d
CFD	Computational Fluid Dynamics
CFM	Cubic Feet per Minute
CIS	Copper indium selenide
CMHC	Canadian Mortgage and Housing Corporation
COP	Coefficient of Performance
DC/AC	Direct Current / Alternating Current
EPS	Expanded polystyrene
HDD	Heating Degree Day, °C-d
HG/LG	High Gain/ Low Gain (solar radiation conditions)
HRV	Heat Recovery Ventilation
HVAC	Heating, Ventilating and Air Conditioning
HW/LW	High Wind/ Low Wind (surface parallel wind flows)
INAC	Indian and Northern Affairs Canada
I-V tracing	Current-voltage tracing
JMSB	John Molson School of Business (BIPV/T facade)
MFR	Mass flow rate, kg/hr
MHG	Metal halide global
MPP	Maximum power point
NRCan	Natural Resource Canada
NSH	Northern Sustainable Houses
NWT	Northwest Territories
NZEB	Net Zero Energy Building
OSB	Oriented strand board
PCM	Phase change material
PV	Photovoltaic

SIP	Structural Insulated Panel
SS	Steady state
SSEC	Solar Simulator / Environmental Chamber Laboratory
STC	Standard Testing Conditions
SW	SolarWall, product of Conserval Engineering
SW-h/SW-v	SolarWall with horizontal corrugation/with vertical corrugation
TG	Transpired Glazing
TMY	Typical meteorological year weather file
TRNSYS	TRaNsient SYstems Simulation program
UTC	Unglazed Transpired Collector

Greek Letters

α	Absorptance
α_s	Solar altitude angle, $^\circ$
β_{PV}	PV module temperature coefficient, $\%/^\circ\text{C}$
Δ	Change in a variable
δ_x	Error of a measured quantity x
ε_{HX}	Effectiveness of transpired collectors
σ	Stephan-Boltzmann constant, $\text{W}/\text{m}^2/\text{K}^4$
ρ	Porosity of perforation for the transpired collectors
ρ_{air}	Density of air, kg/m^3
η_{mp}	Maximum power electrical efficiency of the PV module
η_{EQ}	Thermal equivalent efficiency of PV/T systems
η_{PV}	Nominal electrical efficiency of the PV module
$\eta_{\text{PV@STC}}$	Electrical efficiency at standard test conditions
η_{TH}	Thermal efficiency of PV/T (excluding electric output)
θ	Incidence angle, $^\circ$
γ	Reflectance
τ	Transmittance
μ	Dynamic viscosity of air, $\text{kg}/\text{m}/\text{s}$
μ_x	Uncertainty of a measured quantity x
ν	Kinematic viscosity of air, m^2/s

1. Introduction

1.1 Context and Motivation

1.1.1 Northern Housing Challenges

Canada's North (Yukon, Northwest Territories, Nunavut) accounts for 0.3 percent of Canadian population and over one-third of the total land area. With a population of just over 100,000 dispersed across 3.5 million square kilometers of latitude 55°N and beyond, housing in the North is confronted by unique climatic and socio-economic challenges.

Natural Resource Canada (NRCan) categorizes four climate zones (A, B, C and D) in Canada based on an average annual temperature indicator called heating degree-day (HDD), which is the annual sum of the degrees of the average daily temperature for all days below 18°C averaged over 30-year period. Most of the three northern territories fall in Zone D (>8000 HDDs) and generally have little to no cooling requirements even in the summer. To put the numbers into perspective, the HDD of Montreal (45°N) is calculated to be around 4575 °C-day under Zone B (NRCan, 2011).



Figure 1.1 Three Northern Territories (left) and Climate Zones of Canada (right), Picture from NRCan, 2011

In addition to the high heating requirements, low ambient temperature in the North increases the building susceptibility to heat loss due to thermal bridges, under-insulated envelope and air leakage. Extreme harsh weather (snow storm, hail, etc) in the winter imposes serious structural and hygrothermal stress on buildings. Moreover, labor shortage and limited transportation season are major roadblocks associated with budget and timeline for construction in northern remote regions.

At the same time, there is significant housing shortage in the Territories. In Nunavut, even with the presence of 51% (4400 units) social housing, the current housing shortfall is estimated at 3000 units (Statistic Canada, 2010). In fact, the native communities in Northern Canada have the highest birth rate and overcrowding percentage in the country.

Though rich in natural resources such as crude oil and natural gas, Canada's North relies almost completely on imported fossil fuel from southern locations. Coupled with difficulty in distribution and transportation, the cost of energy in the North can be extreme. Electricity price per kilowatts-hour (kWh) in some communities is over 10 times higher than the Canadian average. Per capita energy cost in the North is almost double the national average. (National Energy Board, 2011)

The energy use pattern in the North is also very different than southern locations. Natural gas, as the major fuel in Canada (excluding transportation) and the cleanest of all fossil fuels, accounts for only 12% of energy use in the North (National Energy Board, 2011). The majority of houses in the North are heated by heating oil, which is shipped up from southern locations with inherent transportation footprint.

Energy from renewable sources constitutes a negligible amount (less than 0.02% for solar and less than 0.12% for wind) of the total energy and electricity source. For instance, Nunavut uses 100% diesel-generated electricity with small local grids (National Energy Board, 2011). As cost of central grids is prohibitive for remote communities, Northern energy supply has a unique decentralized pattern that is almost completely dependent on imported fossil fuel.

1.1.2 Opportunities for Housing in High-Latitude

Challenges also go hand in hand with opportunities. In response to the high heating loads and costly energy, northern housing design is motivated to move towards greater building efficiency and the harnessing of renewable energy.

In Canada, buildings accounts for 31% of the total energy use (Natural Resource Canada, 2010), the amount of which is even higher in the North. As part of the essential infrastructure that has a typical service life span of 50 to 100 years, the building sector in Northern Canada entails vast potential for better energy efficiency, especially with the current housing shortage.

Significant savings from energy conservation can be achieved at very low added cost, by using high-performance building envelope and strategically sizing the south-facing window area as well as thermal mass to maximize passive solar gains. In 2009, Yukon announced the SuperGreen housing standard, following the most stringent building energy compliance nation-wide with prescriptive requirements of RSI-4.93 walls and RSI-10.56 ceilings, as well as triple glazed windows of less than 15% wall area (Yukon Housing Corporation, 2009).

Building envelope can also serve beyond its traditional role as a passive enclosure. Emerging development of building-integrated photovoltaic/thermal (BIPV/T) technologies allows designers to integrate an active energy-capturing skin as part of the envelope system.

In fact, the high energy cost and dependency on imported fuel in northern communities offers a more competitive payback time for well-researched renewable technologies such as the photovoltaic (PV) and solar thermal. Compared to southern locations, the marginal price increase per kWh produced by solar panels is quickly offset by the reduction of expensive fossil fuel and associated transportation cost for remote locations.

Contrary to common perception, Canada's North has an abundant potential for solar energy. For south-facing photovoltaic panels with latitude tilt, the yearly PV potential for Iqaluit (Latitude 63.8°N, 1059 kWh/kW) and Fort Smith (Latitude 60°N, 1126 kWh/kW), are comparable to, or even higher than, southern locations like Montreal (Latitude 45°N, 1185 kWh/kW) and Halifax (44.7°N, 1074 kWh/kW) (Natural Resource Canada, 2007).

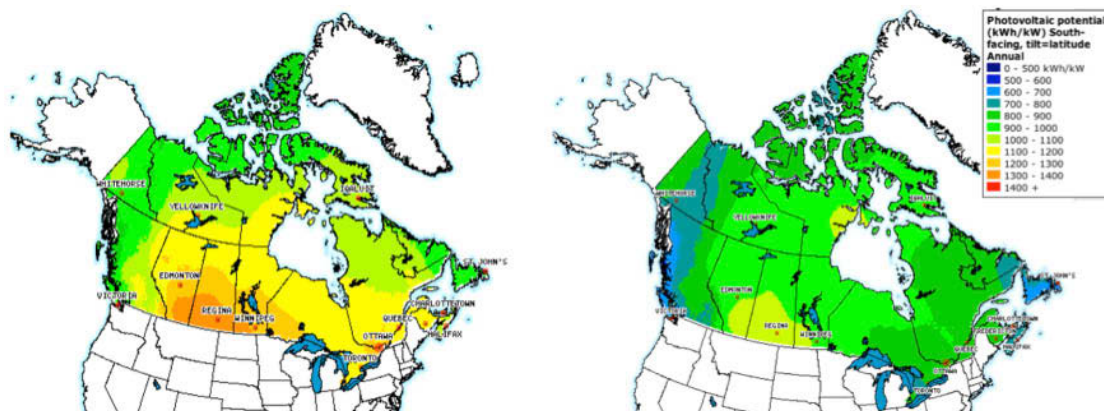


Figure 1.2 Photovoltaic Potential kWh/kW of Canada at Latitude tilt (left) and Vertical tilt (right), Picture from NRCan, 2007

The real challenge pertaining to solar utilization in the North is the strong seasonal pattern of daily global radiation and its misalignment with heating loads (e.g. long daylight hours in the summer and almost no sunlight in the winter when heating load is the highest). This seasonal mismatch between solar availability and heating loads is also present in southern locations, but much more pronounced near the arctic.

The decentralized energy pattern and fossil fuel dependency in the North is aggravated in remote communities by the lack of grid infrastructure for energy distribution. With the rising prices and impending depletion of imported fossil fuels, on-site renewable generation can offer a complementary local source of energy in summer and shoulder seasons at a competitive price rate.

1.2 Research Scope

1.2.1 Passive and Active Design Principles

When subjected to harsh environmental conditions, the regulative functions of building envelope are amplified. Passive measures of solar utilization can be adopted at minimal cost, by optimizing interlinked design variables such as house insulation value, south-facing window area and thermal mass. This thesis will focus on the investigation of facade-integrated active solar components suitable for Nordic climate.

Though wood-frame structures is currently the main form of construction in the Canadian North, a pre-fabricated high-performance envelope system, Structural Insulated Panel (SIP), offers an attractive alternative for northern housing by minimizing installation time and difficulty. The pre-fabricated nature of the SIP envelope is

extendable to the integration of solar collectors, which also obviates the need for exterior cladding to further reduce the installation and labor cost.

Combining passive measures of conservation (high-performance envelope) and active generation (on-site solar energy), the building sector in Northern Canada can readily achieve considerable displacement of expensive fossil fuel and its associated transportation cost. At the same time, the motivations and innovations exhibited by the active envelope research for high latitudes may also be applicable for housing design in temperate climates.

1.2.2 Scope and Limitations

The thesis work investigates both solar electric (Photovoltaic) and solar thermal technologies, as well as the use of Building Integrated Photovoltaic/Thermal (BIPV/T) technology to co-generate valuable electricity as well as heated air. Note that building-integrated solar system is designed to maximize efficiency and output in shoulder seasons, while imported fuel is still necessary for winter heating.

Only air-based collectors are discussed as design options to avoid encountering high risks of winter freezing, though literature review (Chapter 2) also includes solar domestic hot water installations or other liquid-based solar collectors. To account for the maintenance difficulty and lack of technical personnel in remote locations, only off-the-shelf low maintenance technologies are considered. The active envelope system is designed to be pre-fabricated and easy to assemble on site, adding feasibility to real-world adoption.

In addition, the thesis scope is limited by:

- Physical restrictions of the laboratory setting: see Section 4.1, Solar Simulator and Environmental Chamber (SSEC) Laboratory;
- A manageable level of complexity pertaining to the design and evaluation of the façade-integrated solar collectors.

1.3 Research Objectives

The research work investigates the potential of energy generation and conservation by full-scale solar-harnessing envelope systems designed for cold climate. The combined efforts of experiments and simulation aim to fulfill the following quantifiable objectives:

- To design and optimize an array of façade-integrated solar collectors that are potentially suitable for cold climate;
- To experimentally evaluate and compare collectors' performance under indoor-simulated climatic conditions (irradiance, temperature, humidity and wind);
- To develop custom thermal network models for the novel solar collectors and validate simulation results using experimental data;
- To perform parametric studies of low cost adaptations to improve collector suitability and overall system compatibility to the real Nordic conditions;
- To explore system-level optimizations regarding the usage of solar electricity and heated air, as well as auxiliary HVAC systems;
- To determine annual energy saving potential for Arctic low energy houses using building integrated solar systems.

1.4 Thesis Overview

Chapter 1, the introductory chapter, includes information on the background and context of this thesis project, the scope and limitations of the investigation, a summary of main objectives and implications of the research work.

Chapter 2 presents a literature and technology review on relevant subjects, including Arctic low energy building best practices, high-performance building envelope systems, innovative building-integrated solar technologies, heat transfer theories for glazed and transpired collectors, and suitable auxiliary mechanical systems.

Chapter 3 summarizes the design methodology and prototype construction of an array of building integrated solar collectors potentially suitable for high latitude applications. It is followed by Chapter 4, which contains detailed experimental evaluation of the proposed solar prototypes, using the state-of-the-art Solar Simulator and Environmental Chamber Laboratory facility.

Chapter 5 discusses the development of custom thermal network models for the façade-integrated solar prototypes. Forced convective heat transfer coefficients induced by parallel wind and surface suction are investigated for transpired collectors. Steady-state simulation results are validated using experimental data.

The discrepancy between experimental results obtained from the Solar Simulator and from the Environmental Chamber is corrected numerically based on heat transfer principles to address the systematic differences between the two facilities. Additionally, annual performance of the solar prototypes is evaluated based on steady-state performance. Lastly, conclusions and recommendations for future work are presented in Chapter 6.

This thesis also includes two research reports (Appendix F and G), investigating the current state of performance for two solar technologies common in Canada's North. Fieldwork were conducted by the author to inspect existing solar installations at high latitudes, including six solar transpired collectors in Northwest Territories and a façade photovoltaic system in Nunavut. By addressing and learning from the current operational issues, the case studies gave a practical perspective to the research of building integrated solar technologies suitable for high latitudes.

2 Literature Review

Chapter 2 discusses the different studies and pilot projects regarding low energy building practices and integrated solar technologies in Nordic climate. Both passive envelope strategies and active solar integration are covered in the literature and technology review.

2.1 Best Practice of Nordic Low Energy Building Design

2.1.1 Survey of Nordic Low Energy Buildings Outside Canada

Table 2.1 below provides a comprehensive survey of existing low-energy building projects in Nordic countries outside Canada, featuring vigorous passive solar design and state-of-the-art building integrated solar technology.

Table 2.1 Summary of Nordic Low Energy Buildings outside Canada

Project Location (Outside Canada)	Latitude	System Size	Design Features					
			Passive Solar Design	Solar Thermal (Space heating)	Heat Recovery Ventilation (HRV)	Heat Pumps	Photovoltaic System (PV)	Solar Domestic Hot Water Heating (DHW)
IEA5 Solar House, Pietarsaari, Finland	63.5°N	10 m ² collector, 2.1kwp PV	✓	✓	✓	✓	✓	✓
Low Energy House, Sisimiut, Greenland	67°N	200 m ²	✓		✓			✓
28 Apartment buildings, Løvåshagen, Bergen, Norway	60.5°N	112 m ²	✓	✓				✓
Rønne-bækhave II, Næstved, Denmark	55°N	28 m ²	✓		✓	✓	✓	✓
SOLTAG (pre-fab houses), Copenhagen, Danmark	55.5°N	2 m ² collector, 3.5 m ² PV	✓	✓	✓	✓	✓	✓

As shown in Figure 2.1 (left), Norling et al. (2006) outlined the design of a low energy house in Sisimiut, Greenland. With careful design and installation of a well-insulated, air-tight building envelope, the 200m² house consumes only half the energy permitted in the building code. Based on this case study, Vladykova et al. (2008)

performed sensitivity analysis in Bsim to model the effects of changing insulation thickness and window types. Optimal south-facing window area to effectively capture solar gains is also discussed in their studies.



Figure 2.1 Left: Low energy house in Sisimiut, Greenland, 67°N, 2005 (Norling et al. 2006); Right: IEA5 Solar House in Pietarsaari, Finland, 62°N, 1994 (IEA, 1997)

Figure 2.1 (right) features the IEA5 Solar House with the integration of a 2.1kW PV system and a 10m² solar collector on the south-facing roof. IEA (1997) reports that the solar combisystem and water tank, supply more than 50% of the DHW demand and all space heating demand from April to September, while in the winter a ground-source heat pumps supplements the energy demand. The building is airtight and constructed with super-insulation and high-performance windows. Floor heating, is used and a Heat Recovery Ventilation (HRV) unit is incorporated in the ventilation systems.

In Denmark, researchers take facade photovoltaic (PV) integration to a new level by venting the space behind the PV panels (Jensen, 2001). The three-storey building (Figure 2.2, left) in Skovlunde hosts the field-testing of 5 different PV-VENT systems. The PV gable (front wall) pre-heats the ventilation air and cools the PV panel. Three solar chimneys are powered with bands of PV panels integrated into the building facades. DC

fans are directed connected to PV for active ventilation and air-to-air heat exchangers of 80% efficiency are used. However, Bosanac et al, (2003) concluded that pre-heating ventilation air via PV facades is of little economic benefit in this particular case, due to the high heat loss from the PV facades to the cold exterior.



Figure 2.2 Left: PV-Vent facade in Skovlunde, Denmark, 56°N, 2001 (Jensen, 2001); Right: Rønnebækhave house in Næstved, Denmark, 55°N, 2005 (Andresen et al., 2008)

The Rønnebækhave passive house (Figure 2.2, right) built with a German ‘Passiv Haus’ standard of a yearly heat consumption of 15 kWh/m² (Andresen et al., 2008). As the PassiveHaus standard is normally meant for mild climate, the overall building design is challenging considering its Nordic location (55°N). In addition to thick insulation and high performance windows, the house incorporates a 5kWp PV system, a ground source heat pump, HRV systems, 28 m² flat-plat solar collector for DHW use coupled with 8 storage tanks (240L each) using 2 internal heat exchangers (Pedersen, 2008).

Pedersen (2008) also discussed about another Danish pilot net zero energy project, the SOLTAG house in Copenhagen (55.5°N). As a EU demonstration project, the SOLTAG house features a prefabricated active roof prototype that integrates hot air collectors and PV panels as a single roof unit. The hot air preheated by the active double

skin solar roof is supplemented by a small air-source heat pump to supply under-floor heating for the house. The DHW tank also functions as a buffer storage for the solar heated air. The passive solar design and well-insulated envelope reduced the heating demand to 30 kWh/m², allowing the house to be net zero energy and CO₂ neutral during operation. (Danish Technological Institute, 2008)

2.1.2 Survey of Low Energy Building Practices in Northern Canada

Led by the Canadian Mortgage and Housing Corporation (CMHC), several housing initiatives took place to promote sustainable building practices in Canada. As part of the Equilibrium Sustainable Housing Demonstration Initiative, the Eco-Terra house (Eastman, Quebec) is the first Equilibrium project aiming for the net-zero energy target. The design of the Eco-Terra focuses on coupling low energy demands with an active pre-fabricated air-based BIPV/T roof component. The generated electricity supplies fans and appliances, while the solar heated air assists space heating, domestic water heating and clothes drying (Chen et al., 2010).

Located in Edmonton (53.5°N), the Riverdale house was completed in 2008, as the most northern of all Equilibrium homes with the highest insulation values (Brostrom & Howell, 2008). After careful deliberation and cost-benefit analysis, the house used double stud construction with R-56 walls, R-100 ceilings and quadruple-glazed windows. As shown in Figure 2.3 (left), solar hot water collectors are tilted at a wintertime optimal angle of 90°, and supply 78.1% of the space heating requirements and 93.8% of the domestic hot water heating. A 5.3 kW high efficiency PV array, mounted at an annual optimum tilt of 53°, enables the net-zero energy target over the course of a year (Habitat Studio & Workshop Ltd., 2007).



Figure 2.3 Left: Riverdale NetZero House, Edmonton, 53.5°N, 2008 (Howell, 2008);
Right: Northern Sustainable House, Inuvik, 68°N, 2011 (Photo taken by author)

CMHC (2009), together with local housing corporations, were key players for the construction of three Northern Sustainable Houses (NSHs) in Arviat (Nunavut, 2006), Dawson City (Yukon, 2006), and Inuvik (NWT, 2011). Unlike Alberta where the Riverdale house is located, the three northern Territories are more difficult to access and there is a large proportion of aboriginal population. To address the unique social and cultural issues of northern communities, the integrated design charrette of all three NSHs involved stakeholders including designers, builders, municipal representatives, prospective residents and community elders.

Due to restrictions of up-front funding, the NSH in Arviat and Dawson city were designed to be solar-ready, with a tilted façade surface allocated for solar installations. In 2011, the most recent NSH was completed in Inuvik (Figure 2.3, right) and the monitoring phase will commence later in 2012. The duplex implemented double-wall construction with a Structural Insulated Panel floor, high efficiency appliances and heat recovery ventilation (HRV) systems. The NWT Housing Corporation (NWT HC, 2012) concluded an approximately 20% cost increase than typical construction, plus additional funding from CMHC for the roof mounted photovoltaic arrays and solar hot water collectors.

While double-wall construction may be suitable in northern locations accessible by road (e.g. part of Yukon and NWT), the labor and material intensity required by double-wall is still prohibitive for locations accessible only by Sea Lift (e.g. most of Nunavut). With the shortage of skilled labor and the limited building season, it is challenging to construct super-insulated envelope quickly and airtight.

As a result, a unique Structural Insulated Panel (SIP) system was developed for Nunavut social housing in 2009 by KOTT Group (Armstrong, 2011). Unlike the predecessors that are thin, urethane SIPs, the Kott SIP is composed of two 16 mm oriented strand board (OSB) skins sandwiching 273 mm of rigid expanded polystyrene (EPS), bonded by urethane glue that also acts as the vapor barrier (Figure 2.4).



Figure 2.4 Structural Insulated Panel House (left) and SIP cross-section (right). Picture: Armstrong, 2011

Each SIP panel is manufactured with wood I-joists and thermal breaks at joints and serves as an all-in-one system of structure, insulation and air/weather barrier and vapor control. As a result, the SIP building can be put together at a fraction of time compared to wood-frame constructions. It was demonstrated that the entire floor SIP system was complete in 3.5 hrs by a five-man crew. The ease in construction also comes with additional benefits of minimized thermal bridges and better air-tightness. A typical SIP

house offers an overall RSI of 7.9 m²K/watt (R-40 Floor, R-36 Walls, R-50 Roof) and a blower-door tested air-tightness of 0.2ACH at 50Pa.

Table 2.2 summarizes some of the low energy buildings in Northern Canada mentioned before. Note that the first two projects in Fort Smith and in Iqaluit are merely traditional buildings added with renewable technologies (unglazed transpired collector and photovoltaic, respectively). These two building-integrated solar technologies are the most popular and widely implemented in Canada’s North. Further information can be found in Appendix F and G (case studies).

Table 2.2 Summary of Solar Technologies used in Buildings in Northern Canada

Project Location (Within Canada)	Latitude	System Size	Design Features					
			Passive Solar Design	Solar Thermal (Space heating)	Heat Recovery Ventilation (HRV)	Heat Pumps	Photovoltaic System (PV)	Solar Domestic Hot Water Heating (DHW)
Fort Smith Recreation Center, NWT	60°N	150 m ²		✓	✓			
Nunavut Arctic College, Iqaluit, Nunavut	63.5°N	26 m ² 3.2 kwp PV			✓		✓	
Northern Sustainable House, Inuvik, NWT	68°N	20 m ² PV, 18 m ² DHW			✓		✓	✓
Northern Sustainable House, Dawson City, Yukon	64°N	N/A	✓		✓			
E/9 House (SIP), Dawson City, Yukon	64°N	6 m ² DHW, 6 m ² PV	✓		✓		✓	✓
Riverdale NetZero Energy Home	53.5°N	21 m ² DHW, 33 m ² 5.6kw PV	✓	✓	✓	✓	✓	✓

2.2 Design Principles for Low Energy Houses in Cold Climate

2.2.1 Low Energy Building Practices in Northern Europe and Canada

As shown in Section 2.1.1 and 2.1.2, the sustainable building practices in different Nordic countries have many interesting similarities, but also differ in important ways. The rule of thumb applies to all cold climate construction: ‘insulate, build tight and

ventilate right'. Under extreme climatic loads, the design and installation of a well-insulated, air-tight building envelope is crucial for the longevity of high-latitude constructions (Kalema and Pylsy, 2008).

Cornick et al. (2009) investigated four high performance wall systems in comparison with two baseline walls, using a parametric energy model analyzed for seven Canadian arctic locations. It is concluded that while the most highly insulated wall system exhibits best performance regarding space-heating consumption, it is not the only concern in the North when selecting one envelope system over another. The estimated lifetime space heating saving must also offset the increased material, transportation and labor costs, which are of significant amounts at high latitudes. Their research indicates that pre-fabricated systems (e.g. SIP) may have more saving potentials compared to traditional labor-intensive wall systems of similar thermal properties.

While passive solar design principles are widely employed in Nordic countries in Europe, the concept is still relatively new to constructions in Northern Canada. Though Canadian building codes (Canadian Commission on Building and Fire Codes, 2011) have stringent recommendations of insulation value and air-tightness, the building orientation, south-facing window area and thermal mass are not design mandates for high-latitude construction.

To make the implementation of passive solar principles more difficult, transportation and grid infrastructure in northern Europe is much more developed than northern Canada, partially due to the higher population density in Europe. To save on transportation cost, Canada's North uses light-frame construction that typically has no thermal mass inherent

to building materials. Canadian researcher Harold Strub (1996) pointed out that window design in Northern Canada often ignores the high heat gain through glass in springtime during long daylight hours. As the room is usually super-insulated and built of light weight materials, it has no way to store the excess heat during the day and windows empties out the indoor warmth at night by quick conductions.

Recent development and on-going price drop in high-performance windows and lightweight thermal storage (phase-change-materials) offer solution to this dilemma. Darkwa et al. (2006), among other researchers, reported that addition of phase-change-materials (PCM) tiles or drywall to the building fabric significantly increases the minimum room temperature at night for a passive solar house in cold climate.

As shown in Table 2.1 and 2.2, low energy building design in Nordic climate favors multi-unit (duplex or more) construction. Due to the lowered surface-to-volume ratio and shared mechanical/sewage systems, multi-unit dwellings can achieve better energy efficiency at a lower added cost. For example, the Nunavut Social Housing program has started to make a conscious shift from single-family houses to multi-family building design for better energy efficiency (Statistic Canada, 2010).

In the 2006 budget alone, the Canadian government invested up to \$300million dollars to address the acute housing needs in Yukon, North West Territories and Nunavut (INAC, 2006). Given the high energy consumption in the northern building sector and increasing demands for new construction, the market for low energy buildings and building integrated renewable technologies is expected to grow and mature with continuing research and engineering efforts.

2.2.2 Suitability of Air Based or Liquid Based Solar Thermal Collectors

For a typical Canadian home, space heating accounts for 60% of the total residential energy used annually, followed by hot water heating of 20% (NRCan, 2003). Thus, incorporating solar thermal collectors or solar hot water heating system onto building envelope entails tremendous energy saving potential for cold climate.

Note that solar thermal collectors can use a heat transfer medium of either air or liquid. In General, air based collectors are easier to install and less maintenance intensive, while liquid based collectors are more efficient yet cost more to install and maintain. Andersen et al. (2008) conducted a comprehensive survey of building integrated solar thermal collectors in northern Europe. Despite the systems complexity and propensity to freezing, they confirmed that liquid based solar hot water or solar combisystems (space heating and hot water) are common among arctic low energy buildings (Table 2.1).

At the same time, Canadian low energy buildings favor simple air-based solar thermal systems. One of the most widely implemented solar thermal systems in Northern Canada is a product named SolarWall, a low-cost unglazed transpired collector producing solar heated air (discussed in Section 2.3). The main reason behind the different preferences is that European market is more attuned to complex liquid systems that require expertise for installations and maintenance, while the Northern Canadian market still struggles with transportation difficulty and skilled labor shortage.

While northern Europe and Canada may be of similar latitudes, the oceanic climate in Europe is more temperate than the continental climate in Northern Canada. To avoid any freezing problems and long-term durability concerns, this thesis will discuss only air-

based solar systems suitable for Northern Canada.

2.2.3 Suitability of Roof or Façade Integration

It is widely accepted that an equator-facing orientation is optimal for photovoltaic panels (Hussein et al., 2004), and the optimum tilt angle of a photovoltaic panel should be equal to the site's latitude for maximum annual output.

Swedish researchers Rönnelid et al. (1996) concluded that for high latitude locations (more than 60°N), the winter solar radiation only contribute marginally to the total collectible energy year-round and thus, for a fixed solar collector, the 'tilt=latitude' concept is invalid as the collector should be oriented to receive maximum light during the summer peak (e.g. mid Sweden, latitude = 60°, optimal tilt =45°).

Cheng et al. (2009) performed a series of calculations for 20 locations worldwide and states that latitude of the site can be used as the optimal angle of PV tilt without too much compromise in annual output. Their findings revealed a maximum difference (9.7%) in receivable solar energy occurs at arctic conditions and no discrepancy at the equator. As low-slope roof construction is common in Northern Canada to minimize wasted attic space, it is a reasonable compromise to use façade integrated solar collectors (90° tilt) than roof integration (10° to 30°).

Moreover, reflected sunlight from the snow (albedo>0.8) in early spring and late fall enhances the façade system performance, partially compensating for the shorter sunny duration in northern locations. If conditions permit, a slightly tilted façade (e.g. 60° to 85°) can maximize the overall insolation received by the surface, provided that snow shedding and drainage are considered.

As long as the ease in construction can justify the loss in collectible solar energy due to non-optimal tilting, either vertical or near-vertical integration of solar collectors are acceptable options for high-latitudes. The most important consideration is “integration”, as active solar components often becomes “added” systems and ignores the interaction between solar skin and the building envelope. If well designed and factory mounted, the solar skin can replace the exterior cladding of the building envelope without penetrating any air/vapor barriers, and act as an integral part of the active envelope system.

2.3 Transpired Solar Collector Technology in Northern Canada

2.3.1 Unglazed Transpired Collector

As one of the most widely implemented solar technologies in Canada’s North, the Unglazed Transpired Collector (UTC) is essentially a perforated dark sheet with pores of 0.5%-2% opening area and an air cavity/plenum behind the cladding. A Canadian company (Conserval Engineering, 2010a), has developed a product called SolarWall® using corrugated dark metal cladding with distributed perforation (Figure 2.5).

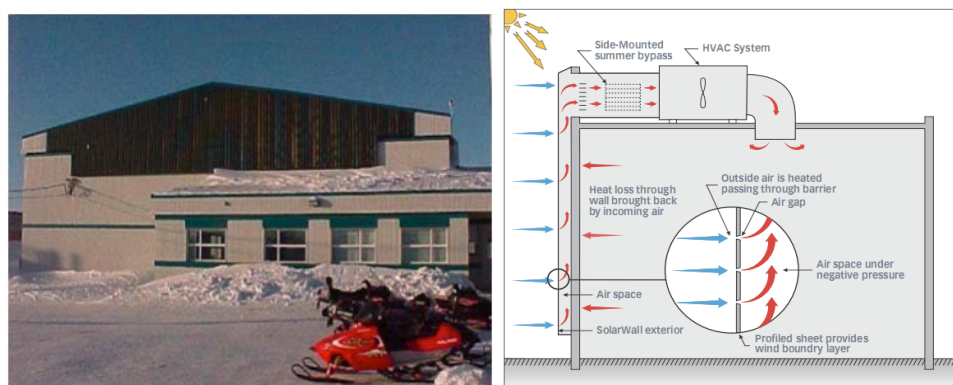


Figure 2.5 Left: Dark UTC façade, product name SolarWall, Rankin Inlet, Nunavut, 67°N; Right: Schematics of how SolarWall works; Pictures: Conserval Engineering, 2009

UTC (SolarWall) is a low-cost and highly efficient solar thermal system that is well suited for façade integration to pre-heat ventilation air in residential and commercial buildings. At night, the air plenum also recaptures heat loss from the building envelope and contributes to the overall energy savings.

The research on perforated plates for solar collectors started mainly with Kutscher et al. (1993), with the development of the basic heat loss theory for flat plate UTCs. Compared to conventional glazed solar thermal collectors, UTC has distributed air inlets across the dark absorber surface, which effectively lowered the surface losses (Kutscher et al., 1993). As there is no need for glazing or covers, the optical losses and collector cost are also reduced. Those distinct advantages of UTC work particularly well in northern cold climate. Many of such UTC facades (SolarWall) have already been implemented in the far North at latitudes as high as 68°N (Inuvik) to pre-heat building ventilation air.

One of the most important indicators for UTC performance is the collector exchanger effectiveness, ϵ_{HX} , which characterizes how “effective” a system is at converting the captured heat from its absorber to useful energy. In order to find a numerical expression for ϵ_{HX} , Kutscher (1994) performed experiments on several plates of different thicknesses, hole diameters and pitches on a triangular layout, by subjecting the plate to a parallel wind.

Van Decker et al. (2001) furthered Kutscher’s work to flat plate UTC with circular holes laid out in square pitch, also taking into account back loss and surface loss. The UTC effectiveness is expressed in three parts: the heat transfer occurring at the front face

ϵ_f , in the sides of the holes ϵ_h , and at the back of the plate ϵ_b . Further details on how to calculate UTC effectiveness are discussed in Section 5.1.3 and results are presented in Section 5.3.4.

$$\epsilon_{HX} = 1 - (1 - \epsilon_f)(1 - \epsilon_h)(1 - \epsilon_b) \quad (2.7)$$

Researchers from University of Waterloo, Summers (1995) and Delisle (2008) developed TRNSYS models to predict the performance of UTC collectors, by solving a set of energy balance equations. The auxiliary fan power is also optimized to minimize the amount of auxiliary energy needed. Summers' model uses Kutscher's relation (Kutscher, 1994) to calculate the Nusselt number, but does not account for any wind effects or for the corrugated shape of the absorber plate. As a result, Summers' model over-predicts the temperature rise at low suction rate and under-predicts the recaptured wall heat losses.

Other correlations of convective heat transfer coefficients for transpired collectors point to strong dependency on wind speed and suction velocity (Carpenter et al., 1999; Kutscher et al., 1991;) Detailed calculations on convective heat losses will be further discussed in Section 5.1.2 and 5.3.2.

2.3.2 Potential Improvements for Unglazed Transpired Collectors

Commercially available UTC systems commonly use corrugated dark metal sheets perforated with distributed pores (e.g. SolarWall). Unglazed transpired systems are particularly prone to convective wind loss, often aggravated by the corrugated profile. Gawlik & Kutscher (2002) studied numerically and experimentally the wind losses from UTCs with sinusoidal corrugations. Interestingly, they discovered that depending on

combinations of surface wind speed, suction velocity, and plate geometry, the flow on the UTC plate could be either attached or separated. In the case of attached flow, the wind heat losses were similar to flat plate UTCs, while convective wind losses from corrugated plates could be as high as 17 times greater than for flat plates.

Fleck et al. (2002) investigated UTC performance under different wind directions, speeds and fluctuation intensities based on outdoor experiments. Contrary to the parallel laminar boundary layer assumption used by Kutscher et al. (1993), Fleck et al. (2002) observed that turbulence occurs near the UTC surface and greater turbulence reduce the collector efficiency. Surprisingly, the collector's peak efficiency does not occur at zero wind speed, but at 1 to 2 m/s wind.

As the UTC absorber is exposed to the exterior environment, in addition to the surface convective loss attributed to surface wind and local suction, the surface radiant loss to outside can be significant as well. For sunny cold days at low heat removal rate, UTC surface (the absorber) is inevitably heated by solar radiation and its temperature can rise by over 40 °C greater than ambient temperature (Conserval Engineering, 2010a).

Therefore, an improved UTC system is proposed with transpired glazing (TG) as the exterior layer. A Quebec company, Enerconcept (2010) developed a novel transpired collector, Lubi-Wall, using high-transmittance weather-resistant polycarbonate sheets perforated with distributed air inlets. The transpired glazing is placed in front of existing walls and creates an second air plenum, while the wall exterior is painted dark as the absorber.

As the exterior layer (flat transpired glazing) remains cold during the sun-lit hours, the surface radiant loss and convective loss are both minimized for system compared to conventional UTC system. For northern applications when wind is strong (greater than 4m/s) year round, a flat exterior surface with lower surface temperature would be preferable in cold, windy regions.

Leon & Kumar (2007) conducted parametric studies on UTC collectors of varying porosity, airflow rates, solar radiation, and solar absorptivity/thermal emissivity. Kutscher's relation was used to calculate the absorber plate effectiveness. They concluded that solar absorptivity, hole pitch and air flow rate had the strongest effect on the collector heat exchange effectiveness and efficiency. Their results can be referenced when optimizing pitch and hole size for transpired collector/glazing design.

In fact, many SolarWall installations in Northern Canada have reported frost problems in winter and general under-performance compared to southern installations. The author, in collaboration with the Arctic Energy Alliance and Aurora Research Institute, conducted a field inspection and monitoring project in May 2012 to survey all the SolarWall installations in Northwest Territories.

Out of the six SolarWall systems inspected, only two are currently in operation. Only one system (Fort Smith) was monitored from 2000 to 2002 (Enermodal Engineering, 2001, 2002 and 2005). The rest of the installations have no monitoring mandates, making it difficult to evaluate the technical feasibility and energy output of such solar systems. Moreover, many of the SolarWall installations in NWT are oriented off south to different extents, contributing to significant annual loss and prolonged

payback time. There has also been cases of vegetation growth in front of the collectors, obstructing the collectible solar gain.

In terms of economical feasibility, it is extremely complex to evaluate real energy cost in Canada's North, as infrastructure costs for fossil fuel (e.g. tanks and pipeline) are not included in the actual energy price (Enermodal Engineering, 1997b). With additional government subsidy injected to keep the energy price affordable, calculation of payback time for solar installations is conducted on unlevel playing fields when compared with traditional fossil fuel prices in the Territories.

Based on findings from this applied research survey, it is recommended that incentive programs for SolarWall and other renewable systems should make ongoing monitoring mandatory for all new installations, to avoid the 'build and forget' mentality. Details of this field survey report can be found in Appendix G.

2.4 Building Integrated Photovoltaic Technology for Cold Climate

2.4.1 Flat Plate Photovoltaic Panels

Photovoltaic (PV) technology offers a reliable, on-site, complementary source of energy in summer and shoulder seasons at a competitive price rate for the North. In 1995, a 3.2kWp PV system was installed over 25m² of façade in Iqaluit at 63.8°N. The system has been delivering an average of 2016±200kWh of electricity annually (Poissant et al., 2004), which represents roughly 20% of electricity consumption by a Canadian average household. Since then, flat plate PV module prices have dropped from CAD\$11.09/watt in 1999 to \$3.31/watt in 2009 (Ayoub et al., 2009). At 80cents/watt in 2012, PV module

price is still dropping, while fossil fuel prices have risen dramatically since 1999 and will continue to climb in the next decade.

Diesel price (excluding transportation) has increased from 54 cents/Liter in 1999 to \$1.29/Liter in 2012 (NRCan, 2012). The life-cycle generation cost of diesel-generated electricity in remote communities can reach \$1.30/kWh (Canadian Electricity Association, 2006). Coupled with increasing efforts to minimize emissions, the current fossil fuel dependency in northern communities can be diluted in an economically feasible manner using rigorous solar technologies.

Compared to other renewable technologies such as wind turbines, flat plate solar panels are more suitable for building integration and typically have no moving parts. Using façade-integrated PV also obviates the need for exterior cladding and can be pre-fabricated with envelope panels to further reduce the installation and labor cost.

Once installed, photovoltaic modules are practically maintenance-free, as demonstrated by the Iqaluit PV façade project mentioned previously. The entire photovoltaic array (including the inverter) is in working order as inspected in April 2012, after 17 years of reliable performance and outlasting two monitoring systems.

Though some of the instruments are still capable of reading measurements, the most recent monitoring systems stopped feeding data since 2006. Calibration of the pyranometer is much needed and future monitoring projects should take into consideration the long-term pyranometer drift in high latitude locations (Thevenard 2005; Thevenard 2006).

Two types of single crystalline silicon PV panels were present in the PV array, Siemens M55 and Solec S53 modules (Poissant et al., 2004). The current output on a snowy day of the Siemens array is at 9.3% overall, 30% less than its original rated efficiency. However, the Solec array is producing only at 6.2% overall, 50% less than its original rated efficiency. (Appendix F)

Moreover, among the nine experimental modules tested by the author, all of the Siemens experimental modules are functional while two out of four Solec modules output no voltage. This finding indicates that some of the Solec panels in the array have also reached their end-of-life, contributing to the significant efficiency drop in the Solec array. In summary, though the initial rated output of the two PV types are very similar, in a long run, Siemens panels are performing more reliably than Solec modules.

The fact that the full-scale photovoltaic façade is feeding AC electricity to the school since 1995 is encouraging. Photovoltaic has been proven to be a reliable technology even under the harsh weather of the far North. Details of the field report can be found in Appendix F.

2.4.2 Concentrator-type Photovoltaic for Northern Applications

One of the innovations that promote solar market deployment is partially replacing the PV cells with inexpensive reflector materials, in order to increase the electric power generation per unit area. In northern Ireland, Mallick et al. (2004) designed and evaluated a novel non-imaging asymmetric compound parabolic photovoltaic concentrator (ACPPVC) at University of Ulster (55°N). Experiments showed that a power increase of

62% is achieved by adding the ACPVC under $400\text{W}/\text{m}^2$ irradiance comparing to a non-concentrating PV panel.

Similarly, an innovative concentrator system using bi-facial cell is developed by Swedish researchers to maximize winter output. The “Maximum Reflector Collector” (MaReCo) was evaluated experimentally for high latitude BIPV applications (Adsten, 2002; Norton et al., 2009;).

Concentrator PV systems are traditionally not building-integration friendly (Hansen et al., 2007), but other Swedish researchers Brogren et al. (2003) proposed an interesting concept of concentrating photovoltaic wall element, optimized for maximum collection at latitude 60°N from 15th March to 1st October. The ready-to-use façade system consists of the CIS thin-film PV modules, aluminum reflector and back insulation. The electricity production of this system is estimated to be twice as much as a non-concentrating system on an annual basis.

However, for all parabolic concentrating PV systems, non-uniform illumination on the solar cells will occur due to light concentration, and the system performance is determined by the lowest current output (least illuminated cell). The problem may be solved by custom design of the solar cell wiring connections according to the non-uniform illumination, which also lead to unwanted extra costs.

Aside from parabolic concentrators, lens concentrators, while effective for concentrating direct sunlight, are not suitable for high latitude applications due to the high content of diffused light. For the scope of this thesis, concentrator photovoltaic, though may be a valid alternative, will not be included in the design options in Chapter 3.

2.4.3 Suitability of Photovoltaic Technology in the High North

Compared to low latitude locations, Nordic solar conditions are characterized by low solar irradiance, high incidence angle (nearly horizontal), large portion of diffused radiation due to snow/ground reflection, and altered spectral distribution due to large air mass (Stamenic et al., 2004). The change in spectral characteristics, incidence angle and reduction in intensity can lead to a PV efficiency drop of up to 30% from solar irradiance of 1000 to 200W/m² (Eikelboom and Jansen, 2000).

TamizhMani et al. (1998) have shown a 57% drop of module efficiency, only 15% of which is due to the change in incidence angle and spectral alternation, while the rest attributable to non-ideal PV cell behavior at low irradiance. Their experimental and simulation findings stated that seasonal efficiency of PV for northern locations (Iqaluit) is generally: Spring> Fall> Winter> Summer.

The Standard Testing Conditions (STC) of photovoltaic cells is conducted under 1000W/m² and 25°C, while in northern locations like Iqaluit (64° N), 30% of total yearly radiation is below 200 W/m² and average temperature is below freezing for eight months of the year (Poissant et al., 2004). Furthermore, Nagano et al. (2003) reported degraded electrical efficiency by 9% in the winter due to condensation on the PV glass cover.

Field test of four types of common PV cells have confirmed the efficiency decline due to low irradiance (Poissant, 2009). His experimental results show that all four PV types perform similarly at low light conditions with high diffused content, though crystalline PV (c-PV) is preferred in northern locations due to its higher efficiency per area transported. In summary, PV performance based on commercial STC results needs

to be re-evaluated for high latitude applications. Mindful selection of the appropriate type and configuration of BIPV technology is particularly important to high latitude solar electric installations.

2.5 Building Integrated Photovoltaic/Thermal (BIPV/T) for Cold Climate

As most flat-plate crystalline photovoltaic panels yield 10% to 20% of electric efficiency, the rest of absorbed solar energy is turned into waste heat. The heat trapped behind the PV module also leads to increased module temperature that is detrimental for electric efficiency. A building integrated photovoltaic/thermal (BIPV/T) systems co-generates valuable electricity and thermal energy using the same building surface area. Pre-engineered building components with in-factory integration of hybrid solar systems (PV/T) serve as a competitive option for further market penetration (Affolter et al., 2005).

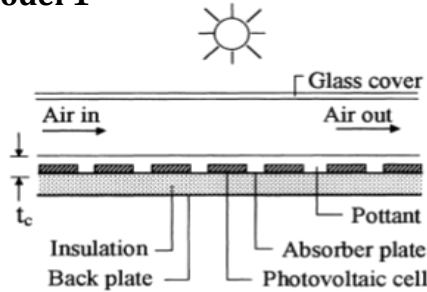
While the Danish PV-VENT systems in Lundebjerg (Jensen, 2001) reports poor thermal efficiency, it adopted a simple configuration of PV+cavity+insulation. Researchers have investigated many other system configurations of PV/T in an attempt to economically improve the PV/T system's thermal efficiency without jeopardizing its electric output.

Hegazy (2000) explored different PV/T (air) configurations as shown in Figure 2.6. He found Model 1 (single pass) has the lowest overall performance and Model 3 (double-pass) has the best performance at high mass flow rate ($>0.02 \text{ kg/s/m}^2$). For low ambient temperature and low solar radiation (e.g. northern conditions), it is concluded

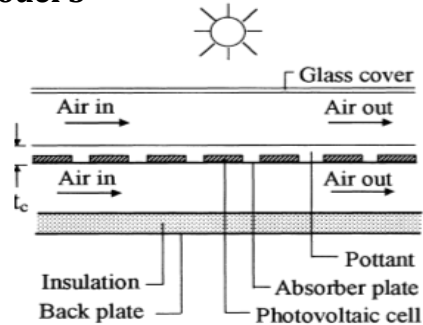
disadvantageous to use high flow due to the increased fan power and more heat loss.

Model 3 stands out as a suitable option due to its least consumption in fan power.

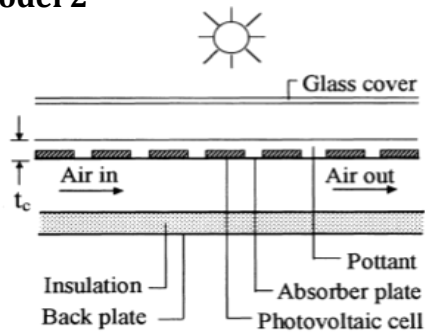
Model 1



Model 3



Model 2



Model 4

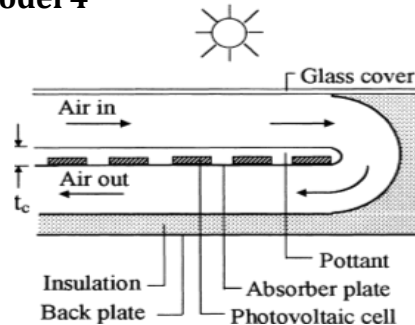


Figure 2.6 Schematic drawings of four different PV/Tair Models (Hegazy, 2000)

Tonui and Tripanagnostopoulos (2007) investigated cheap modifications to improve the thermal efficiency of PV/T (air) by adding fins, or by inserting a metallic sheet in the middle of the air cavity. Both adaptations enhance the useful heat convection and collector's efficiency, and may therefore be suitable for cold climates.

The combined cost of BIPV/T system is generally cheaper than same-size PV and thermal collectors installed separately (Chow, 2010). However, the International Energy Agency (IEA PV/T roadmap, 2002) did an extensive survey of the current-state development of BIPV/T and concluded that today's domestic PV/T systems is still far

from economic for Northwestern European countries, except for a few experimental pilot projects with BIPV/T (e.g. SOLTAG house).

Mei et al. (2003) created a dynamic TRNSYS thermal model for a ventilated PV façade/solar air collector for three European locations. The results suggest that the higher the latitude, the less heating energy can be saved by pre-heating ventilation air using the cavity behind PV façade: 2% heating saving for Loughborough (53°N), while 12% heating saving for Barcelona (41°N).

In Canada, research on a different type of BIPV/T air collectors started in the late 1990's with Hollick (1998). While simply ventilating behind the PV may not be effective, Hollick combined unglazed transpired collector (UTC) and photovoltaic by partially covering the part of the corrugations of a SolarWall with crystalline silicon PV cells. Experimental results show that even though thermal efficiency of UTC decreased due to the addition of PV cells, the total combined efficiency (electrical + thermal) was greater than stand-alone UTC.

In 2009, a state-of-the-art commercial-scale solar facade with UTC and the PV/T technology has been implemented in Montreal (45°N) based on an outdoor prototype studied by Athienitis et al. (2011). Custom-sized dark-framed PV panels are integrated onto the corrugated transpired SolarWall cladding (Figure 2.7), covering 70% of the total 288 m² façade of the John Molson School of Business (JMSB) building.

In addition to the electricity generation, heat is actively drawn from the back of the PV modules and the exposed UTC pores (Figure 2.7, left), contributing to heating the ventilation air while cooling the PV panels. In many regions of Northern Canada where

space heating is needed almost all year round, co-generation adds more incentives to adopting active envelope systems.

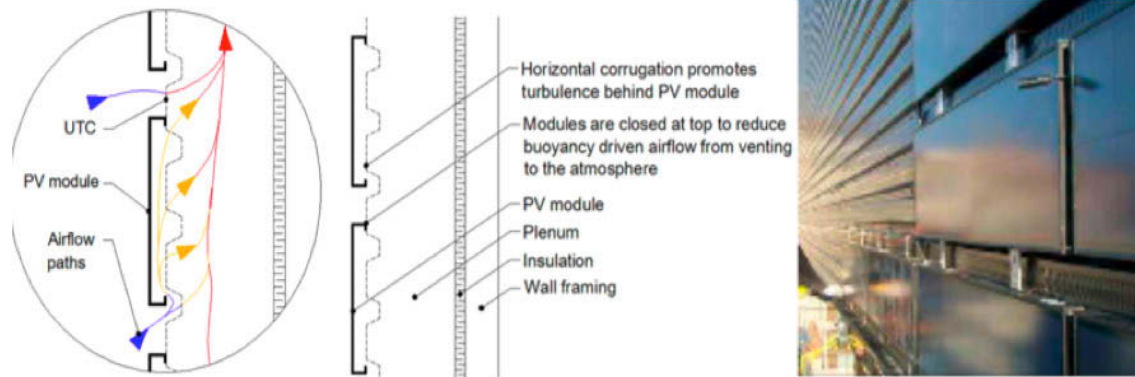


Figure 2.7 A BIPV/T demonstration project using UTC and PV/T solar facade in Montreal, Canada (Athienitis et al., 2011)

While BIPV/T systems conserve material and maximize overall output, the system thermal efficiency is lower than UTC system alone, due to the high emissivity of PV laminate and high surface temperature (Santbergen et al., 2010). Therefore, the inevitable trade-off between electric and thermal output for BIPV/T systems should be designed for according to energy needs and local climate.

2.6 Auxiliary Systems

As shown in Table 2.1 and 2.2 before, the application of heat recovery ventilation (HRV) systems is ubiquitous in most Nordic regions. HRV is a heat exchanger that recovers the heat from the exhaust air to preheat the fresh incoming air (McQuiston, 2005). At very low added cost, it is one of the most cost effective energy saving retrofit measures for cold climate.

Indoor air quality due to overcrowding and smoking is a known issue among the native communities in Northern Canada. CMHC (2010) published a survey showing improvement in air quality and better child respiratory health as a result of the installation and operation of HRV and increased ventilation rates.

However, there have been many reported cases when occupants open windows or doors to ventilate the building, instead of turning on the HRV. The author had personal experience in Nunavut and Northwest Territories that building residents use windows or fire exits as a form of ventilation, disregarding the warning that it will unbalance the HRV systems.

A façade UTC (SolarWall) system coupled with a HRV system was installed at the Fort Smith Recreation Centre (60°N) in NWT. Two-year of monitoring data showed that the combined system contribute to 78% of total energy required for ventilation air heating (Conserval Engineering, 2010b, 2010c). Enermodal Engineering (2005) reported that colder climates result in better performance of the combined system and thus, a shorter simple payback period than temperate climates, due to the greater temperature difference in HRV, longer heating season and higher solar radiation on vertical collector in Nordic locations.

It is also worth noting that even though the combined system perform better than SolarWall or HRV by itself, the energy saving is less than the sum of the two individual systems (Enermodal Engineering, 2005). This is because the SolarWall increases the fresh air temperature before it reaches the HRV, and HRV is consequently functioning at a lower efficiency as HRV efficiency is proportional to temperature differential between

incoming and exhaust air. Therefore, the addition of SolarWall is truly beneficial only when it offsets the HRV defrost coil load.

Extending the solar system design with HRV and/or heat pumps may also be cost-effective as the whole system performance is optimized. When BIPV/T systems are used, the low-temperature heat extracted from the PV module can be used to pre-heat ventilation air, or to drive a heat pump for domestic water heating or space heating. Depending on the existing auxiliary system and the desired end usage of solar electric/thermal energy, other equipment such as heat exchangers and storage tanks may be needed and will add to the system cost.

Zondag (2008) also pointed out that a large amount of storage is required for northern climate to obtain a significant solar fraction for space heating, while direct solar heating can fulfill most of the heating loads in southern regions. Seasonal storage is generally difficult for the North as geothermal storage risks disturbing the permanent frost. By the same token, ground-source heat pump is not suitable for construction on permanent frost either, as it also de-stabilizes the permanent frost and consequently the foundation (Strub, 1996).

On the other hand, short-term storage is achievable even for remote Nordic locations. Though challenged by the light-weight construction materials present in northern housing, short-term thermal storage can be attained by phase-change-material drywall, adding mass to envelope, or utilizing the domestic hot water tank.

3 Design Methodology of Façade-Integrated Solar Prototypes

3.1 Design Considerations

3.1.1 Prototype Design Guidelines

To keep the experimental investigation focused within the thesis scope, a set of guidelines are developed for the design of the solar prototype:

- Use SIP wall as substrate for solar integration; Whole assembly is pre-fabricated;
- Design the experimental prototype to accommodate several solar configurations;
- Investigate only air-based collectors, explore both Photovoltaic and Solar Thermal technologies, incorporate electric/thermal cogeneration (BIPV/T);
- Apply and extend the concept of distributed inlets in Unglazed Transpired Collectors (UTC) to reduce surface radiant and convective heat loss;
- Conduct parametric studies and optimize collector's efficiency (electric and thermal) prior to constructing experimental set-up;
- Repeat experiments under controlled climatic loads in the laboratory; Compare indoor experimental results with outdoor monitoring data from similar full-scale projects as well as published data from the Manufacturers.

3.1.2 Configuration Design and Features

It is important to note that all the components of the experimental prototype are off-the-shelf products that are commercially available and easily attainable. For northern applications, pre-fabricated air-based solar envelope systems are selected for simplicity, cost effectiveness and low maintenance requirements.

The designs of the collector configurations started with a simple UTC (product name SolarWall) layer. Additional layers of transpired glazing, glazing, and photovoltaic panels are added and mismatched to configure the best-suited collector for applications in Northern Canada.

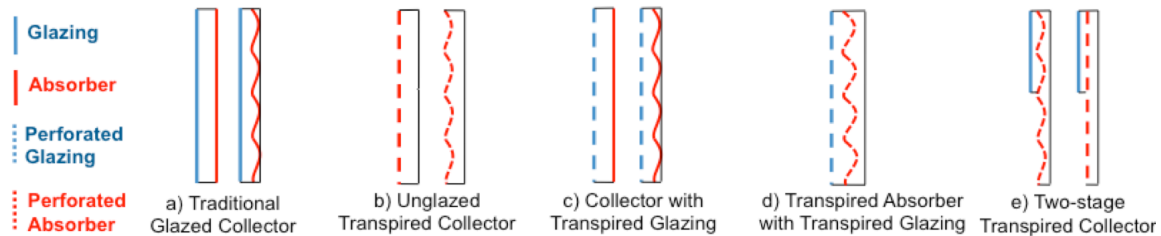


Figure 3.1 Design of façade collector configurations

Traditional UTC (Figure 3.1b), though widely implemented in Canada’s North and performing favorably compared to glazed collectors (Figure 3.1a), has a few fatal drawbacks in cold, windy climate. Firstly, the corrugated profile and perforated nature of UTC contributes to surface turbulence and significant wind-induced convective loss. Secondly, since the absorber of such UTC systems is the exterior metal cladding, it gets heated by the sun and results in high surface temperature and high radiant loss during sun-lit hours.

Therefore, the effect of extending the concept of distributed air inlets to transpired glazing is investigated (Figure 3.1c, 3.1d). High-transmittance weather-resistant polycarbonate sheets are perforated to 1% porosity as flat transpired glazing, and can be used to create a second air plenum in front of the transpired absorber (Figure 3.1d). The corrugated profile of the UTC absorber in Figure 3.1d creates in-plenum turbulent flows and actually increases the useful heat transfer.

The effect of partially covering the UTC with glazing is also explored (Figure 3.1e). Note that the glazing in this set up is interchangeable with photovoltaic panels to test the PV/T thermal performance. The sealed front surface of PV or glazing and the two-plenum design could minimize convective loss by harboring the heated air away from the direct wind penetration.

3.1.3 System-Level Design and Optimization

As a building integrated system, the solar collector should be sized according to the building energy demand and existing auxiliary systems. On one hand, the PV-generated electricity is a valuable high-grade energy that can be used for all households' electric needs. On the other hand, the solar heated air is useful only within a certain temperature range, depending on the end use. Note that system-level optimization of solar electricity and solar heated air will be left for future work. Only qualitative discussion is covered by the scope of this thesis.

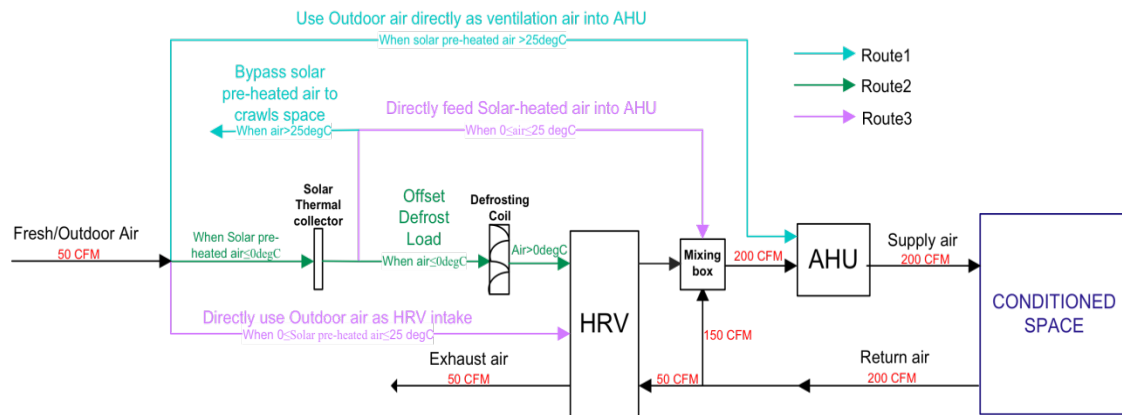


Figure 3.2 Utilization of solar pre-heated air, System-Level Schematics; Route 1: Solar heated air > 25°C; Route 2: Solar heated air < 0°C; Route 3: 0°C < Solar heated air < 25°C; Volume flow rates (cfm) shown are hypothetical values that follows mass balance.

Figure 3.2 illustrates the possible usage options for solar heated air at high latitude locations. Route 1 occurs during the warm months (e.g. July) when the received solar radiation is excessive and solar heated air is greater than 25°C (rare for high latitudes). In this case, outdoor fresh air directly feeds to the Air Handling Unit (AHU) and solar heated air is ducted into the unoccupied crawl space for storage.

Route 2 depicts the other extreme when solar heated air is lower than 0°C (cold or gloomy days). As Heat Recovery Ventilation (HRV) units is commonly installed in buildings in Northern Canada (CMHC, 2010), a defrost coil is necessary to heat the incoming air to above-freezing before pumping it into the HRV. Solar pre-heated air can therefore be supplied (replacing outdoor air) to offset the defrost coil load before reaching the HRV core.

Route 3 illustrates the intermediate case when solar heated air lies between 0 and 25°C (which means outdoor air is still below 0°C). Note that HRV relies on the temperature difference between cold outdoor air and warm return air to perform most efficiently. Therefore, in this case, the solar heated air can be directly ducted to the AHU to offset overall space heating load.

For BIPV/T co-generation systems, the photovoltaic electricity could be used to drive a DC fan for ducting solar heated air. For all transpired collectors with surface perforations, drainage will be provided at the bottom of the collector in real-world outdoor applications. The active envelope should also include a pre-engineered wall penetration behind the collector to pass through a 4” or 6” duct with an operable, insulated damper that opens only on demand.

3.2 Components and Configurations

3.2.1 Experimental Assembly and Components

In an effort to experimentally evaluate a range of building integrated solar collectors in an efficient manner, a BIPV/T prototype is designed and constructed to accommodate a dozen of testing configurations. Each layer of the test assembly can be taken apart and reassembled easily, allowing changes in configuration as the experiments move forward.

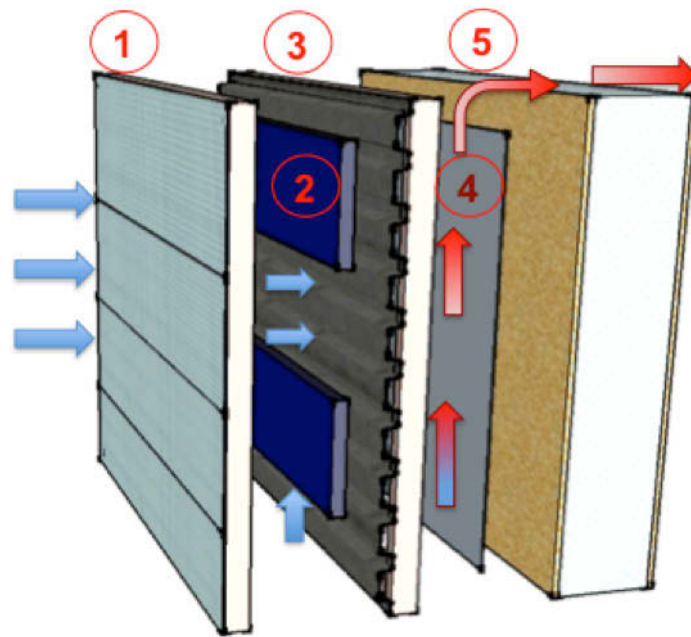


Figure 3.3 BIPV/T-SIP Prototype Experimental Assembly

The components of the whole test assembly illustrated in Figure 3.3 are listed as follows:

1. Transpired Glazing and/or Glazing (90% transmittance)
2. Photovoltaic Panels (60W) with dark frame and backing
3. Corrugated Transpired Absorber (can be rotated 90°)
4. Dark metal Absorber
5. Structural Insulated Panel Wall (Substrate)

The prototype is designed to be square (1.5m x 1.5m) and the corrugated absorber (number 3) can be rotated 90° to create scenarios of flow-against-corrugation and flow-along-corrugation. UTC used in the experimental set up is an off-the-shelf product, SolarWall, manufactured by Conserval Engineering. The corrugation profile (to scale) is illustrated in Figure 3.4 and the exact dimensions can be found in Appendix A.

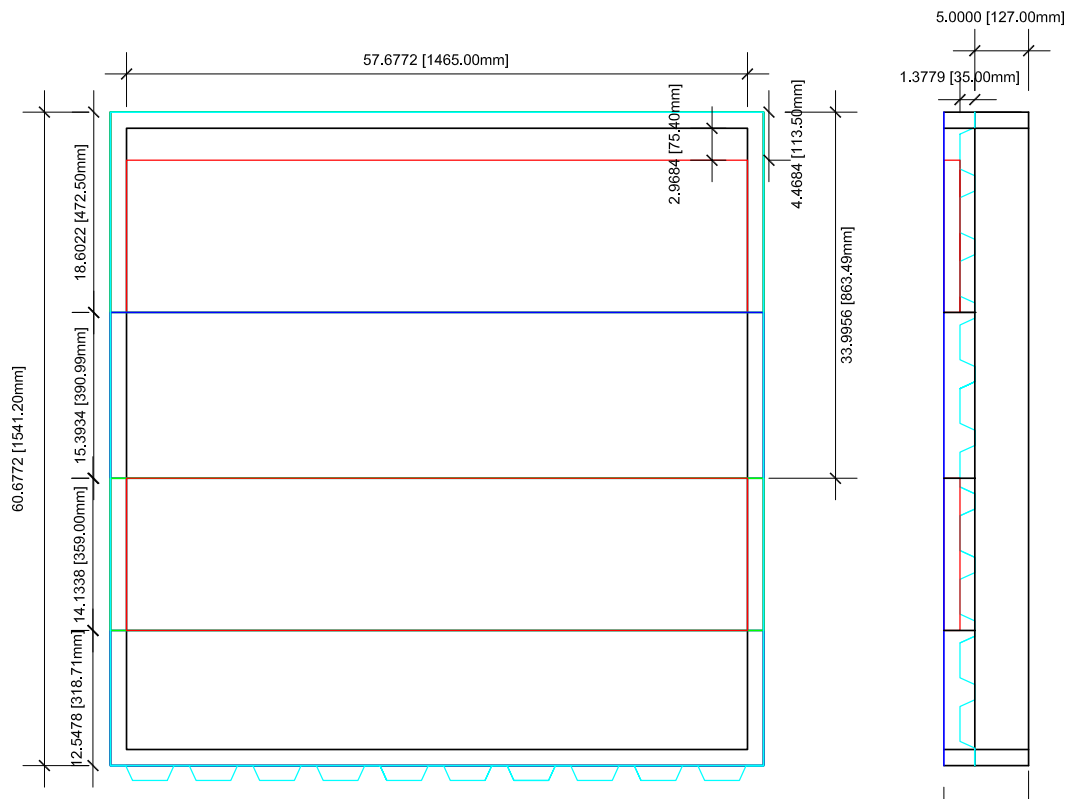


Figure 3.4 Schematic of the Experimental Assembly (SIP not shown)

The transpired glazing (leftmost in Figure 3.3) layer is designed to be level with the top surface of the photovoltaic panel. The pitch (14mm) and pore size (1.6mm) of the transpired glazing is carefully chosen to maximize the system efficiency while being practical. As a rule of thumb, transpired collectors perform better when the pore is small and well distributed (Leon & Kumar, 2006). The 1.6mm pore size used for the transpired

glazing is the smallest of the laser drill bit size available for custom perforation and 14mm pitch is selected to attain an overall of 1% porosity. If similar prototype were to be mass-produced in a commercial scale, the polycarbonate sheet can be thermo-formed for any pore-pitch configuration at very low added cost.

For the design of air-based BIPV/T systems, the height of the PV panel significantly affects the thermal efficiency of the whole system, as the thermal performance of PV worsens with increasing module height. The width of the PV is restricted only by the size of testing facility in the laboratory. The PV modules used in the experimental assembly are custom sized (0.36m high by 1.47m wide, Day4Energy) with dark frame to maximize system thermal performance. The same PV modules are also used for the JMSB building BIPV/T facade at Concordia University (Athienitis et al., 2011).

3.2.2 Possible Configurations and Testing Capacity

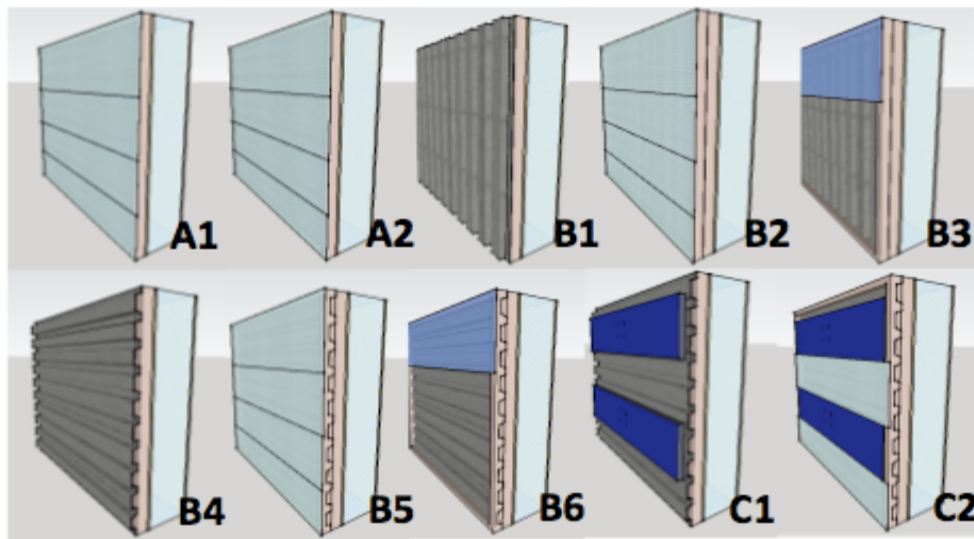


Figure 3.5. Test Configurations: A1. Collector with Transpired Glazing (TG) and flat absorber; A2. TG and finned absorber; B1. UTC with corrugation along flow (UTC-v); B2. UTC-v + TG; B3. UTC-v with top glazing; B4. UTC with corrugation against flow (UTC-h); B5. UTC-h + TG; B6. UTC-h with top glazing; C1. UTC-h + PV/T (PV coverage 50%); C2. UTC-h + PV/T + TG;

A total of ten configurations have been tested using the same basic BIPV/T-SIP prototype, illustrated in Figure 3.5. UTC surface is covered with transpired glazing, glazing, and/or photovoltaic panels. Performance of different collector types were quantified and compared in controlled, repeatable laboratory conditions. Details of each testing configuration are summarized in Table 4.1 to 4.3 in Section 4.2.

The SIP system serves as a compact envelope of structure, insulation, and air/vapor barriers. Thermal storage can be provided by adding an inner layer of phase-change-material (PCM) drywall or floor tiles. The whole active envelope system is intended to be pre-fabricated before shipped to site. As shown in Figure 3.6, the BIPV-SIP facade is also mounted on a test room as an integrated system for the testing in the Environmental Chamber (Section 4.4).

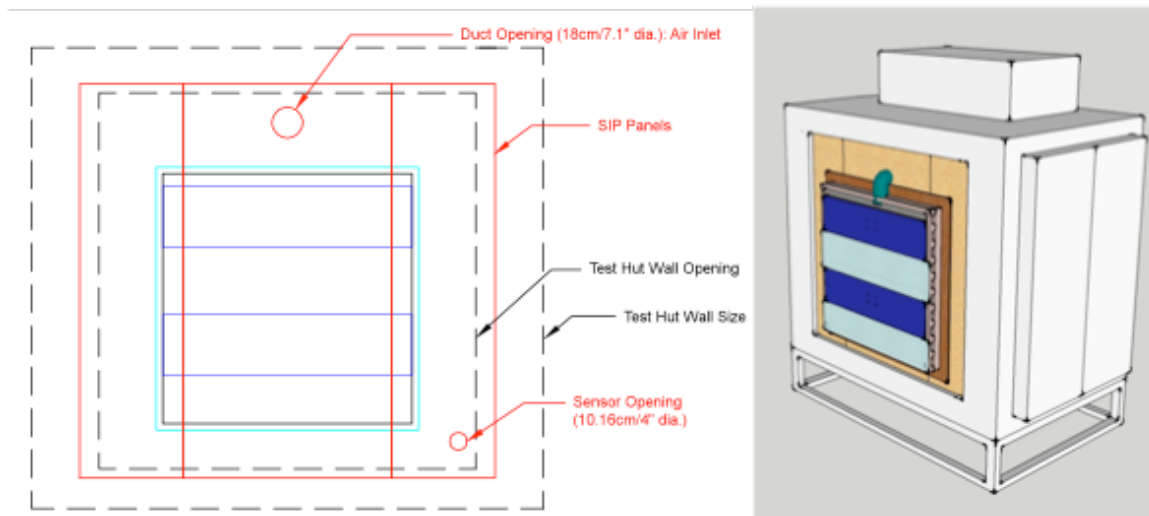


Figure 3.6 Left: BIPV/T prototype integrated with SIP façade; Right: BIPV/T-SIP facade mounted on a Test Room

3.3 Instrumentation

Van Decker et al. (2001) stated that only about one-third of or less of the plane is found to be asymptotic, in other words, edge effects will be predominant at the one-third

sides of the collector. Therefore, the majority of thermocouples in all layers are placed slightly offset to the right on the collector plane, before the 1/3 edge zone. Thermocouples are also present in the middle of the collector plane, as well as within the edge zone to confirm and establish the central zone, whose results are more consistent and representative of the collector performance. Figure 3.7 depicts the dimensioned location of thermocouples for the transpired glazing (TG) and glazing (G).

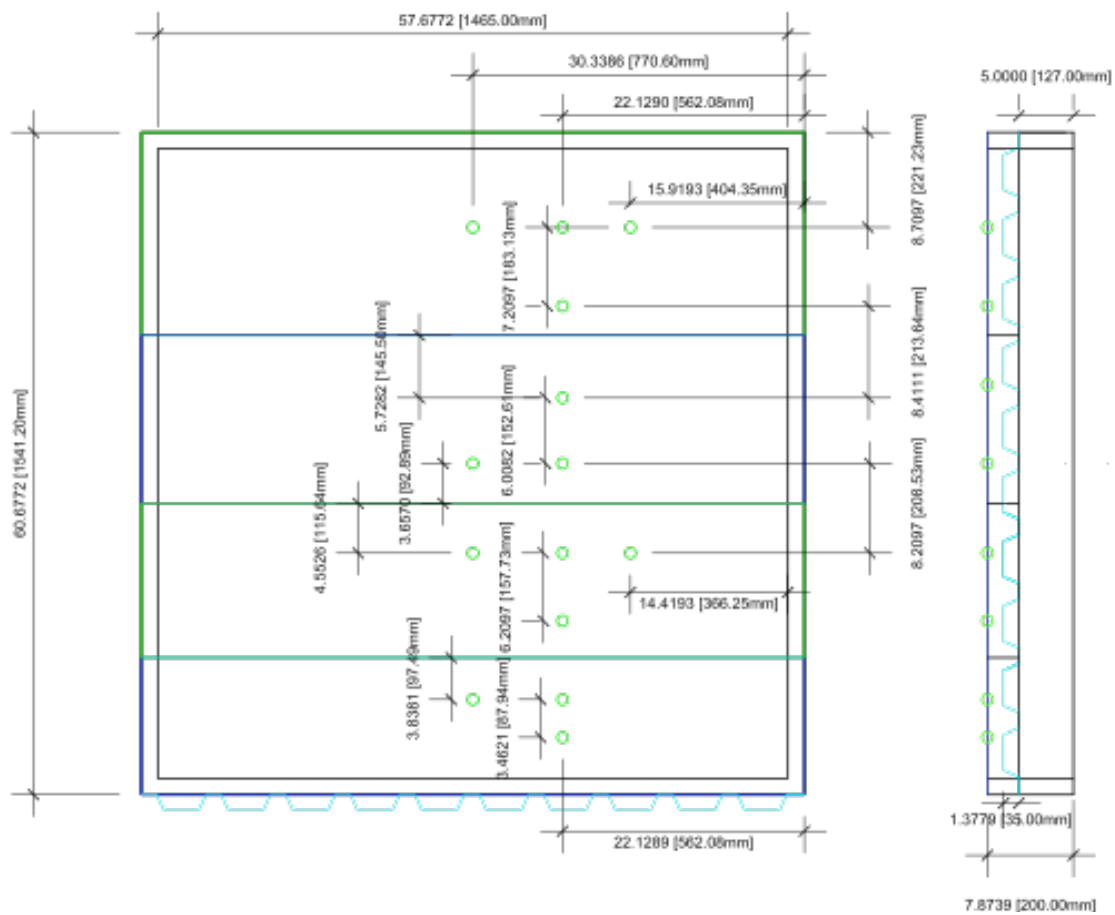


Figure 3.7 Thermocouple locations for the layer of Transpired Glazing (TG)

The placement of thermocouples on the corrugated UTC (SolarWall) is a little more complex than other layers in this assembly, as the plate is allowed to rotate 90° in some

experiments. Figure 3.8 illustrates the relative locations and names of all the thermocouples present in the layer of SolarWall, with the current orientation being flow-against-corrugation (SW-h). The plate can be rotated counterclockwise by 90° to form the flow-along-corrugation configuration (SW-v).

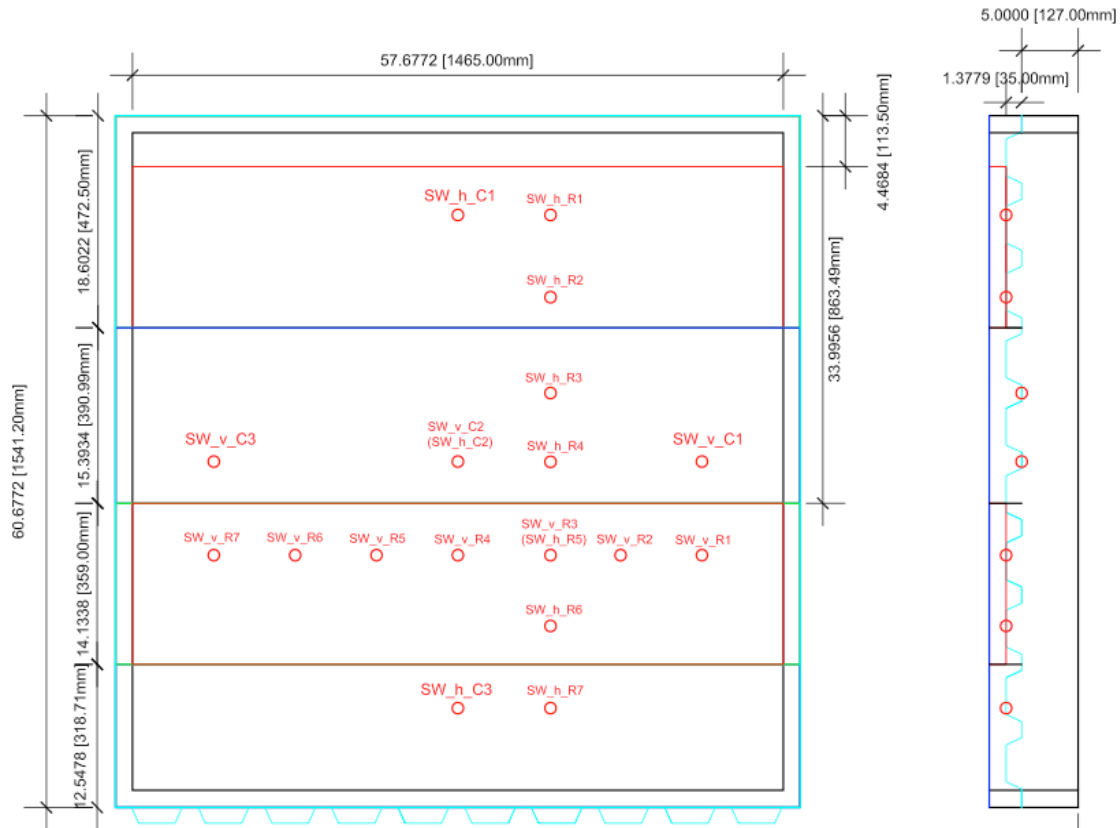


Figure 3.8 Thermocouple Names for the layer of SolarWall (UTC)

A naming system is developed to keep track of all the thermocouples present for the experiments (Figure 3.8). In short, a uniform format of “X_Y_Z#” is adopted. X indicates the component of the assembly (E: exterior air; TG: transpired glazing; G: glazing; SW: solarwall; B: back; OT: outlet top; OL: outlet low). Y indicates the four slots that the collector is divided into (i.e. from top to bottom: panel a, b, c, d). Z is the location of the thermocouples on the collector (e.g. F: front; B: back; C: center; L: left; R: right; B:

boundary). For example, as shown in Figure 3.8, two sensors are shared between the two corrugation orientations (SW-h_C2=SW-v_C2; SW-h_R5=SW-v_R3).

To better establish a comprehensive thermal profile of the entire system, the thermocouples on different layers of the assembly are aligned on the (x, y) coordinate, super-imposing by layers. The reason why the majority of thermocouples are placed slightly offset to the right, instead of at the center of plane, is to avoid the junction box protruding from the back (center) of the photovoltaic panels.

The thermocouples installed on the back plate (layer 5 in Figure 3.3) and PV modules (layer 2 in Figure 3.3) are plotted in Appendix A. There are also 4 thermocouples (E_L1/L2/R1/R2) measuring the exterior temperature immediately near the collector, located at 1.5” above the top transpired glazing layer. At the duct outlet where the solar heated air is drawn, there are two in-duct thermocouples 5” apart from each other and one RTD sensor fixed in the middle of the duct cross-section, to ensure accurate temperature measurement at the collector outlet.

A total of 65 thermocouples and 2 RTDs were used, the signals of which are wired to 4 data acquisition modules by National Instrument and sent to a laptop via LAN connection (Appendix A).

In addition, an I-V tracer was used to evaluate the instantaneous electric performance of the PV panel. During the BIPV/T experiments, rheostats are used to continuously consume the electric output by the PV panel, so that the system’s thermal performance is realistic.

4 Experimental Evaluation

4.1 Solar Simulator / Environmental Chamber (SSEC) Laboratory

4.1.1 Introduction to the Laboratory Facility

The Concordia Solar Simulator and Environmental Chamber (SSEC) Laboratory is a state-of-the-art indoor research facility, designed to simulate natural sunlight and other climatic conditions (wind, temperature, humidity, etc.) in order to test various active systems such as PV or PV/T modules, solar air/water collectors, building-integrated solar systems as well as building envelope systems. There are two parts to this test facility: the Solar Simulator (Section 4.1.2) and the Environmental Chamber (Section 4.1.3).

4.1.2 Solar Simulator

The central component of the Solar Simulator facility is the **Main Lamp Field** consisting of eight special metal halide (MHG) lamps, producing a dense multiline spectrum of rare earth metals comparable to a continuous solar spectrum (PSE AG, 2011). Combined with special glass filters, the MHG lamp field provides a spectral distribution very close to natural sunlight (Figure 4.1) in accordance with the specifications of EN12975:2006 (European Committee of Standardization, 2006) and ISO9806-1:1994 (ISO, 1994).

In order to eliminate long wave infrared irradiation emitted by the hot lamps, an **artificial sky** is positioned in front of the main lamp field. The artificial sky consists of two panes of low iron glass with antireflective coating, creating a cavity in between which cold air at 10°C is circulated in a closed loop and cooled by a heat exchanger.

Figure 4.2 shows the Solar Simulator Main Lamp Field and Test Platform at 0° (left) and 45° (right) tilt angles.

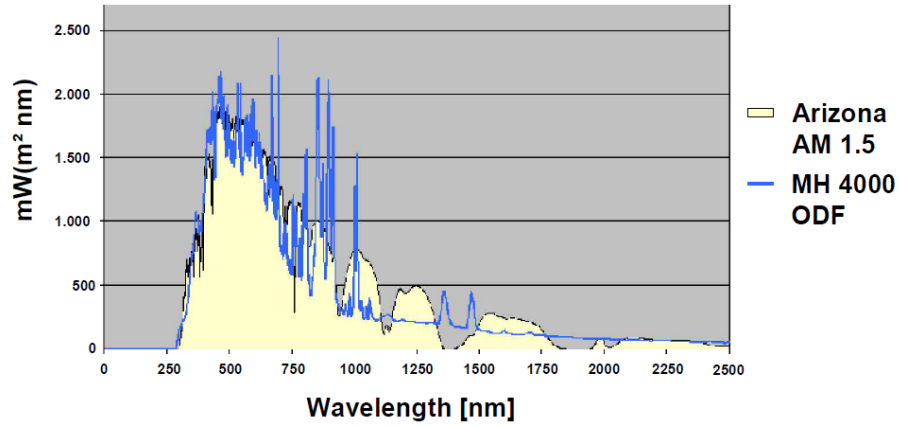


Figure 4.1 Spectral Intensity Distribution of MHG lamps compared to Natural Sun Light, (PSE AG, 2011)

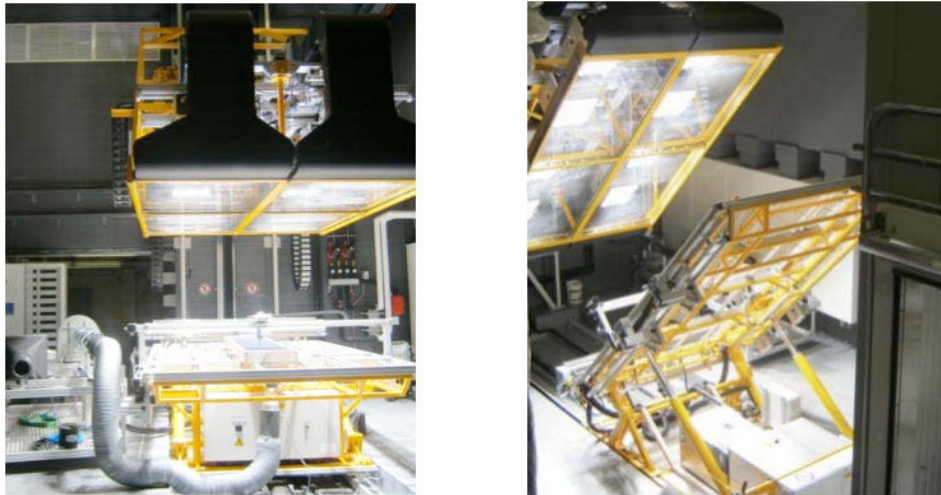


Figure 4.2 Solar Simulator in Operation: Main Lamp Field and Test Platform at 0° (left) and 45° (right) tilt angles

Note that the natural sky has an irradiation temperature slightly below the ambient air temperature. The installation of artificial sky is necessary to simulate the radiant loss from the hot collector surface to the cold glass panes (collector to sky), without which the

radiant loss would be reversed (lamps to collector) as the MHG lamps can reach temperatures of over 100°C during operation (Athienitis et al., 2012).

Directly below the main lamp field, the **Collector Test Platform** is mounted on a track to host any experimental setup (solar collectors or building envelope). Using a touch-screen control, the 1-axis rotation test platform and the main lamp field can both be tilted at any angle between horizontal (0°) and vertical (90°) position within accuracy of 1° (Figure 4.2). The geometric arrangements of lamps can be adjusted to maintain a constant solar radiation level and uniformity within 5% or less, depending on the collector area.

A **Ventilation Unit (blower)** is mounted at the bottom of the test platform, which blows grazing airflow parallel to the collector surface to simulate parallel wind conditions (up to 4m/s). This parallel flow is assumed to be driven by the ventilation unit only, independent of the suction velocity perpendicular to the surface of transpired collectors.

The parallel airflow velocity and the height of the ventilation unit can be adjusted via the control touch screen. However, the wind profile is not uniform across the collector length, as the wind speed dissipates with increasing collector height. The percentage difference between peak wind speeds (maximum at collector bottom, minimum at top) compared to the average wind speed across the collector length can be as high as 25%.

An automated **X-Y Scanner** is installed on the test platform above and parallel to the collectors. By taking irradiance and wind measurements at discrete point on a X-Y grid, the scanner is able to accurately determine the distribution and uniformity of solar

radiation on the collector surface. Once the desired uniformity is achieved, the entire collector test platform is moved up to the plane where the scanning had been carried out.

A built-in **Fluid Circuit for Solar Water Collectors** is integrated at the bottom of the test platform to circulate heating or cooling fluid using a closed-loop water pump.

A custom **Solar Air Collector Stand** is available on a mobile platform (Figure 4.3), with its components numbered and explained. With an adjustable inlet and outlet orifices, both open and closed-loop air systems can be tested under controlled conditions (measured inlet/outlet temperatures, mass flow rates and pressure differentials). Capable of controlling and monitoring the air circulation in and out of the collector, the solar air collector stand is normally used in conjunction with the solar simulator and the collector platform (where solar air collector is mounted). With appropriate duct extensions, the Solar Air Collector Test Stand can also be used for experiments of solar air collectors in the Environmental Chamber (Section 4.2.2).

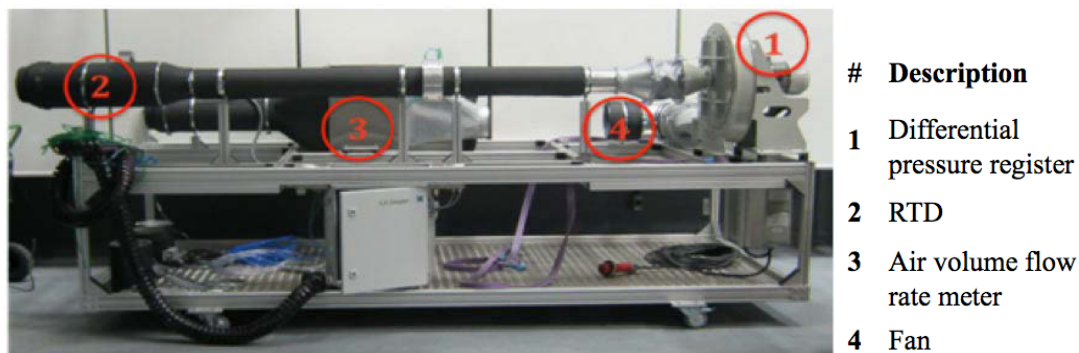


Figure 4.3 Custom Solar Air Collector Test Stand

4.1.3 Environmental Chamber

The Environmental Chamber is a research facility for testing different building envelope technologies under controlled exterior/interior microclimates. Two HVAC

units (central and mobile) are employed to precisely condition the chamber space. The setup allows for testing of a full-scale, two-storey wall, with one side (hot side) conditioned between 4°C and 50°C by the mobile HVAC, and the other side (cold side) between -40°C and 50°C using the central HVAC unit.

Temperature, humidity and atmospheric pressure are controlled and monitored automatically at several measuring points inside the Environmental Chamber. A range of 20% to 90% relative humidity and a differential pressure of ± 300 Pa can be controlled and sustained inside the chamber.

The front façade of the Chamber is hollowed out and the apertures are covered with 10 windows of 2.2 m x 2.2 m each (Figure 4.4, left). A **Mobile Lamp Field** of six MHG lamps (Figure 4.4, left) can be positioned in front of the glazed façade to illuminate the test surface inside the Environmental Chamber.



Figure 4.4 Left: Mobile Lamp Fields and Environmental Chamber (main façade with glazed apertures); Right: Portal Test Hut inside the Environmental Chamber

The individual lamps of the mobile lamp field can be manually moved on 3-axis. Lamp intensity can be automatically dimmed down to 60% ($600\text{W}/\text{m}^2$) with relatively low effects on spectral distribution. For small-scale testing (e.g. this thesis project), a portable cooling chamber (Figure 4.4, right) can be used to host the building-integrated solar collector.

For the purpose of this thesis, the portable cooling chamber is referred to as **Test Hut** (Figure 4.4 Right) so not to confuse the readers, as the test hut at room temperature (20°C) is in fact in heating mode as temperature in the Environmental Chamber is low. A low iron, antireflective-coated glazing is in place on the main façade of the test hut as the default mode (Figure 4.4, right). The rest of the test hut envelope is made of 120 mm of polyurethane insulation to minimize heat loss.

A **Portable X-Y Scanner**, similar to the X-Y Scanner on the solar simulator test platform, is used to measure the solar intensity distribution and uniformity on the test surface by taking discrete measuring points. Despite the difficulty due to framing of the glazed apertures of the Chamber, $\pm 10\%$ uniformity and a maximum of $1200\text{W}/\text{m}^2$ irradiance can be achieved on the test hut facade inside the chamber.

4.2 Test Sequence under the Solar Simulator

Ten configurations of building integrated solar collectors were tested at the SSEC laboratory in late 2011. Compared to outdoor tests that would normally take a calendar year to fully characterize a collector's performance, indoor testing facilities with controllable and repeatable environmental conditions significantly compressed the experimental timeline. Figure 4.5 illustrates the experimental set up using the Solar Simulator and the Solar Air Collector Stand.

Grazing wind (parallel surface flow) up to 3.5m/s average is created by the blower at the bottom of the collector test stand (Figure 4.5). The exterior temperature (laboratory temperature) is monitored at the base of the fan (one sensor on each side of fan), inside the lab space, and near the collector surface (4 thermocouples measuring air temperature at 1.5” above the collector surface). Note that there are significant differences (up to 4°C) between temperature measurements inside the lab space, at base of fan, and near collector surface. Implications of this observation are discussed in Section 4.3.1.

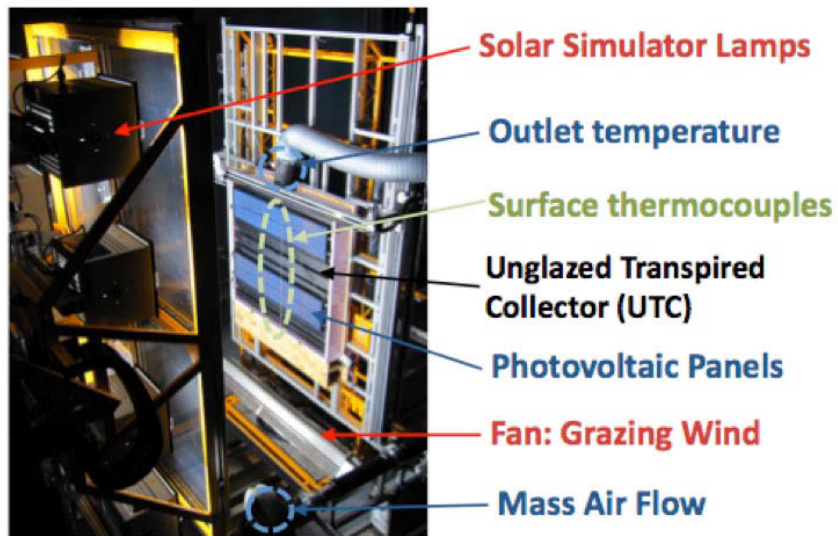


Figure 4.5 Experiments in Progress under the Solar Simulator

There are two thermocouples mounted inside the duct outlet (elbow section) and a resistance temperature detector (RTD) probe inserted right after the thermocouples in the straight duct section, to measure the air temperature exiting the collector. As collector inlet and outlet temperatures are two very important parameters in calculating the collector efficiency, redundancy in instrumentations is beneficial.

The amount of air passing through the collector is measured at the Air Collector Stand (Figure 4.5) using a laminar flow element (LFE) accurately monitoring and

controlling the mass flow rate of air removing heat from the collector absorber. The solar heated air is then dumped into the conditioned lab space, completing the open loop.

Due to height restriction by the X-Y scanner, the SIP envelope was too thick to fit under the scanner tracks. Therefore, a 2” expanded polystyrene insulation is added at the back of the collector prototype and back loss is corrected by simulation (Section 5.4.3). The SIP envelope is integrated with solar collectors during the Environmental Chamber experiments. Table 4.1, 4.2 and 4.3 below summarize all ten collector configurations based on the same basic prototype, arranged in the order of experimental evaluations.

Table 4.1 Test Stage A (Transpired Glazing/Glazing)

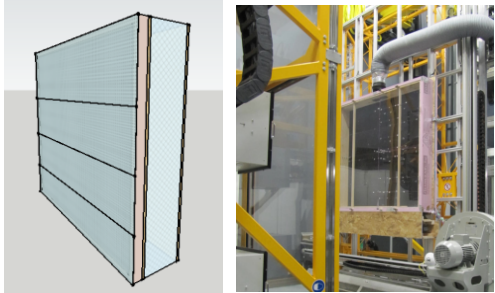
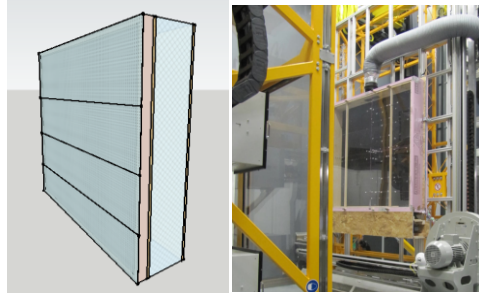
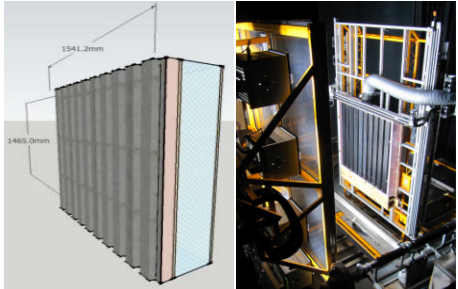
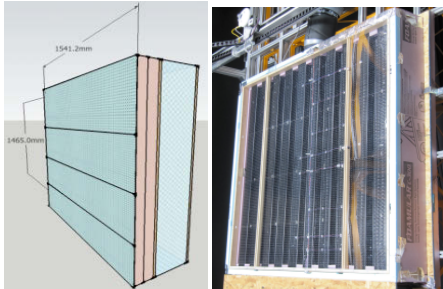
<p>A1. TG (Transpired Glazing with absorber at the back)</p>	<p>A2. TG + fins (Transpired Glazing + fins at the back absorber)</p>
	

Table 4.2 Test Stage B (SolarWall, Transpired Glazing/Glazing)

<p>B1. SW flow ALONG corrugation: SW-v (SolarWall Vertical)</p>	<p>B2. SW-v + TG (SolarWall Vertical + Transpired Glazing)</p>
	

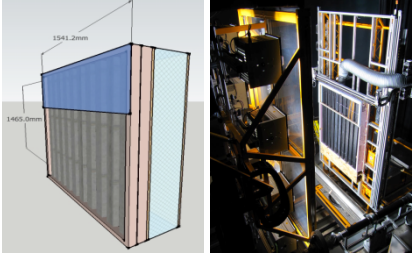
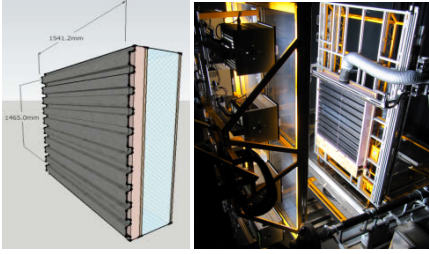
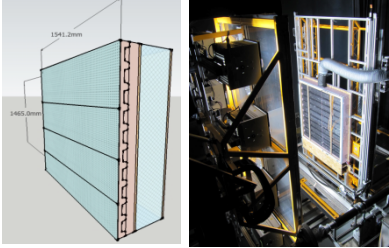
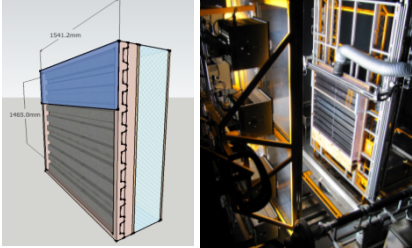
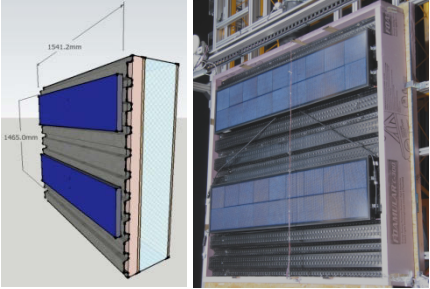
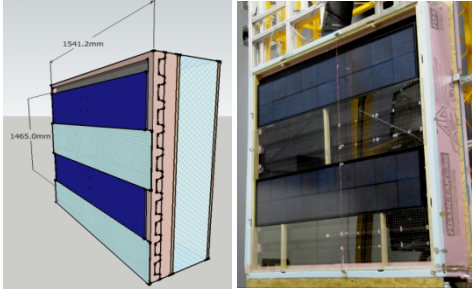
B3. SW-v + G: Two-stage Transpired Collector (SolarWall Vertical + Glazing)	B4. SW flow AGAINST corrugation:SW-h (SolarWall Horizontal)
	
B5. SW-h + TG (SolarWall Horizontal + Transpired Glazing)	B6. SW-h + G: Two-stage Transpired Collector (SolarWall Horizontal + Glazing)
	

Table 4.3 Test Stage C (SolarWall, Transpired Glazing/Glazing, PV Panels)

C1. SW-h + PV: JMSB setup (Solarwall Horizontal + PV panels)	C2. SW-h + PV + TG (Solarwall Horizontal+PV+Transpired Glazing)
	

Each collector underwent four sets of tests (HG-HW, HG-LW, LG-HW, and LG-LW), with abbreviations explained in Table 4.4. Each test set involves five mass flow rates to be maintained at steady state. The airflow parallel to the collector surface is

created by the ventilation unit as described in Section 4.1.2. This is considered as parallel wind, distinct from the suction velocity (perpendicular to surface) occurring at the distributed air inlets of a transpired collector.

Table 4.4 Steady-State Testing Conditions (Solar Simulator Testing)

Solar Irradiance ($\pm 5\%$ uniformity)	Air velocity parallel to collector surface (parallel wind)	Mass Flow Rate
High Gain (HG): 1148 W/m ²	High Wind (HW): 3.5m/s	150, 125, 100, 75, 50
Low Gain (LG): 838 W/m ²	Low Wind (LW): 1m/s	kg/hr/m ²

In addition to a total of 240 hours of valid steady-state evaluations in the laboratory, there were many test sets repeating the same environmental conditions in order to confirm repeatability of the experimental results.

The Solar Radiation on the collector surface is scanned at discrete points with 150mm increments in both x and y directions. By dimming the Solar Simulator lamps from 100% to 75%, two irradiance levels averaging 1148 and 838 W/m² are employed for testing, known as High Gain (HG) and Low Gain (LG).

The irradiance distribution is shown in the contour plots in Figure 4.6 for LG condition. Across the target collector plane (1.5m by 1.5m), the irradiance is optimized to reach a 5% standard deviation in distribution, shown in Figure 4.7.

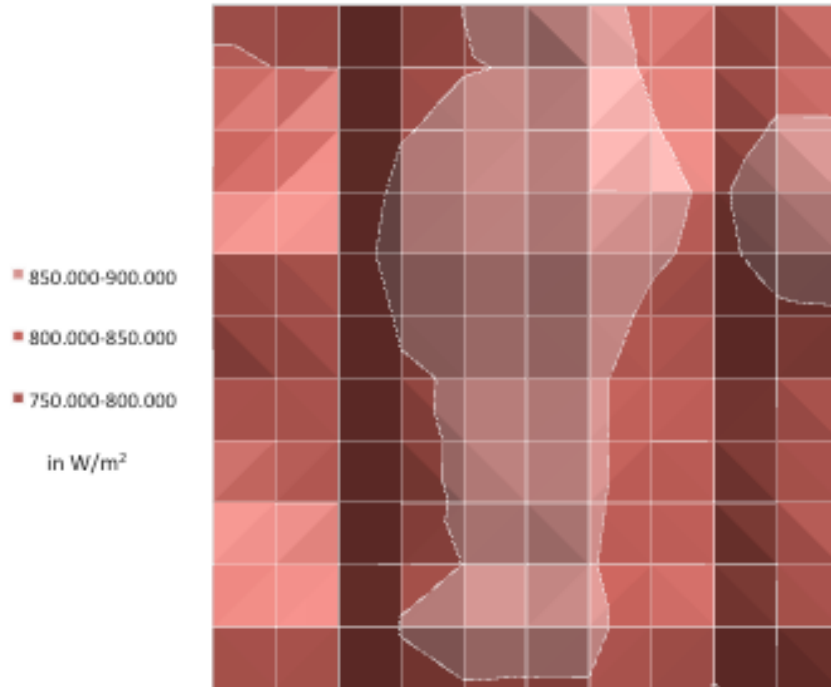


Figure 4.6 Irradiance Distribution on the Collector Surface (Solar Simulator), average 838 W/m²

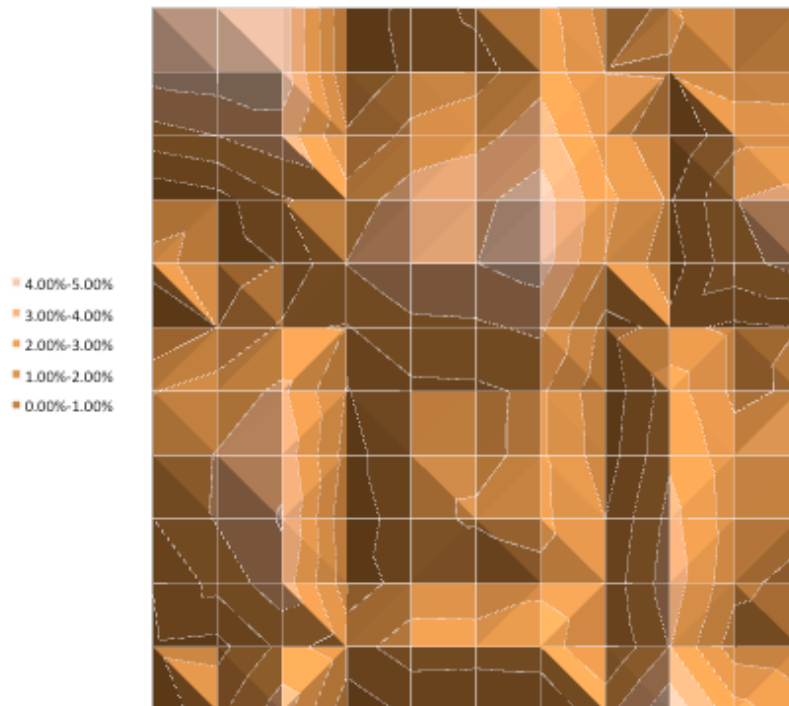


Figure 4.7 Standard deviation of solar distribution at Collector Surface (Solar Simulator), 5% maximum

4.3 Results and Discussion – Solar Simulator Experiments

4.3.1 Benchmarking Commercially-Available Collectors' Performance (A1 and B1)

Collector B1 (SW) in Table 4.2 employs a commercially available UTC known as SolarWall, manufactured by Conserval Engineering. Collector A1 (TG) in Table 4.1 is similar in design to a commercial product (LubiWall) manufactured by Enerconcept. Compared to the LubiWall, collector A1 adopts polycarbonate sheet of higher transmittance with custom perforation using laser punching. To benchmark the experimental work done with the Solar Simulator, Figure 4.8 and 4.9 compares the manufacturers' published data with experimental results obtained at the laboratory for the two types of collectors (A1 and B1).

Steady-state efficiency, adopted as the common performance gauge to compare collectors, is calculated by:

$$\eta_{th} = \frac{Q_u}{G} = \frac{MFR \cdot c_p \cdot (T_{plm} - T_{amb}) \cdot A_{col}}{(I \cdot A_{col})} \quad (4.1)$$

where T_{plm} (°C) is the temperature at collector plenum outlet; T_{amb} (°C) is the temperature at collector inlet, using either ambient lab temperature or measured temperature near the collector surface; MFR is the mass flow rate (kg/s/m²) for heat removal; c_p is the specific heat capacity of air (J/kg/K); A_{col} is the collector area; G is the incident solar gain (W) on the façade.

Although the efficiency data are following the exponential increase with increasing mass flow rate and generally in agreement with manufacturer's claims, there is a noticeable discrepancy as shown in Figure 4.8 and 4.9.

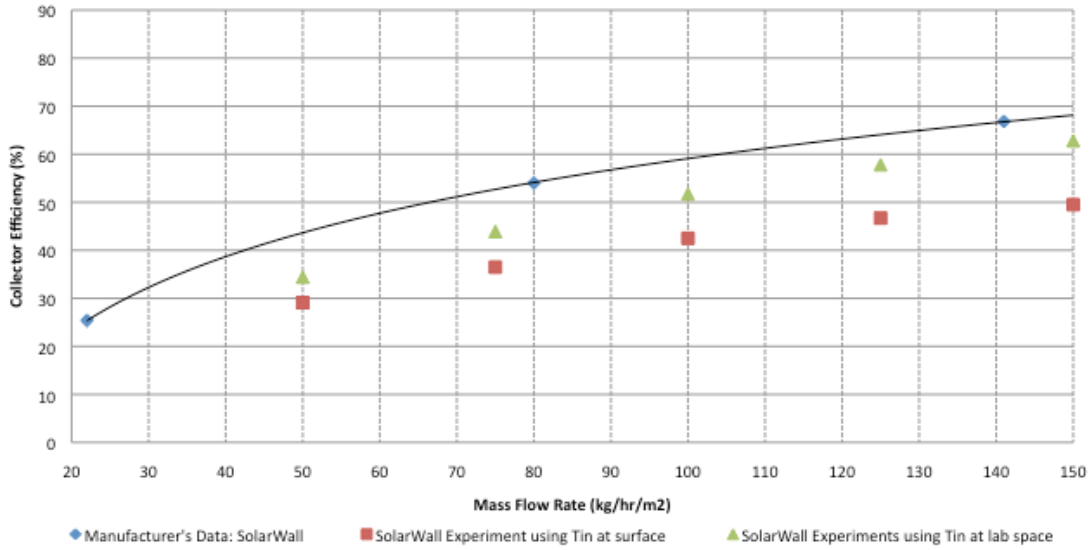


Figure 4.8 Collector B1 (SWv) Performance: SolarWall manufacturer's data (wind condition unknown) compared to Experimental data (at 0.8m/s average parallel wind)

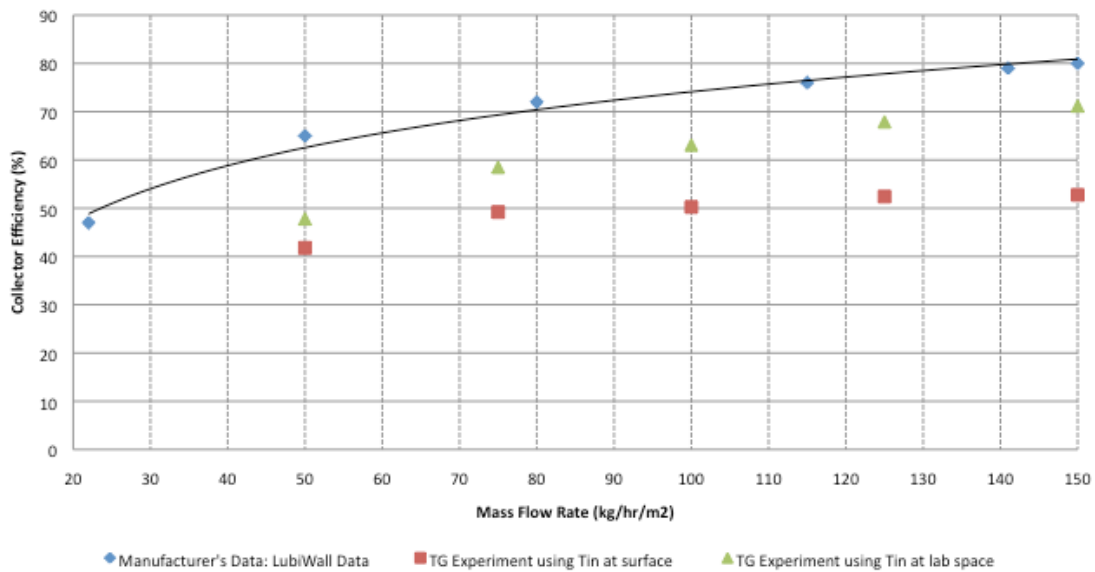


Figure 4.9 Collector A1 (TG) Performance: LubiWall Manufacturer's data (wind condition unknown) compared to Experimental data (at 0.9 m/s average parallel wind)

All the results are obtained under irradiance ranging from 900 to 1100 W/m², and ambient temperature from 20 to 25°C. However, neither manufactures published the wind or surface flow conditions under which their performance tests took place. For transpired

collectors that are particularly prone to surface convective loss, efficiency varies significantly depending on the surface wind conditions.

While Manufacturers' data may provide a good reference for research work, this thesis will compare all the proposed collectors using experimental data under specified environmental conditions. Moreover, using inlet temperature at collector surface and in the lab space also leads to different efficiency results, as shown by the red (square) and green (square) dots in Figure 4.8 and 4.9. For consistency in results presentation from here on, all efficiency calculations will use **inlet temperature near collector surface**, averaged from 4 thermocouples located 1.5" above the collector exterior.

As each collector is tested under two solar irradiance in combination with two parallel wind speeds, effects of convective loss and efficiency at different solar radiation can be evaluated. For example, for ideal solar thermal collectors that maintain its solar fractions at all radiation levels, equation 4.2 shows that collector temperature rise (outlet and inlet temperature difference, ΔT) should be linearly proportional to irradiance (W/m^2), at the same mass flow rate.

$$MFR_1 \cdot \Delta T_1 / I_1 = MFR_2 \cdot \Delta T_2 / I_2 \quad (4.2)$$

Figure 4.10 plots collector temperature rise (ΔT) against the two irradiance levels under which Collector B1 (SW-v) was tested (with 3.5m/s average parallel surface flow). The linear agreement for all mass flow rates (50, 75, 100, 125, 150 kg/hr/m²) confirmed the validity of test results. Using this linear approximation, collector temperature rise can be interpolated for all irradiance between 0 to 1148 W/m². For low parallel surface flow conditions and other collectors tested, similar plots can be found in Appendix B.

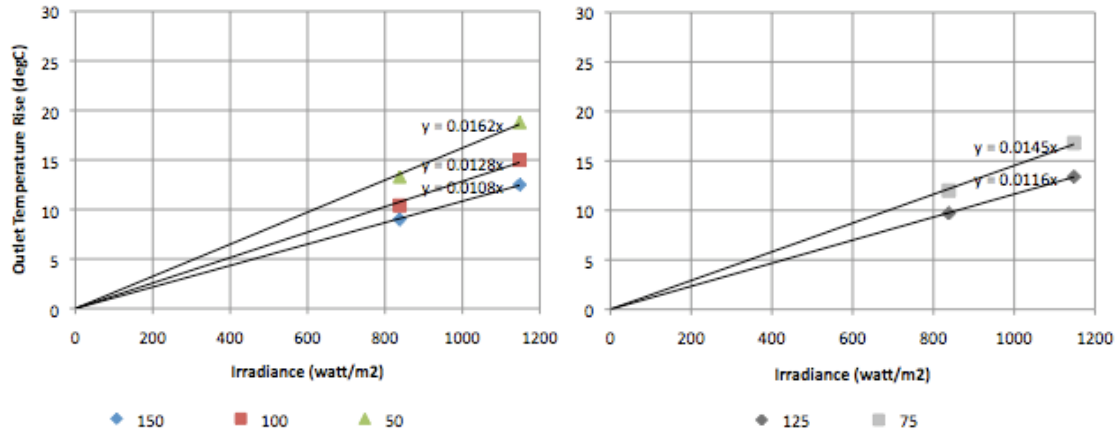


Figure 4.10 Collector B1 (SWv) temperature rise at different irradiance with five mass flow rates, tested at 3.5m/s parallel surface flow

4.3.2 Effects of Fins, Transpired Glazing, and Transpired Absorber (A1, A2 and B1)

Three transpired collectors (A1, A2 and B1) are compared in this Section, all of which benefit from the distributed air inlets at the surface. However, the exterior surface of B1 (SW-v) collector is also the absorber, while A1 and A2 hides the absorber behind the transpired glazing exterior.

A1 (TG no Fins) and A2 (TG with Fins) are identical, except that A2 has five 8 cm high dark fins mounted on the back absorber to increase the useful heat transfer. Figure 4.11 shows the systems' performance at 1148W/m² with different surface airflows (parallel wind). Results under 838W/m² irradiance is very similar and can be found in the tables of Appendix B.

At both parallel wind conditions (Figure 4.11), A2 (TG with Fins) is able to increase efficiency by up to 13% compared to A1 (TG without Fins), especially at high mass flow rates when the fins in the plenum creates turbulent flow and further increasing useful heat transfer at the absorber.

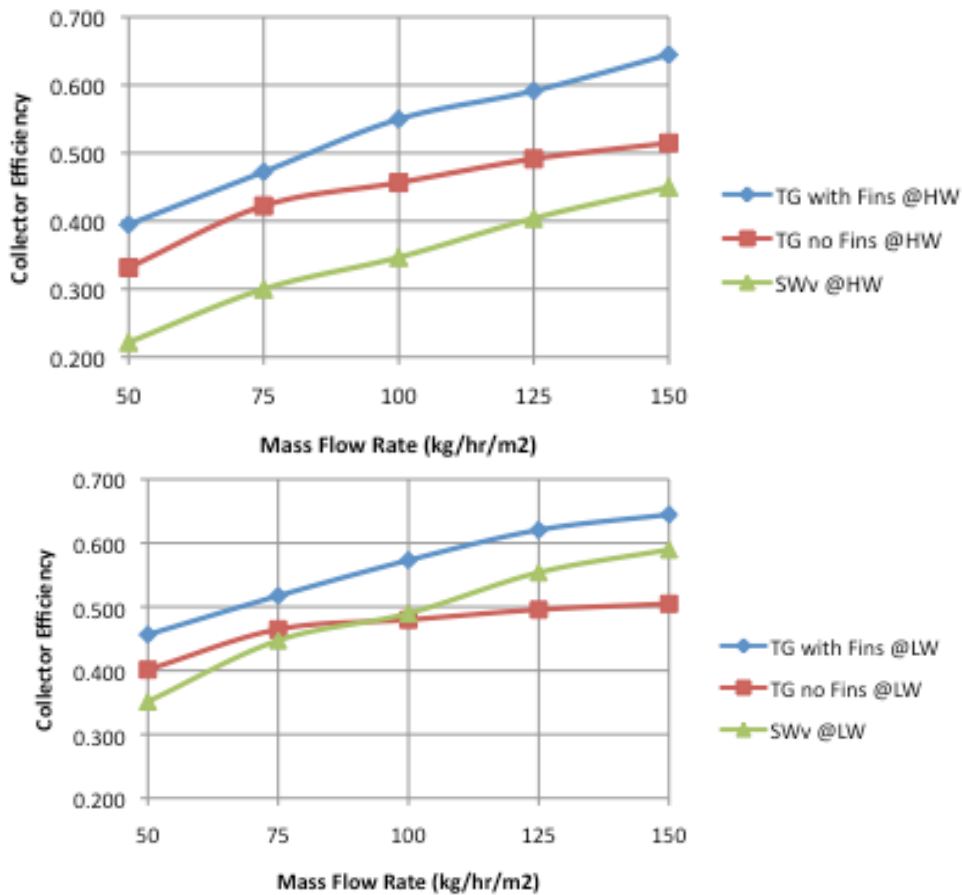


Figure 4.11 Collector A1 (TG no Fins), A2 (TG with Fins) and B1 (SW-v): Efficiency at high (top) and low (bottom) surface parallel flows, steady state at five mass flow rates;

TG with fins (A2) performs better than traditional collector with transpired absorbers (B1, SWv) at both surface flow (parallel wind) conditions. Moreover, both collectors with transpired glazing (TG) exhibit better resilience against convective loss due to increase in parallel surface flow. As shown by the orange and red lines in Figure 4.12, the wind loss only affects TG collector (A1) marginally at low flow rates. On the contrary, the SWv collector (with exterior transpired absorber) drops over 15% in efficiency under high wind condition (green and blue lines in Figure 4.12).

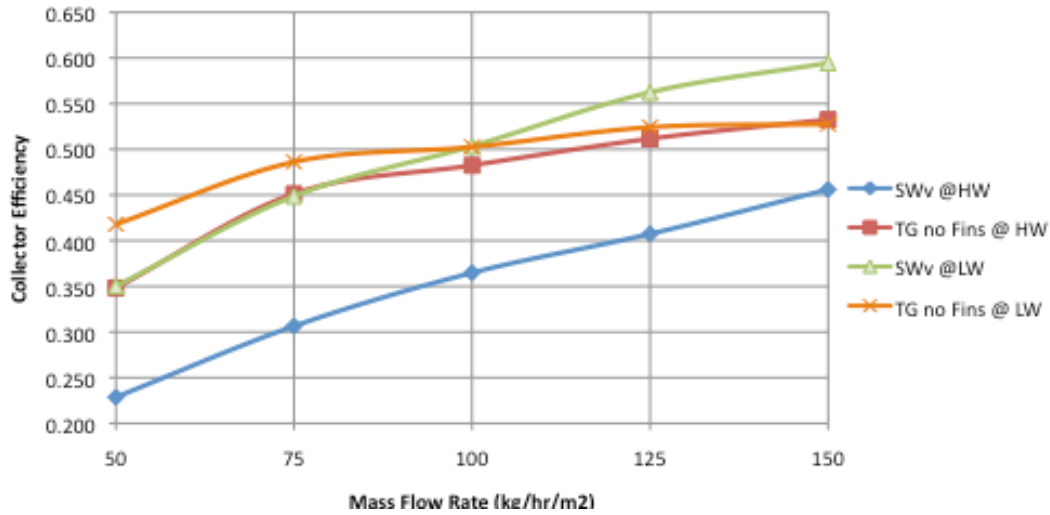


Figure 4.12 Collector A1 (TG no Fins) and B1 (SW-v): Efficiency at high and low surface parallel flows (HW and LW), steady state at five mass flow rates;

4.3.3 Effects of Corrugation Orientation in Transpired Absorber (B1 and B4)

As a common practice, most commercial SolarWall installations orient the corrugation vertically (B1, SW-v) to promote natural ventilation, while occasionally there are some installations with corrugation oriented horizontally (B2, SW-h), usually due to architectural considerations.

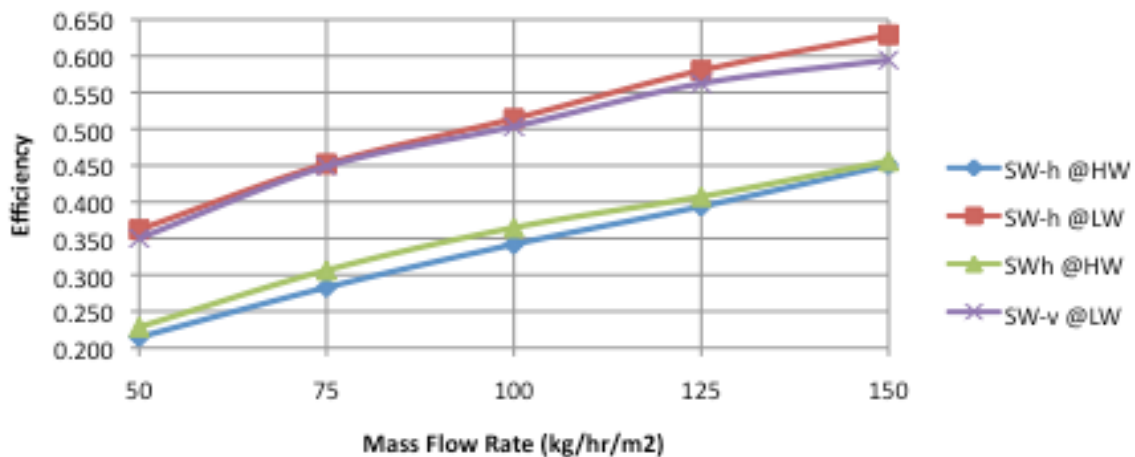


Figure 4.13 Collector B1 (SW-v) and B4 (SW-h): Efficiency at high and low surface parallel flows (High Wind/HW and Low Wind/LW), steady state at five mass flow rates;

Figure 4.13 plots the efficiency of SW_v and SW_h at high and low surface wind conditions under irradiance of 1148 W/m², confirming that there are only minimal differences between the two collectors.

It is interesting to note that SW_v performs slightly better at high wind while SW_h performs better at low wind (Figure 4.13). However, the uncertainty of efficiency lies beyond the difference between the collectors. Therefore, no definitive conclusions can be drawn from the experimental results here.

To fully study the effect of corrugation orientations in transpired collectors, a large-scale experimental set up (more than 1.5m by 1.5m) and more accurate instrumentation are required to amplify the efficiency differences while minimizing experimental uncertainty. Details of uncertainty propagation and error analyses can be found in Section 5.3.1 and Appendix C.

4.3.4 Effects of Adding Glazing on Transpired Absorber (B1, B3, B4, and B6)

This section investigates the effect of adding glazing to the top one-quarter area of the transpired absorbers. Both corrugation orientations (SW-h and SW-v) are evaluated, however, only results comparing B3 (SW-h) and B4 (SW-h +Glazing) at 1148 W/m² are presented in Figure 4.14, as the results under low solar gain condition and for SW-v collectors are very similar and can be found in Appendix B.

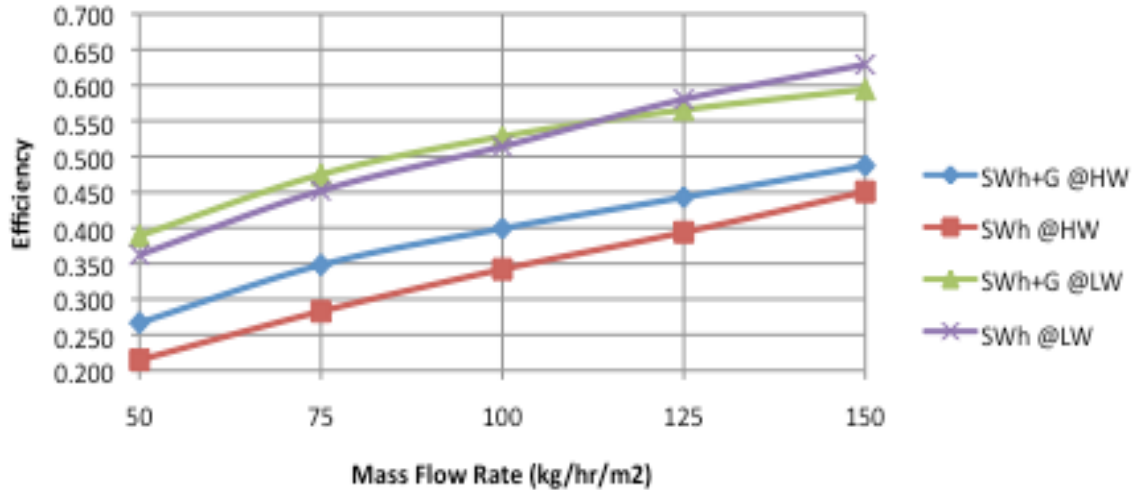


Figure 4.14 Collector B4 (SWh) and B6 (SWh+G): Efficiency at high and low surface parallel flows (High Wind/HW and Low Wind/LW), steady state at five mass flow rates

It can be concluded from Figure 4.14 that the performance of a partially glazed collector (SWh+G) is similar to SolarWall (SWh) at low parallel surface flow (LW, 0.9m/s), while the addition of glazing increases the collector performance by up to 8% at high surface flow (HW, 3.5m/s). This finding validated the assumption that partially covering the distributed air inlets of transpired absorber will enhance SolarWall's resilience to convective wind loss, especially at low heat removal rates (mass flow rates).

In addition, the glazing also creates a double plenum at the top of the collector, which doubles the absorber area and increases useful heat transfer. As shown in Figure 4.15, the exterior temperature of the glazing is also lower than the transpired absorber (SolarWall), contributing to less surface radiant loss.

Emissivity of SolarWall, glazing, transpired glazing, and wood frame surfaces are experimentally tested using a hand-held emissivity meter. As all materials exhibit

emissivity between 0.8-0.9, no emissivity correction is needed to adjust the thermal imaging pictures in Figure 4.15 (normalized temperature range from 15 to 70 °C).

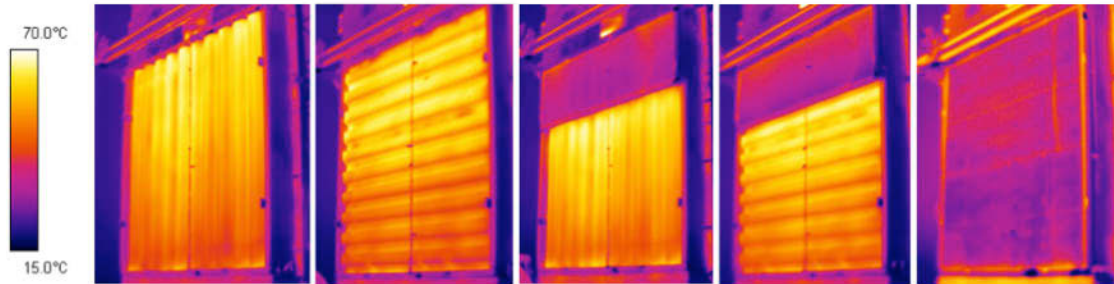


Figure 4.15 Infrared evaluation of SW_v (B1), SW_h (B4), SW_v+G (B3), SW_h+G (B6) and SW_h+TG (B5) at 1148 W/m² and 1m/s parallel wind, with mass flow rate of 50 kg/hr/m²

4.3.5 Effects of Adding Transpired Glazing to Transpired Absorber (B1, B2, B4, B5)

As shown in Figure 4.15, collectors covered with transpired glazing (e.g. B5) have very low surface temperature compared to collectors with exposed absorber (B1 and B4, SW_v and SW_h). The reduced surface radiant loss contributes partly to the efficiency increase of SW+TG illustrated in Figure 4.16.

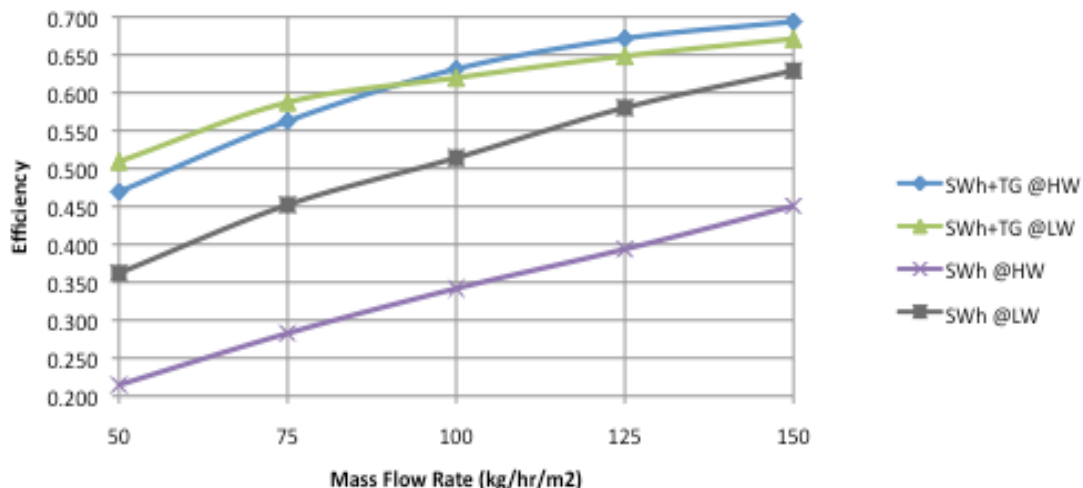


Figure 4.16 Collector B4 (SW_h) and B5 (SW_h+TG): Efficiency at High and Low surface flows (parallel wind)

Figure 4.16 shows the performance of B4 (SWh) and B5 (SWh+TG) at 1148 W/m², while results from B1 (SWv) and B2 (SWv+TG) follow the same trend. At both high and low wind (HW and LW) conditions, SWh+TG collector (Blue and Green lines) performs adequately with only slight drop in efficiency at low mass flow rates. While SWh exhibits over 18% efficiency drop under high parallel surface flow (3.5m/s) than under low flow (0.9 m/s), shown by the grey and purple lines in Figure 4.16.

At 0.9m/s surface flow, the efficiency of SWh+TG is 13% to 18% higher than SWh system. As SWh+TG system is less affected by surface wind loss, its efficiency is 23% to 28% higher than that of the conventional SWh system at high parallel wind (3.5m/s).

The SW+TG collector derives its resilience to convective wind loss from the addition of transpired glazing. Figure 4.17 indicates that both SWh+TG (B5) and TG (A1) collectors perform well under high and low parallel wind conditions, suggesting excellent resilience of the transpired glazing itself to convective losses, as opposed to the transpired absorber (SolarWall).

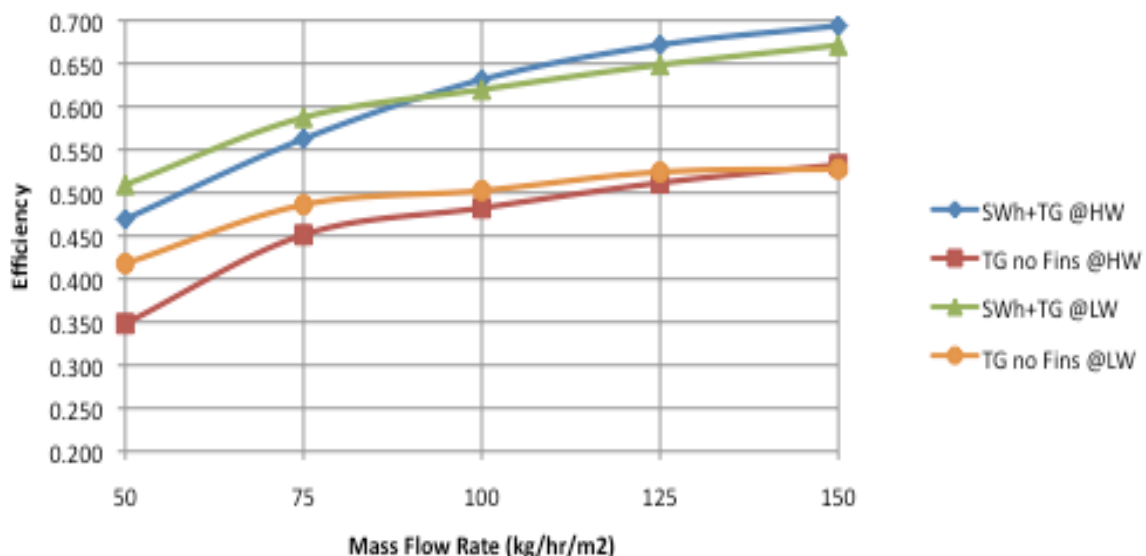


Figure 4.17 Collector B5 (SWh+TG) & A1 (TG no Fins): Efficiency at High&Low Wind

The results shown in Figure 4.15 and 4.16 revealed the two important characteristics of transpired glazing:

1. TG lowers surface temperature and radiant loss to the cold exterior;
2. TG ameliorates transpired absorber's susceptibility to convective wind loss.

These are particularly relevant findings with regard to collectors' suitability for cold, windy northern climate. The transpired (perforated) nature of the absorber is also advantageous by allowing simultaneous heat transfer at multiple inlets, especially when hidden behind an exterior layer of transpired glazing (B2 and B5).

4.3.6 Effects of Adding PV and Transpired Glazing to Transpired Absorber (C1,C2)

In addition to solar thermal collectors, the possibility of integrating solar electric components (photovoltaic panels) onto UTC systems is also evaluated. Delisle (2008) and researchers in Waterloo University have endeavored on the possibility of adding small PV cells onto SolarWall substrate. For this thesis project, two custom size (1.47m wide by 0.36m high) photovoltaic panels with dark metal frame are mounted on the SolarWall cladding covering approximately 50% of the collector area.

The two PV modules are wired in series with a resistance of 2.5 Ohm, to use up the generated electricity at maximum power point (MPP) and eliminate interference with the collector thermal output during the experiments.

As summarized in Table 4.5, MPP is obtained at I_{peak} and V_{peak} . Specifications from the manufacturer's (Day4Energy) data are confirmed by I-V tracer results at high and low solar gain (I-V curves see Appendix B).

Table 4.5 Photovoltaic Module Electric Characterizations

	Power (W)	Isc (Amp)	Voc (Volt)	Ipeak (Amp)	Vpeak (Volt)	Irradiance (W/m ²)	Temp PV (°C)
Module Specification (Day4Energy)	62.4	7.08	11.4	7.08	8.81	1000 (STC)	25 (STC)
2 Panels in series (HG)	123.5	9.01	20.11	8.45	14.61	1148 (HG)	54.19
2 Panels in series (LG)	89.8	6.05	20.43	5.74	15.64	838 (LG)	42.92

The electric efficiency of photovoltaic modules can be calculated in either one of the two ways, as described in equation 4.3 and 4.4.

$$\eta_{PV} = \eta_{PV@STC} \cdot [1 - \beta_{PV}(T_{PV} - T_{STC})] \quad (4.3)$$

where β_{PV} (=0.0046) is PV module temperature coefficient, T_{STC} (=25°C) is PV cell temperature at Standard Test Conditions, $\eta_{PV@STC}$ is the PV electric efficiency at STC.

$$\eta_{PV} = \text{ElectricOutput}_{PV} / (\text{Irradiance} \cdot \text{ModuleArea}) \quad (4.4)$$

For example, for 2 modules at High Gain (1148W/m²), the spontaneous efficiency of the array (module temperature at 54.19°C) can be calculated by equation 4.3:

$$12.1\% * [1 - 0.0046 * (54.19 - 25)] = 10.47\%$$

Alternatively, efficiency using equation 4.4 is:

$$(123.5W/2) / (1148W/m^2 * 1.47m * 0.35m) * 100\% = 10.45\%$$

The values of PV spontaneous efficiency are very similar using both methods, confirming experimental validity using the I-V tracer and using temperature adjustment.

Collector C1 (SWh+PV) draws air from the exposed portion of SolarWall cladding, and then behind the PV modules, eventually feeding to the plenum and outlet duct. The movement of heated air is indicated in Figure 4.18.

Collector C2 (SWh+PV+TG) covers the exposed SolarWall with transpired glazing (50% coverage), while the PV modules are still directly exposed to the exterior environment. The infrared pictures in Figure 4.18 present much reduced exterior temperature where the SolarWall is covered by transpired glazing (C2), resulting in lowered radiant loss to the cold ambience.

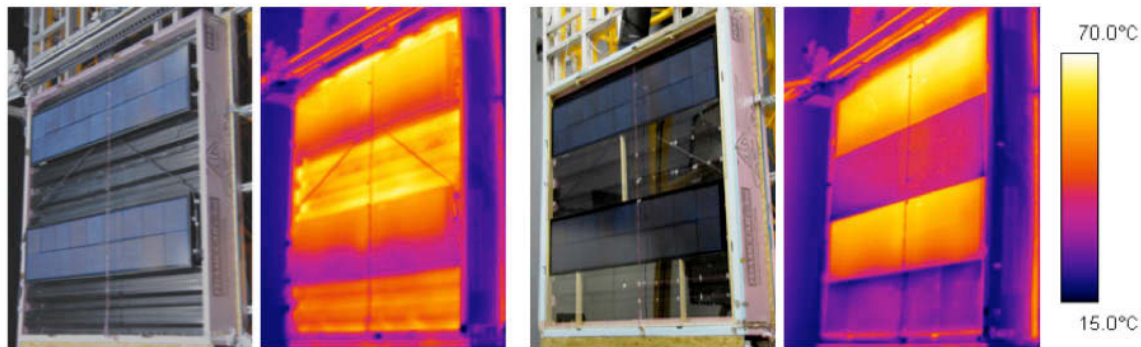


Figure 4.18 Infrared evaluation of C1 (SWh+PV) and C2 (SWh+PV+TG) at 1148 W/m^2 and 0.9 m/s surface parallel flow, with mass flow rate of 50 kg/hr/m^2

Moreover, the surface temperature of PV modules becomes more uniformly distributed with the addition of 50% TG. As shown in Figure 4.18, the bottom of PV modules in collector C1 are cooled by incoming cold air from outdoor, while the addition of transpired glazing in collector C2 effectively reduces the temperature stratification in the PV modules. As temperature differential between PV cells creates electric mismatch and is detrimental to PV's electric production, the transpired glazing in C2 improves the collector's electric performance. Additionally, the transpired glazing in C2 lowers the

surface radiant and convective losses, contributing to the improved thermal output of C2 compared to C1.

The PV modules and mounting techniques used in Collector C1 and C2 are identical to the 288m² SolarWall+PV/T façade of the JMSB building at Concordia University, shown in Figure 2.7. Therefore, the outdoor monitoring data from the JMSB project (with PV coverage of approximately 70%) is used to benchmark the prototype performance under controlled lab conditions.

To address the difference in PV coverage, a measure accounting for both thermal and electric output of collectors is proposed by Athienitis et al. (2011) for similar evaluations. The Thermal Equivalent Efficiency (η_{EQ}) as calculated in equation 4.5:

$$\eta_{EQ} = \eta_{TH} + (A_{PV} / A_{Col}) \cdot COP \cdot \eta_{PV} \quad (4.5)$$

where η_{TH} is the steady-state thermal efficiency of the collector derived from heated air alone; A_{PV}/A_{col} is the percentage area covered by PV; COP describes the coefficient of performance of a heat pump that converts one unit of PV-generated electricity to four units of thermal energy (Athienitis et al., 2011). The assumption of COP equals to four is a reasonable estimate for commercially available air source heat pumps at source temperatures above 0 °C (ASHRAE, 2009).

Figure 4.19 shows the experimental thermal efficiency for C1 (SWh+50%PV) and C2 (SWh+50%PV+50%TG) at 1148W/m², as well as the spring thermal efficiency of the JMSB façade (SWh+70%PV). Figure 4.20 presents the thermal equivalent efficiency (η_{EQ}) calculated from equation 4.3 for the three collectors. Note that the black dash line

indicating thermal efficiency of JMSB (SWh+70%PV) is very similar to the efficiency curve of collector C1 (SWh+50%) at low wind in Figure 4.19, while in Figure 4.20, the black dash line is bounded by efficiency curves of C1 and C2 under low surface wind.

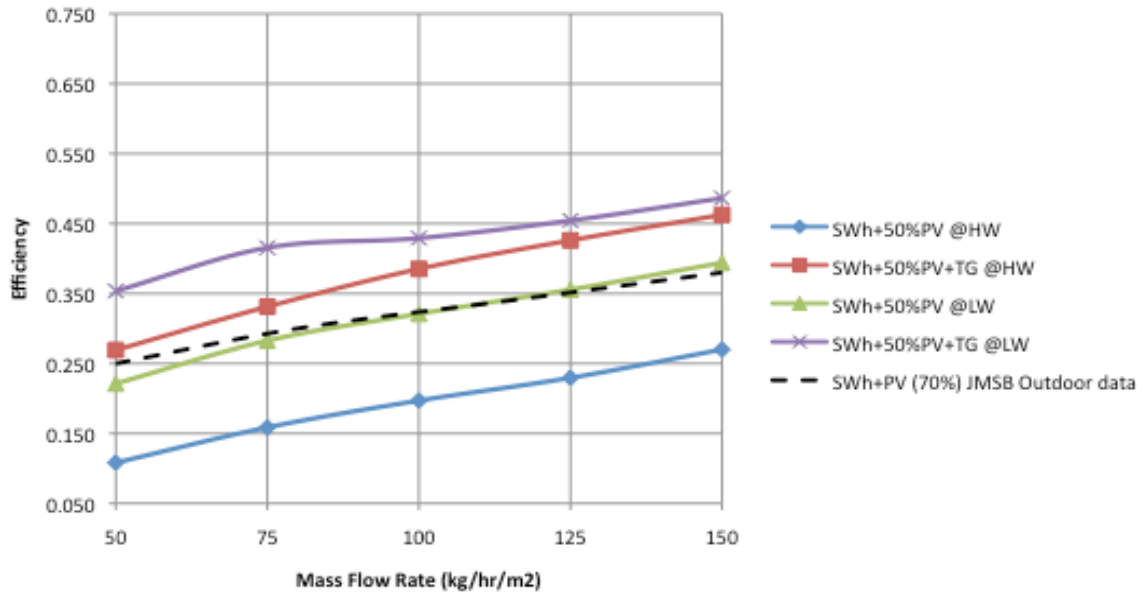


Figure 4.19 Collector C1 (SWh+PV) and C2 (SWh+PV+TG) Thermal Efficiency; Outdoor Data for SWh+70%PV spring efficiency (Athienitis et al., 2011);

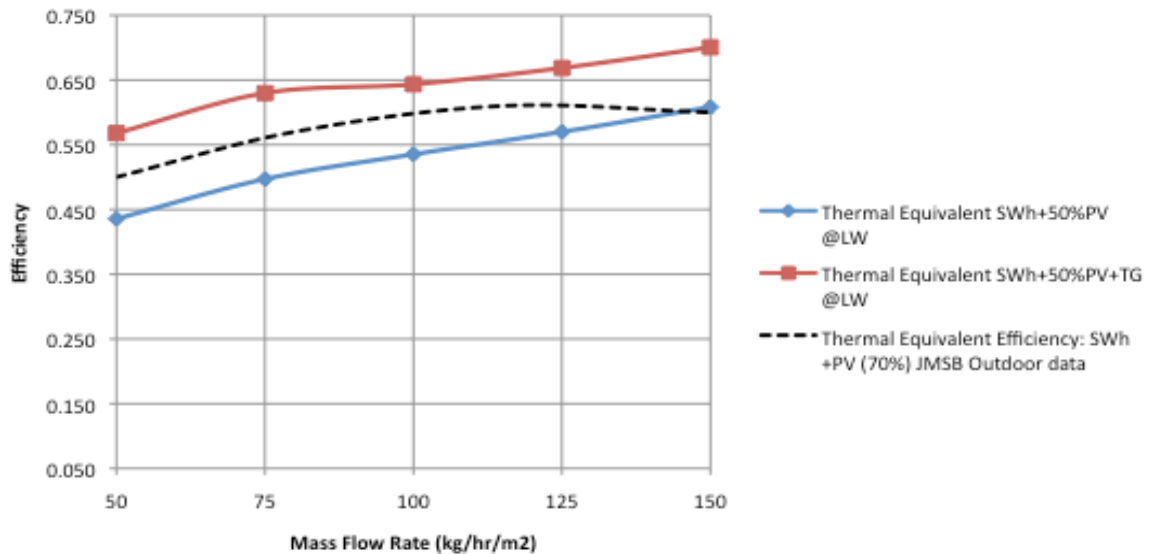


Figure 4.20 Thermal Equivalent Efficiency: Collector C1 (SWh+PV) and C2 (SWh+PV+TG); Outdoor Data for SWh+70%PV (Athienitis et al., 2011);

Figure 4.20 indicates that the thermal equivalent efficiency of C1 (SWH+50%PV) is lower than JMSB (SWH+70%PV), since less collector area is covered by PV modules. However, by covering the exposed SolarWall cladding with transpired glazing, collector C2 with only 50% PV coverage, scores a thermal equivalent efficiency higher than the JMSB setup with 70% PV (Figure 4.20). This finding proves that adding more PV doesn't necessarily mean generating more energy, as thermal efficiency of transpired collectors is actually lowered by PV coverage.

Figure 4.19 also shows that C2 (SWH+50%PV+TG) exhibited low susceptibility to wind-induced surface convective loss, especially at high mass flow rates. With 50% transpired glazing coverage, C2 performs 16%-20% higher in efficiency than C1 (without TG) at high surface flow (high wind), and 10%-14% higher at low wind. Therefore, it is concluded that even partial addition of transpired glazing is beneficial in reducing collector surface (radiant and wind) losses.

4.3.7 Detailed Temperature Profiles (B1 and B2)

For each collector configuration mentioned before, temperatures are measured at many discrete points on each component layers (Instrumentation diagrams see Figure 3.7 and 3.8). By averaging temperature measurements at each layer (e.g. transpired glazing, SolarWall, backplate, etc.), we can plot the average temperature rise for each component of the collector. Detailed temperature measurements along the height of the collector can be found in Appendix B. Temperature rise values are calculated based on exterior temperature near the collector surface. The uncertainty analysis of temperature rise is shown in Appendix C and the error bars are shown in Figure 4.21 and 4.22.

Take collector B1 (SWv) and B2 (SWv+TG) for example: Temperature rise of Tmid (middle layer) of SWv+TG and both Tsurf (surface layer) of SWv and SWv +TG systems are plotted at different mass flow rates in Figure 4.21 and 4.22.

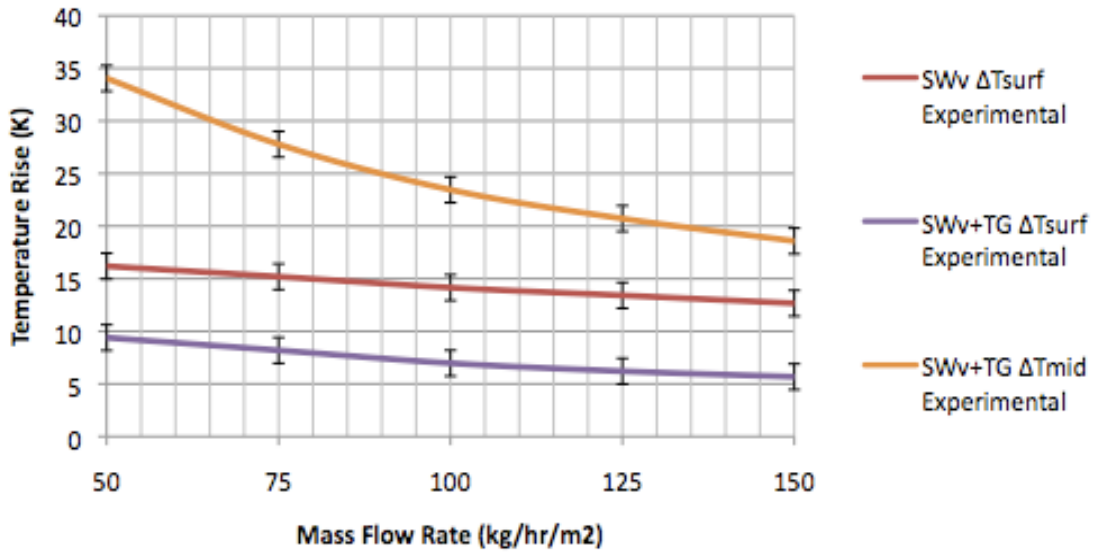


Figure 4.21 Temperature Rise at each layer: Collector B1 (SWv) and B2 (SWv+TG), 0.9m/s parallel surface airflow created by fan

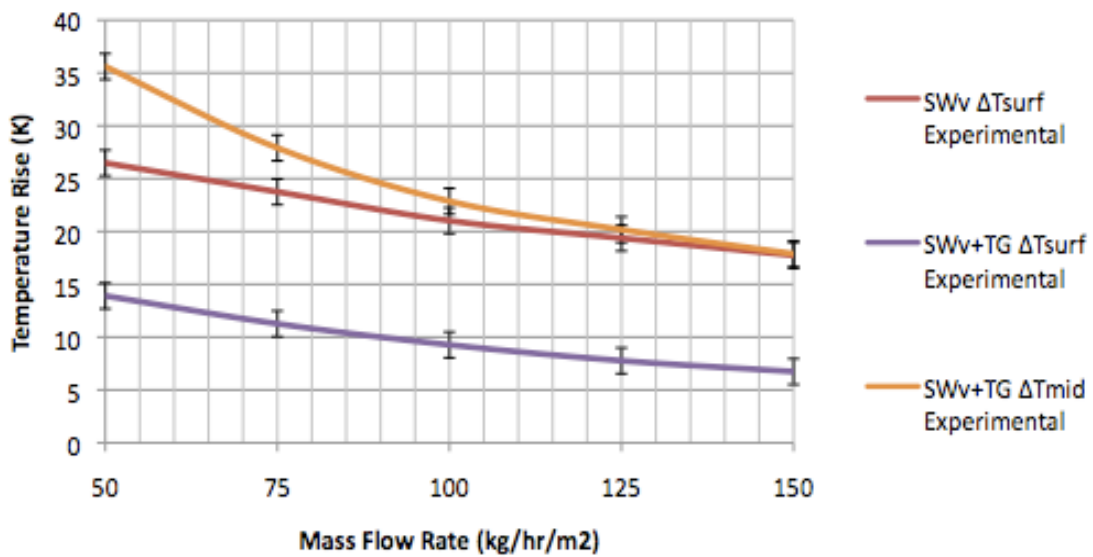


Figure 4.22 Temperature Rise at each layer: Collector B1 (SWv) and B2 (SWv+TG), 3.5m/s parallel surface airflow created by fan

Note that ΔT_{mid} is the absorber (SolarWall) temperature rise for SW_v+TG system, and ΔT_{surf} for SW_v+TG is the temperature rise at transpired glazing. For SW_v system, ΔT_{surf} means the temperature rise at surface (SolarWall), which is also the absorber.

Under both wind conditions, the absorber temperature of SW_v +TG (ΔT_{mid}) is higher than the absorber temperature of SW_v system (ΔT_{surf}). Comparing absorber temperatures of the two collectors, ΔT_{mid} remains almost invariant at high or low wind, while ΔT_{surf} of SW_v is significantly lowered by high wind conditions.

As absorber temperature is directly linked to collector outlet temperature and useful heat delivered, Figure 4.21 and 4.22 explained the higher efficiency of SW_v+TG system due to the reduction of surface convective wind loss. Moreover, the surface temperature of SW_v+TG system is effectively lower than ΔT_{surf} of SW_v system, resulting in less surface radiant loss less compared to conventional SolarWall (SW_v) systems.

More details on temperature at nodes (layers) for each collector can be found in Section 5.3.3, in combination with simulation results from custom thermal network models built in MATLAB. Appendix B summarizes the efficiency and temperature rise of the ten collectors in Table B.2 to B.11. The efficiency curves of all ten collectors are shown from Figure B.8 to B.11.

4.4 Testing Sequence for the Environmental Chamber

As shown in Figure 4.23, four best-performing configurations (B4, B5, C1 and C2 as referred to in Table 4.2 and 4.3) are tested in the Environmental Chamber. Compared to the experiments under the Solar Simulator, the Environmental Chamber is capable of

maintaining an ambient temperature of -20°C with incoming solar irradiance of $824\text{W}/\text{m}^2$ on the test plane, validating collectors' performance in cold environment. The experimental climatic conditions are summarized in Table 4.6.

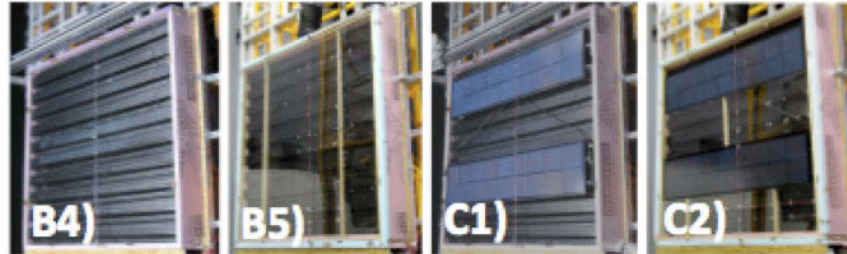


Figure 4.23 Collectors tested in the Environmental Chamber: B4: SolarWall (SWh); B5: SolarWall covered with transpired glazing (SWh+TG); C1: SWh+PV; C2: SWh+PV+TG

Table 4.6 Steady-State Testing Conditions (Environmental Chamber Testing)

Solar Irradiance ($\pm 10\%$ uniformity)	Exterior (Chamber) temperature/RH	Interior (Test Hut) temperature	Mass Flow Rate
$824\text{ W}/\text{m}^2$	$-20^{\circ}\text{C} / 45\%$	20°C	150, 125, 100, 75, 50 $\text{kg}/\text{hr}/\text{m}^2$

The schematic of the test set up is presented in Figure 4.24, showing half of the active façade of BIPV/T-SIP, which replaces the entire glazed façade of the Test Hut (Figure 4.4, right).

The Test Hut is maintain at room temperature (20°C) and exposed to solar radiation ($824\text{ W}/\text{m}^2$) and -20°C exterior temperature. The solar heated air from the collector outlet is ducted through the Test Hut without mixing with the air inside the Test Hut. An auxiliary heater with built-in control system is responsible for maintaining the interior of Test Hut at room temperature.

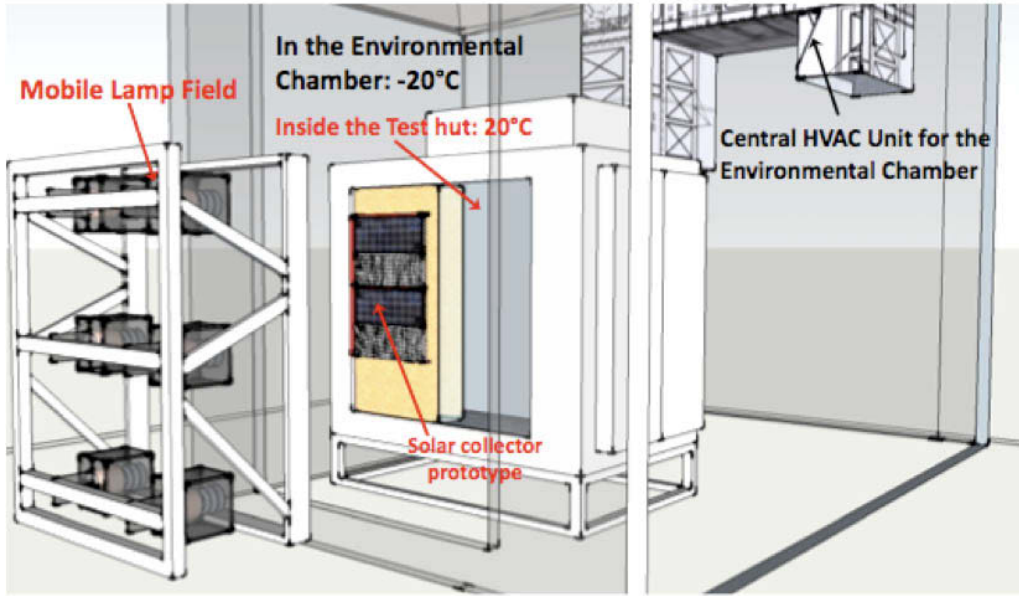


Figure 4.24 Schematic Drawing of experimental set up in the Environmental Chamber

The insulated duct transports the solar heated air outside the Environmental Chamber through a pre-engineered connection (Figure 4.25). Construction details of the experimental assembly in Environmental Chamber can be found in Appendix A.



Figure 4.25 Photo of experimental set up in the Environmental Chamber, showing Mobile Lamp Field, Test Hut with active façade, and Duct exiting the Chamber;

The duct from the collector outlet runs all the way out from the Environmental Chamber and ends up at the Air Collector Stand (Figure 4.3) where the fan is located. The solar heated air is sucked out by the fan and dumped into the lab space. Though the Chamber is slightly depressurized due to removal of air by the Air Collector Stand, there are two pressurizing/depressurizing fans built into the Chamber to stabilize the internal pressure of conditioned space.

As this is the first experiment carried out in the environmental chamber, some limitations, which may be improved for future experiments, were encountered. Firstly, no wind is blown on the surface of the collector to evaluate wind-induced convective losses at cold temperature. Secondly, the tests were conducted at 45% relative humidity (RH), while ideally, 55% to 75% RH is representative of winter conditions in Northern Canada (e.g. Iqaluit, Yellowknife, etc.).

Unique in set up with the incoming solar radiation, the Environmental Chamber receives 27.6kW of thermal energy from the lamps, which imposes additional loads on the cooling coil of the Chamber. To effectively lower the Chamber temperature with incoming solar radiation, relative humidity inside Chamber is maintained at 45% to relieve the cooling coil from defrost cycles and to exercise its capacity.

In addition, the incoming solar radiation heats up the glazed façade of the Chamber and leads to radiant gain on the collector surface. This error is experimentally corrected at the Solar Simulator with the use of the Artificial Sky, which is cooled to 10°C to simulate the cold sky. Numerical correction is needed to offset the radiant gain for the Chamber test, details are discussed in Section 5.4.

Figure 4.26 shows the Mobile Lamp Field in action (left) and explains the components of the Test Hut (right). A portable X-Y scanner is mounted in front of the collector to scan for solar uniformity. Once the optimal location is determined, the scanner is removed and the Test Hut is moved forward into the scan plane where the desired irradiance uniformity is achieved.

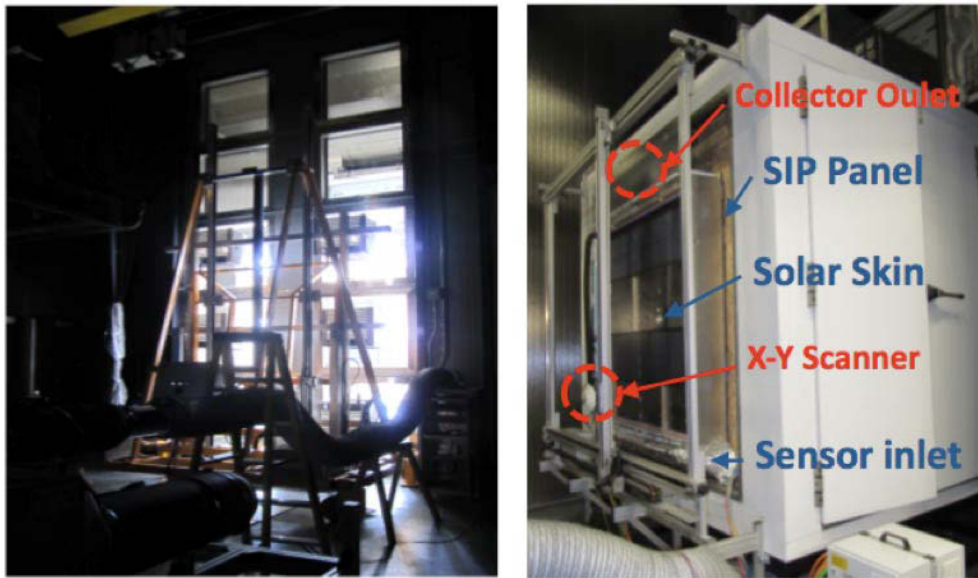


Figure 4.26 Photos of experiments in progress in the Environmental Chamber; Left: Lamps in action; Right: details of Test Hut assembly;

Due to the framing effects and the diffused light bouncing off multiple surfaces before reaching the scan plane, irradiance uniformity is able to reach $\pm 10\%$, as compared to $\pm 5\%$ uniformity with Solar Simulator main lamp field (Figure 4.7).

Figure 4.27 and 4.28 illustrate the solar distribution obtained from the portable X-Y scanner on the test plane. Note that there are some hot and cold spots on the irradiance distribution. For future experiments, better uniformity inside the Chamber may be obtained by strategic placement of insect screens to diffuse the incoming light.

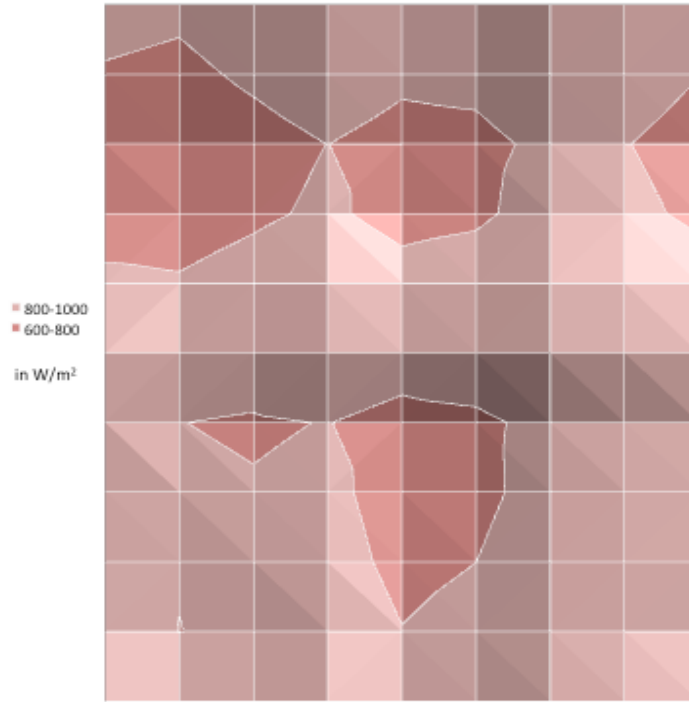


Figure 4.27 Irradiance Distribution at Collector surface (inside Chamber), average 824 W/m²

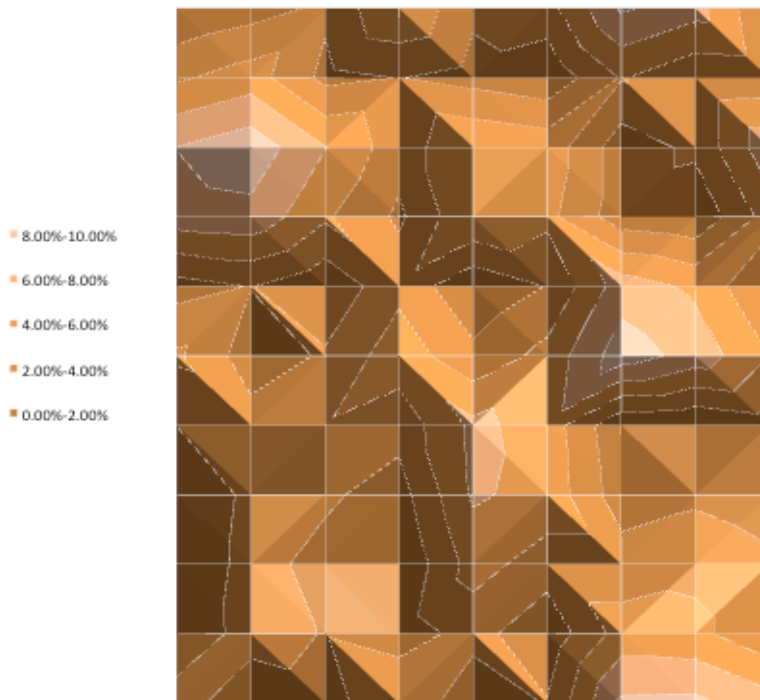


Figure 4.28 Standard deviation of solar distribution at Collector Surface (inside Chamber), 10% maximum

4.5 Results and Discussion – Environmental Chamber Experiments

4.5.1 Discrepancy in Results between Solar Simulator and Environmental Chamber

This two-part laboratory facility offers different strengths and capacities: the Solar Simulator is optimized for quick, accurate characterization of solar collectors or building components at room temperature, while the Environmental Chamber allows for evaluation under near in-situ conditions (with cold temperature and solar radiation) at the expense of incurring some systematic limitations. Table 4.7 summarizes the hardware limitations that cause the same collector to perform differently under the Solar Simulator and inside the Environmental Chamber.

Table 4.7 Summary of reasons contributing to different efficiency results between tests under Solar Simulator and test in the Environmental Chamber

Cause of discrepancy in collector performance	Tests under Solar Simulator	Tests in the Environmental Chamber
Different air leakage in duct run	Short duct run (15') from collector outlet to fan	Long duct run (45') from collector outlet to fan
Different back insulation	2" EPS behind collector	Full SIP (1') behind collector
Radiation gain at collector surface	Corrected by the artificial sky	Uncorrected as Chamber's glazed façade is heated by lamps
Different surface wind condition	Tested at 3.5m/s (high) or 0.9m/s (low) wind	Tested with no wind

The last three error sources mentioned in Table 4.7 are mathematically corrected via numerical simulation (elaborated in Section 5.4). This Section only investigates the error due to air leakage in ducts, using experimental corrections.

4.5.2 Effects of Air Leakage in Environmental Chamber

At the end of all Chamber experiments, the duct is disconnected at the collector outlet and at the fan from the Air Collector Stand. One end is sealed off and the other end is connected to a calibrated fan, while the rest of the duct run and its connectors remain undisturbed. A series of duct leakage test was performed at different levels of pressurization at room temperature. The calibrated fan measures automatically the pressure loss at the fan. In-duct pressure differentials due to fan pressurization are measured by a pressure sensor at the sealed end of the duct run.

Five mass flow rates, each corresponding to a certain internal pressure build-up, are evaluated in the leakage test. Results are shown in blue dots in Figure 4.29. Percentage losses in duct at different mass flow rates are relatively uniform, ranging from 10.5% to 11.1% in leakage tests.

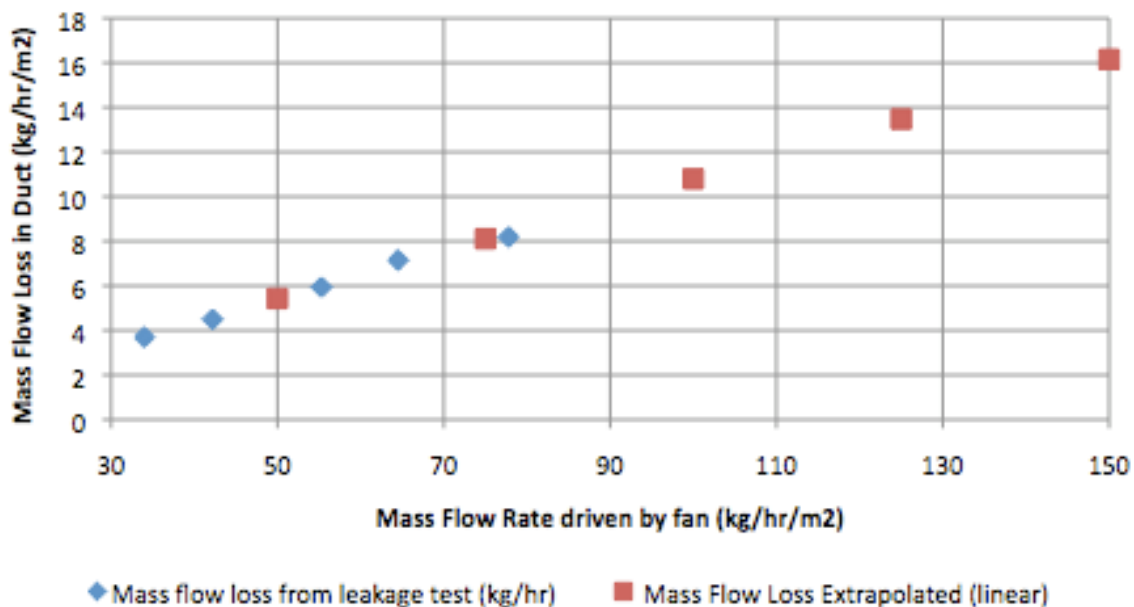


Figure 4.29 Duct Air Leakage Test results and extrapolated flow loss for Experimental Mass flow Rates

The red dots in Figure 4.29 are extrapolated linearly from the leakage test data (blue dots) for the five actual mass flow rates (50-150kg/hr/m²) used in the experiments. The leakage test determined that the average percentage in-duct mass flow loss is 10.8% for all mass flows, taking into consideration all connections along the 30' duct run from collector outlet to Air Collector Stand. Note that only the 30' that is addition to the 15' duct run used in Solar Simulator tests was evaluated, in order to find out the ADDITIONAL air leakage rate caused by a longer duct run and more connections during the Chamber tests. Details of the duct leakage test results and calculations can be found in Appendix B.

The 10.8% of leakage rate is a significant contributor to the overestimation of collector performance measured inside the Environmental Chamber. When the fan at the Air Collector Stand thinks it is drawing 150kg/hr/m² of air from the collector, there is only in fact 133.8 kg/hr/m² of air at the collector intake, the rest of air is lost in the numerous duct connections. As the efficiency values are directly proportional to the mass flow rate used in calculation (equation 4.1), the over-estimation of mass flow also leads to significant over-estimation of collector efficiency.

Figure 4.30 and 4.31 illustrate the corrected efficiency (red curve) as compared to the measured results (green curve) with duct leakage of 10.8%. The correction for duct leakage is particularly effective at high mass flow rates. Though the corrected efficiency curve (red curve) is still higher than the efficiency curves obtained from the Solar Simulator (blue curve), the duct leakage test eliminated the most significant source of error using reliable experimental data for correction.

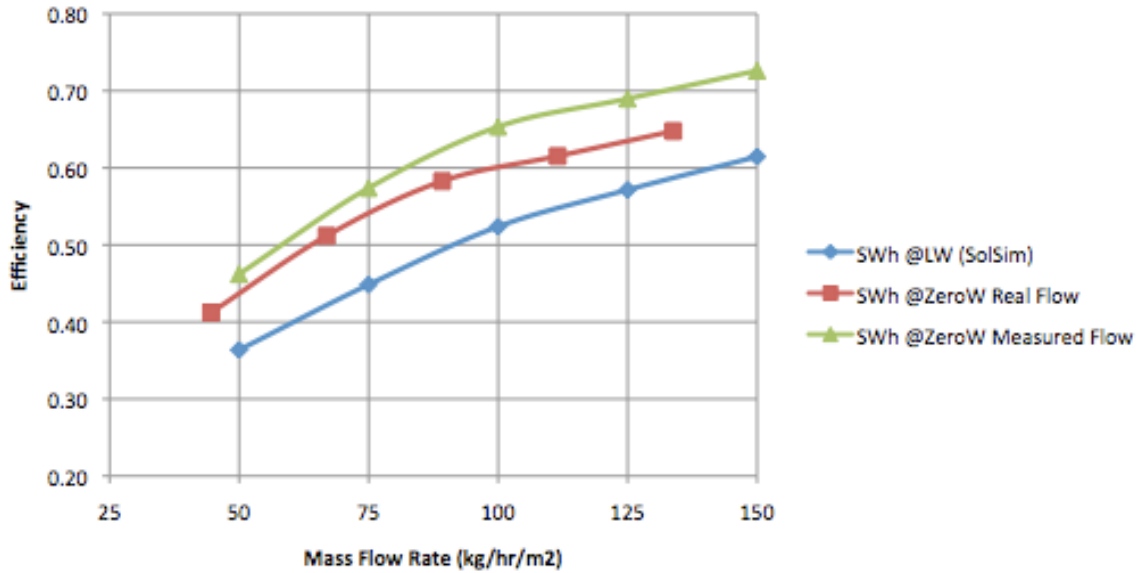


Figure 4.30 Duct Air Leakage Correction for Collector B4 (SWh)

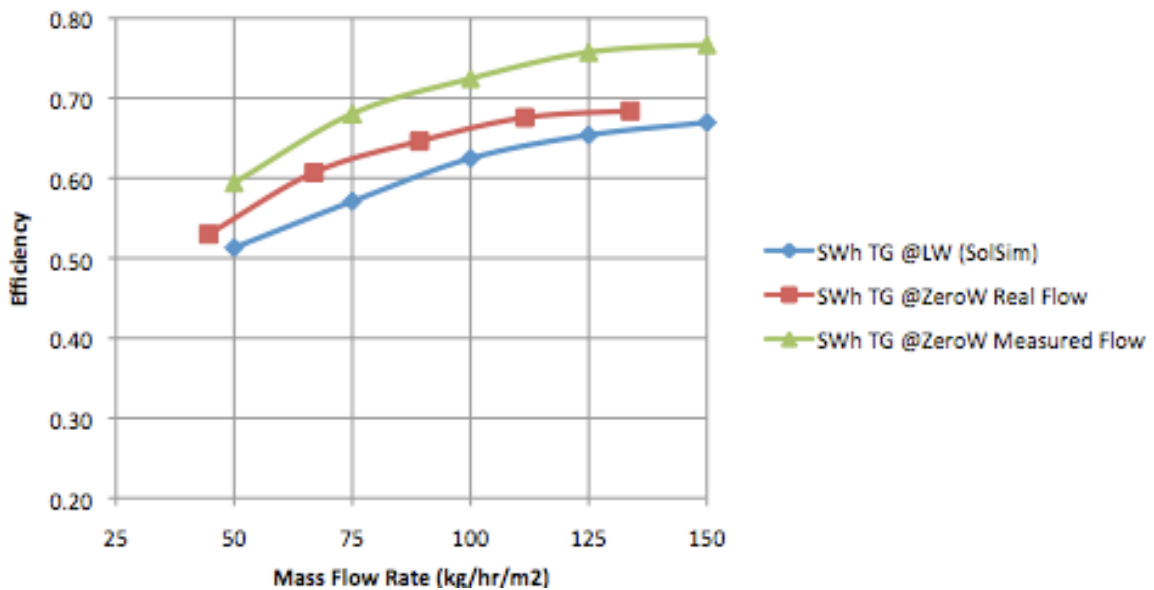


Figure 4.31 Duct Air Leakage Correction for Collector B5 (SWh+TG)

Collector B5 (SWh+TG) shows good agreement of 4% to 5% between the corrected efficiency (red curve) and the efficiency calculated from the Solar Simulator experiments (blue curve), while B4 (SWh) exhibits more discrepancy of 6% to 10%. It is because the SWh is more prone to the other sources of overestimation such as radiant gain and wind

effects as mentioned in Table 4.7. As presented in Figure 4.32 and 4.33, performance curves from Collector C1 and C2 show similar trends.

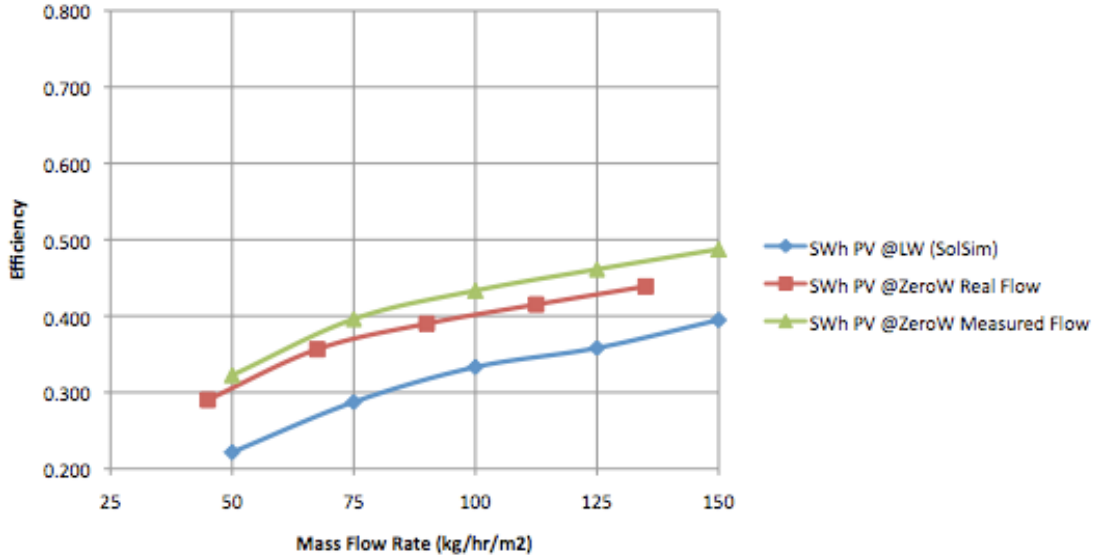


Figure 4.32 Duct Air Leakage Correction for Collector C1 (SWH+PV)

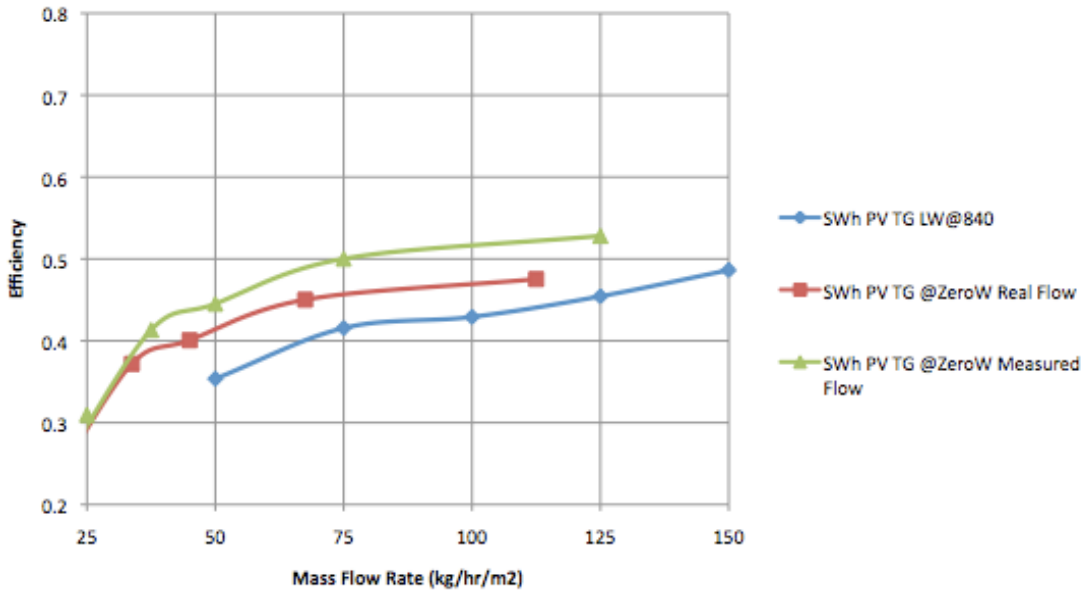


Figure 4.33 Duct Air Leakage Correction for Collector C2 (SWH+PV+TG)

After the leakage correction, collector with partial coverage of transpired glazing (C2: SWH+PV+TG) exhibits only 4% to 6% discrepancy between efficiency from

Chamber tests (red curve) and from Solar Simulator tests (blue curve, Figure 4.33). Comparatively, collector C1 (SWh+PV) shows 8% to 10% difference in efficiency (Figure 4.32), as transpired absorber is more susceptible to other uncorrected errors such as radiant gain and convective wind loss.

Moreover, all the results from Solar Simulator tests (blue curves) need to be corrected to account for higher back loss, resulting from the 2" back insulation as compared to the 1" insulation (SIP) during Chamber tests. Further elaboration of results correction using numerical methods will be presented in Section 5.4.

In conclusion, the general trend of efficiency curves obtained from experiments in the Environmental Chamber is in good agreement with results from the Solar Simulator. The differences in collectors' performance under the Solar Simulator and in the Environmental Chamber are explained qualitatively by theories of heat transfer, and quantitative corrections will be applied accordingly (Section 5.4).

As the first researcher to conduct experiments using both facilities, the author laid groundwork for future research involving result comparison of the Solar Simulator and the Environmental Chamber. At the same time, experimental results from the Environmental Chamber provided a valuable reference for predicting collectors' behaviors in cold climatic conditions pertaining to high latitudes.

5 Simulation and Model Validation

In order to predict the performance of various façade-integrated solar collectors, custom models derived from energy balance and heat transfer principles are developed in MATLAB/Simulink platform. Simulation results of collectors' performance are compared with experimental data obtained from the Solar Simulator and Environmental Chamber laboratory. This section describes four thermal network models for Collector B1/B4 (SW), B3/B5 (SW+TG), C1 (SW_h+PV) and C2 (SW_h+PV+TG).

5.1 Steady State Models of Two Transpired Collectors

5.1.1 Model Assumptions

Some assumptions are made to effectively manage the model complexities and computation time:

1. The temperature of each plate (e.g. SolarWall, Transpired Glazing, Back plate, etc.) is assumed to be uniform. This assumption is common in many simulation algorithms including in SWift99, RETScreen and in Summers' model. Though experimental data found a temperature gradient of up to 9°C across the plate, an averaged value of all sensors located in the central zone of each plate is used as the plate temperature.
2. Instrumentation of the absorber (SolarWall) and transpired glazing are positioned at the back of the plate. The temperatures at front surface of the plate are assumed to be equal, or similar to the temperature at the back of plate. This is particularly true for the absorber, as the metal plate is highly conductive.

3. The suction rate at the surface is considered to be uniform. Porosity of SolarWall uses 0.25%, assuming circular holes on a square pitch.
4. The collector test stand and the SIP wall, on which the collector is mounted, are assumed to be isothermal.
5. Calculation for air properties uses the temperature measured inside the plenum (averaged from 6 thermocouples).
6. Corrugation orientation is assumed to have little effect on collector performance, as indicated by experimental data in Section 4.3.3 (2% difference in efficiency between SWv and SWh) for collector size of 1.5m by 1.5m.

5.1.2 Heat Transfer Theory

Heat transfer in conventional Unglazed Transpired Collector (Collector B1: SWv) has been modelled by Dymond & Kutscher (1997) assuming uniform suction rate at the surface. Figure 5.1 presents the heat transfer exchanges occurring in the SWv system, with transpired absorber on the exterior.

The energy balance of SWv collector can be described by:

$$Q_s = Q_{RO} + Q_{wind} + Q_u + Q_b \quad (5.1)$$

where Q_s is the absorbed solar radiation (W), Q_{RO} is the radiant loss to the outside (W), Q_{wind} is the convective heat loss due to wind (W), Q_u is the useful heat transferred into the building (W), and Q_b is the heat loss at the back of the collector (W); all temperatures (K) at nodes are labeled accordingly.

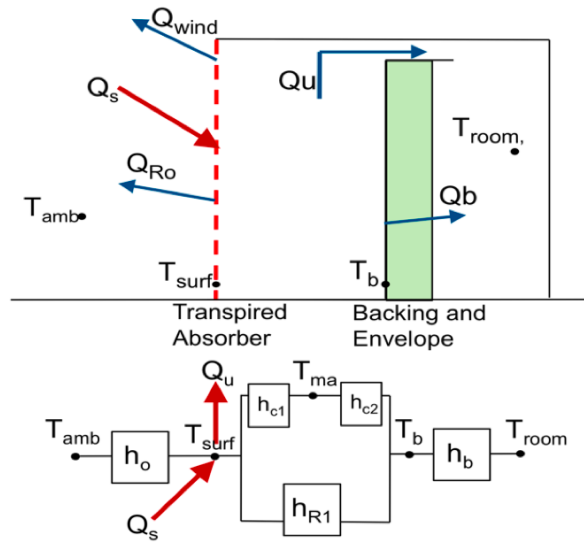


Figure 5.1 Energy Balance and Thermal Network models of conventional Unglazed Transpired Collector (Collector B4: SWH); Plenum exaggerated.

Similarly, for an improved transpired collector with transpired glazing cover (SWv+TG), system energy balance shown in Figure 5.2 can be written as:

$$Q_{s1} + Q_{s2} = Q_{RO} + Q_{wind} + Q_u + Q_b \quad (5.2)$$

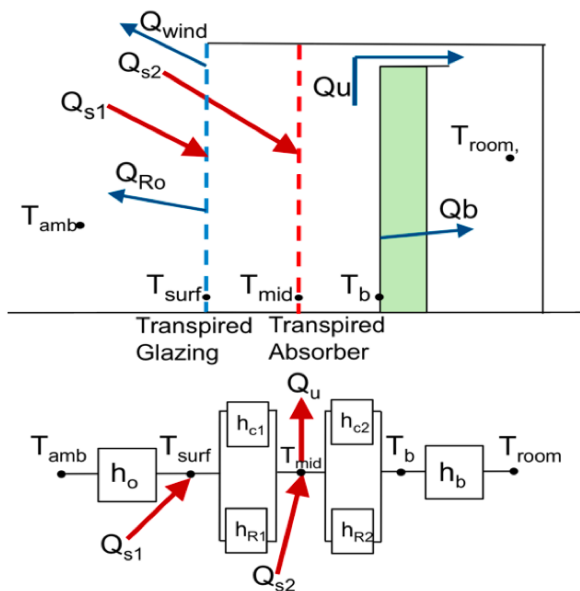


Figure 5.2 Energy Balance and Thermal Network models of improved UTC with Transpired Glazing (Collector B2: SWv+TG) Plenum exaggerated.

Q_{S1} and Q_{S2} are the absorbed solar gain (W) by collector surface (transpired glazing) and by the transpired absorber, respectively, shown in equation 5.3.

$$Q_{s1} + Q_{s2} = \alpha_1 G + \tau_1 \alpha_2 G \quad (5.3)$$

where α_1 and τ_1 is the absorptance and transmittance of the transpired glazing, respectively; α_2 is the absorptance of SolarWall (transpired absorber); Note that Q_{S1} is much less in quantity compared to Q_{S2} , as the transpired glazing transmits more than 90% of solar radiation to the absorber. Kirchoff's law dictates that the relation between the absorptance, α , transmittance, τ , and reflectance, γ , of a surface is given by:

$$1 = \alpha + \tau + \gamma \quad (5.4)$$

The surface radiant and convective losses to outside are described by for both thermal models (Figure 5.1 and 5.2):

$$Q_{RO} + Q_{wind} = (h_{RO} + h_{wind}) \cdot (T_{surf} - T_{amb}) \cdot A_{col} \quad (5.5)$$

where A_{col} is the collector area; h_{RO} is the radiant heat transfer coefficient to outside ($W/m^2/K$), which can be calculated by describing radiant heat transfer between the hot collector surface and the cooler surroundings:

$$h_{RO} = \frac{e \cdot \sigma \cdot (T_{surf}^4 - T_{amb}^4)}{(T_{surf} - T_{amb})} \quad (5.6)$$

where σ is the Stephan-Boltzmann constant ($W/m^2/K^4$); T_{surf} and T_{amb} are temperatures (K) at collector surface and of the ambient lab air, respectively; e is the emissivity of collector surface.

The convective heat transfer coefficient due to wind (h_{wind}) is affected by surface conditions (corrugation and perforation), suction velocity, wind direction and speed, etc. Without going into details about turbulent flows near the corrugation and pores, several correlations (equation 5.7 to 5.11) are investigated.

The common empirical forms for h_{wind} (grazing wind on facades) follow linear or exponential increase with increasing wind speed (Palyvos 2008):

$$h_{wind} = a \cdot V_{wind}^b \cdot L^c = A \cdot V_{wind}^b \quad (5.7)$$

$$h_{wind} = A \cdot V_{wind} + B \quad (5.8)$$

$$h_{wind} = A \cdot \left(\frac{V_{wind}}{L \cdot V_s} \right) \quad (5.9)$$

where a, b, c, A, B are constants depending on wind conditions, L is the collector characteristic length (m). In addition, lab scale flat-plate transpired collector by the Solar Thermal Research Laboratory at University of Waterloo (STRL) shows correlation of convective loss in relation to surface wind speed (V_{wind}) and suction velocity (V_s):

$$h_{wind} = 6.0 + 4 \cdot V_{wind} - 76 \cdot V_s \quad (5.10)$$

Experiments from the Solar Simulator (Section 4.2) at two different surface wind speeds also suggest that surface wind loss corresponds strongly with wind speed and suction velocity following the same logic:

$$h_{wind} = C + B \cdot V_{wind} + A \cdot V_s \quad (5.11)$$

where A, B, C are constants that need to be fitted using the node temperatures and known heat balances. Note that equation 5.10 is still a good approximation for convective wind losses of flat-plate transpired collectors (e.g. SWv+TG). However, the general form of equation 5.11 takes care of surface convective loss and possible losses from the collector sides and due to air leakage from plenum connections. Details of acceptable expressions for convective heat transfer coefficients (h_{conv}) are discussed in Section 5.3.2.

The back plate of the collector is heated by the solar radiation and may potentially lose heat to the ambience. In the Solar Simulator experiments, the back of the collector is exposed to room temperature (20°C), insulated to RSI-1.32 equivalent (5/8" OSB and 2" EPS). Therefore, the back loss can be expressed as:

$$Q_b = h_b (T_b - T_{room}) A_{col} \quad (5.12)$$

h_b is the combined heat transfer coefficient of wall insulation and interior air film (W/m²/K), For the experiments in the Environmental Chamber, a SIP wall backing of RSI-7.9 is used, and Q_b is significantly reduced. Details on the correction can be found in Section 5.4.3. In real applications in cold climate, the collector is integrated into a conditioned space maintained a temperature higher than exterior temperature. The back loss could become back gains when there is no incident solar radiation on the collector (e.g. at night). Q_b will be expressed in negative value and it is known as the heat recapture at night, beneficial for overall building energy efficiency.

Lastly, the useful heat captured in the form of heated air is calculated by:

$$Q_u = MFR \cdot c_p \cdot (T_{plm} - T_{amb}) A_{col} \quad (5.13)$$

where MFR is the mass flow rate (kg/s/m²), c_p is the specific heat capacity of air (J/kg/K), and $(T_{plm} - T_{amb})$ is the temperature rise of heated air in the plenum. The collection of heat balances can be calculated simultaneously from equation 5.1, 5.2, 5.3, 5.5, 5.12, and 5.13. Details of heat transfer coefficients and node temperatures are discussed in Section 5.1.3 below.

5.1.3 Thermal Network Models

Surface temperatures are evaluated through an energy balance of the thermal networks shown in Figure 5.1 and 5.2 for conventional Unglazed Transpired Collector (SW) and improved Transpired Collector (SW+TG), described by equation 5.14 and 5.15, respectively.

$$T_{surf_SW} = \frac{Q_s + (h_{RO} + h_{wind}) \cdot T_{amb} + h_{R1} \cdot T_b + h_{C1} \cdot T_{ma} + MFR \cdot c_p \cdot \epsilon_{HX} \cdot T_{amb}}{h_R + h_{wind} + h_{R1} + h_{C1} + MFR \cdot c_p \cdot \epsilon_{HX}} \quad (5.14)$$

$$T_{surf_SW+TG} = \frac{Q_{S1} + (h_{RO} + h_{wind}) \cdot T_{amb} + (h_{R1} + h_{C1}) \cdot T_{mid}}{h_R + h_{wind} + h_{R1} + h_{C1}} \quad (5.15)$$

where ϵ_{HX} is the effectiveness of Unglazed Transpired Collector (UTC), T_{ma} is an equivalent temperature that gives the mean air temperature at mid-plenum (K), T_b is the temperature (K) at the back plate of collectors. T_{ma} and T_b can both be calculated from the thermal network model illustrated in Figure 5.1. For the normal UTC, h_{C1} and h_{C2} are the convective heat transfer coefficients of the two interior surfaces in the air plenum (W/m²/K).

For the improved UTC, T_{mid} is the temperature at the middle layer (equation 5.16), which is the transpired absorber (SolarWall):

$$T_{mid} = \frac{Q_{S2} + (h_{R1} + h_{C1}) \cdot T_{surf} + (h_{R2} + h_{C2}) \cdot T_b + MFR \cdot c_p \cdot \varepsilon_{hx} \cdot T_{amb}}{h_{R1} + h_{C1} + h_{R2} + h_{C2} + MFR \cdot c_p \cdot \varepsilon_{hx}} \quad (5.16)$$

The convective heat transfer from the absorber to the plenum, h_{C1} and h_{C2} are calculated with average Nusselt number in the plenum obtained with the following relations from Incropera & DeWitt (2002). Equation 5.17 is used for laminar flow, while equation 5.18 is used for mixed boundary layer conditions.

$$\overline{Nu}_L = 0.664 Re_L^{1/2} \cdot Pr^{1/3} \quad Re_L \leq 5 \times 10^3 \quad (5.17)$$

$$\overline{Nu}_L = (0.037 Re_L^{4/5} - 871) \cdot Pr^{1/3} \quad 5 \times 10^5 < Re_L \leq 10^8 \quad (5.18)$$

where Pr is the Prandtl number, Re_L is the Reynolds number of the air in the plenum, calculated at average velocity in the plenum, V_{plm} :

$$V_{plm} = \frac{1}{2} V_{max} = \frac{1}{2} \frac{MRF / \rho}{A_{cross-plm}} \quad (5.19)$$

where V_{max} is the maximum velocity in the plenum, and $A_{cross-plm}$ is the cross-section area of the plenum. Lastly, T_{plm} is the average of temperature at plenum top, i.e. outlet temperature. According to Dymond&Kutscher's model, T_{plm} for a UTC system is calculated using:

$$T_{plm_UTC} = \varepsilon_{hx} (T_{surf} - T_{amb}) + T_{amb} \quad (5.20)$$

where ε_{HX} is the effectiveness of transpired collectors. For the SolarWall (SW) collector, ε_{HX} can be calculated based on the work of Van Decker et al. (2001):

$$\varepsilon_{hx} = 1 - (1 - \varepsilon_f) \cdot (1 - \varepsilon_h) \cdot (1 - \varepsilon_b) \quad (5.21)$$

The expression of effectiveness in equation 5.21 is split into three parts: heat transfer occurring at front surface ε_f , in the sides of holes ε_h , and at the back of plate ε_b .

$$\varepsilon_f = 1 - \left[1 + \frac{\max(17.7, 0.708 \text{Re}_{wind}^{0.5})}{\text{Re}_s} \right]^{-1} \quad (5.22)$$

$$\varepsilon_b = 1 - \frac{1}{1 + 3.4 \text{Re}_b^{-1/3}} \quad (5.23)$$

$$\varepsilon_h = 1 - \exp\left(-0.0204 \frac{P}{D} - \frac{20.62t}{\text{Re}_h D}\right) \quad (5.24)$$

$$\text{Re}_{wind} = \frac{V_{wind}P}{\nu} \quad \text{Re}_s = \frac{V_s P}{\nu} \quad \text{Re}_b = \frac{V_s P}{\nu \rho} \quad \text{Re}_h = \frac{V_s D}{\nu \rho} \quad (5.25)$$

where V_{wind} is surface wind speed (m/s), P is distance between pores, i.e. pitch (m), D is diameter of pores (m), ν is kinematic viscosity of air (m^2/s), ρ is porosity of the transpired collector.

The improved transpired collector, SW+TG, behaves in a way similar to the normal SW system in terms of heat transfer from absorber to the plenum air. T_{plm} of SW+TG can be obtained by simply replacing T_{surf} in equation 5.20 with T_{mid} , as the real absorber in the SW+TG is in fact the middle cladding, whereas the absorber in the SW collector is the front surface.

Although the generic form of ε_{HX} (equation 5.21) holds true, directly using equation 5.22 to 5.25 to calculate effectiveness for SW+TG system (Figure 5.2) gives dissimilar

results. Therefore, calibrated effectiveness from experimental data is used in simulations for the SW+TG system. By definition, effectiveness of any UTC can be obtained from equation 5.26:

$$\varepsilon_{hx} = \frac{(T_{plm} - T_{amb})}{(T_{abs} - T_{amb})} \quad (5.26)$$

Finally, the thermal efficiency of both UTC and UTC+TG systems can be obtained:

$$\eta_{th} = \frac{Q_u}{G} = \frac{MFR \cdot c_p \cdot (T_{plm} - T_{amb}) \cdot A_{col}}{(I \cdot A_{col})} \quad (5.27)$$

where I is the incident solar irradiance (W/m²) on the façade, G is the total solar gain (W) on the collector area.

5.2 Steady State Thermal Network Model for PV/T

The actual heat transfer of PV modules mounted on transpired cladding is extremely complex. At sections where the UTC is covered by PV modules, the air is drawn from the bottom of the PV modules and sucked into the cladding perforations behind the PV. Collector C2 (SW+PV+TG) adds to the complexity of the problem by covering the exposed UTC (SolarWall) cladding with transpired glazing.

Figure 5.3 shows a couple of thermal network models by Athienitis et al. (2011), describing the PV/T+UTC system as demonstrated on the JMSB building façade (Figure 2.7). Note that b) is a simplified version of a) in Figure 5.3, with less nodes and combine heat transfer coefficients.

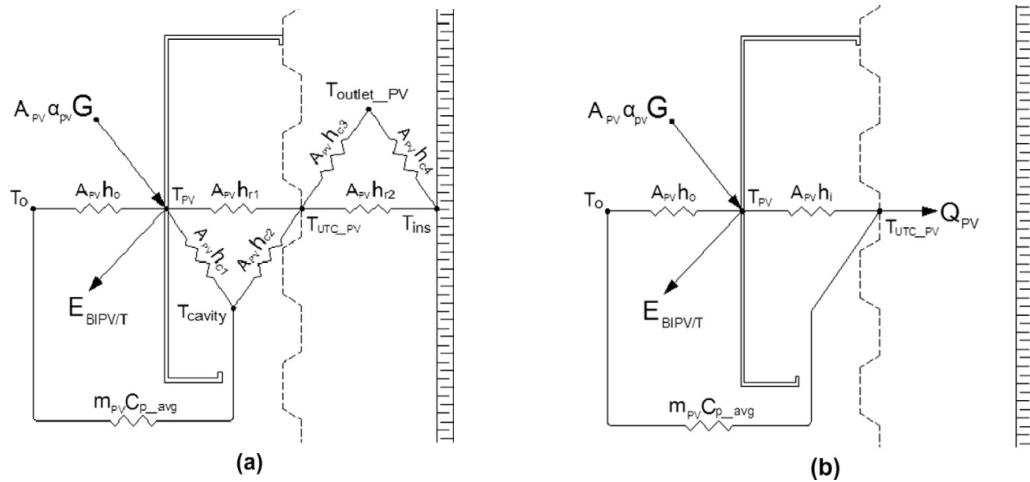


Figure 5.3. Original (a) and Simplified (b) Thermal Network Models for PV mounted on UTC cladding, Athienitis et al. (2011)

To further simplify the problem, the model in Figure 5.4 is proposed for the scope of this thesis project, replacing the node on the surface of the transpired cladding by a fictitious node at mid plenum, where the heated air is assumed to be removed.

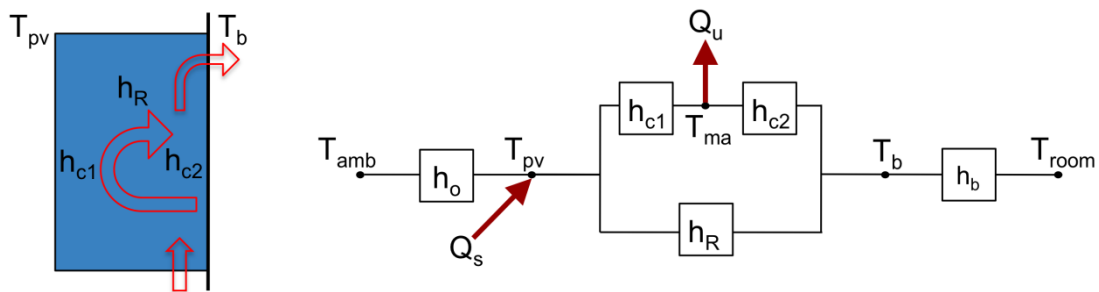


Figure 5.4 Simplified Thermal Network Model for a PV/T system

The basic PV/T model illustrated in Figure 5.4 shows one dark-frame PV panel (1.465m by 0.36m) mounted over a flat wall surface. Q_s describes the effective portion of the incident solar radiation converted to heat:

$$Q_s = \alpha_{PV} (1 - \eta_{PV}) \cdot G \quad (5.28)$$

where α_{PV} is the overall absorptance of the PV panel (frame and backing included), and η_{PV} is the electric efficiency of the PV panel (temperature dependent, equation 4.3).

Equations containing T_{pv} , T_{ma} and T_b can be listed via the thermal network model. T_{top} is the temperature at the plenum top, e.g. outlet temperature; T_{air} is simply the average of T_{top} and T_{amb} (K).

$$T_{pv} = \frac{Q_s + h_o T_{amb} + h_R T_b + h_{C1} T_{ma}}{h_o + h_R + h_{C1}} \quad (5.29)$$

$$T_{top} = \frac{h_{C1}(T_{pv} - T_{air}) + h_{C2}(T_b - T_{air})}{MFR \cdot c_p} + T_{amb} \quad (5.30)$$

The radiative and convective heat transfer coefficients from surface to outside are combined as a film coefficient h_o . In reality, the sky temperature and ground temperature are different, particularly due to the cold sky in the high north. The simplification of h_o , while valid for laboratory conditions, may not be representative for realistic environmental conditions at high latitudes. Similarly, h_b is the combined coefficient of wall insulation and interior air film. Plenum convective heat transfer coefficients h_{C1} and h_{C2} are calculated from Reynolds number and Nusselt numbers, using equations from a PV/T model developed by Liao et al. (2007):

$$Re = \frac{\rho \cdot V_{plm} \cdot 2H}{\mu} \quad (5.31)$$

$$Nu_1(y) = (0.011 Re + 62.856) \cdot e^{-0.475(y/H)} + 2.766 \cdot 10^{-3} \cdot Re + 5.58 \quad (5.32)$$

$$Nu_2(y) = (0.109 Re - 124.344) \cdot e^{(-1.635 \cdot 10^{-5} \cdot Re - 0.593)(y/H)} + 4.098 \cdot 10^{-3} \cdot Re + 3.896 \quad (5.33)$$

where ρ_{air} , μ , k is the temperature dependent properties of air, i.e. density (kg/m^3), dynamic viscosity (kg/m/s), and conductivity (W/m/K), respectively. H is the height of the PV module (0.36m), and y is the distance from the bottom of the PV module (from 0 to 0.36m); V_{plm} is velocity in the plenum directly related to mass flow rate.

h_{C1} (on the PV side) and h_{C2} (on the backing side) vary across the module height as Nusselts number decreases with increasing heights. Therefore, as the height of PV module increases, the thermal efficiency of PV/T decreases. Averaged values of height-dependent h_{C1} and h_{C2} (equation 5.34) are used in simulations.

$$h_{C1}(y) = \frac{Nu_1(y) \cdot k}{H} \quad h_{C2}(y) = \frac{Nu_2(y) \cdot k}{H} \quad (5.34)$$

The useful heat collected (Q_u) is calculated as:

$$Q_u = FR \cdot A_{\text{col}} \cdot [Q_s - U_{\text{tot}}(T_{\text{top}} - T_{\text{amb}})] \quad (5.35)$$

$$FR = \frac{MFR \cdot c_p}{U_{\text{tot}}} \left[1 - \exp\left(\frac{-U_{\text{tot}} \cdot F}{MFR \cdot c_p}\right) \right] \quad F = \left[1 + \frac{U_{\text{tot}}}{h_{C1} + (h_{C2}^{-1} + h_R^{-1})^{-1}} \right]^{-1} \quad (5.36)$$

where FR is the heat removal rate assuming an exponential increase of heat removal as MFR increases, U_{tot} is overall loss from the collector to outside and to the back, i.e. h_o and h_b ($\text{W/m}^2/\text{K}$). The finite difference method is used to evaluate a system of equations (5.28, 5.29, 5.30, 5.34, 5.35, 5.36) until steady state values converge and solve for variables including Q_u and all node temperatures. Similar calculation techniques are also used for a BIPV/T roof model in Chen et al. (2010).

The thermal efficiency of a simple PV/T system is defined as the fraction of Q_u over incident solar gain (G). However, as the system produces electricity at the same time, a combined thermal equivalent efficiency for PV/T, η_{EQ} , is adopted as previously mentioned in Section 4.3 (equation 4.5).

For collector C2 (SWh+PV+TG), the same model in Figure 5.4 is used for the section covered by PV modules, while it is assumed that the section covered with transpired glazing behaves in the same way as collector SWh+TG (Section 5.1). Therefore, the overall efficiency of C2 is modeled as an area-averaged sum of two thermal efficiency results:

$$\eta_{Thermal_SWh+PV+TG} = (A_{PV} / A_{Col}) \cdot \eta_{TH_PV/T} + (A_{TG} / A_{Col}) \cdot \eta_{TH_SWh+TG} \quad (5.37)$$

5.3 Steady-State Simulation Results compared with Experimental Data

5.3.1 Uncertainty Analyses of Experimental Results

Before comparing the simulation results with experimental data, it is essential the errors of experimental quantities are analyzed. The uncertainty of a measured quantity x , μ_v , can be expressed by the combination of bias error, e_{bias} , and precision error, $e_{precision}$, as shown in equation 5.38.

$$\mu_x = \pm(e_{bias}^2 + e_{precision}^2)^{1/2} \quad (5.38)$$

To calculate precision errors related to repeatability, two or more tests under the same climatic conditions are needed. As systematic repetition is not the main objective of

the experimental evaluation, this thesis considers only bias error related to accuracy and calibration error of the instruments.

Simple measured quantities such as solar irradiance, temperatures, pressures, panel size, have inherent bias errors from the measurement instruments. For each calculated quantity f , as a linear function of n independent normally distributed variables $x_1, x_2 \dots x_n$, the error of f , δf , is expressed by:

$$\delta_f = \left[\left(\frac{\partial f}{\partial x_1} \delta_{x_1} \right)^2 + \left(\frac{\partial f}{\partial x_2} \delta_{x_2} \right)^2 + \left(\frac{\partial f}{\partial x_3} \delta_{x_3} \right)^2 + \dots + \left(\frac{\partial f}{\partial x_n} \delta_{x_n} \right)^2 \right]^{\frac{1}{2}} \quad (5.39)$$

where $f = f(x_1, x_2, x_3 \dots x_n)$ (5.40)

Detailed calculations of the uncertainty for all relevant variables are elaborated in Appendix C. Some of the calculated variables such as temperature rise (T_{rise}), mass flow rate (MFR), useful heat captured (Q_u), convective heat transfer coefficient due to wind (h_w), and efficiency (η), summarized in Table 5.1.

Table 5.1 Summary of sample uncertainty values for calculated variables

Variable	Sample Value measured (X)	Error (δx)	Uncertainty ($\delta x/X$)
T_{rise}	15°C	$\pm 1.225^\circ\text{C}$	± 0.0816
MFR	150 kg/hr/m ²	± 5.27 kg/hr/m ²	± 0.035
Q_u	475 W/m ²	± 36.8 W/m ²	± 0.0775
h_w	15 W/K/m ²	± 1.81 W/k/m ²	± 0.121
η	45.9%	$\pm 3.67\%$	± 0.080

5.3.2 Convective Heat Transfer Coefficients

For transpired collectors, most of the heat loss occurs at the front surface due to convective loss, especially in the presence of wind (parallel to surface) and suction (perpendicular to surface). Many research attempts have traditionally employed Nusselt number correlations developed for fully developed flow in smooth pipes and channels. However, these correlations usually do not resemble the actual conditions found in an open-loop perforated surface. Aggravated by non-uniform cross-sections, irregular perforation, non-uniform heat fluxes, non-develop flow and mixed boundary conditions, convective heat transfer between the heated air and transpired collector surface is an extremely complex phenomenon.

General correlations of wind-induced convective heat transfer coefficient were listed in equation 5.7 to 5.11, 5.43 and 5.44, however, there is no perfect correlation that fit for all collectors at all wind conditions.

Given the corrugated profile and non-standard perforation of the SolarWall transpired absorber, the analysis of exact surface convective loss would require Computational Fluid Dynamics (CFD) if studied solely based on heat transfer principles. This section will focus on developing appropriate expressions for convective heat transfer coefficients (h_{conv}) from the experimental results (Section 4.1) under two parallel surface flow conditions (3.5m/s and 0.9m/s average).

Note that the h_{conv} in this thesis is a combination of convective loss from the surface and possible loss from the collector sides (insulated to RSI-1.4m²K/W). It is calculated

based on the energy balance equations of collectors SWv (equation 5.2), and SWv+TG (equation 5.2):

$$h_{conv} = \frac{\alpha_1 G - h_{RO}(T_{surf} - T_{amb}) - Q_U - h_b(T_b - T_{room})}{(T_{surf} - T_{amb})} \quad (5.41)$$

$$h_{conv} = \frac{(\alpha_1 G + \tau_1 \alpha_2 G) - h_{RO}(T_{surf} - T_{amb}) - Q_U - h_b(T_b - T_{room})}{(T_{surf} - T_{amb})} \quad (5.42)$$

where equation 5.41 is for collector SWv and T_{surf} is the SolarWall temperature, while equation 5.42 is for collector SWv+TG and T_{surf} is the Transpired Glazing temperature. In both cases, T_{room} is the lab space temperature as the back of the collector is exposed to lab condition during the Solar Simulator experiments.

Kutscher et al. (1991) showed that the surface convective loss coefficient from the collector to ambient is strongly linked to wind speed (V_{wind}) and surface suction speed (V_s). Assuming uniform suction for flat plate transpired absorber, h_{conv} is written as:

$$h_{conv,col-amb} = 0.82 * \frac{V_{wind} \nu \rho C_p}{LV_s} \quad (5.43)$$

Similarly, Carpenter et al. (1999) used a correlation of the same logic in Swift99 to describe surface heat transfer of transpired plates:

$$h_{wind} = 0.02 \frac{V_{wind}}{V_s} \quad (5.44)$$

To investigate this linear relationship described by equation 5.43 and 5.44, h_{conv} determined experimentally by equation 5.41 and 5.42 is plotted against the ratio of V_{wind}/V_s , discussed in Appendix D. The linear relationship is acceptable within the error

range for SWv at both surface parallel flow (wind) conditions; however, the relationship barely holds true for SWv+TG collector, especially at low wind conditions. Additionally, the slope and intercept of the linear approximation is dissimilar between low and high wind conditions, resulting in difficulty to fit a universal approximation that works for all MFR and at all wind speeds between 0.9m/s to 3.5m/s. Therefore, a linear approximation of h_{conv} using the general form of equation 5.11 were employed in all simulation (applicable for parallel wind speeds between 0.9m/s to 3.5m/s):

$$h_{conv} = 9.06 + 5.99 \cdot V_{wind} - 140.7 \cdot V_s \quad (\text{SWv}) \quad (5.45)$$

$$h_{conv} = 15.68 + 3.368 \cdot V_{wind} - 282.2 \cdot V_s \quad (\text{SWv+TG}) \quad (5.46)$$

The constants in equation 5.45 and 5.46 are fitted from experimental h_{conv} values calculated from equation 5.41 and 5.42, respectively. Figure 5.5 (SWv) and 5.6 (SWv+TG) plotted h_{conv} against V_s , showing that the approximation of h_{conv} is within the error range of the experimental data.

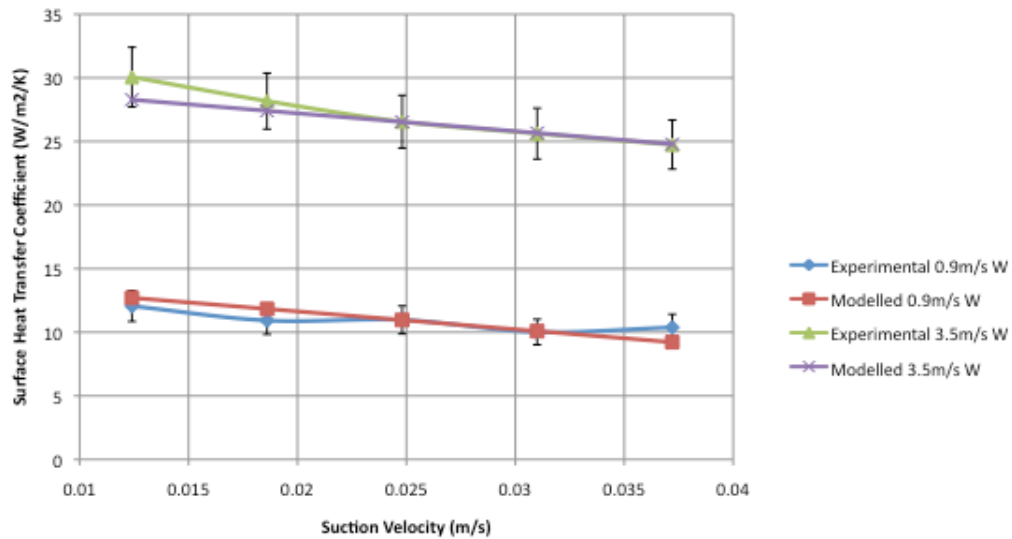


Figure 5.5 Collector SWv: Modelled (equation 5.45) and Experimental results for convective heat transfer coefficient (h_{conv})

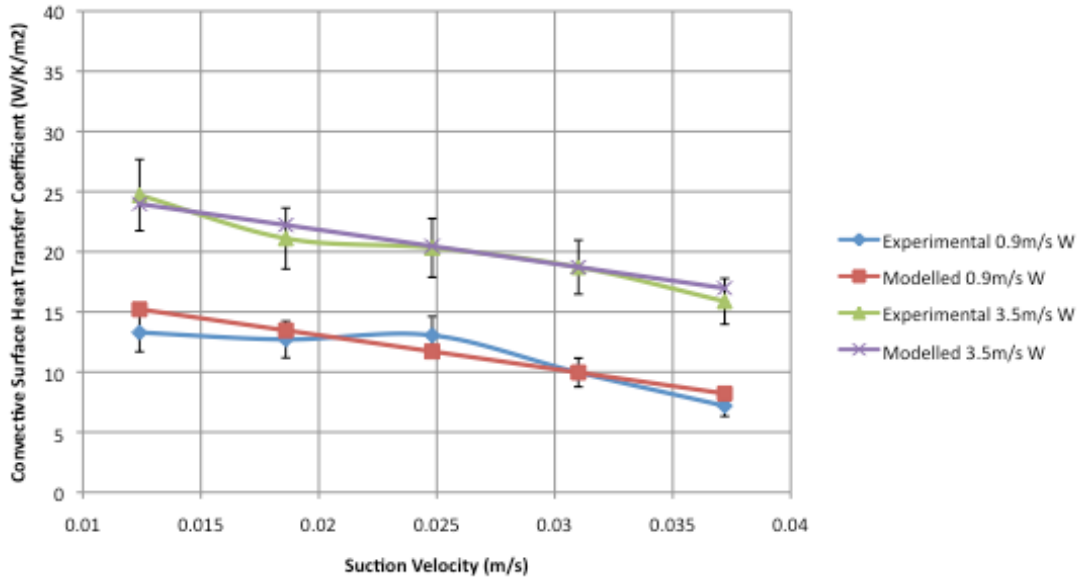


Figure 5.6 Collector SWv+TG: Modelled (equation5.46) and Experimental results for convective heat transfer coefficient (h_{conv})

5.3.3 Temperature Profiles

Using 1-D thermal network models shown in Figure 5.1 and 5.2, steady-state temperatures on each node (collector layer) are evaluated using MATLAB/Simulink platform. Figure 5.7 plots the temperature rise (compared to ambient temperature measured near collector surface) at each layer of the two collectors: SWv and SWv+TG.

T_{mid} of SWv+TG collector, as well as T_{surf} of SWv collector indicates absorber temperature rise. The T_{surf} of SWv+TG is the temperature of transpired glazing, which remains low under both high and low wind conditions, while T_{surf} of SWv is significantly lowered by high wind conditions. As absorber temperature is directly linked to plenum outlet temperature and useful heat delivered, SWv+TG performs better under both parallel wind conditions, as T_{mid} remains almost invariant at different surface wind speeds.

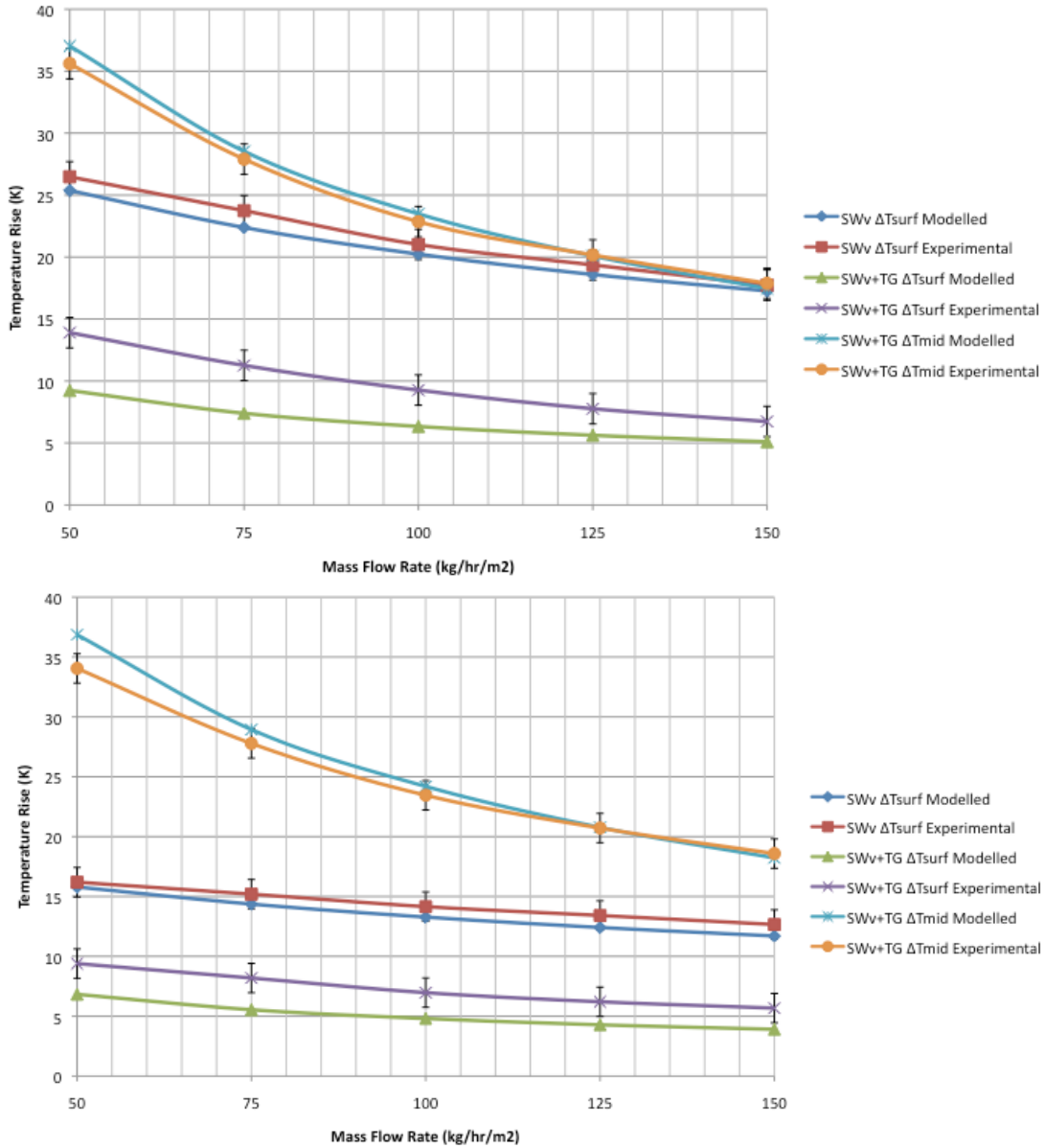


Figure 5.7 Surface and Absorber temperature rise of SWv and SWv+TG (838 W/m²); Above: **Low Wind (0.9m/s)**; Below: **High Wind (3.5m/s)**;

Figure 5.7 explains the higher efficiency of SWv+TG system due to the reduction of surface wind loss. Moreover, the surface temperature of SW+TG system is noticeably lower than T_{surf} of SWv system, resulting in less surface radiant loss less.

The modeled temperatures are generally in good agreement with the experimental data, with the exception of T_{surf} of SWv+TG collector. Aside from the difference in This

is most likely due to the heat gain from incoming solar radiation and the temperature difference at the front and back of the transpired glazing, as thermocouples are only mounted on the interior side of the transpired glazing.

The thermal network model considers the glazing as a single node (no front and back difference) and ignores the local heat transfer occurring at the perforation. Additionally, the absorptance of the transpired glazing is set to be 0.03 in simulations, which may be too low considering the entire spectrum of the solar radiation.

5.3.4 Collector Effectiveness and Efficiency

In order to improve the efficiency of a solar collector with a fixed absorptance, one needs to first eliminate or reduce the surface and back heat losses. For example, introducing distributed air inlets (transpired collector) reduces the surface loss; lowering the emissivity of hot surfaces is also effective at reducing long wave losses. Once all the possible paths of energy losses are minimized, another important consideration, known as the effectiveness of a heat exchanger, ϵ_{HX} , becomes a critical factor.

ϵ_{HX} describes how “effective” a system is at converting the captured heat from its absorber into useful energy. In other words, it characterizes the *amount useful heat recoverable from the absorber temperature*. In the SW model described in Section 5.1, empirical approximation of collector effectiveness from Van Decker et al. (2001) (equations 5.21 to 5.25) was employed. Collector SW+TG, is a highly innovative system and the effectiveness of which is directly calculated using equation 5.26, due to the lack of information on empirical correlations.

Figure 5.8 plots the effectiveness of SW system from experimental results and empirical approximation, indicating a higher discrepancy at high mass flow rates.

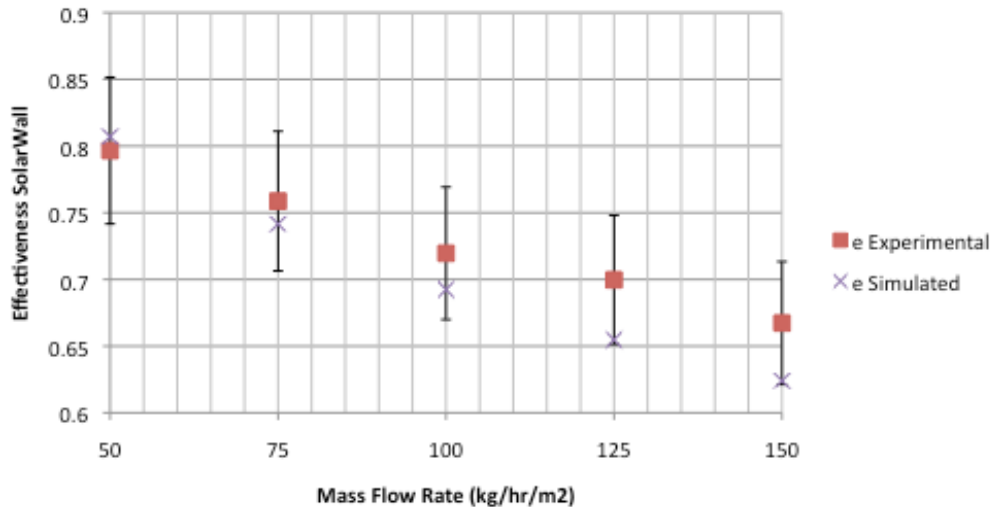


Figure 5.8 Effectiveness of Transpired Collector (SW_v) at Low Gain (838 W/m²) and Low Wind (0.9m/s)

Steady-state simulation and experimental results comparing efficiency of SW_v and SW_v+TG are summarized in Figures 5.9 and 5.10 (uniform scale of 0.05 to 0.85 in efficiency on Y-axis).

Note that modeled efficiency of SW_v+TG shows better agreement with experimental results, within 4% (absolute difference) at low surface parallel wind and within 2% at high wind. For SW_v collector, the effectiveness calculated based on empirical approximation leads to a maximum difference from experimental results of 5.8% at high surface parallel wind and 4.5% at low wind.

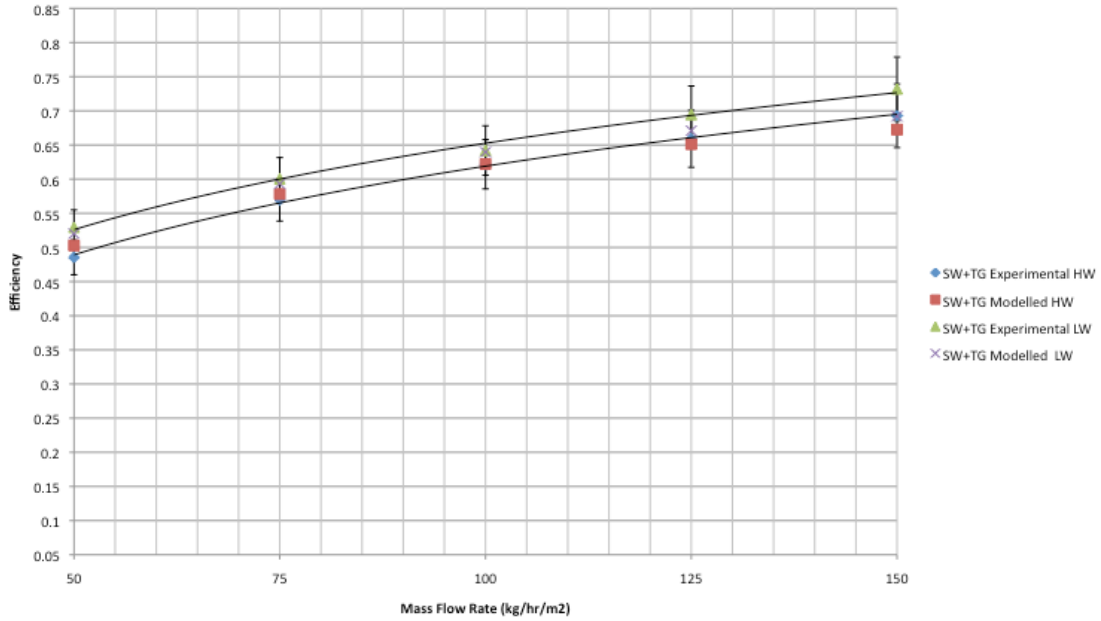


Figure 5.9 Collector SWv+TG: Steady-state efficiency at different flow rates

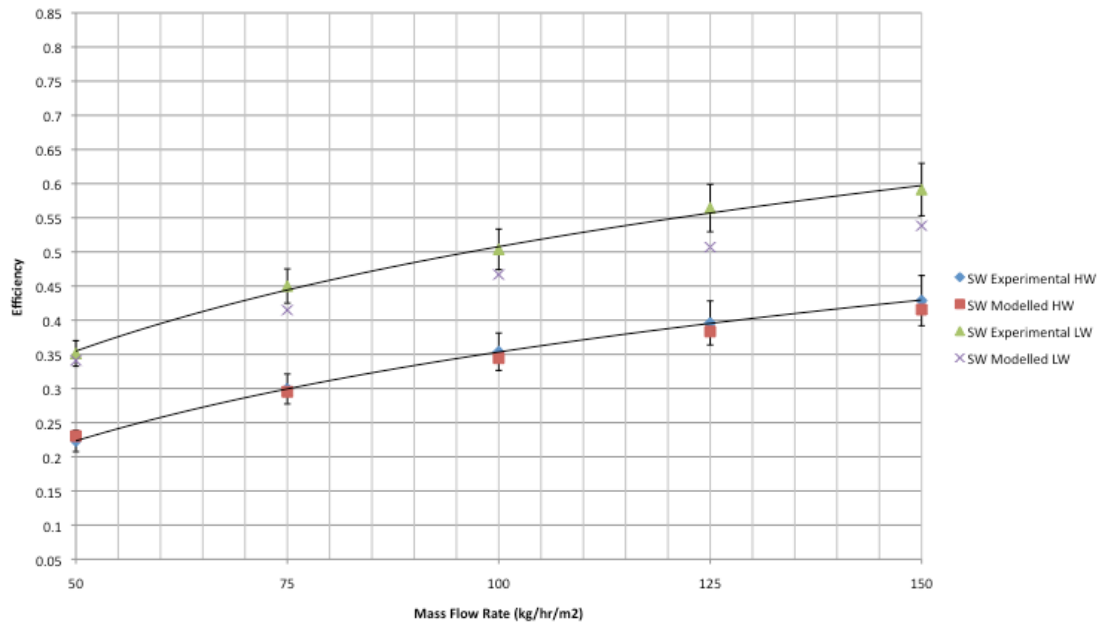


Figure 5.10 Collector SWv: Steady-state efficiency at different flow rates.

Figure 5.11 compares the experimental data of SWh+PV with simulation results from the simple PV/T model discussed in Section 5.1.2. Since the simple PV/T model

does not consider the corrugated/perforated SolarWall backing on which the PV modules are mounted, the simulation results shown reasonable agreement, with an absolute difference of up to 7% at high mass flow rates.

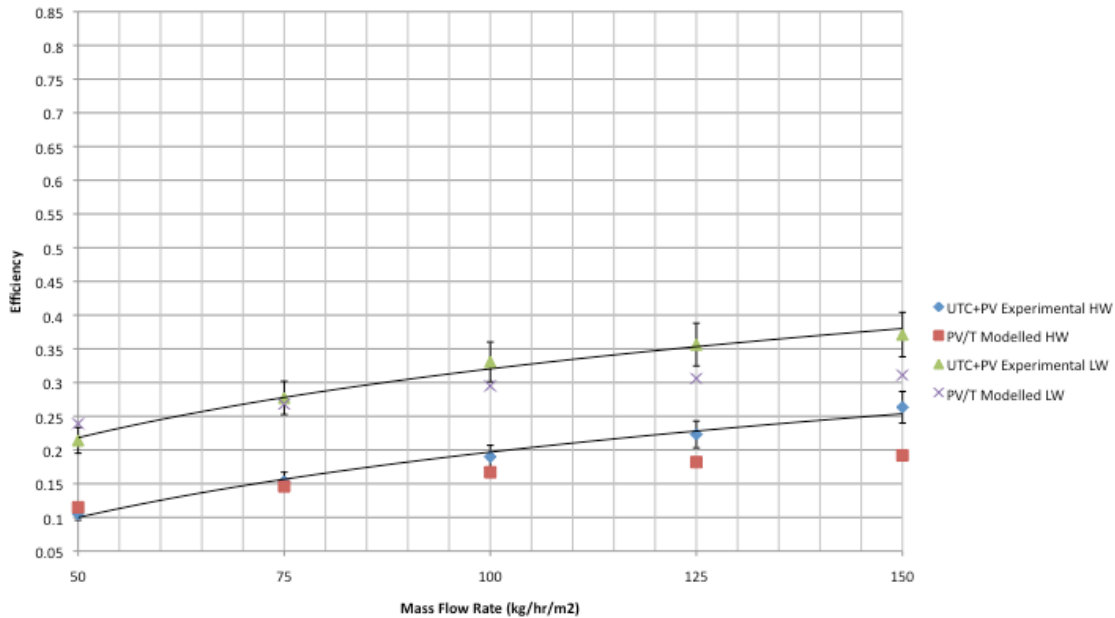


Figure 5.11 Collector SWH+PV/T and PV/T model: Steady-state efficiency.

To approximate the efficiency of SWH+PV+TG (PV coverage 50%, TG coverage 50%), the area-weighted sum combining experimental data of SWH+TG and simulation results of PV/T model is used according to equation 5.37. Interestingly, between experimental data of SWH+PV/T+TG and area-weighted sum of SWH+TG and PV/T systems, the absolute difference compared experimental data is around 3% (Figure 5.12).

Like all collectors with transpired glazing, collector C2 (SWH+PV+TG) shows good reliance against high surface parallel wind (3.5m/s), especially at high mass flow rates (Figure 5.12). Logarithmic curves of efficiency against mass flow rates are fitted to experimental data (within error ranges) of all collectors for visual guidance.

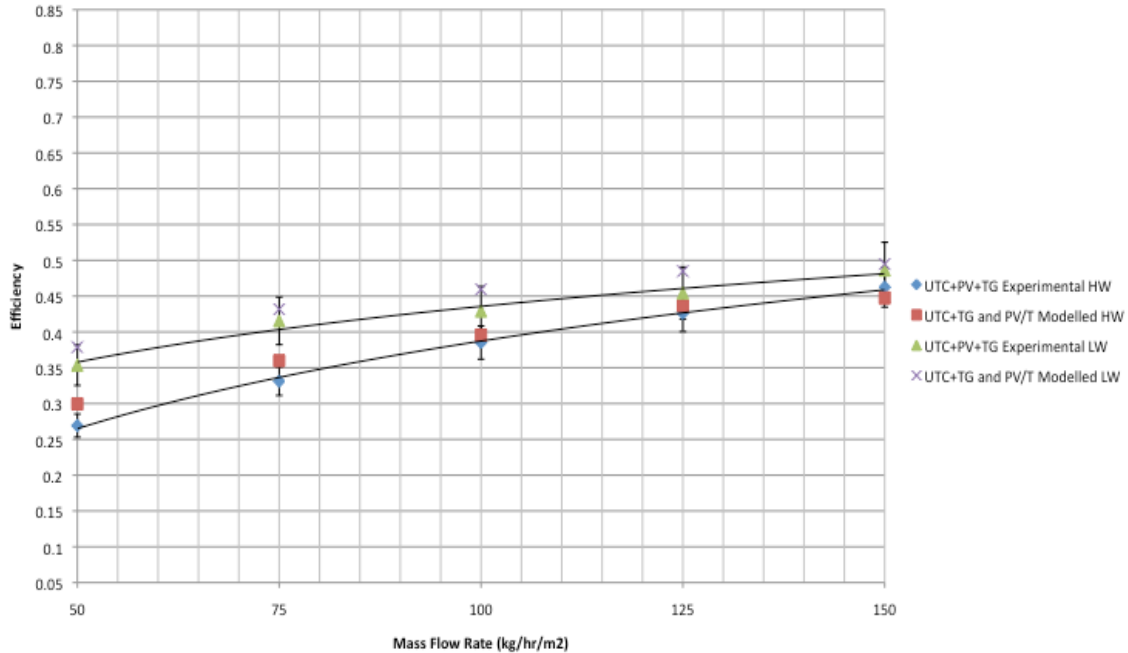


Figure 5.12 Collector SWh+PV+TG compared to PV/T model + SW+TG model: Steady-state efficiency.

5.4 Applying Numerical Corrections to compare Experimental Results from Solar Simulator and from Environmental Chamber

5.4.1 Introduction

Steady-state simulation performed in Section 5.3 matches the ambient conditions of the Solar Simulator experiments. At the same time, experimental results from the Environmental Chamber are 10-15% higher in efficiency compared to the same collector tested under the Solar Simulator. Simulation corrections are required to account for the systematic differences between the Simulator and Chamber tests.

Four main sources of errors are responsible for the discrepancy between the two sets of experiments, summarized in Table 4.7 and their effects listed in Table 5.2.

Table 5.2 Summary: Sources that explain differences between Solar Simulator and Environmental Chamber results

	Source of Discrepancy	Effect
1.	Longer ducts, more connections, higher duct leakage during the Chamber tests	Overestimate efficiency in Chamber
2.	Lack of artificial sky in the Chamber	Overestimate efficiency in Chamber
3.	Higher back loss during Solar Simulator tests (no SIP backing)	Underestimates efficiency in Solar Simulator
4.	No surface wind during Chamber tests (0.9m/s wind under Solar Simulator)	Overestimate efficiency in Chamber

Note that duct leakage has already been addressed in Section 4.5.2 by a leakage test. Other sources of errors from Table 5.2 are illustrated in Figure 5.13 and discussed in Section 5.4.2 to 5.4.4 below.

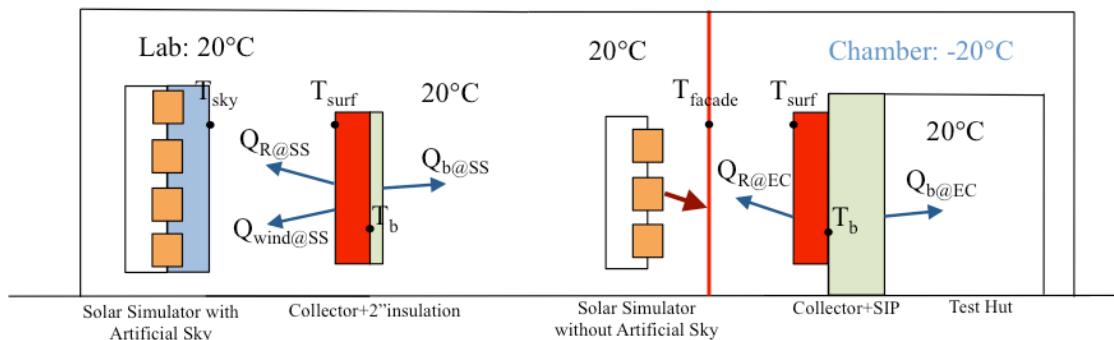


Figure 5.13 Heat Transfer Diagram comparing Experiments under Solar Simulator (left) and Environmental Chamber (right)

5.4.2 Surface Radiant Gain Correction for the Environmental Chamber Results

In outdoor tests, there is significant amount of radiant loss from the collector surface to the cold sky, even during sunny days. The Solar Simulator facility incorporates a component known as the artificial sky to eliminate the infrared radiation from the lamps

and simulate the cold sky (Section 4.1.2). As shown in Figure 5.13, the Environmental Chamber does not correct this radiant gain, as the glazed façade gets heated with incoming solar radiation from the Mobile Lamp Field.

Temperature sensors on the glazed façade surface indicate the façade surface temperature rises to 9.1°C (glazing average) and -8.6°C (opaque spandrel) during a typical experiment (824 W/m², -19.2°C in Chamber). As the cooling unit is mounted at the back of the big Chamber, the -19.2°C given by the temperature sensor near the back of the Chamber is not representative of ambient air temperature near the collector. Sensors placed between the collector and Chamber façade shown that ambient air remains between -13.4°C and -14.3°C near the testing plane (Figure 5.14).

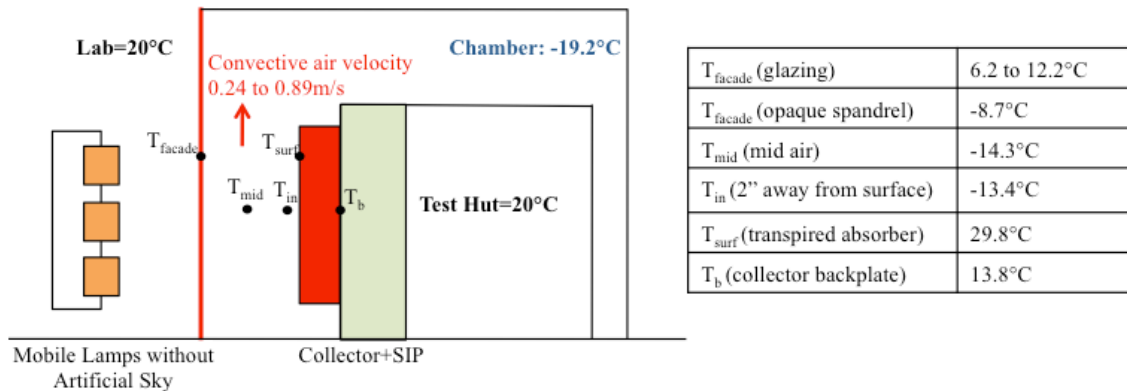


Figure 5.14 Measured Temperatures during Environmental Chamber experiments

The artificial sky of the Solar Simulator maintains a surface temperature of 10°C, as compared to the ambient lab temperature of 20°C. The radiant loss in the Chamber experiments are corrected for conditions that the façade surface should be at sky temperature, T_{sky} , calculated by the correlation from Duffie & Beckman (2006):

$$T_{sky} = T_{amb} \cdot (0.711 + 0.0056T_{dp} + 0.000073T_{dp}^2 + 0.013 \cos(\pi \cdot t / 12)) \quad (5.47)$$

where T_{dp} is the dew point temperature of ambient air; T_{sky} is calculated to be -12.6 °C for ambient air of -14.3°C and 45%RH. The amount of correction is calculated from the difference in radiant loss using equation 5.48. The temperature of Chamber façade T_{facade} is -3°C (average of glazing and spandrel) before the correction, which adopts equation 5.48 and 5.49 and the corrected façade temperature of -12.6°C (T_{sky}). T_{surf} is the exterior surface temperature of the collector.

$$Q_{rad_loss} = (T_{surf} - T_{facade}) \cdot h_{R_{surf-facade}} \quad (5.48)$$

$$h_{R_{surf-facade}} = \frac{\sigma \cdot (T_{surf}^4 - T_{facade}^4)}{\left(\frac{1 - e_{surf}}{A_{surf} e_{surf}} + \frac{1}{A_{facade} F_{facade-surface}} + \frac{1 - e_{facade}}{A_{facade} e_{facade}} \right) \cdot (T_{surf} - T_{facade})} \quad (5.49)$$

where e is the emissivity of the Chamber façade and the collector surface; $F_{facade-surface}$ is the view factor from the Chamber façade to the collector surface, calculated for two finite parallel plates (Appendix D). The radiant heat loss from the collector surface to the Chamber floor or ceiling is ignored. Note that the Solar Simulator experiments also involve possible radiant loss to the lab floor and ceiling.

Results of the radiant gain corrections are presented in Figure 5.15 for collector B4 (SWh) and B5 (SWh+TG). Similar results for collector C1 (SWh+PV) and C2 (SWh+PV+TG) are shown in Appendix D. The corrected efficiency from the Chamber tests is noticeably lower than before. Note that the duct leakage is already accounted for in Section 4.5.2 before commencing this correction in Figure 5.15.

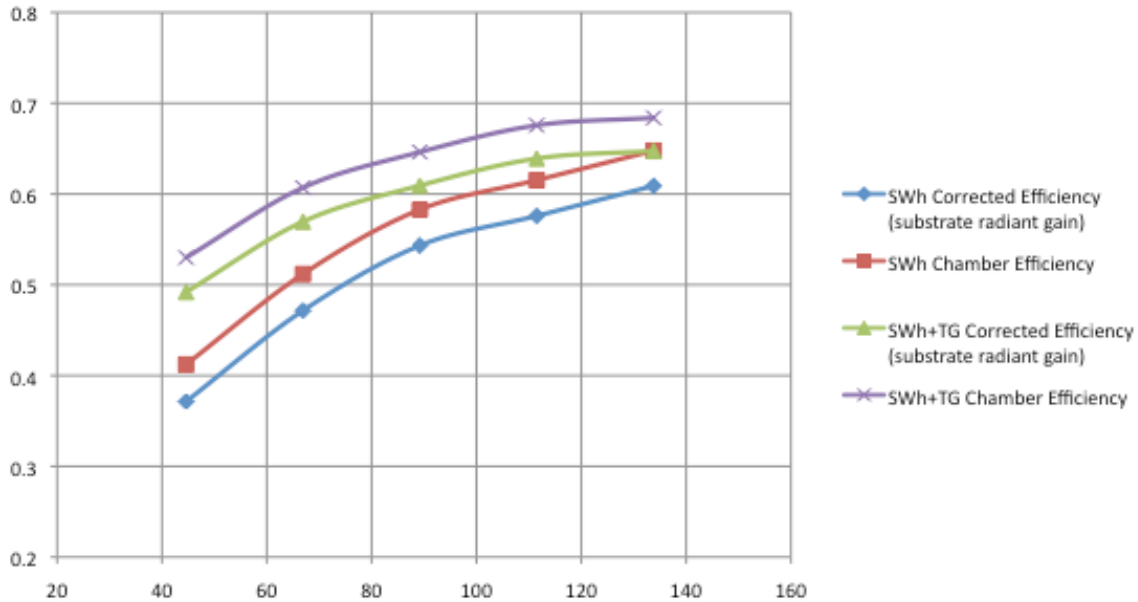


Figure 5.15 Collector SWh and SWh+TG: Efficiency in Chamber corrected for radiant gain to account for heated Chamber façade surface.

5.4.3 Back Loss Correction for the Solar Simulator Results

Due to scanner height restrictions, the collector backing during the Solar Simulator experiments is a 2" EPS insulation. Both front and back of collectors are exposed to the lab temperature at 20°C. The Chamber experiments incorporated the full 1' SIP backing and there is large thermal gradient across the active envelope (front surface at -20°C and back of SIP at 20°C). As the testing conditions in the Chamber are more representative to real-world conditions, the back loss during the Solar Simulator tests are corrected numerically.

The difference in equation 5.50 and 5.51 is added to the useful heat calculated for Solar Simulator results, assuming that all unnecessary back losses would have turned into useful heat. R_{SIP} is rated at $7.9 \text{ Km}^2/\text{W}$ and $R_{2''\text{EPS}}$ at $1.32 \text{ Km}^2/\text{W}$, and heat transfer coefficient of interior air film, h_i , is assumed to be $8.3 \text{ W/m}^2/\text{K}$.

$$Q_b = A_{col} \cdot \frac{1}{(R_{SIP} + 1 / h_i)} \cdot (T_b - T_{TESTHUT}) \quad (5.50)$$

$$Q_b = A_{col} \cdot \frac{1}{(R_{2^{EPS}} + 1 / h_i)} \cdot (T_b - T_{amb}) \quad (5.51)$$

As the back plate temperature of collector (T_b , before insulation) for the Chamber experiments are typically between 5°C to 15°C, there is very little thermal gradient between collector backing and the test hut (at 20°C). With the high thermal resistance of SIP, virtually no back loss is present during the Chamber tests. Results shown that accounting for back loss increases the Solar Simulator results by 1 to 2 % in efficiency, which contributes marginally to the discrepancy between Chamber and Simulator results.

5.4.4 Wind Loss Correction for the Environmental Chamber Results

The efficiency from the Environmental Chamber tests were obtained without any artificial parallel wind generated over the collector surface. Though there are slight air movements on the collector surface due to natural convection and general air circulation in the Chamber, the experiments were considered to be under zero wind condition. This Section will address the wind loss during the Solar Simulator experiments (at 0.9m/s surface parallel wind average), by adjusting the convective heat transfer coefficient to include zero wind condition.

As discussed before, convective heat transfer coefficient for transpired collectors depends on both wind speed parallel to collector surface (V_{wind}) and suction velocity perpendicular to surface (V_s). Kutscher et al. (1991) concluded that natural convective heat losses to the ambient were negligible compared to forced convective heat loss

induced by suction and wind at the transpired surface. The general expression used in Section 5.3.2 is very representative of this relationship:

$$h_{wind} = C + B \cdot V_{wind} + A \cdot V_s \quad (5.11)$$

However, explicit expressions of h_{conv} in equations 5.45 and 5.46 were only validated for experimental data of wind speeds between 0.9m/s and 3.5m/s. In fact, one can predict that at very high surface wind speeds, the convective heat losses will be dominated by wind-induced effects (V_{wind}), and constant B will increase in value to place more importance on surface wind speed.

By the same token, at very low surface wind flow (<0.9m/s), convective heat losses are dominated by suction velocity (V_s) at the surface (linked to mass flow rate), and constant B will decrease in value compared to numbers given in equation 5.45 and 5.46. With no further information on how collectors will behave at quasi-zero wind condition, the same general equation is still adopted for wind speed between 0 to 0.9m/s. B is considered to be less than 3.368 (B=3.368 in equation 5.46) and is constant for all four collectors (SWh, SWh+TG, SWh+PV, SWh+PV+TG) at low surface wind (<0.9m/s). As the first and third terms for h_{conv} cancel out at the same MFR, the difference of convective heat transfer losses from 0.9m/s wind to zero-wind is therefore calculated by:

$$\Delta h_{conv} = B \cdot (V_{wind} - 0 \frac{m}{s}) = B \cdot 0.9, \quad 0 < B < 3.368 \quad (5.52)$$

$$\Delta Q_{conv} = \Delta h_{conv} \cdot (T_{surf} - T_{amb}) = (0.9B) \cdot (T_{surf} - T_{amb}) \quad (5.53)$$

For glazed or covered surfaces (no surface perforation), forced convective heat transfer coefficient is only dependent upon wind speeds (no suction present). Several correlations for non-transpired surfaces are presented in equation 5.54 to 5.56, researched by Test et al. (1981), Sharples & Charlesworth (1998), Duffie & Beckman (2006), expressing h_{conv} as a function of surface wind speed (m/s) only. Those relations provide insights to reasonable estimates for constant B in equation 5.53.

$$h_{conv} = 8.55 + 2.56 \cdot V_{wind} \quad (5.54)$$

$$h_{conv} = 3.347 + 1.52 \cdot V_{wind} \quad (5.55)$$

$$h_{conv} = 5.7 + 3.8 \cdot V_{wind} \quad (5.56)$$

The correction in convective heat losses from 0.9m/s to zero wind conditions are calculated and illustrated in Figure 5.16 (Collector SWh). Knowing that constant B is less than 3.368 and greater than 1.5 (equation 5.55), Figure 5.16 shows B-value equals to 1.5 and 3.5 and its effect on convective wind loss corrections.

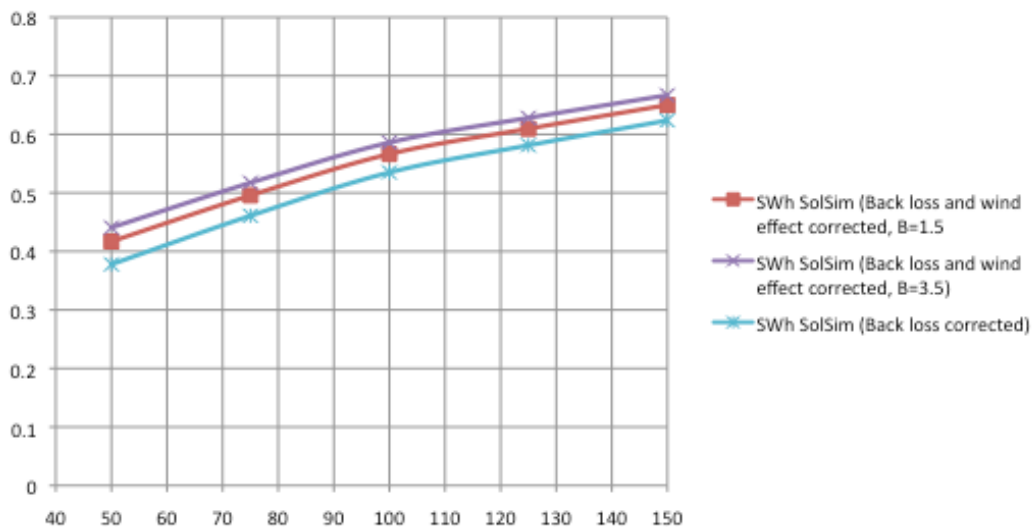


Figure 5.16 Collector SWh: Efficiency in Solar Simulator corrected from 0.9 m/s parallel wind to zero-wind condition

Correction for convective wind losses have very little effects on collectors with transpired glazing (SWh+TG, or SW+PV+TG), regardless of what B-value is used. As transpired glazing has low surface temperature, the convective loss is not sensitive to wind speeds due to the low thermal gradient to the ambience.

Note that the surface flow parallel to collector surface is never truly zero, due to surface natural convection and air mixing inside the Chamber. During the Chamber experiments, measurements of air velocity were taken at discrete points along the collector height. Surface airflows parallel to collector surface are found to be between 0.24m/s and 0.89m/s inside the Chamber, even without any ventilation unit.

Therefore, the results presented in Section 5.4.4 are calculated using a parallel surface flow of 0.56m/s for the Chamber experiments, as opposed to 0.9m/s for Solar Simulator experiments (B=2.5). In general, the difference of convective losses between the two facilities is very minimal.

5.4.5 Corrected Efficiency Results

Figure 5.17 to 5.20 summarize the comparisons of results from Solar Simulator and Environmental Chamber, before and after the corrections made to account for errors shown in Table 5.2. Note that for collectors that are not sensitive to wind-induced convective losses, the efficiency curves actually match better without any wind corrections.

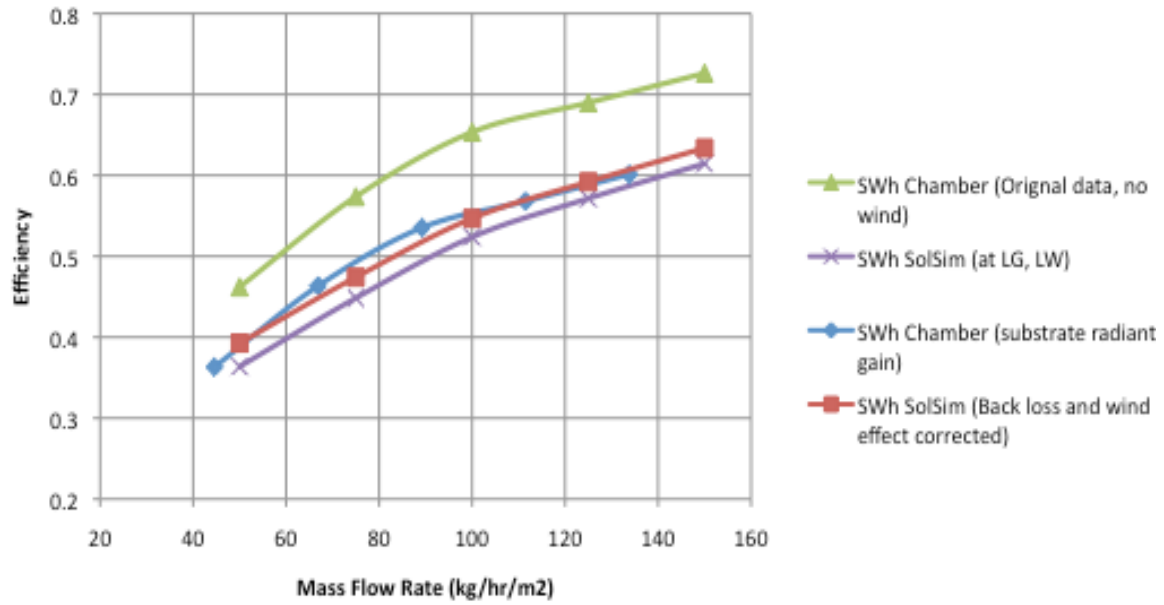


Figure 5.17 Collector B4 (SWh): Efficiency in Solar Simulator and in Environmental Chamber, before and after corrections

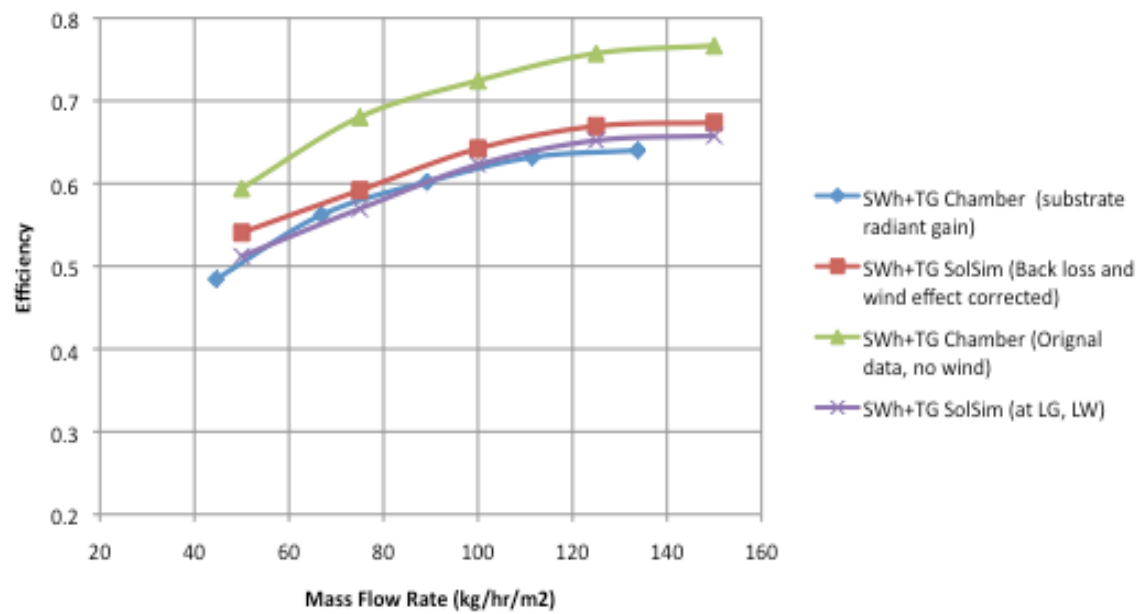


Figure 5.18 Collector B5 (SWh+TG): Efficiency in Solar Simulator and in Environmental Chamber, before and after corrections

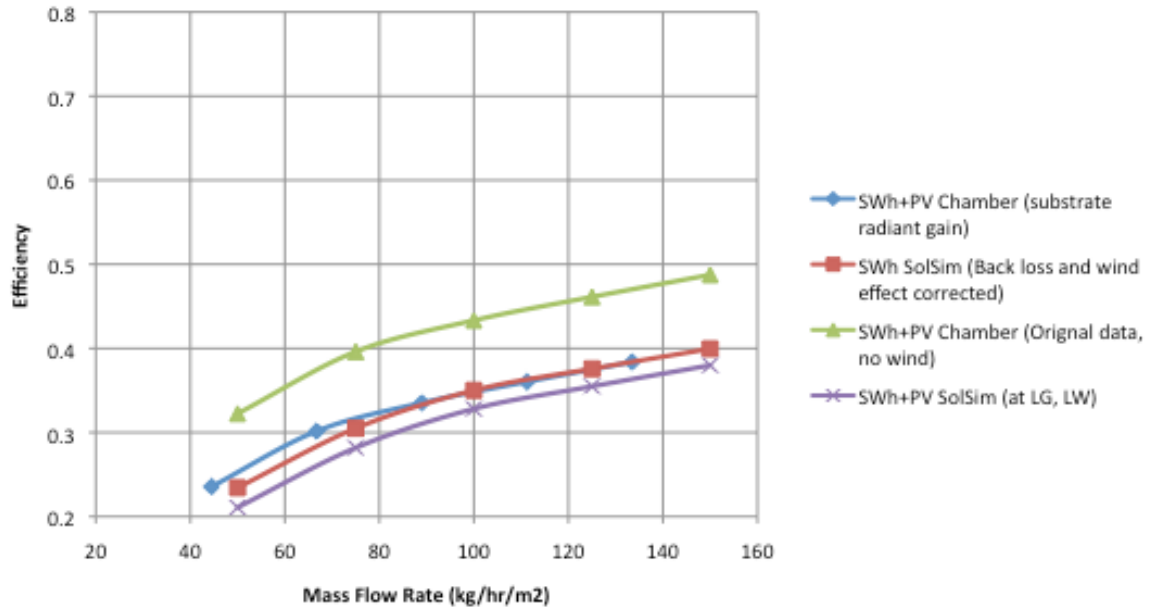


Figure 5.19 Collector C1 (SWh+PV): Efficiency in Solar Simulator and in Environmental Chamber, before and after corrections

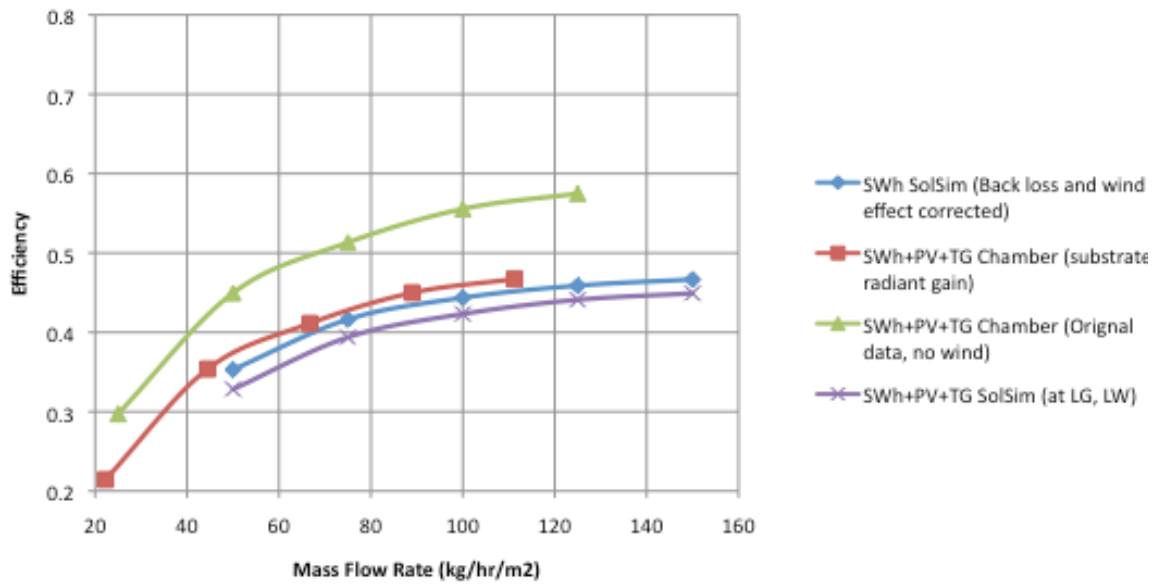


Figure 5.20 Collector C2 (SWh+PV+TG): Efficiency in Solar Simulator and in Environmental Chamber, before and after corrections

Efficiency results before any numerical corrections are displayed in green and purple curves (Figure 5.17 to 5.20), while corrected efficiency curves are shown in red and blue.

The general trends of efficiency obtained from both facilities were in good agreement even without any numerical corrections. After accounting for the systematic differences between the Solar Simulator and Environmental Chamber, the efficiency curves moved closer to one another, validating the experimental repeatability of the laboratory facility.

5.5 Annual Analyses

5.5.1 Model Description

For annual analyses of transpired collectors, there is no real transient model developed in commercial software or by any research work. Available models usually assume that steady state has been reached at every time step. Research by Gogakis (2005) indicated that it is a valid assumption, as the response time of UTC to change in solar radiation is found to be approximately 1 minute. Though in reality, collectors' response time to changes in surface wind profile can take longer, especially for corrugated collectors when turbulence can be unpredictable with different wind speed and directions.

Using the steady state models discussed in Chapter 5, annual analyses are performed in MATLAB/Simulink platform using hourly weather files from three northern Canadian cities. Steady state calculations are conducted at every time step (1 hour) and using convective heat transfer coefficients (equation 5.45 and 5.46) validated for wind speed 0.9m/s to 3.5m/s.

Several factors could temper with the simulation results. Firstly, reliable weather data of northern Canadian cities are very difficult to obtain, especially the solar radiation files. In this simulation, Typical Meteorological Year (TMY) weather files from the

TRNSYS database are used (University of Wisconsin Madison, 2012), averaged from Canadian government data. Interpolation and extrapolation techniques are used to replace the out-of-range data and there are still short periods of missing data present in the TMY file. For Nordic weather stations that run into more mal-functioning incidents than southern locations, the deviation in the TMY weather files from reality is inevitable.

Table 5.3 below presents the weather output for the three northern cities used in the model, Iqaluit (Nunavut), Whitehorse (Yukon), and Fort Smith (Northwest Territories). The annual sum of solar radiation (south-facing facade) from RETScreen output at a lower resolution (monthly) is compared with TMY hourly data in Table 5.3, and the deviations of annual insolation between RETScreen and TMY files range from 3 to 14%.

Table 5.3 Summary of Weather Data for Iqaluit, Whitehorse and Fort Smith

	Iqaluit	Whitehorse	Fort Smith
Location (Latitude)	NU (63.8°N)	YT (60.7°N)	NWT (60°N)
Annual average temperature	-9.4°C	-0.9°C	-2.9°C
(Coldest Monthly temperature)	(-26.8°C Feb)	(-18.7°C Jan)	(-25.4°C Jan)
(Warmest Monthly temperature)	(7.7°C July)	(14°C July)	(16.3°C July)
Annual average wind speed	4.4m/s	3.8m/s	3.2m/s
Total Heating-Degree days (HDD)	10,017°C-day	6,915°C-day	7,916°C-day
Total Cooling-Degree days (CDD)	0 °C-day	243 °C-day	448 °C-day
Annual Insolation on Façade (TMY, summed from hourly data)	4.45 GJ/m ²	4.13 GJ/m ²	4.77 GJ/m ²
Annual Insolation on Façade (RETScreen, summed from month data)	4.58 GJ/m ²	3.82 GJ/m ²	4.15 GJ/m ²

Secondly, the expressions for convective heat transfer coefficients are only validated by experimental results of surface parallel wind speeds ranging from 0.9m/s to 3.5m/s. At higher or lower wind speeds or with different incoming wind directions, the expressions may no longer apply, and surface convective loss could be over or under-estimated. As shown in Table 5.3, the average wind speeds experienced by Nordic cities are slight above the validated range, and a more suitable expression for convective heat transfer coefficients at high wind speed ($>3.5\text{m/s}$) is needed for better model accuracy.

5.5.2 Annual Potential for Three Northern Cities

Annual analyses using the hourly weather files of three Nordic cities (Iqaluit, Whitehorse, and Fort Smith) are performed for collectors B4 (SWh), B5 (SWh+TG), C1 (SWh+PV) and C2 (SWh+PV/T+TG). For example, for the city of Whitehorse (Yukon), the annual potential of solar captured heat at every time step is illustrated in Figure 5.21.

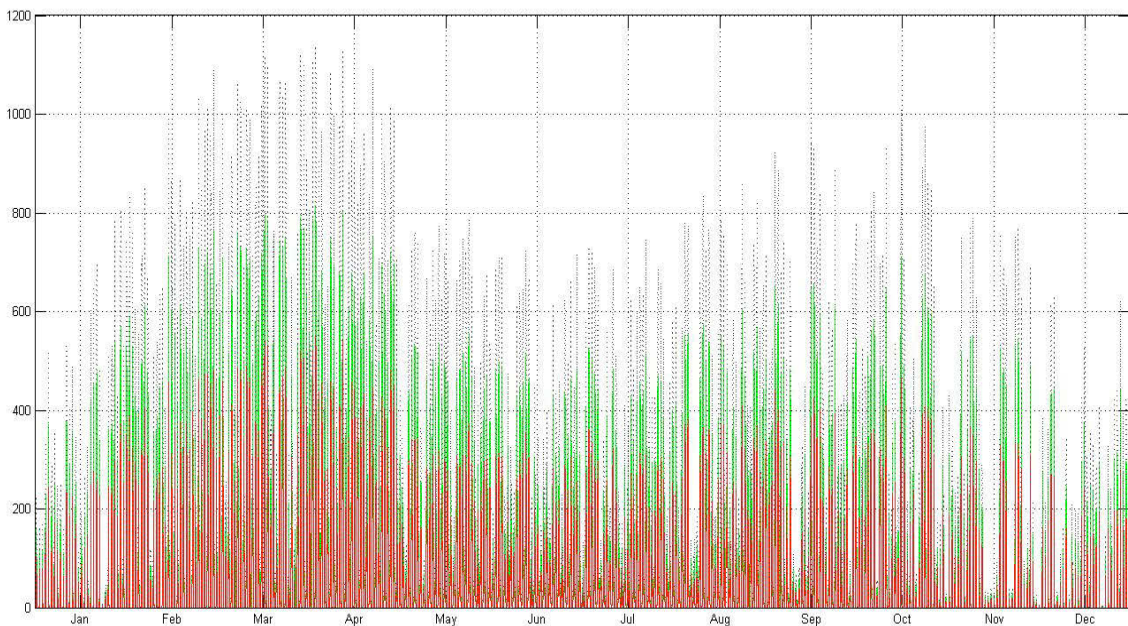


Figure 5.21 Useful power (W/m^2) collected by SW+TG (green), and SW+PV (red), and total irradiance on Facade (black). MFR=150kg/hr/m²; Whitehorse;

As shown in Figure 5.21, the black dotted lines indicate solar irradiance on a south-facing façade (W/m^2). The green and red lines show the instantaneous thermal output at every time step by the collectors with highest and lowest thermal efficiency, SW+TG and SW+PV, respectively. Similar annual results for Iqaluit and Fort Smith are shown in Appendix E.

The generated thermal power is integrated at every time step and annual results are summarized in Table 5.4. All solar thermal results are normalized by area, while solar electric output is normalized by kW, as photovoltaic modules could be of different efficiency.

Table 5.4 Annual Simulation results for three Northern locations

		Iqaluit	Whitehorse	Fort Smith
Location (Latitude)		NU (63.8°N)	YT (60.7°N)	NWT (60°N)
Annual Insolation on Façade (TMY, summed from hourly data)		4.45 GJ/m ²	4.13 GJ/m ²	4.77 GJ/m ²
Heat Collected by SW (SolarWall)	@150kg/hr/m ²	1.9 GJ/m ²	1.86 GJ/m ²	2.2 GJ/m ²
	@50kg/hr/m ²	1.07 GJ/m ²	1.08 GJ/m ²	1.3 GJ/m ²
Heat Collected by SW+TG	@150kg/hr/m ²	3.15 GJ/m ²	2.92 GJ/m ²	3.38 GJ/m ²
	@50kg/hr/m ²	2.46 GJ/m ²	2.27 GJ/m ²	2.63 GJ/m ²
Heat Collected by SW+PV (50%)	@150kg/hr/m ²	1.17 GJ/m ²	1.09 GJ/m ²	1.26 GJ/m ²
	@50kg/hr/m ²	0.445 GJ/m ²	0.410 GJ/m ²	0.463 GJ/m ²
Heat Collected by SW+ PV (50%) +TG	@150kg/hr/m ²	1.95 GJ/m ²	1.86 GJ/m ²	2.16 GJ/m ²
	@50kg/hr/m ²	0.931 GJ/m ²	1.01 GJ/m ²	1.22 GJ/m ²
Annual PV potential (solar electricity)		955 kWh/kW	773 kWh/kW	940kWh/kW

Note that the thermal output in Table 5.4 is likely to be over-estimated systematically, as the convective heat transfer coefficients used in models tend to underestimate wind-induced convective losses at surface wind speed greater than 3.5 m/s, which is a common condition for the three Nordic cities.

For the theoretical yield of annual solar potentials shown in Table 5.4, only a portion of the captured thermal energy can be used in reality. The useful fraction of collected thermal energy depends on the desired end use of the solar heated air. As discussed in Section 3.1.3, collector outlet temperature of less than 0°C (still higher than ambient temperature) can be fed into an HRV inlet to save on defrost load, as most HRV are equipped with a defrost coil to heat below-zero incoming air with electricity.

For collector outlet temperature from 0°C to 25°C, the heated air can be used for space heating either directly or via a heat pump. If solar heated air is greater than 30°C, it is necessary to pass the air to the unoccupied crawlspace for short-term storage, or through a heat exchanger for domestic hot water heating. Note that the more end users a solar collector is supplying, the more likely that all the heat generated will be used and the higher the system cost will be.

In addition, though electricity is valuable and demand is generally high, more photovoltaic panels doesn't necessarily mean a better solar-capturing system overall. As the coverage of PV reduces the thermal efficiency of the collector, compromises between electric and thermal energy is essential. Too much electric generation would call for inverters and battery of higher capacity, consequently drive up system cost.

Therefore, while keeping the cost concerns in mind, there are smart designs and control strategies that can be adopted for low energy houses at high latitudes. At the early design stage, the auxiliary HVAC systems should be determined together with the Solar Component selection. For residential applications, once the desired end uses are decided, the type and size of the solar skin should be selected accordingly to optimize the output within useful outlet temperature range.

Lastly, the collector outlet temperature can be controlled with heat removal rate (mass flow rate, MFR) determined by the fan. Figure 5.22 and 5.23 (Whitehorse) plot the outlet temperature of SWh+TG (green), SWh+PV (red) and outdoor temperature (black) for MFR of 150 and 50 kg/hr/m², respectively.

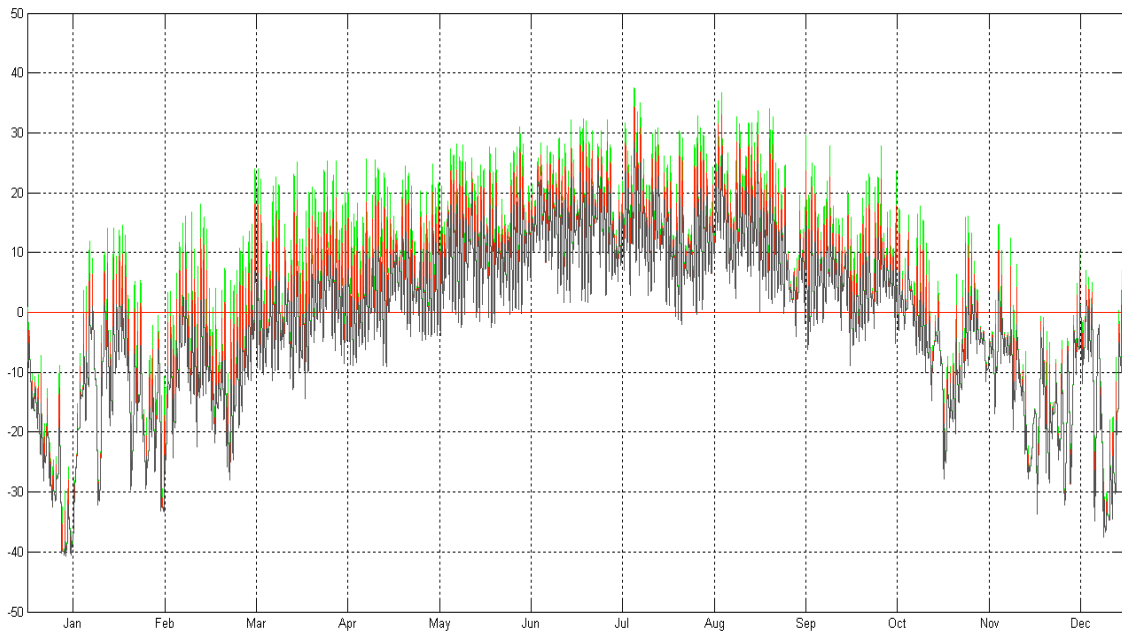


Figure 5.22 Collector Outlet temperatures of SW+TG (green), and SW+PV (red), and outdoor temperature (black). MFR=150kg/hr/m²; Whitehorse;

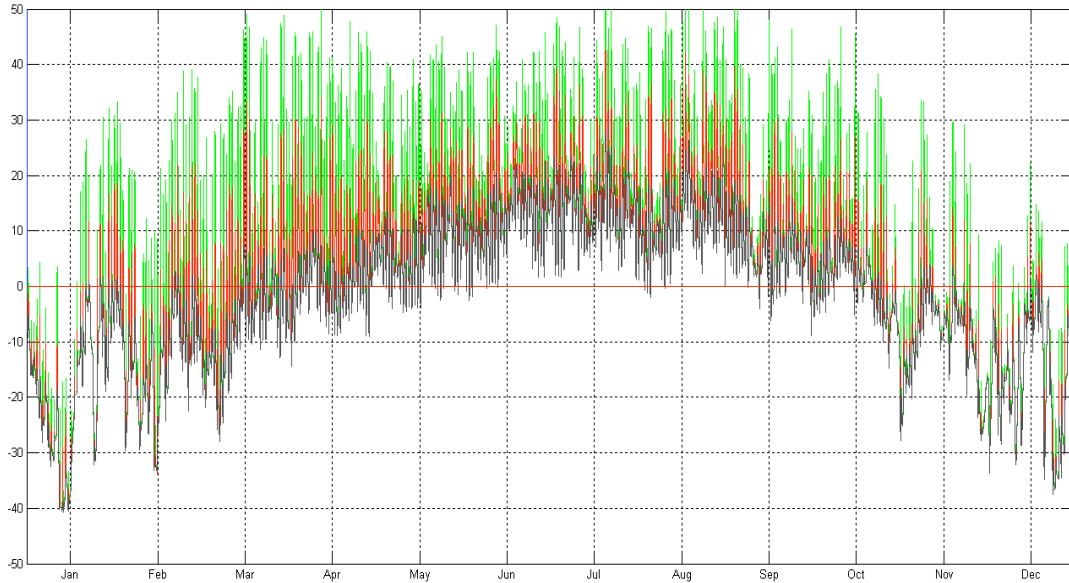


Figure 5.23 Collector Outlet temperatures of SW+TG (green), and SW+PV (red), and outdoor temperature (black). MFR=50kg/hr/m²; Whitehorse;

At high MFR, collector performs more efficiently at the expense of higher fan power. At low MFR, collector performance decreases while outlet temperature increases. Figure 5.22 and 5.23 (scale -60°C to 50°C) shown close to 20°C peak difference in outlet temperature from MFR changes only.

The wide range of possible outlet temperatures offers crucial flexibility in solar collector selection. Though collector efficiency generally increases with ascending MFR (Table 5.4), the actual outlet temperature is sometimes more important in maximizing the solar fraction, as captured thermal energy with outlet temperature too low or too high does not actually contribute to the overall energy generation. In addition, high MFR also consumes more fan power, resulting in less net production when irradiance is low (low-sun conditions). Therefore, algorithms for optimizing collector outlet temperature depending on end-uses and fan power consumption are needed for future work.

6 Conclusions and Recommendations

6.1 Conclusions

This thesis presents the design and evaluation of building-integrated solar technologies suitable for high-latitude applications. An array of active envelope prototypes has been designed and studied for Nordic climate, by incorporating suitable solar collectors onto a structural insulated panel (SIP) wall.

Ten façade-integrated solar collector configurations were experimentally evaluated using the state-of-the-art Solar Simulator and Environmental (SSEC) laboratory. The flexible design of the envelope prototype allows for detailed experimental characterization of different solar-harnessing systems within a compressed timeframe, compared to conventional outdoor tests.

Controlled climatic conditions inside the laboratory led to highly consistent and repeatable experimental results. It is the first research project to utilize the full potential of the SSEC facility, taking into account the systematic differences between results obtained from the Solar Simulator and from the Environmental Chamber.

Methods and algorithms used to model the integrated solar technologies are also presented. Steady-state simulation results are compared with experimental data to validate and calibrate the custom thermal models. For transpired collectors, it is concluded that surface convective losses is a complex yet vital factor in determining the systems' performance. Convective heat transfer coefficients are experimentally evaluated and numerical approximations have been developed for the transpired solar collectors pertaining to this thesis.

The suitability of different active envelope systems for high-latitude applications is studied. Figure 3.5 and Table 4.1 to 4.3 illustrated all the solar configurations tested, including: A1. Collector with Transpired Glazing (TG) and flat absorber; A2. TG and finned absorber; B1. Unglazed Transpired Collector (UTC) with corrugation along flow (UTC-v); B2. UTC-v+ Transpired Glazing (TG); B3. UTC-v with top glazing; B4. UTC with corrugation against flow (UTC-h); B5. UTC-h+TG; B6. UTC-h with top glazing; C1. UTC-h+PV/T (PV coverage 50%); C2. UTC-h+PV/T+TG.

Off-the-shelf technologies such as transpired collectors and photovoltaic panels are combined and utilized in innovative manners. The effects of glazing, transpired glazing, transpired absorber, finned absorber, and PV coverage are studied. Experimental and simulation findings revealed that performance of conventional unglazed transpired collector (UTC) as well as photovoltaic/thermal (PV/T) collector can be effectively improved simply by adding an exterior layer of transpired glazing (collector B2, B5, C2). Simulation and experimental results confirmed collector efficiency rise of up to 28% (in absolute difference) due to the simple addition of transpired glazing. The improved design successfully minimized surface radiant loss and lowered collector's susceptibility to wind loss, which are particularly beneficial features for northern applications.

Finned absorber with transpired glazing (A2) increases the performance by up to 13% compared to collector with flat absorber (A1). Collector with coverage of 50% PV (C1) over the total collector area is compared with the output of similar full-scale collector with PV coverage of 70%. The concept of thermal equivalent efficiency is adopted to combine the electric and thermal performance of PV/T systems. As higher PV

coverage reduces the thermal efficiency of the system, design compromise between electric and thermal output is necessary.

Furthermore, the current state of solar installations in Northern Canada is presented in case studies (Appendix F and G) involving two common building-integrated solar technologies (unglazed transpired collector and photovoltaic system). The author conducted on-site fieldwork in Northwest Territories and Nunavut to investigate operation issues for existing building-integrated solar installations. The hands-on experience revealed that, in order to further the renewable penetrations in the North, the human factors and social aspects are just as important as technical expertise.

By combining passive measures of conservation (building science) and active generation of on-site solar electric/thermal energy, the building sector in Northern Canada can readily achieve considerable displacement of expensive fossil fuel and its associated transportation cost. In the meantime, design innovations on compact envelope, BIPV/T facade and pre-fabricated assembly may also be appropriate for general applications in temperate climates.

6.2 Recommendations for Solar Integration on SIP Envelope

This thesis project established extensive expertise regarding integrated solar technologies suitable for cold climates. Several important considerations and recommendations are summarized for future Solar+SIP applications at high latitudes:

1. For active envelope design, pre-fabricated systems are extremely beneficial in eliminating installation errors and saving on-site labor cost in Northern Canada. The SIP system, as a passive enclosure, satisfies all the necessary envelope functions

(air/vapor barrier, insulation, structure, etc.). The solar collector can be designed to replace exterior cladding without puncturing the air/weather barrier and can be installed prior to arrival on site. For transpired collectors, appropriate drainage is necessary to account for snow penetration.

2. For Nordic locations where heating loads are high and energy is expensive, there are vast potentials for well-researched renewable technologies. However, as technical support is scarce and ongoing maintenance is expensive, low-tech and maintenance-free systems are preferred. For example, flat plate PV modules, air-based solar thermal systems offer the necessary simplicity and are more suitable for Northern Canada, compared to other renewable technologies such as wind turbines and liquid-based thermal collectors.
3. The duct intake where the solar heated air penetrates the envelope constitutes as a weak point. Special attention should be given to the installation and open-close control of the insulated damper at air intake. Quality control can be conducted in factory for pre-fabricated systems. If this duct opening is able to bypass the solar collector when needed, the air intake for solar heated air can be doubled as the fresh air intake for building ventilation needs.
4. While it is important to optimize the performance of the solar component itself, system-level optimizations could offer even more immediate benefits. The type, size and flow rate of the façade-integrated solar collectors should be determined in accordance with the energy demands (electric and thermal). The term “integration” not only refers to the physical addition of solar collector onto the envelope system, it also involves integration of collector energy output into the building HVAC system.

5. To truly achieve low energy buildings in Northern Canada, the social aspect and human factors of local communities cannot be under-stated. The designer should be conscious about considerations such as vandalism, occupants turning off HRV or opening windows during winter, as well as the common mentality of “build-and-forget”. Possible measures include providing adequate diffusers and better indoor air circulation, enabling control on furnace and room thermostats, continuing education efforts and maintenance support, etc.

6.3 Future Work

Further research work in the following aspects are recommended:

1. Future building codes or design guidelines should include passive solar house principles for Nordic locations. Inter-linked variables such as the south-facing window-to-floor ratio, insulation level, and thermal storage need to be considered simultaneously to optimize for an objective function such as building energy efficiency. Designers could also input cost functions to compare or decide between passive building design measures and active solar collector integration.
2. Development of pre-fabricated active facades with seamless collector integration onto building envelope. As opposed to the common practice of ‘building-added’ solar systems, a true integrated active envelope system replaces the exterior cladding with solar skin, while taking barrier penetration, damper design and drainage into consideration.
3. The second level of solar integration in buildings calls for efficient building mechanical systems in optimal combination with efficient collector design.

Depending on the end uses for the photovoltaic electricity and solar heated air, the design of building HVAC systems should be selected and sized accordingly. Future arctic low energy buildings can design building integrated solar collectors in conjunction with building HVAC systems in the early design stage.

4. For solar thermal collectors, control algorithms can be used to optimize fan speed and collector heat removal rates. The goal would be to produce solar heated air with outlet temperature bounded by the useful range, to maximize the amount of useful thermal energy without wasting energy input on fan power.
5. Short-term thermal storage within the envelope or building space is necessary in order to achieve more ambitious energy targets at Nordic locations. Seasonal thermal storage could also be considered, bearing in mind the challenges of long winters and permafrost stability.
6. Transpired collectors are particularly prone to surface convective losses, due to the combined effect of parallel surface wind and the suction flow perpendicular to surface. Much research work is needed to fully explain and quantify the surface convective heat loss for transpired collectors.
7. For the design of co-generation systems (i.e. PV/T), the optimal coverage of PV can be analyzed based on technical and economical considerations. As solar electricity and useful heat production are competitive objectives, life-cycle cost-benefit analyses will determine the optimal PV coverage, considering maintenance costs and savings in building energy demands. In addition, the optimal combination of PV and thermal will vary depending on future price uncertainties. For example, PV price has dropped dramatically in the last decade due to incentive programs and technology maturity,

and module efficiency has improved. In combination with other economic factors such as future fossil fuel price and renewable subsidy, the optimal PV/T design requires more in-depth research work. The relative importance of electric and thermal outputs also needs to be gauged on a case-by-case basis for such optimization.

References

Adsten, M. (2002). "Solar Thermal Collectors at High Latitudes: Design and Performance of Non-Tracking Concentrators. ." Uppsala University, Sweden.

Affolter, P., Eisenmann, W., Fechner, H., Rommel, M., Schaap, A., Sørensen, H., Tripanagnostopoulos, Y., and Zondag, H. (2005). "PV-Thermal System Marketing and R&D Roadmap " *PV Catapult*, H. Zondag, ed., ECN, Westerduinweg, Netherlands.

American Society of Heating Refrigerating and Air-Conditioning Engineers., and Knovel (Firm). (2009). "2009 ASHRAE handbook fundamentals." <<http://www.knovel.com/knovel2/Toc.jsp?BookID=2554> MIT Access Only>.

Andresen, I., Ellehauge, K., Karlsson, B., and Nieminen, J. (2008). "Solar heating systems for passive houses in the Nordic countries – An overview." *Ist Nordic passive house conference Passivhus Norden*, Norway, 336-344.

Armstrong, J. (2011). "Northern SIP Building System." K. N. D. Kott Group, ed.

Athienitis, A., Fazio, P., Rao, J., Kapsis, C., Bambara, J., and Chen, Y. (2012). "Simulateur Solaire et Chambre Climatique (Laboratoire SSEC)." *Association Québécoise pour la Maîtrise de l'Énergie*, Montreal.

Ayoub, J., Dignard-Bailey, L., and Poissant, Y. (2009). "National Survey Report of PV Power Applications in Canada " *CO-OPERATIVE PROGRAMME ON PHOTOVOLTAIC POWER SYSTEMS, Task 1*, International Energy Agency.

Bosanac, M., Sørensen, B., Katic, I., Sørensen, H., Nielsen, B., and Badran, J. (2003). "Photovoltaic/Thermal Solar Collectors and Their Potential in Denmark." Danish Technological Institute, Solar Energy Centre; Novator Advanced Technology Consulting; Esbensen Consulting Engineers Ltd.

Brogren, M., Wennerberg, J., Kapper, R., and Karlsson, B. (2003). "Design of concentrating elements with CIS thin-film solar cells for faÁade integration." *Solar Energy Materials and Solar Cells*, 75(3-4), 567-575.

Brostrom, M., and Howell, G. (2008). "The Challenges of Designing and Building a Net Zero Energy Home in a Cold High-Latitude Climate." *3rd International Solar Cities Congress*, Adelaide, South Australia.

Canadian Commission on Building and Fire Codes. (2011). "National Energy Code of Canada for Buildings (NECB)."

Canadian Electricity Association, C. (2006). "Power Generation in Canada - A Guide."

Carpenter, S., Daniels, S., Kemp, S., Kokko, J., and Van Decker, G. (1999). "New Tools for Assessing the Performance of Solar Ventilation Air Heating Systems." *8th Biannual Conference of Solar Energy in High Latitudes (North sun '99)*
25th Annual Conference of the Solar Energy Society of Canada Inc. (SESCI), Edmonton, AB, Canada.

Chen, Y., Athienitis, A. K., and Galal, K. (2010a). "Modeling, design and thermal performance of a BIPV/T system thermally coupled with a ventilated concrete slab in a low energy solar house: Part 1, BIPV/T system and house energy concept." *Solar Energy*, 84(11), 1892-1907.

Chen, Y., Galal, K., and Athienitis, A. K. (2010b). "Modeling, design and thermal performance of a BIPV/T system thermally coupled with a ventilated concrete slab in a low energy solar house: Part 2, ventilated concrete slab." *Solar Energy*, 84(11), 1908-1919.

Cheng, C. L., Sanchez Jimenez, C. S., and Lee, M.-C. (2009). "Research of BIPV optimal tilted angle, use of latitude concept for south orientated plans." *Renewable Energy*, 34(6), 1644-1650.

Chow, T. T. (2010). "A review on photovoltaic/thermal hybrid solar technology." *Applied Energy*, 87(2), 365-379.

CMHC. (2009). "The Northern Sustainable House: An Innovative Design Process." *Research Highlight Technical Series 09-104*, Canadian Mortgage and Housing Corporation.

CMHC. (2010). "Increasing Nunavut Housing Ventilation Rates with HRVs " *Research Highlight Technical Series 10-102*, Canadian Mortgage and Housing Corporation.

Conserval Engineering. (2009). "SolarWall Example: Arctic Schools, Nunavut and Northwest Territories."

Conserval Engineering. (2010a). "SolarWall Air Heating."
<<http://solarwall.com/en/products/solarwall-air-heating/how-it-works.php>>.

Conserval Engineering. (2010b). "SolarWall plus HRV."
<<http://solarwall.com/en/products/solarwall-air-heating/architects-and-engineers/solarwall-with-hrvs.php>>.

Conserval Engineering. (2010c). "SolarWall: Fort Smith Recreation Center, NWT."

Cornick, S. M., Rousseau, M. Z., and Parekh, A. (2009). "An energy simulation study of wall systems for Canadian Arctic Homes ", National Research Concouil Canada, NRC.

Danish Technological Institute, D. (2008). "SOLTAG - energy housing: results of the EU "Demohouse" Research Project." E.-B. Club, ed.

Darkwa, K., O'Callaghan, P. W., and Tetlow, D. (2006). "Phase-change drywalls in a passive-solar building." *Applied Energy*, 83(5), 425-435.

Delisle, V. (2008). "Analytical and Experimental Study of a PV/Thermal Transpired Solar Collector." *Mechanical Engineering*, University of Waterloo, Waterloo, Ontario, 241.

Duffie, J. A., and Beckman, W. A. (2006). *Solar engineering of thermal processes*, 3rd Ed., Wiley, Hoboken, NJ.

Dymond, C., and Kutscher, C. (1997). "Development of a flow distribution and design model for transpired solar collectors." *Solar Energy*, 60(5), 291-300.

Eikelboom, J. A., and Jansen, M. J. (2000). "Characterisation of PV Modules of New Generations: Results of tests and simulations." Holland.

Enerconcept, E. I. (2010). "Lubi -Wall-mounted Solar Heater."
<<http://www.enerconcept.com/en/lubi-technical-specs>>.

Enermodal Engineering, L. (1997). "The Market for Solar Preheated Ventilation Systems in Candian Remote Communities."

Enermodal Engineering, L. (2001). "Monitoring Report for the Fort Smith Recreation Centre SolarWall Ventilation Air Heating System March 2001 to May 2001."

Enermodal Engineering, L. (2002). "Monitoring Report for the Fort Smith Recreation Centre SolarWall Ventilation Air Heating System: Final Report."

Enermodal Engineering, L. (2005). "Comparison of combined SolarWall + HRV system with SolarWall only and HRV only systems."

European Committee for Standardization. (2006). "European Standard: Thermal solar systems and components - Solar collectors - Part 2: Test methods." *Operating and Service Instructions*, Germany, 14.

Fleck, B. A., Meier, R. M., and Matovičá, M. D. (2002). "A field study of the wind effects on the performance of an unglazed transpired solar collector." *Solar Energy*, 73(3), 209-216.

Gawlik, K. M., and C., K. (2002). "Wind Heat Loss from Corrugated, Transpired Solar Collectors." *Transactions of the ASME*, 124(3), 256-261.

Gogakis, C. (2005). "Theoretical and Experimental Analysis of SolarWall Technology." The University of Reading, UK.

Habitat Studio & Workshop Ltd. (2007). "Riverdale NetZero Project, Request for Proposals, CMHC Net Zero Energy Healthy Housing Initiative."

Hansen, J., Sorensen, H., Bystrom, J., Collins, M., and Karlsson, B. (2007). "Market, Modelling, Testing and Demonstration in the Framework of IEA SHC Task 35 on PV/Thermal Solar Systems." *22nd European Photovoltaic Solar Energy Conference and Exhibition*, Milan, Italy.

Hegazy, A. A. (2000). "Comparative study of the performances of four photovoltaic/thermal solar air collectors." *Energy Conversion and Management*, 41(8), 861-881.

Hollick, J. C. (1998). "Solar cogeneration panels." *Renewable Energy*, 15(1,Äi4), 195-200.

Howell, G. (2008). "RiverdaleNetZeroProject - Presentation." Howell-Mayhew Engineering, Edmonton.

Hussein, H. M. S., Ahmad, G. E., and El-Ghetany, H. H. (2004). "Performance evaluation of photovoltaic modules at different tilt angles and orientations." *Energy Conversion and Management*, 45(15-16), 2441-2452.

IEA. (1997). *Solar Energy Houses - Strategies, Technologies, Examples*, International Energy Agency.

IEA. (2002). "PV/T Solar Energy Systems: Status of the Technology and Roadmap for Future Development." International Energy Agency.

Incropera, F. P., and D.P., D. (2002). *Fundamentals of Heat and Mass Transfer*, 5 Ed., John Wiley & Sons, Inc., New York.

Indian and Northern Affairs Canada, I. (2006). "Northern Housing." <<http://www.ainc-inac.gc.ca/ai/mr/is/abhsg-eng.asp>> 2010).

ISO, I. O. o. S. (1994). "Test methods for solar collectors - Part 1: Thermal performance of glazed liquid heating collectors including pressure drop." 14.

Jensen, S. Ø. (2001). "Results from measurements on the PV-VENT systems at Lundebjerg." Danish Technological Institute.

Kalema, T., and Pylsy, P. (2008). "Low-energy house concepts for Nordic countries " *1st Nordic passive house conference Passivhus Norden*, Norway, 66-72.

Kutscher, C. F. (1994). "Heat Exchange Effectiveness and Pressure Drop for Air Flow through Perforated Plates with and without Crosswind." *Journal of Heat Transfer, Transactions of the ASME*, 116(2), 391-399.

Kutscher, C. F., C., C., and G., B. (1991). "Unglazed Transpired Solar Collectors: An Analytical Model and Test Results." *Solar World Congress*, 1245-1250.

Kutscher, C. F., C., C., and G., B. (1993). "Unglazed Transpired Solar Collectors: Heat Loss Theory." *Journal of Solar Energy Engineering, Transactions of the ASME*, 115(3), 182-188.

Leon, M. A., and Kumar, S. (2007). "Mathematical modeling and thermal performance analysis of unglazed transpired solar collectors." *Solar Energy*, 81(1), 62-75.

Liao, L., Athienitis, A. K., Candanedo, L., Park, K.-W., Poissant, Y., and Collins, M. (2007). "Numerical and Experimental Study of Heat Transfer in a BIPV-Thermal System." *Journal of Solar Energy Engineering*, 129(4), 423-430.

Mallick, T. K., Eames, P. C., Hyde, T. J., and Norton, B. (2004). "The design and experimental characterisation of an asymmetric compound parabolic photovoltaic concentrator for building facade integration in the UK." *Solar Energy*, 77(3), 319-327.

McCluskey, B. (2001). "Ft. Smith Solarwall Performance Reporting." R. Alward, ed., Arctic Energy Alliance.

McQuiston, F. C., Parker, J. D., and Spitler, J. D. (2005). *Heating, ventilating, and air conditioning : analysis and design*, 6th Ed., John Wiley & Sons, Hoboken, N.J.

Mei, L., Infield, D., Eicker, U., and Fux, V. (2003). "Thermal modelling of a building with an integrated ventilated PV facade." *Energy and Buildings*, 35(6), 605-617.

Nagano, K., Mochida, T., Shimakura, K., Murashita, K., and Takeda, S. (2003). "Development of thermal-photovoltaic hybrid exterior wallboards incorporating PV cells in and their winter performances." *Solar Energy Materials and Solar Cells*, 77(3), 265-282.

National Energy Board. (2011). "Energy Use in Canada's North: An Overview of Yukon, Northwest Territories, and Nunavut." *Energy Facts*.

Natural Resources Canada, N. (2003). "Energy Use Data Handbook." 22.

Natural Resources Canada, N. (2007). "Photovoltaic municipal rankings in terms of yearly PV potential." <<https://glfc.cfsnet.nfis.org/mapserver/pv/rank.php?lang=e>>.

Natural Resources Canada, N. (2011). "Personal: Residential Climate Zones – ENERGY STAR." <<http://oee.nrcan.gc.ca/residential/personal/windows-doors/climate-zones.cfm?attr=4>>.

Natural Resources Canada, N. (2012). "Energy Sources - Average Retail Price." <<http://www2.nrcan.gc.ca/eneene/sources/>>.

Norling, C. R., Rode, C., Svendsen, S., Kragh, J., and Reimann, G. (2006). "A low-energy building under arctic conditions – a case study." *3rd International Building Physics Conference*, Montreal, 587-594.

Norton, B., Eames, P. C., Mallick, T. K., Huang, M. J., McCormack, S. J., Mondol, J. D., and Yohanis, Y. G. (2009). "Enhancing the performance of building integrated photovoltaics." *Solar Energy*, In Press, Corrected Proof.

NWT Housing Corporation, N. (2012). "2012/13 Annual Business Plan."

Pedersen, P. V. (2008). "The first experiences in Denmark with passive house design and use of architecturally optimised solar roofs." *1st Nordic passive house conference*, Trondheim, Norway, 22-27.

Poissant, Y. (2009). "Field assessment of novel PV module technologies in Canada." N. Natural Resources Canada, ed., Varennes.

Poissant, Y., Thevenard, D., and Turcotte, D. (2004). "Performance monitoring of the Nunavut Arctic College PV system: Nine years of reliable electricity generation."

PSE, A. (2011). "Indoor Test Stand for Solar Thermal Collectors." *Operating and Service Instructions*, Germany.

Santbergen, R., Rindt, C. C. M., Zondag, H. A., and van Zolingen, R. J. C. (2010). "Detailed analysis of the energy yield of systems with covered sheet-and-tube PVT collectors." *Solar Energy*, 84(5), 867-878.

Sharples, S., and Charlesworth, P. S. (1998). "Full-scale measurements of wind-induced convective heat transfer from a roof-mounted flat plate solar collector." *Solar Energy*, 62(2), 69-77.

Stamenic, L., Smiley, E., and Karim, K. (2004). "Low light conditions modelling for building integrated photovoltaic (BIPV) systems." *Solar Energy*, 77(1), 37-45.

Statistics Canada, and Nunavut Bureau of Statistics. (2010). "Nunavut Housing Needs Survey 2009/2010."

Strub, H. (1996). *Bare Poles - Building Design for High Latitudes*, Carleton University Press.

Summers, D. (1995). "Thermal Simulation and Economic Assessment of Unglazed Transpired Collector Systems. ." University of Wisconsin, Madison.

TamizhMani, G., Dignard-Bailey, L., Thevenard, D., and Howell, D. G. (1998). "Influence of low-light module performance on the energy production of Canadian grid-connected PV systems." *Renewable Energy Technologies in Cold Climates*, Montreal.

Test, F. L., Lessmann, R. C., and Johary, A. (1981). "Heat Transfer During Wind Flow over Rectangular Bodies in the Natural Environment." *Journal of Heat Transfer*, 103(2), 262-267.

Thevenard, D. (2005). "Evaluation of the Monitored Data from the Photovoltaic System at Nunavut Arctic College, Iqaluit, Nunavut (Year 2004)." Levelton Consultants Richmond.

Thevenard, D. (2006). "Evaluation of the Monitored Data from the Photovoltaic System at Nunavut Arctic College, Iqaluit, Nunavut (Year 2005)." Levelton Consultants Richmond.

Tonui, J. K., and Tripanagnostopoulos, Y. (2007). "Improved PV/T solar collectors with heat extraction by forced or natural air circulation." *Renewable Energy*, 32(4), 623-637.

University of Wisconsin, M. (2012). "TMY Weather data for TRNSYS 17." <<http://sel.me.wisc.edu/trnsys/weather/weather.htm>>.

Van Decker, G. W. E., Hollands, K. G. T., and Brunger, A. P. (2001). "Heat-exchange relations for unglazed transpired solar collectors with circular holes on a square or triangular pitch." *Solar Energy*, 71(1), 33-45.

Vladykova, P., Rode, C., Nielsen, T. R., and Pedersen, S. (Year). "Passive Houses for Arctic Climates." *1st Nordic passive house conference*, Trondheim, Norway.

Zondag, H. A. (2008). "Flat-plate PV-Thermal collectors and systems: A review." *Renewable and Sustainable Energy Reviews*, 12(4), 891-959.

Appendix A. Experimental Set Up

Table A.1 List of Materials needed for prototype construction

Item	Description	Qty	Company	Note
Custom size PV panel	Dark frame, custom size	2	Day4Energy	Left from JMSB setup
NON-Perforated Polycarbonate Sheets	Transparent sheets ordered from MasterCarr	4	MasterCarr	Purchased
Perforated Polycarbonate Sheets	Transparent sheets perforated by Laser	4	CBR Laser Inc	Purchased
Perforated Corrugated Dark Metal Cladding	SolarWall cladding 5' by 5'	1	Conserval Engineering	Left from JMSB setup
Dark Metal Absorber	TiNOX Steel, high absorbance and low emissvity, 5' by 5'	1	Almecco	Left from Luis' experiment
Structural Insulated Panel	One full-size (4' by 8'), two half size (2' by 8')	3	KOTT	In kind support

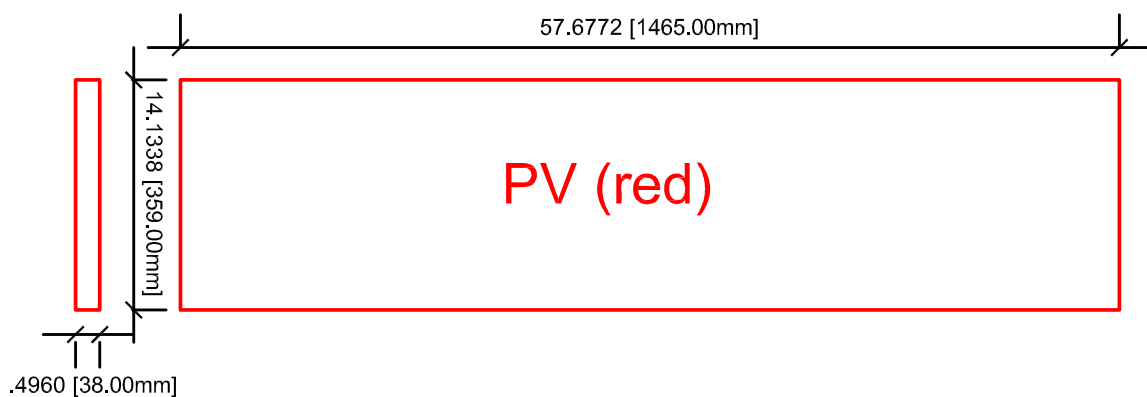


Figure A.1 Custom sized PV panel dimensions

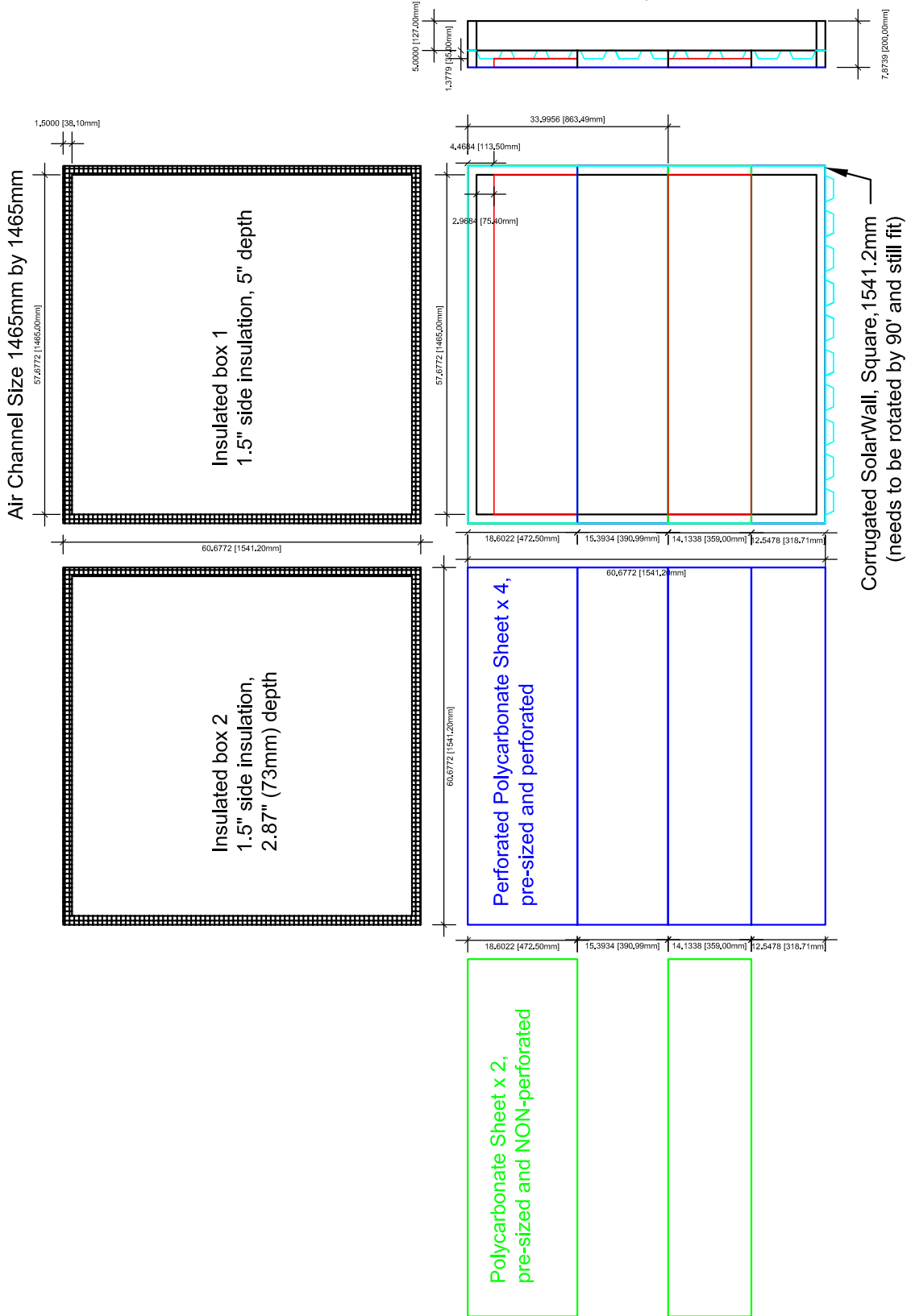


Figure A.2 Components of the Experimental Assembly (CAD drawing, to scale)

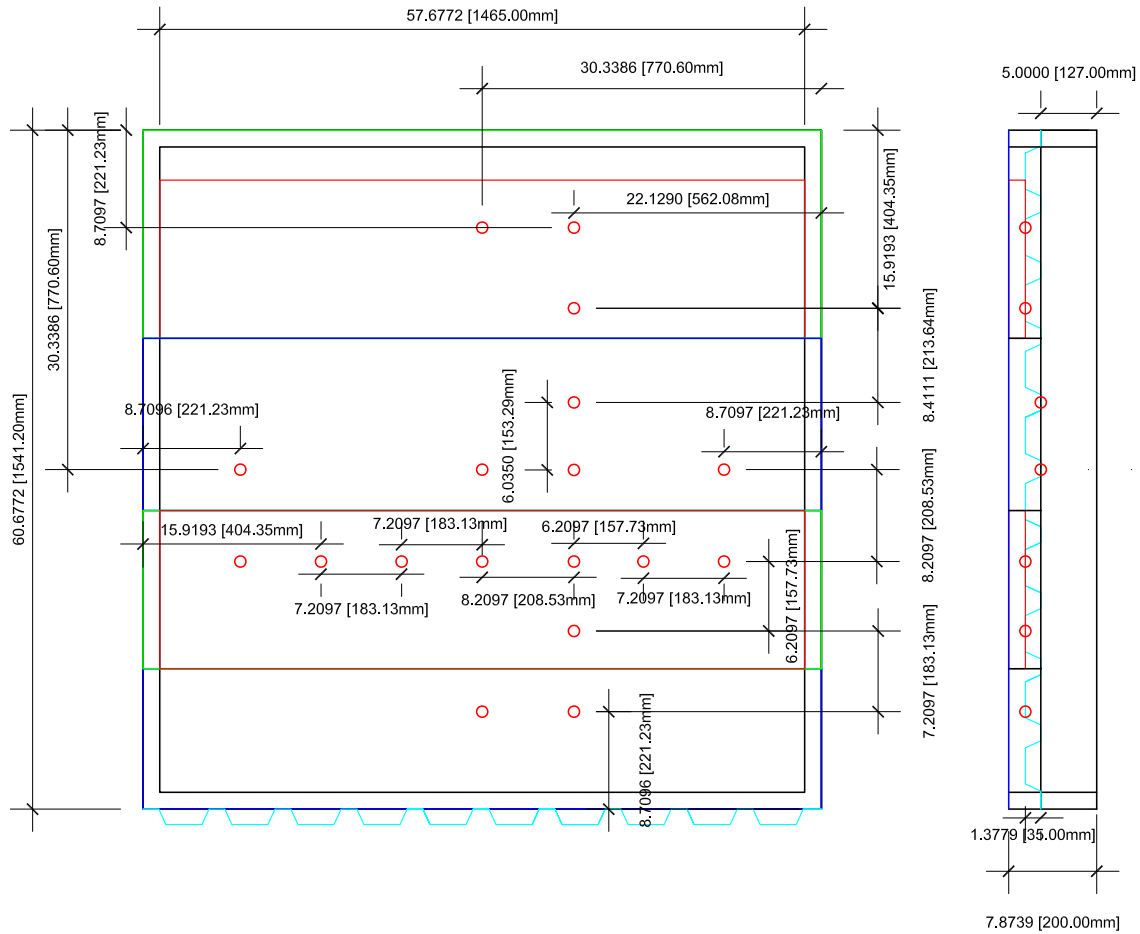


Figure A.3 Instrumentation Diagram of SolarWall Layer; Able to accommodate two orientations for testing;

In Figure A.3, the SolarWall plate can be rotated counterclockwise by 90° to form the flow-along-corrugation configuration (SW-v). Two sensors are shared between the two configurations (SW-h_C2=SW-v_C2; SW-h_R5=SW-v_R3). The current orientation in Figure A.3 is flow-against-corrugation (SW-h).

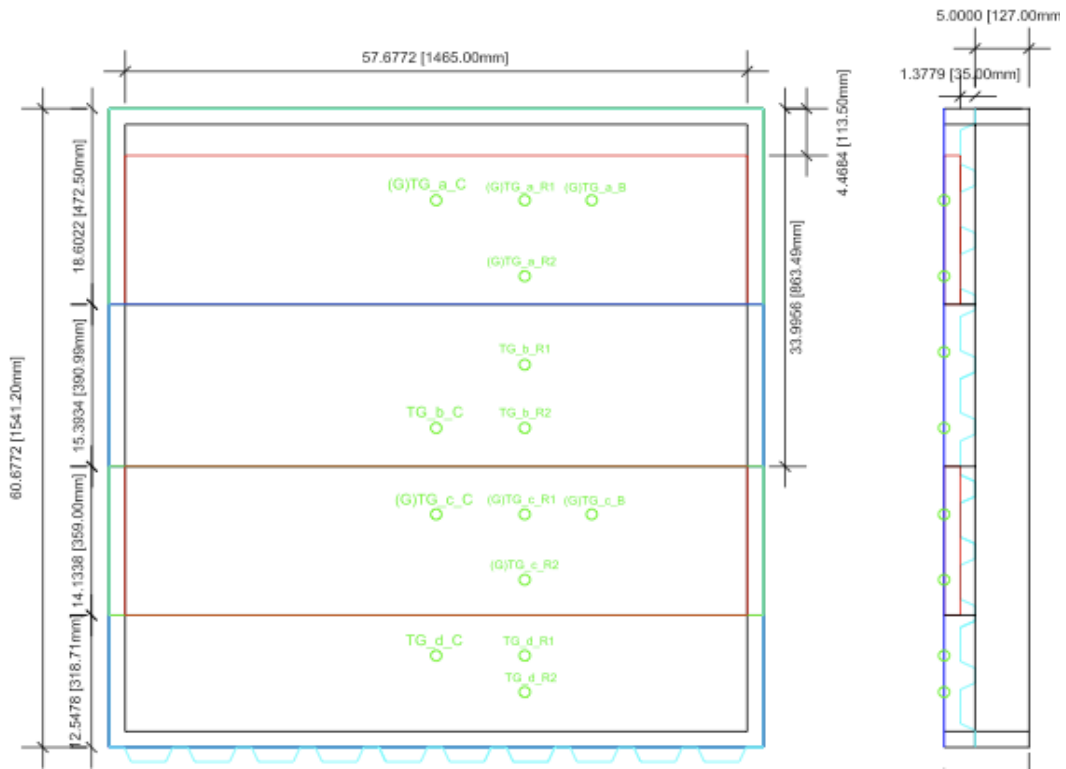


Figure A.4 Instrumentation Diagram of Transpired Glazing/Glazing Layer

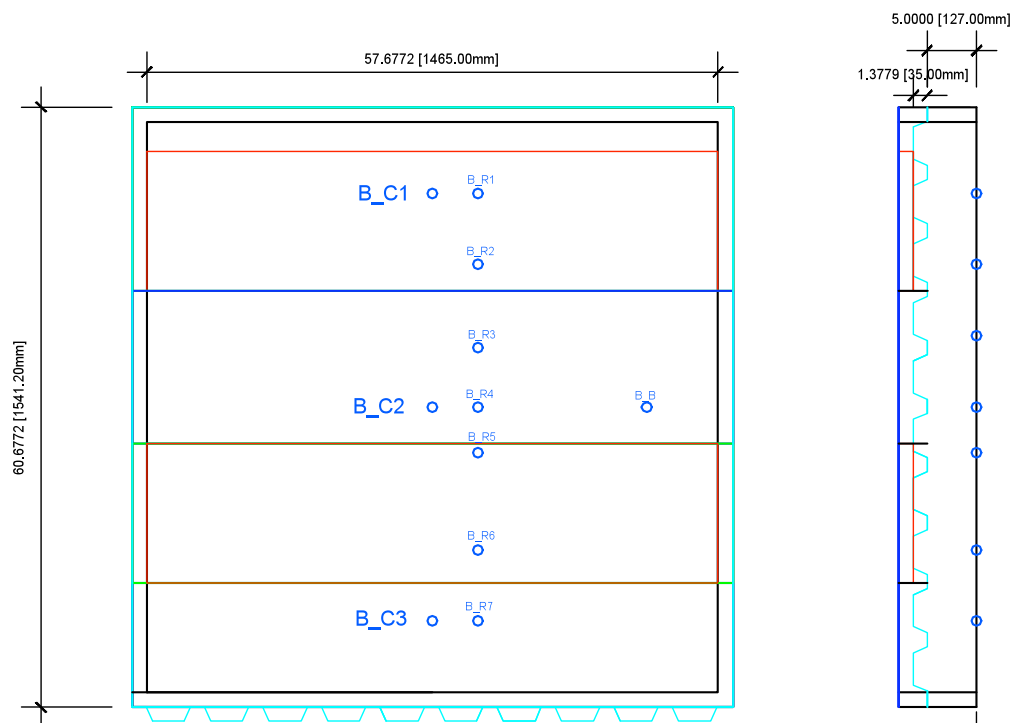


Figure A.5 Instrumentation Diagram of Back Plate Layer

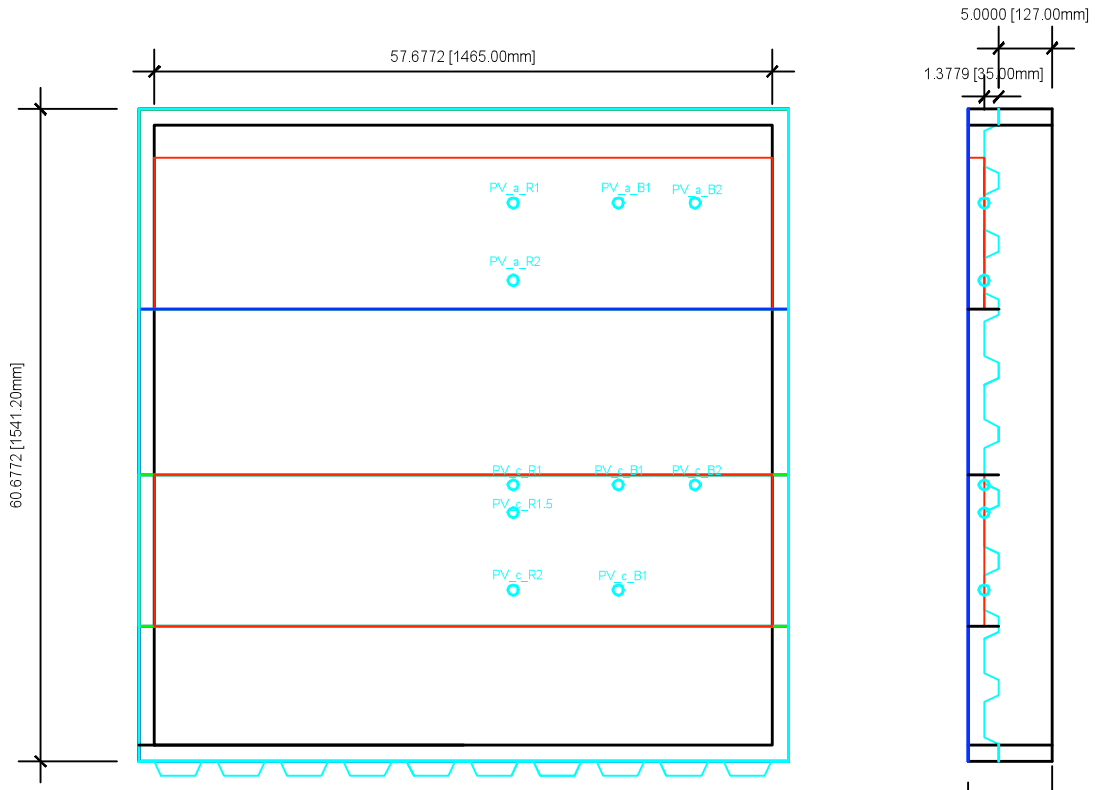


Figure A.6 Instrumentation Diagram of PV modules Layer

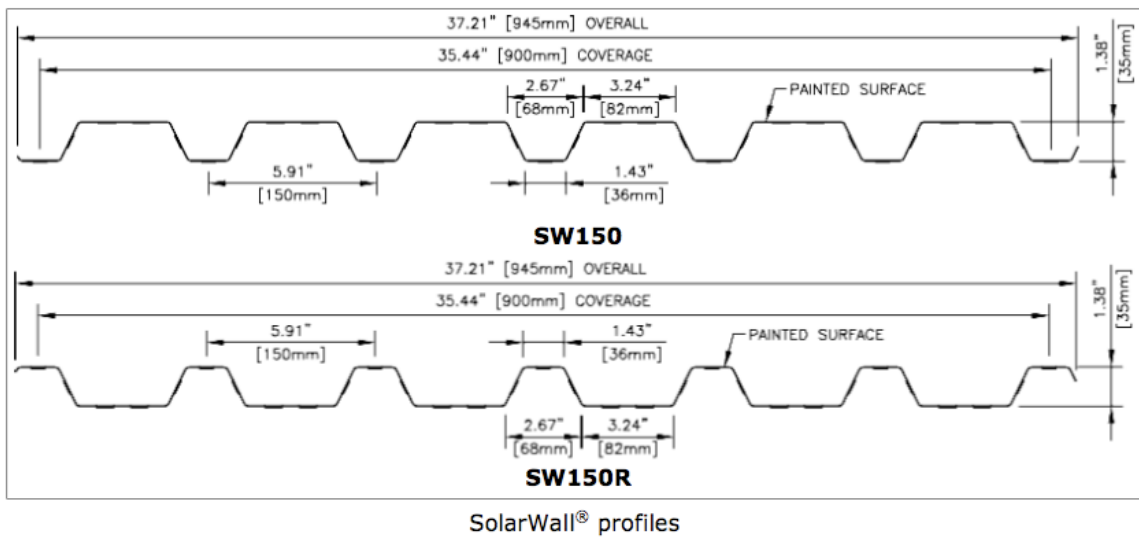


Figure A.7 SolarWall Corrugation Dimensions (Conserval Engineering, 2010)

Table A.2 Thermocouple Master List

Thermocouples		Name: XX_X_XX#	Name: Location_Slot (a-d)_Left/Right/Center/Front/Back/Boundary						
Location	Code	DAQ	DAQ	Coordinates (Bottom Left Upmost= 0,0,0)			Distance (m)		
L/R/C; Front/Back; Boundary	(XX_X_XX#)	Mod	Channel	x (in)	y (in)	z (in)	Pnt to DAQ		
Ext. Air	R1	E_R1	Mod1	0	33.4646	50.4676	1.5	4.998	
Ext. Air	R2	E_R2	Mod1	1	33.4646	34.8468	1.5	4.602	
Ext. Air	R3	E_R3	Mod1	2	33.4646	24.2126	1.5	4.332	
Ext. Air	R4	E_R4	Mod1	3	33.4646	7.2096	1.5	3.900	
OutletTop	OT1	OT1	Mod1	4	28.8386	60.6772		5.375	
OutletTop	OT2	OT2	Mod1	5	28.8386	60.6772		5.375	
Back	C1	B_C1	Mod1	6	28.8386	50.4676	-7.8739	5.116	
Back	C2	B_C2	Mod1	7	28.8386	28.8386	-7.8739	4.567	
Back	C3	B_C3	Mod1	8	28.8386	7.2096	-7.8739	4.017	
Back	R1	B_R1	Mod1	9	33.4646	50.4676	-7.8739	4.998	
Back	R2	B_R2	Mod1	10	33.4646	43.2579	-7.8739	4.815	
Back	R3	B_R3	Mod1	11	33.4646	34.8468	-7.8739	4.602	
Back	R4	B_R4	Mod1	12	33.4646	28.8386	-7.8739	4.445	
Back	R5	B_R5	Mod1	13	33.4646	24.2126	-7.8739	4.332	
Back	R6	B_R6	Mod1	14	33.4646	14.4193	-7.8739	4.083	
Back	R7	B_R7	Mod1	15	33.4646	7.2096	-7.8739	3.900	
Back	B	B_B	Mod2	0	50.4676	28.8386	-7.8739	4.017	
Cavity	C1	C_C1	Mod2	1	28.8386	28.8386	-3.74015748	4.567	
Cavity	C2	C_C2	Mod2	2	28.8386	28.8386	-5.118110236	4.567	
Cavity	C3	C_C3	Mod2	3	28.8386	28.8386	-6.496062992	4.567	
Cavity	R1	C_R1	Mod2	4	33.4646	28.8386	-3.74015748	4.445	
Cavity	R2	C_R2	Mod2	5	33.4646	28.8386	-5.118110236	4.445	
Cavity	R3	C_R3	Mod2	6	33.4646	28.8386	-6.496062992	4.445	
TG_a	C1	TG_a_C	Mod2	7	28.8386	50.4676	0	5.116	
TG_a	R1	TG_a_R1	Mod2	8	33.4646	50.4676	0	4.998	
TG_a	R2	TG_a_R2	Mod2	9	33.4646	43.2579	0	4.815	
TG_a	B1	TG_a_B1	Mod2	10	43.2579	50.4676	0	4.750	
TG_a	B2	TG_a_B2	Mod2	11	50.4676	50.4676	0	4.567	
TG_b	C2	TG_b_C	Mod2	12	28.8386	28.8386	0	4.567	
TG_b	R1	TG_b_R1	Mod2	13	33.4646	34.8468	0	4.602	
TG_b	R2	TG_b_R2	Mod2	14	33.4646	28.8386	0	4.445	
TG_b	B2	TG_b_B	Mod2	15	50.4676	28.8386	0	4.017	
TG_c	C1	TG_c_C	Mod3	0	28.8386	24.2126	0	4.445	
TG_c	R1	TG_c_R1	Mod3	1	33.4646	24.2126	0	4.332	
TG_c	R2	TG_c_R2	Mod3	2	33.4646	14.4193	0	4.083	
TG_c	B1	TG_c_B	Mod3	3	43.2579	24.2126	0	4.083	
TG_d	C1	TG_d_C	Mod3	4	28.8386	7.2096	0	4.017	
TG_d	R1	TG_d_R1	Mod3	5	33.4646	7.2096	0	3.900	
TG_d	R2	TG_d_R2	Mod3	6	33.4646	3.7475	0	3.812	
Glazing_a	C1	G_a_C	Mod3	7	28.8386	50.4676	0	5.116	
Glazing_a	R1	G_a_R1	Mod3	8	33.4646	50.4676	0	4.998	
Glazing_a	R2	G_a_R2	Mod3	9	33.4646	43.2579	0	4.815	
Glazing_a	B1	G_a_B	Mod3	10	43.2579	50.4676	0	4.750	
Glazing_c	C1	G_c_C	Mod3	11	28.8386	20.629	0	4.358	
Glazing_c	R1	G_c_R1	Mod3	12	33.4646	20.629	0	4.241	
Glazing_c	R2	G_c_R2	Mod3	13	33.4646	14.4193	0	4.083	
Glazing_c	B1	G_c_B	Mod3	14	43.2579	20.629	0	3.992	
PV_a	R1	PV_a_R1	Mod4	9	33.4646	50.4676	-0.4	7.201	
PV_a	R2	PV_a_R2	Mod4	10	33.4646	43.2579	-0.4	7.018	
PV_a	B1	PV_a_B1	Mod4	11	43.2579	50.4676	-0.4	6.952	
PV_a	B2	PV_a_B2	Mod4	12	50.4676	50.4676	-0.4	6.769	
PV_c	R1	PV_c_R1	Mod4	13	33.4646	24.2126	-0.4	6.534	
PV_c	R1.5	PV_c_R1.5	Mod4	14	33.4646	21.629	-0.4	6.468	
PV_c	R2	PV_c_R2	Mod4	11	33.4646	14.4193	-0.4	6.285	
PV_c	B1	PV_c_B1	Mod4	12	43.2579	14.4193	-0.4	6.036	
PV_c	B2	PV_c_B2	Mod4	13	50.4676	24.2126	-0.4	6.102	

Table A.2 (Continued) Thermocouple Master List

Thermocouples		Name: XX_X_XX#	Name: Location_Slot (a-d)_Left/Right/Center/Front/Back/Boundary					Distance (m)
Location	Code	DAQ	DAQ	Coordinates (Bottom Left Upmost= 0,0,0)			Pnt to DAQ	
L/R/C; Front/Back; Boundary	(XX_X_XX#)	Mod	Channel	x (in)	y (in)	z (in)		
SWv	R1	SWv_R1	Mod3	7	50.4676	24.2126	-1.496	6.102
SWv	R2	SWv_R2	Mod3	8	43.2579	24.2126	-1.496	6.285
SWv	R3=(SWh_R5)	SWv_R3	Mod3	9	33.4646	24.2126	-1.496	6.534
SWv	R4	SWv_R4	Mod3	10	28.8117	24.2126	-1.496	6.652
SWv	R5	SWv_R5	Mod3	11	20.629	24.2126	-1.496	6.860
SWv	R6	SWv_R6	Mod3	12	14.4193	24.2126	-1.496	7.018
SWv	R7	SWv_R7	Mod3	13	7.2096	24.2126	-1.496	7.201
SWv	C1	SWv_C1	Mod3	14	50.4676	28.8386	-2.8739	6.220
SWv	C2=(SWh_C2)	SWv_C2	Mod3	15	28.8386	28.8386	-2.8739	6.769
SWv	C3	SWv_C3	Mod4	0	7.2096	28.8386	-2.8739	7.318
SWh	R1	SWh_R1	Mod4	1	33.4646	50.4676	-1.496	7.201
SWh	R2	SWh_R2	Mod4	2	33.4646	43.2579	-1.496	7.018
SWh	R3	SWh_R3	Mod4	3	33.4646	34.8468	-2.8739	6.804
SWh	R4	SWh_R4	Mod4	4	33.4646	28.8117	-2.8739	6.651
SWh	R5=(SWv_R3)	SWh_R5	Mod3	9	33.4646	24.2126	-1.496	6.534
SWh	R6	SWh_R6	Mod4	5	33.4646	14.4193	-1.496	6.285
SWh	R7	SWh_R7	Mod4	6	33.4646	7.2096	-1.496	6.102
SWh	C1	SWh_C1	Mod4	7	28.8386	50.4676	-1.496	7.318
SWh	C2=(SWv_C2)	SWh_C2	Mod3	15	28.8386	28.8386	-2.8739	6.769
SWh	C3	SWh_C3	Mod4	8	28.8386	7.2096	-1.496	6.220

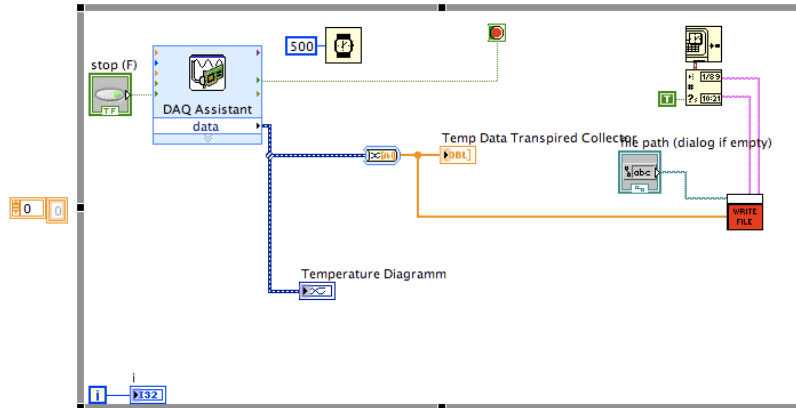
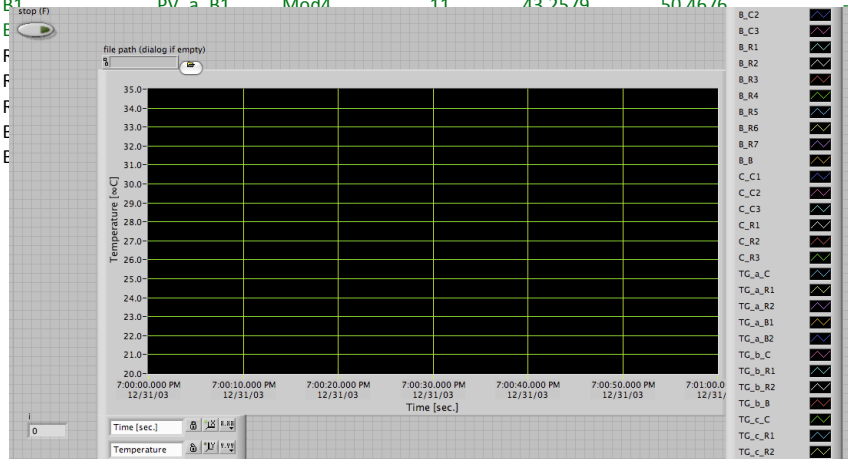


Figure A.8 LabVIEW DAQ Interface (above) and Block Diagram (below);



Figure A.9 Construction Photo: Collector base with instrumentation;

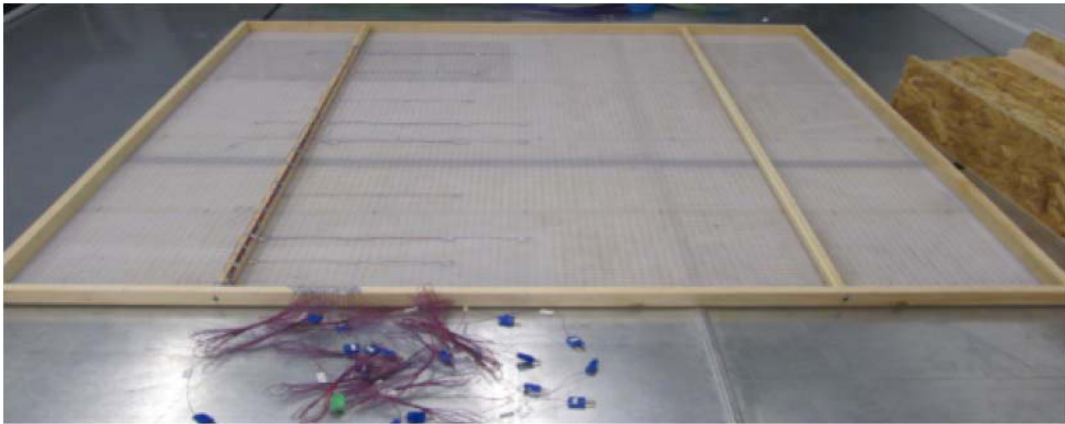


Figure A.10 Construction Photo: Transpired Glazing top with instrumentation;

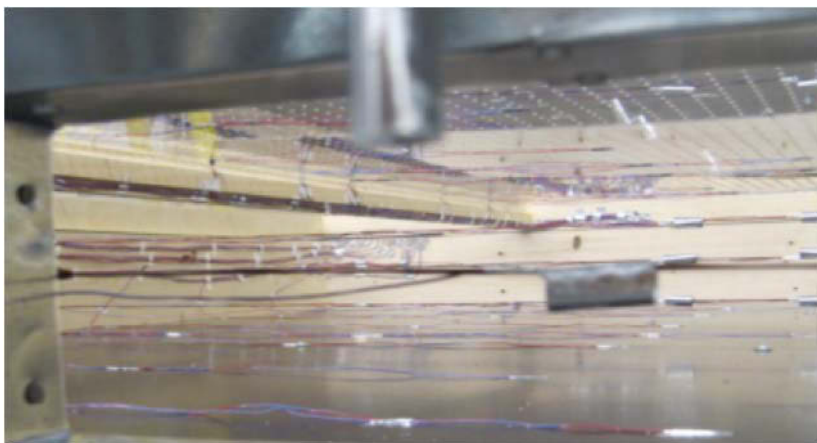


Figure A.11 Construction Photo: Instrumentation seen from duct outlet

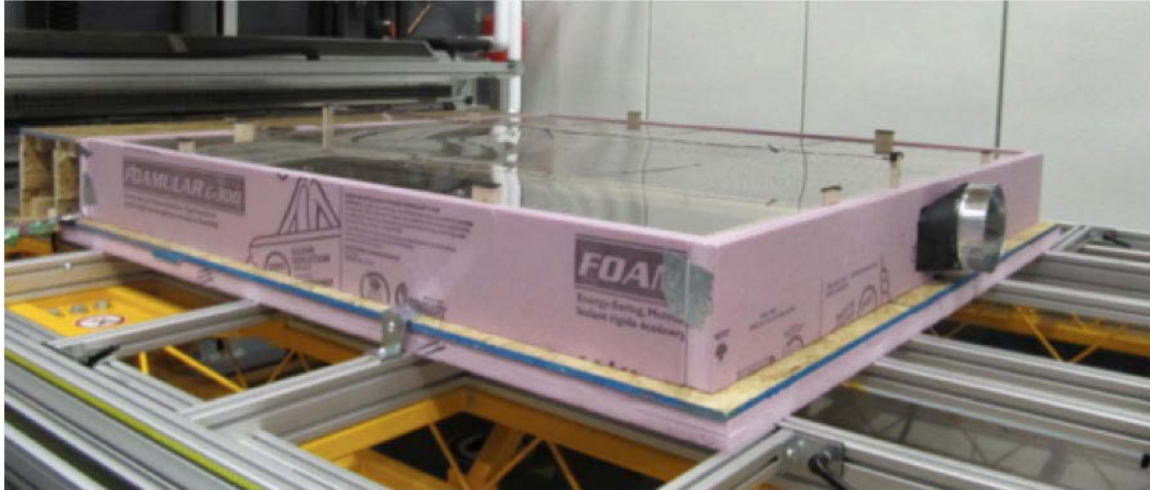


Figure A.12 Construction Photo: Assembled collector A1 mounted on collector test stand



Figure A.13 Construction Photo: Collector A1 at vertical tilt with duct outlet connected

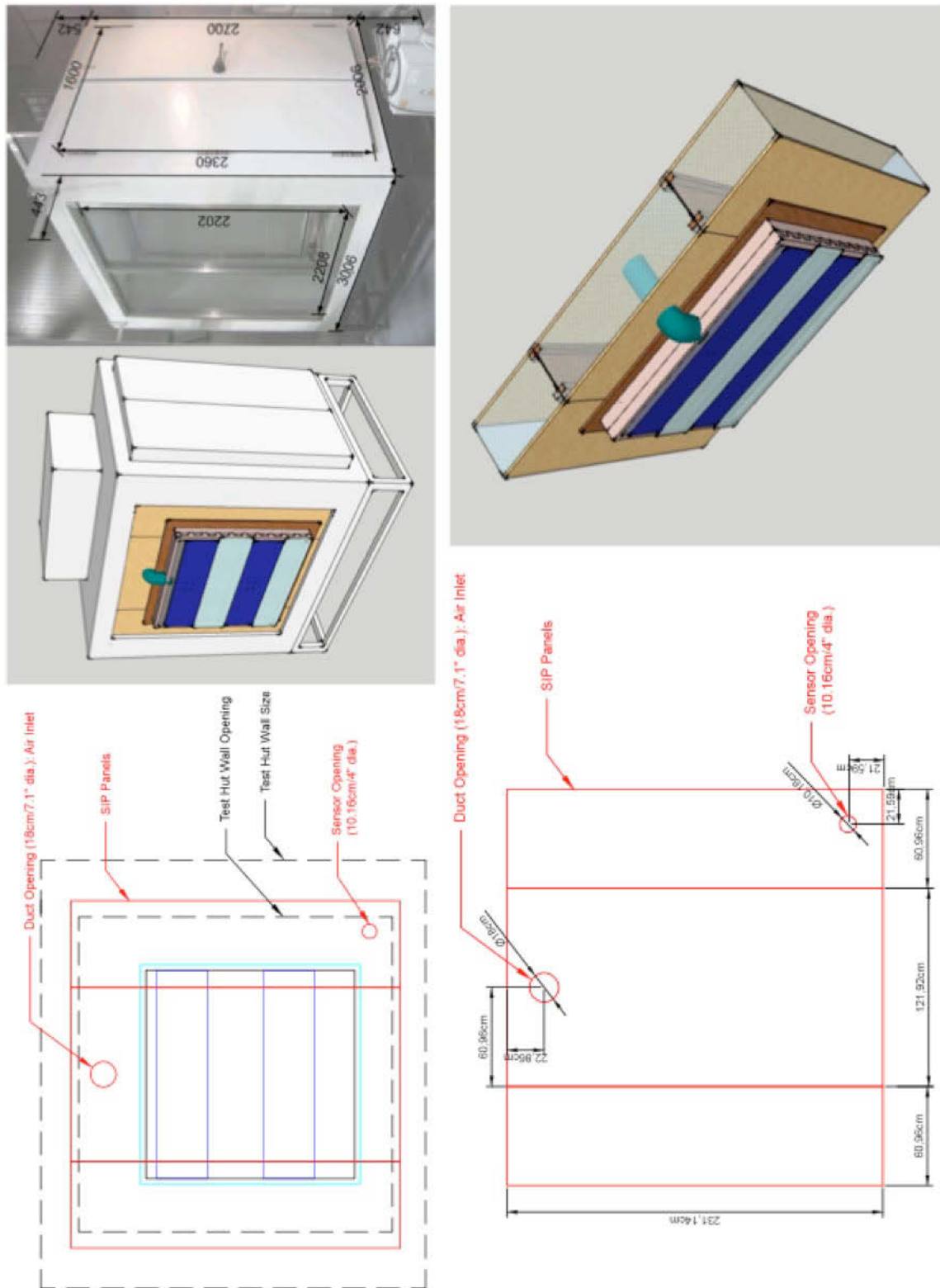


Figure A.14 Schematics of BIPV/T-SIP integration for the Environmental Chamber tests



Figure A.15 Construction photo: SIP shipment in three pieces (left) and Test Hut with hollow façade (right)



Figure A.16 Construction photo: Sensor feeding into the test hut before insulation and sealing (left); Duct installation from outside (top right) and inside (bottom right) Test Hut

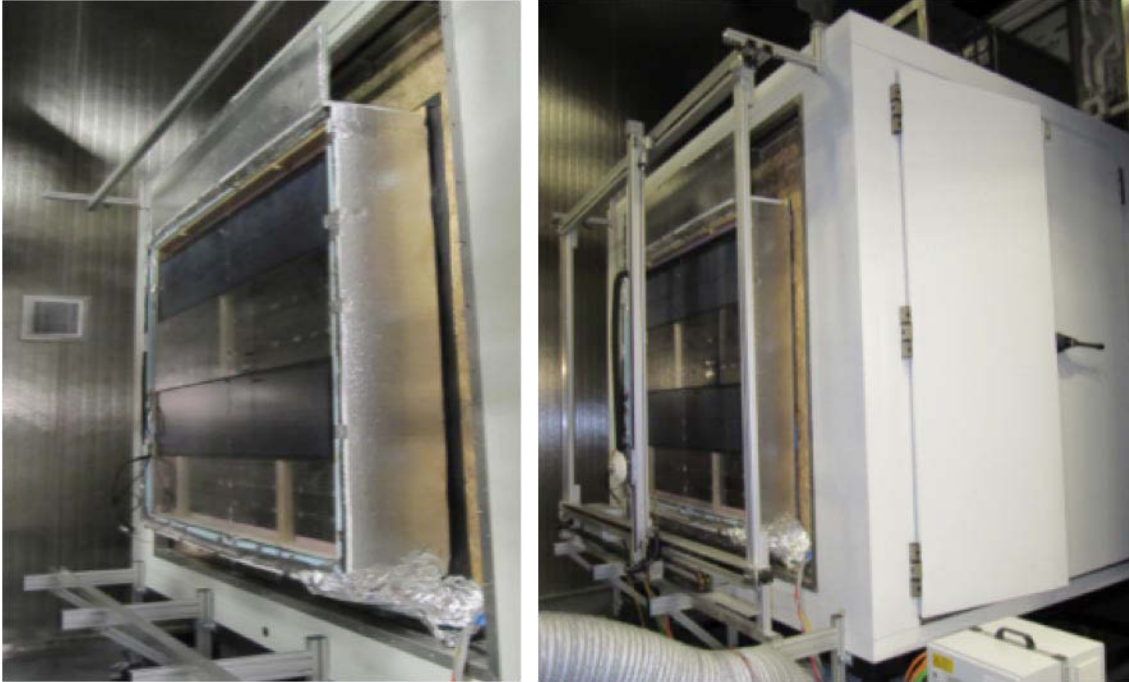


Figure A.17 Construction photo: Complete Integration of Collector onto SIP without scanner (left), with scanner (right)

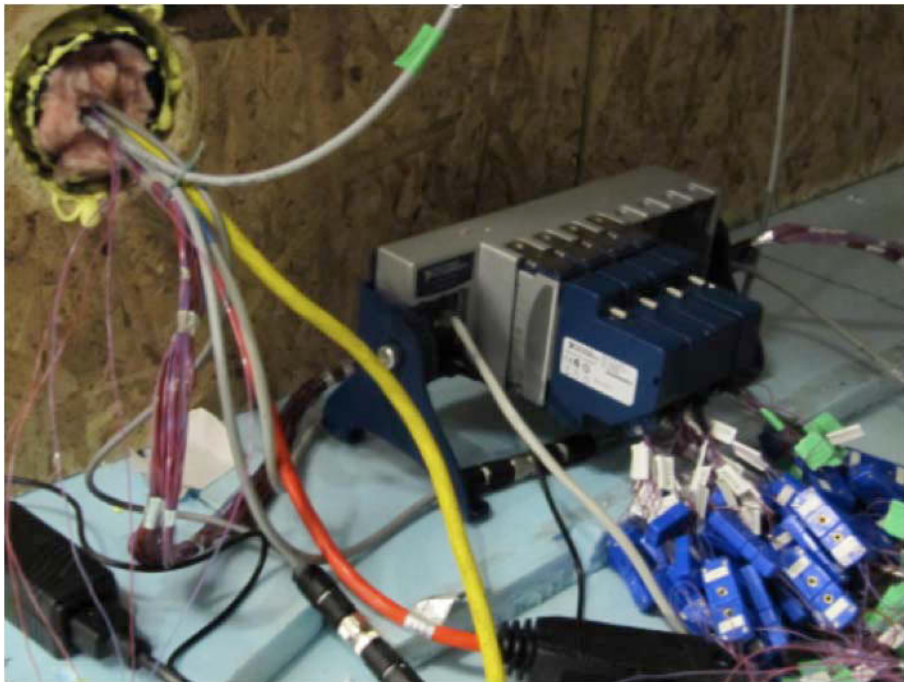


Figure A.18 National Instrumentation, Data Acquisition modules and chassis

Appendix B. Experimental Results

Table B.1 Scan results of wind speed across collector height

Distance (mm) from middle of the collector, 2 readings on each height	Wind speed at 25% fan power (m/s),	Wind speed at 100% fan power (m/s)
	AVERAGE;1.02	AVERAGE;3.44
	MINIMUM;0.69	MINIMUM;2.55
	MAXIMUM;1.49	MAXIMUM;4.80
-872.4779052734375;	1.486103 ; 1.348728 ;	4.795315 ; 4.608440 ;
-722.4779052734375;	1.131785 ; 1.090449 ;	4.163286 ; 3.745512 ;
-572.4779052734375;	1.209237 ; 1.102416 ;	3.944597 ; 3.496511 ;
-422.4779052734375;	1.151100 ; 0.969389 ;	3.725790 ; 3.357467 ;
-272.4779052734375;	1.169085 ; 1.055867 ;	3.651813 ; 3.306551 ;
-122.4779052734375;	0.991761 ; 0.994012 ;	3.490931 ; 3.083949 ;
27.5220947265625;	1.078239 ; 0.875709 ;	3.556386 ; 3.131274 ;
177.5220947265625;	1.010910 ; 0.877233 ;	3.310549 ; 2.927415 ;
327.5220947265625;	0.932954 ; 0.883445 ;	3.150075 ; 3.065596 ;
477.5220947265625;	0.897042 ; 0.767752 ;	2.983349 ; 2.821360 ;
627.5220947265625;	0.808148 ; 0.690165 ;	2.850808 ; 2.554035 ;

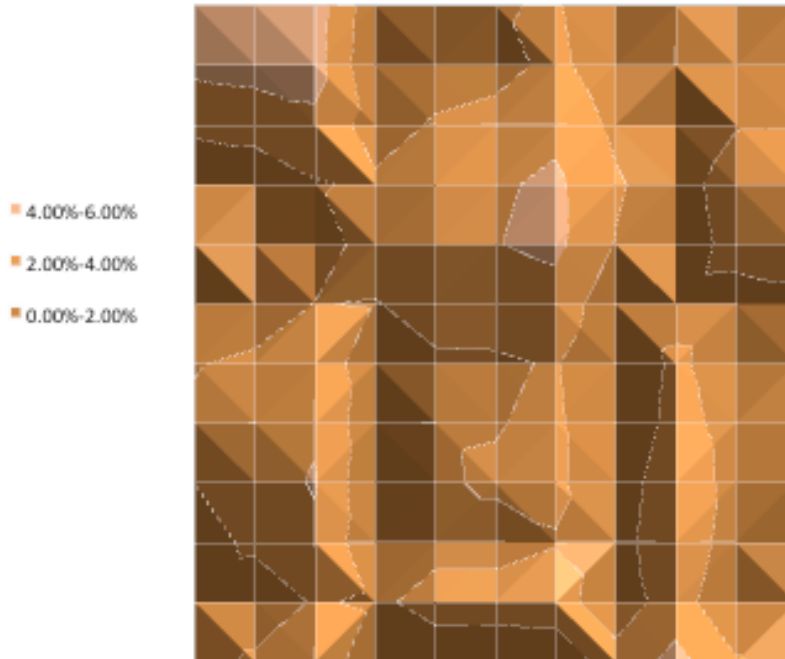


Figure B.1 Irradiance Distribution at Collector surface (Solar Simulator), average 1148 W/m²

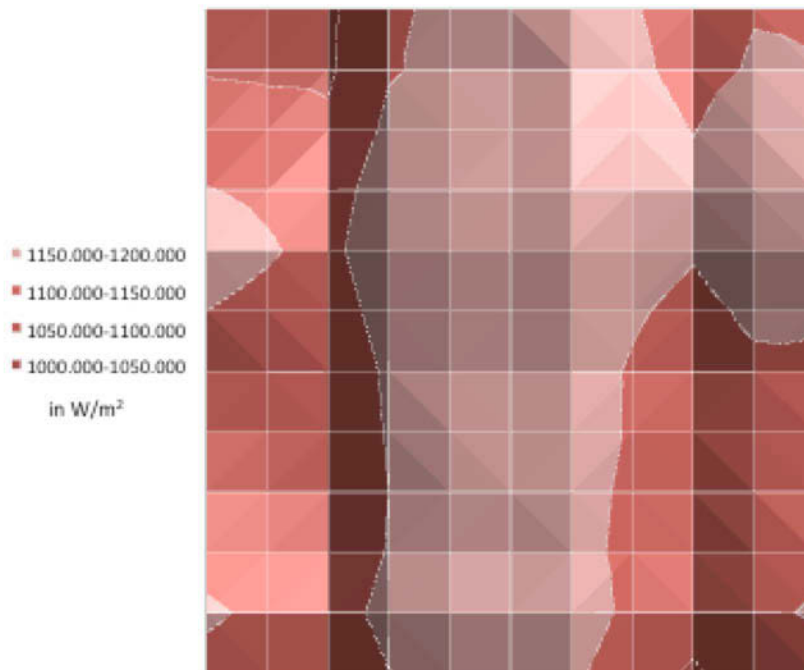


Figure B.2 Standard deviation of solar distribution at Collector Surface (Solar Simulator), 5 % maximum

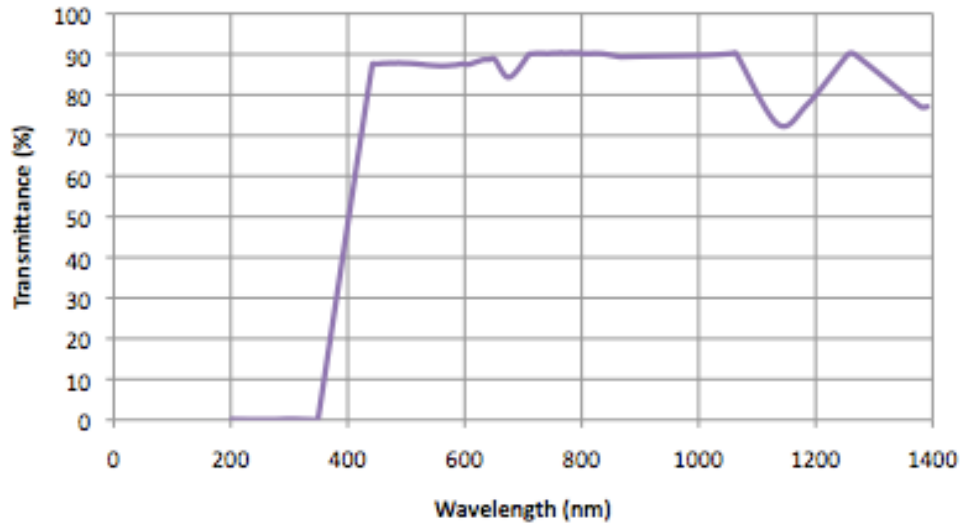


Figure B.3 Transmittance results for UV-resistant high-performance polycarbonate sheet, tested by the Agilent Spectrophotometer; Average transmittance of 0.89 at visible and near infrared range

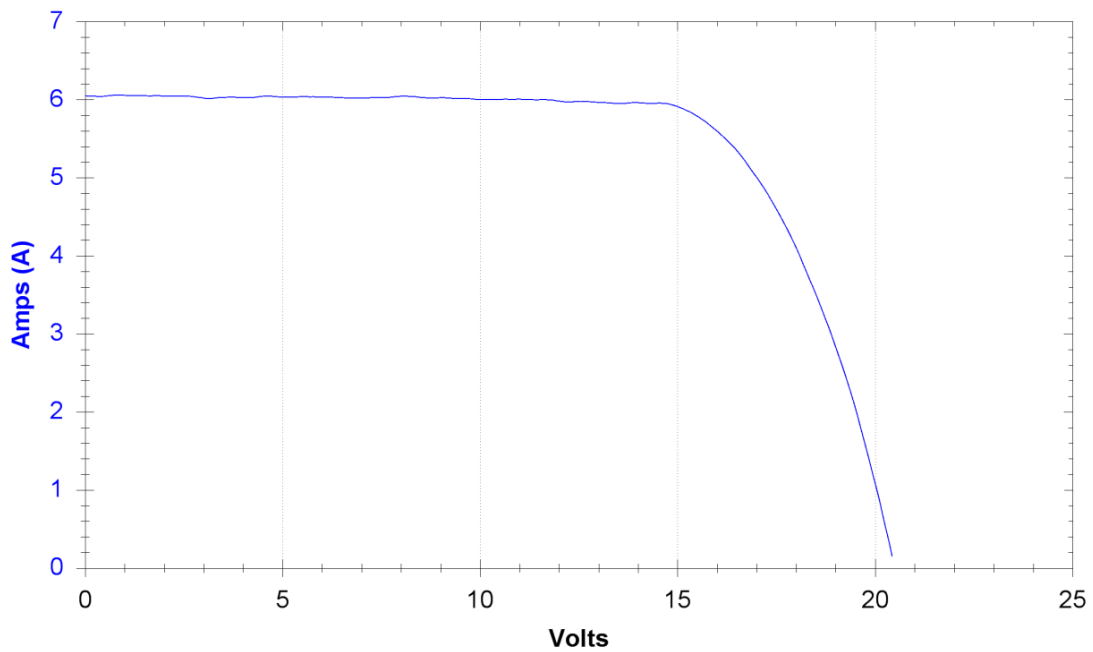


Figure B.4 I-V tracer results for two 60W PV modules at 838 W/m², details in Table 4.5

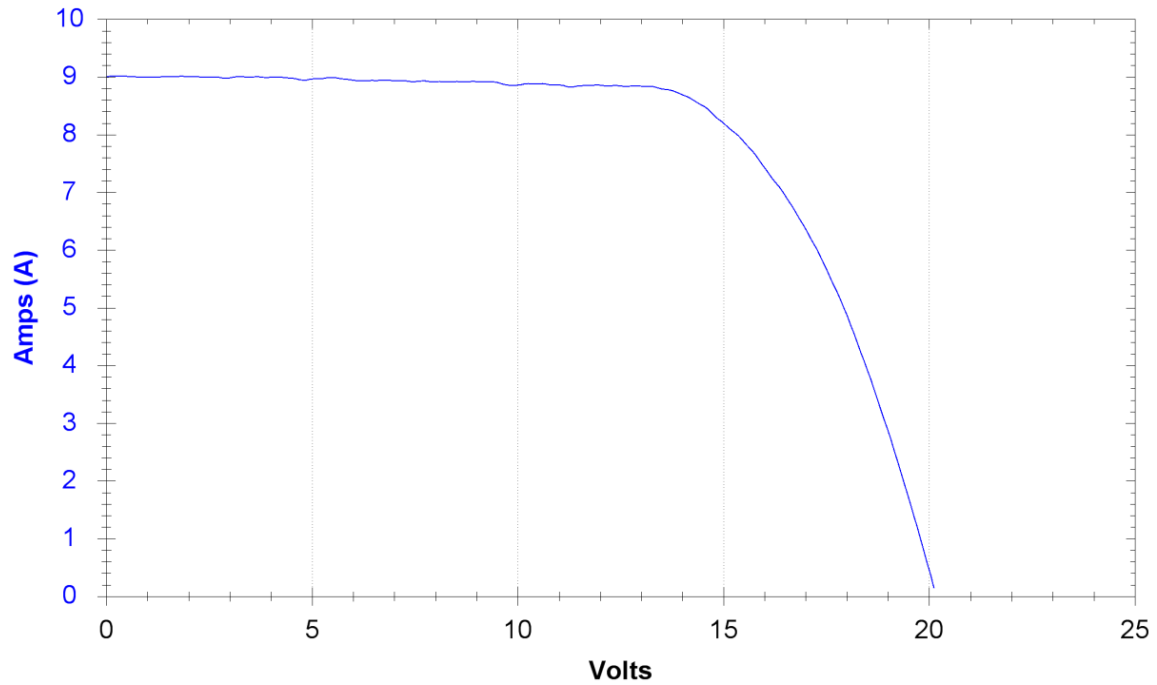


Figure B.5 I-V tracer results for two 60W PV modules at 1148 W/m², details in Table 4.5

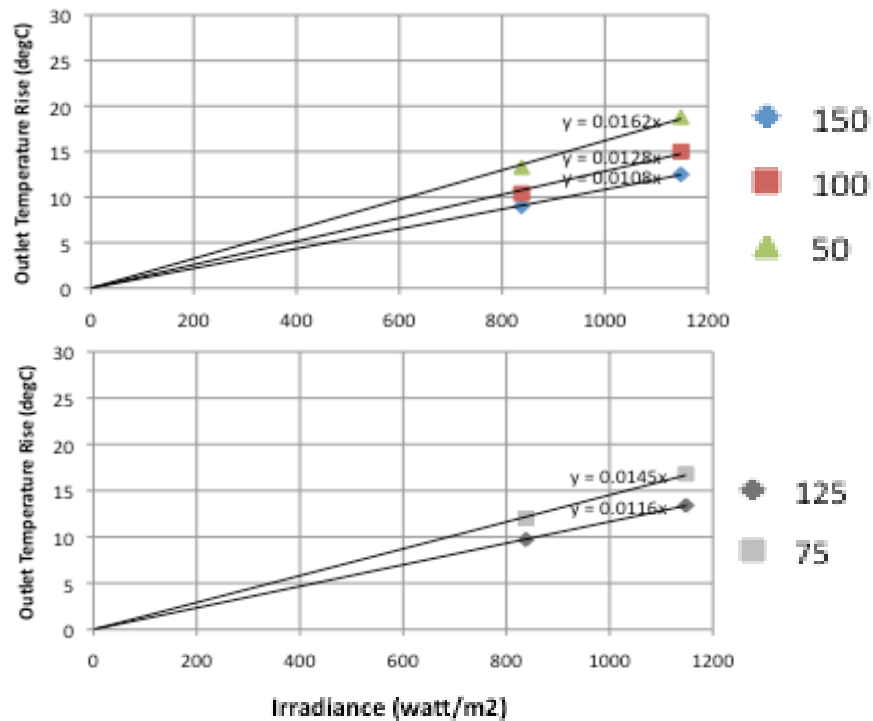


Figure B.6 Collector (B1: SWv) outlet temperature rise at 3.5m/s wind and under different solar irradiance and different mass flow rates; Linear relationship of collector outlet temperature rise with increasing Irradiance

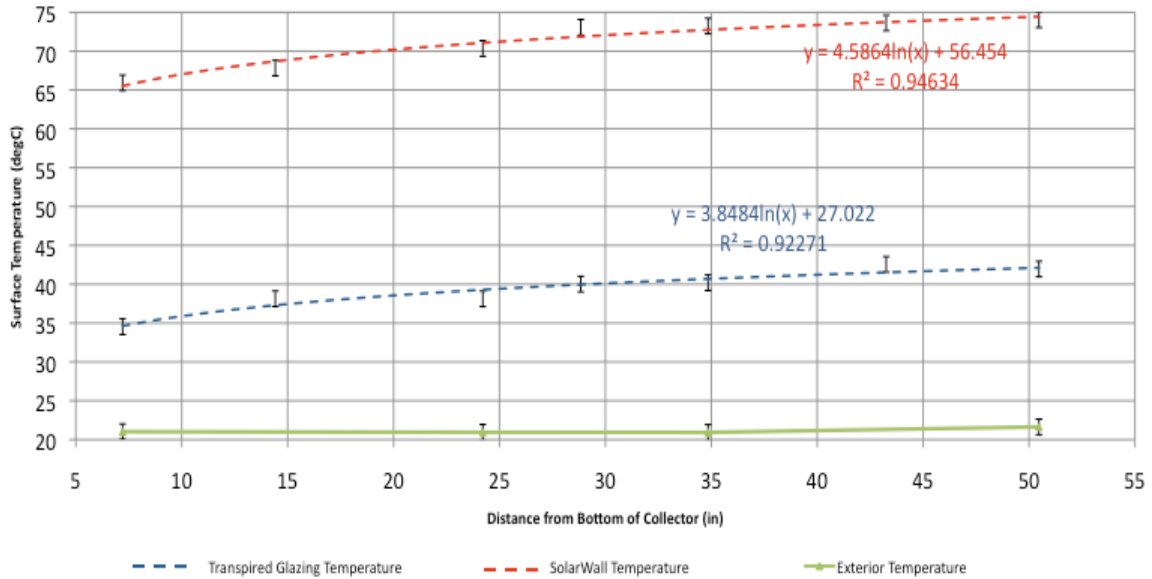


Figure B.7 Temperature readings across collector height (B2: SWv+TG) at 1148 W/m², 1m/s wind, and constant mass flow rate of 50kg/hr/m². Error bars of ±0.5°C; Exponential fit (dash lines) appropriate for temperature readings with increasing collector height

Experimental Results from Solar Simulator

Table B.2 Collector A1 (TG) Performance under Solar Simulator

A1-100W-HG			A1-25W-HG		
Flow Rate (kg/hr/m ²)	TG Efficiency @1148 HW	ΔT @1000 (degC)	Flow Rate (kg/hr/m ²)	TG Efficiency @1148 HW	ΔT @1000 (degC)
150.000	0.533	13.100	150	0.527549788	12.97615
125.000	0.512	15.100	125	0.524100569	15.46957143
100.000	0.482	17.800	100	0.502537267	18.541375
75.000	0.451	22.200	75	0.486126062	23.9145
50.000	0.348	25.700	50	0.417929193	30.83943182

A1-100W-LG			A1-25W-LG		
Flow Rate (kg/hr/m ²)	TG Efficiency @838 HW	ΔT @838(degC)	Flow Rate (kg/hr/m ²)	TG Efficiency @838 LW	ΔT @838 (degC)
150.000	0.515	10.300	150	0.504698687	10.1
125.000	0.491	11.800	125	0.49553749	11.9
100.000	0.456	13.700	100	0.479713604	14.4
75.000	0.422	16.900	75	0.464722554	18.6
50.000	0.331	19.900	50	0.401427009	24.1

Table B.3 Collector A2 (TG with fins) Performance under Solar Simulator

A2-100W-HG			A2-25W-HG N/A		
Flow Rate (kg/hr/m ²)	TG @1000 WITH fins	ΔT @1000 (degC)	Flow Rate (kg/hr/m ²)	TG @1000 WITH fins	ΔT @1000 (degC)
150.000	0.631	17.300	150	N/A	N/A
125.000	0.602	19.800	125	N/A	N/A
100.000	0.550	22.600	100	N/A	N/A
75.000	0.471	25.800	75	N/A	N/A
50.000	0.400	32.900	50	N/A	N/A

A2-100W-LG			A2-25W-LG		
Flow Rate (kg/hr/m ²)	TG with Fins @HW	ΔT @838 (degC)	Flow Rate (kg/hr/m ²)	TG with Fins @LW	ΔT @838 (degC)
150.000	0.645	12.900	150	0.645	12.9
125.000	0.591	14.200	125	0.620	14.9
100.000	0.550	16.500	100	0.573	17.2
75.000	0.472	18.900	75	0.517	20.7
50.000	0.395	23.700	50	0.456	27.4

Table B.4 Collector B1 (SWv) Performance under Solar Simulator

B1-100W-HG			B1-25W-HG		
Flow Rate (kg/hr/m ²)	Efficiency of SWv HW@1148	ΔT @1148 (degC)	Flow Rate (kg/hr/m ²)	Efficiency of SWv LW@1148	ΔT @1000 (degC)
150.000	0.459	12.581	150.000	0.588	16.133
125.000	0.418	13.753	125.000	0.561	18.449
100.000	0.370	15.228	100.000	0.502	20.636
75.000	0.307	16.832	75.000	0.447	24.513
50.000	0.227	18.672	50.000	0.350	28.780

B1-100W-LG			B1-25W-LG		
Flow Rate (kg/hr/m ²)	Efficiency of SWv HW@838	ΔT @840 (degC)	Flow Rate (kg/hr/m ²)	Efficiency of SWv LW@838	ΔT @838 (degC)
150.000	0.429	8.579	150.000	0.591	11.835
125.000	0.396	9.510	125.000	0.564	13.551
100.000	0.354	10.624	100.000	0.504	15.123
75.000	0.299	11.980	75.000	0.450	18.017
50.000	0.223	13.394	50.000	0.351	21.092

Table B.5 Collector B2 (SWv+TG) Performance under Solar Simulator

B2-100W-HG			B2-25W-HG		
Flow Rate (kg/hr/m ²)	Efficiency of SWv+TG HW@1148	Efficiency of SWv+TG HW@838	Flow Rate (kg/hr/m ²)	Efficiency of SWv+TG LW@1148	ΔT @1000 (degC)
150.000	0.693	18.995	150.000	0.732	20.071
125.000	0.659	21.683	125.000	0.695	22.850
100.000	0.622	25.567	100.000	0.642	26.401
75.000	0.570	31.241	75.000	0.600	32.924
50.000	0.485	39.927	50.000	0.529	43.545

B2-100W-LG			B2-25W-LG		
Flow Rate (kg/hr/m ²)	Efficiency of SWv+TG HW@838	ΔT @840 (degC)	Flow Rate (kg/hr/m ²)	Efficiency of SWv+TG LW@838	ΔT @840 (degC)
150.000	0.692	13.848	150.000	0.712	14.250
125.000	0.655	15.733	125.000	0.676	16.242
100.000	0.607	18.233	100.000	0.627	18.810
75.000	0.561	22.443	75.000	0.587	23.487
50.000	0.471	28.287	50.000	0.504	30.280

Table B.6 Collector B3 (SWv+G) Performance under Solar Simulator

B3-100W-HG			B3-25W-HG		
Flow Rate (kg/hr/m ²)	SWv+G @HW	ΔT @1148 HW (degC)	Flow Rate (kg/hr/m ²)	SWv+G @LW	ΔT @1148 LW (degC)
150.000	0.485	13.300	150	0.576	15.800
125.000	0.444	14.600	125	0.547	18.000
100.000	0.392	16.100	100	0.503	20.700
75.000	0.321	17.600	75	0.441	24.200
50.000	0.242	19.900	50	0.354	29.100

B3-100W-LG			B3-25W-LG		
Flow Rate (kg/hr/m ²)	SWv+G HW@840	ΔT @840 (degC)	Flow Rate (kg/hr/m ²)	SWv+G LW@840	ΔT @840 (degC)
150.000	0.455	9.100	150	0.580	11.6
125.000	0.421	10.100	125	0.541	13
100.000	0.370	11.100	100	0.480	14.4
75.000	0.307	12.300	75	0.447	17.9
50.000	0.232	13.900	50	0.360	21.6

Table B.7 Collector B4 (SWh) Performance under Solar Simulator

B4-100W-HG			B4-25W-HG		
Flow Rate (kg/hr/m ²)	SWh HW@1148	ΔT @1148 (degC)	Flow Rate (kg/hr/m ²)	SWh LW@1148	ΔT @1148 (degC)
150.000	0.451	12.356	150.000	0.629	17.248
125.000	0.394	12.954	125.000	0.580	19.090
100.000	0.342	14.058	100.000	0.514	21.142
75.000	0.283	15.506	75.000	0.452	24.792
50.000	0.215	17.657	50.000	0.362	29.785

B4-100W-LG			B4-25W-LG		
Flow Rate (kg/hr/m ²)	SWh HW@838	ΔT @838 (degC)	Flow Rate (kg/hr/m ²)	SWh LW@838	ΔT @838 (degC)
150.000	0.428	8.572	150.000	0.615	12.299
125.000	0.382	9.176	125.000	0.571	13.724
100.000	0.342	10.276	100.000	0.524	15.722
75.000	0.281	11.262	75.000	0.448	17.949
50.000	0.209	12.526	50.000	0.364	21.834

Table B.8 Collector B5 (SWh+TG) Performance under Solar Simulator

B5-100W-HG			B5-25W-HG		
Flow Rate (kg/hr/m ²)	SWh+TG HW@1000	ΔT @1000 (degC)	Flow Rate (kg/hr/m ²)	SWh+TG LW@1000	ΔT @1000 (degC)
150.000	0.694	19.021	150.000	0.671	18.401
125.000	0.672	22.094	125.000	0.649	21.335
100.000	0.631	25.963	100.000	0.620	25.486
75.000	0.563	30.845	75.000	0.587	32.207
50.000	0.469	38.609	50.000	0.509	41.890

B5-100W-LG			B5-25W-LG		
Flow Rate (kg/hr/m ²)	SWh HW@840	ΔT @840 (degC)	Flow Rate (kg/hr/m ²)	SWh LW@840	ΔT @840 (degC)
150.000	0.695	13.900	150.000	0.658	13.160
125.000	0.670	16.100	125.000	0.652	15.659
100.000	0.626	18.800	100.000	0.623	18.695
75.000	0.552	22.100	75.000	0.570	22.794
50.000	0.470	28.200	50.000	0.512	30.745

Table B.9 Collector B6 (SWh+G) Performance under Solar Simulator

B6-100W-HG			B6-25W-HG		
Flow Rate (kg/hr/m ²)	SWh+G @HW	ΔT @1148 (degC)	Flow Rate (kg/hr/m ²)	SWh+G @LW	ΔT @1148 (degC)
150.000	0.487	13.200	150	0.594	16.500
125.000	0.443	14.800	125	0.566	18.900
100.000	0.399	16.600	100	0.528	22.200
75.000	0.348	19.200	75	0.475	26.700
50.000	0.267	21.900	50	0.389	31.900

B6-100W-LG			B6-25W-LG		
Flow Rate (kg/hr/m ²)	SWh+G HW@838	ΔT @838 (degC)	Flow Rate (kg/hr/m ²)	SWh+G LW@838	ΔT @838 (degC)
150.000	0.465	9.300	150	0.585	11.7
125.000	0.433	10.400	125	0.554	13.3
100.000	0.380	11.400	100	0.526	15.8
75.000	0.330	13.200	75	0.460	18.4
50.000	0.258	15.500	50	0.385	23.1

Table B.10 Collector C1 (SWh+PV) Performance under Solar Simulator

C1-100W-HG			C1-25W-HG		
Flow Rate (kg/hr/m ²)	SWh+PV HW@1148	ΔT @1148 (degC)	Flow Rate (kg/hr/m ²)	SWh+PV LW@1148	ΔT @1148 (degC)
150.000	0.263	7.220	150.000	0.371	10.174
125.000	0.223	7.340	125.000	0.356	11.725
100.000	0.190	7.814	100.000	0.331	13.601
75.000	0.153	8.407	75.000	0.277	15.200
50.000	0.105	8.656	50.000	0.214	17.618

C1-100W-LG			C1-25W-LG		
Flow Rate (kg/hr/m ²)	SWh+PV HW@838	ΔT @838 (degC)	Flow Rate (kg/hr/m ²)	SWh+PV LW@838	ΔT @838 (degC)
150.000	0.256	5.114	150.000	0.380	7.603
125.000	0.220	5.283	125.000	0.355	8.521
100.000	0.186	5.578	100.000	0.328	9.849
75.000	0.150	6.017	75.000	0.282	11.278
50.000	0.099	5.950	50.000	0.211	12.659

Table B.11 Collector C2 (SWh+PV+TG) Performance under Solar Simulator

C2-100W-HG			C2-25W-HG		
Flow Rate (kg/hr/m ²)	SWh+PV+TG HW@1148	ΔT @1148 (degC)	Flow Rate (kg/hr/m ²)	SWh+PV+TG LW@1148	ΔT @1148 (degC)
150.000	0.463	12.681	150.000	0.486	13.332
125.000	0.426	14.016	125.000	0.454	14.946
100.000	0.385	15.840	100.000	0.429	17.648
75.000	0.331	18.161	75.000	0.416	22.782
50.000	0.269	22.140	50.000	0.354	29.082

C2-100W-LG			C2-25W-LG		
Flow Rate (kg/hr/m ²)	SWh+PV+TG HW@838	ΔT @838 (degC)	Flow Rate (kg/hr/m ²)	SWh+PV+TG LW@838	ΔT @838 (degC)
150.000	0.439	8.786	150.000	0.449	8.988
125.000	0.412	9.895	125.000	0.441	10.592
100.000	0.372	11.165	100.000	0.423	12.703
75.000	0.325	13.011	75.000	0.394	15.760
50.000	0.250	15.014	50.000	0.328	19.711

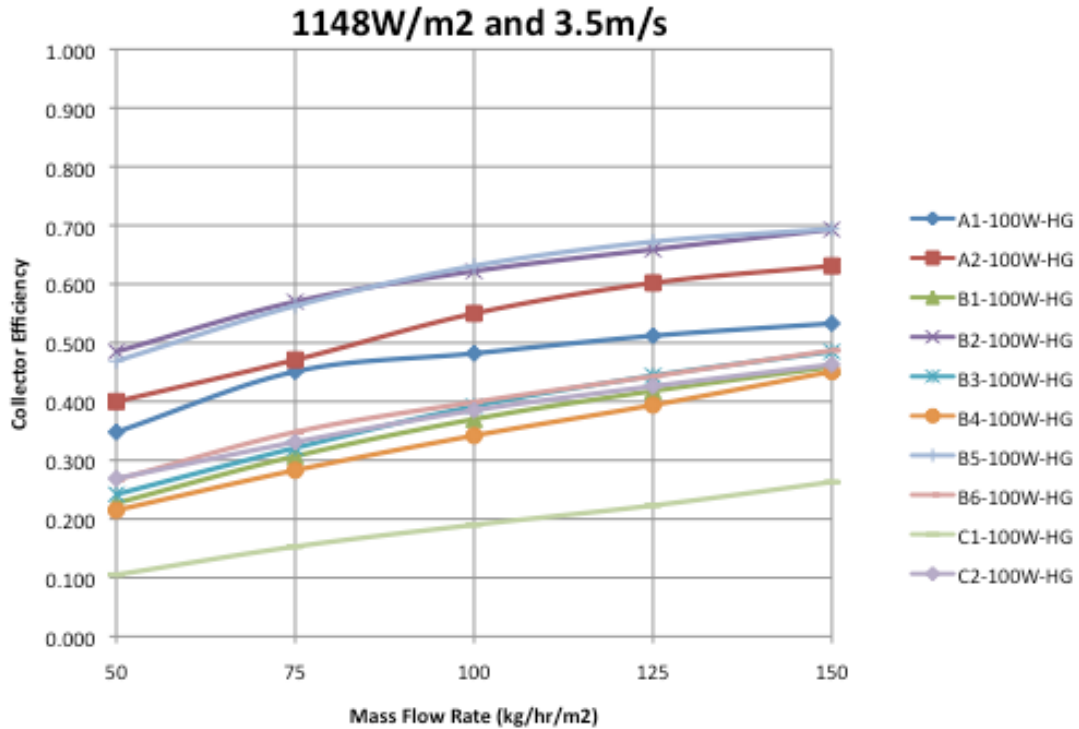


Figure B.8 All Collectors Performance at 1148W/m² irradiance, 3.5m/s air velocity parallel to collector surface

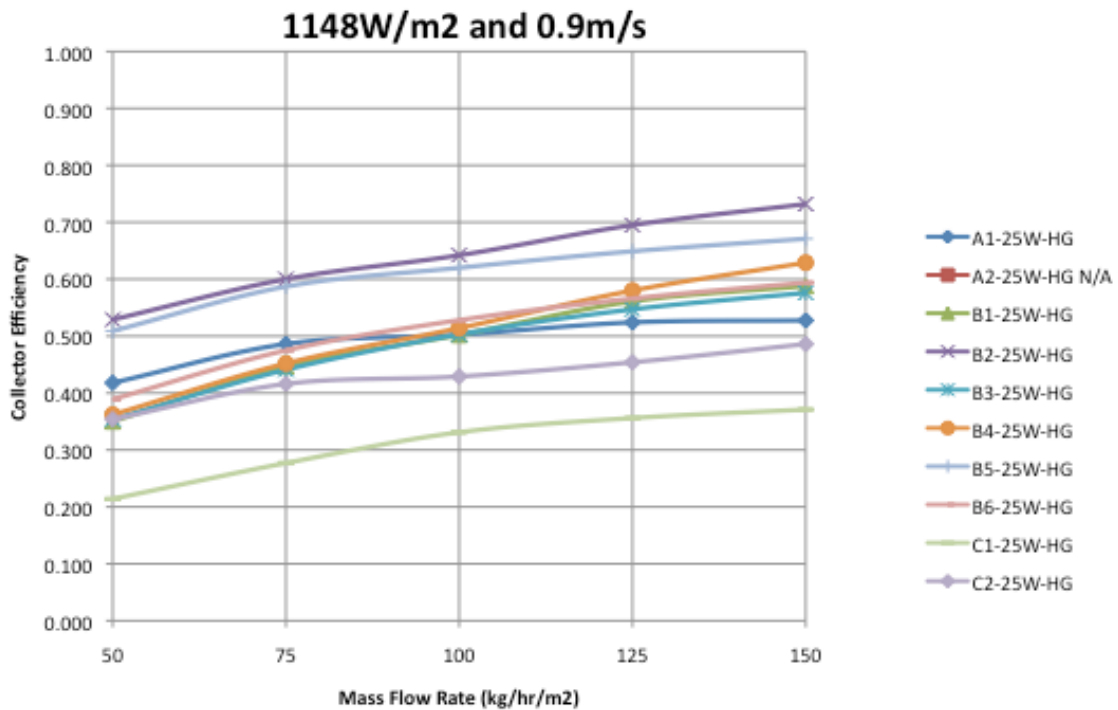


Figure B.9 All Collectors Performance at 1148W/m² irradiance, 0.9m/s air velocity parallel to collector surface

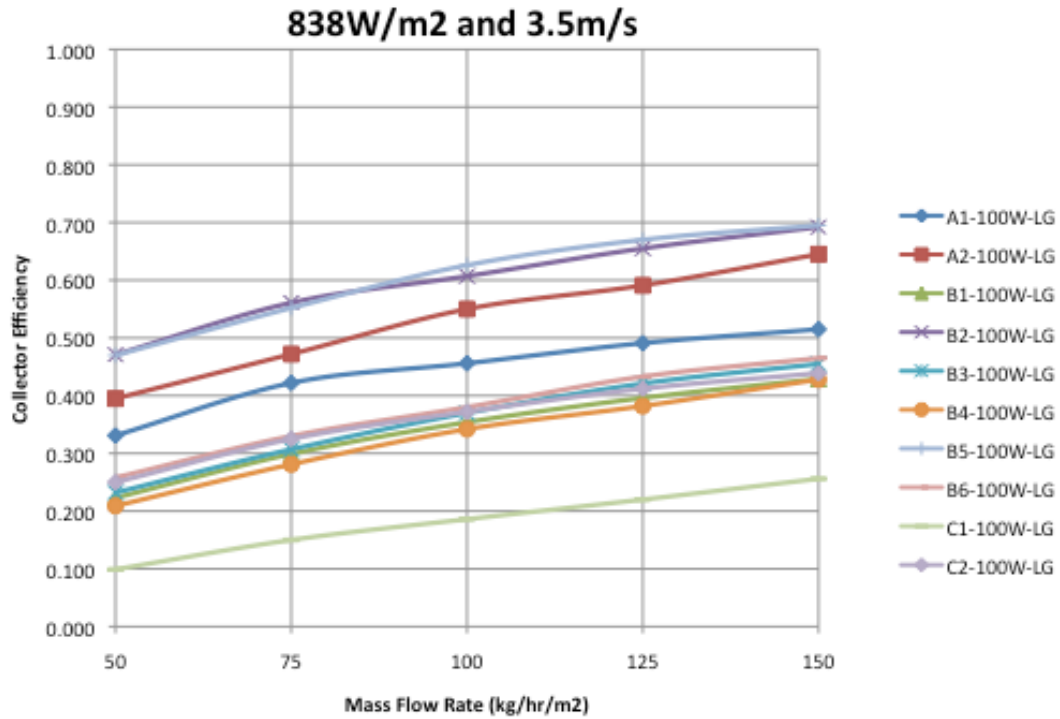


Figure B.10 All Collectors Performance at 838W/m² irradiance, 3.5m/s air velocity parallel to collector surface

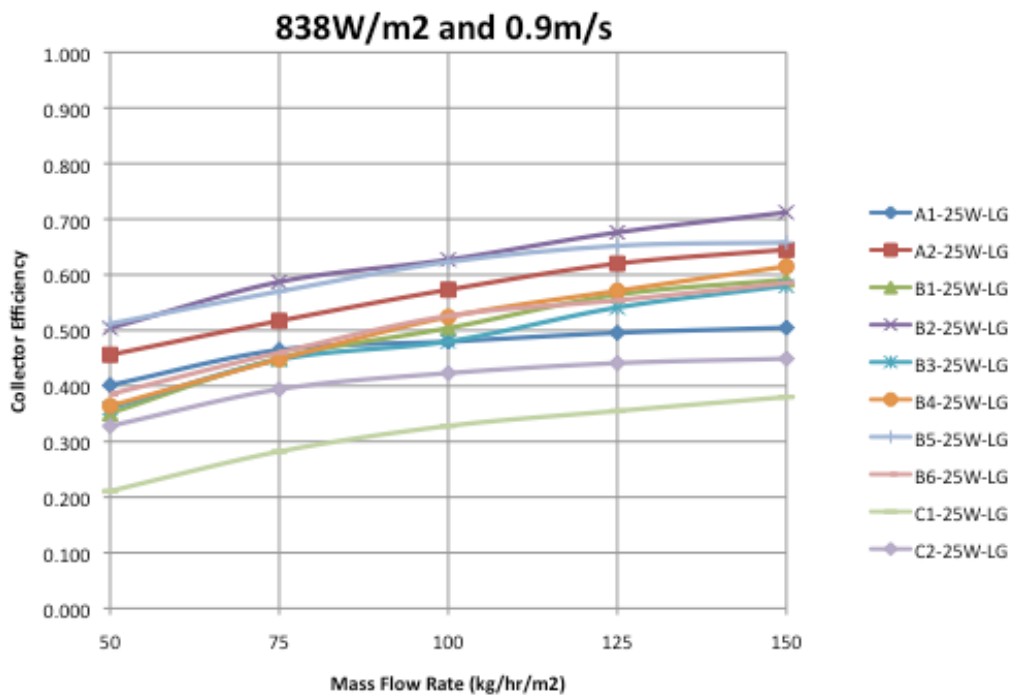


Figure B.11 All Collectors Performance at 838W/m² irradiance, 0.9m/s air velocity parallel to collector surface

Collector Performance: Experimental Results from Environmental Chamber

Table B.12 Collector B4 (SWh) and B5 (SWh+TG) Performance at Environmental Chamber, no wind, irradiance 824 W/m² (Raw data, uncorrected)

B4: SWh			B5: SWh+TG		
Flow Rate (kg/hr/m ²)	Efficiency SWh, No wind at 824	ΔT @824 no wind (degC)	Flow Rate (kg/hr/m ²)	Efficiency SWh+TG, No wind at 824	ΔT @824 no wind (degC)
50.000	0.492	29.034	50.000	0.616	36.369
75.000	0.613	24.113	75.000	0.738	29.030
100.000	0.662	19.534	100.000	0.750	22.523
125.000	0.673	15.896	125.000	0.787	18.580
150.000	0.778	15.309	150.000	0.772	15.198

Table B.13 Collector C1 (SWh+PV) and C2 (SWh+PV+TG) Performance at Environmental Chamber, no wind, irradiance 824 W/m² (Raw data, uncorrected)

C1: SWh+PV			C2: SWh+PV+TG		
Flow Rate (kg/hr/m ²)	Efficiency SWh+PV, No wind at 824	ΔT @824 no wind (degC)	Flow Rate (kg/hr/m ²)	Efficiency SWh+PV+TG, No wind at 824	ΔT @824 no wind (degC)
50.000	0.350	20.645	50.000	0.450	26.539
75.000	0.434	17.090	75.000	0.513	20.199
100.000	0.498	14.706	100.000	0.555	16.396
125.000	0.497	11.738	125.000	0.575	13.575
150.000	0.499	9.820	25.000	0.297	35.116

Table B.14 Duct leakage Testing Data using a calibrated fan

Duct internal pressure (Pa)	Mass flow rate by the calibrated fan (kg/hr)	Read Pressure loss at fan (in H ₂ O)	Corresponding flow loss from Chart (cfm)	Mass flow loss from leakage test (kg/hr)	Percentage of Mass flow loss (%)
40.35	55.3	0.2	2.9	5.94	10.7
18.93	42.2	0.15	2.2	4.5	10.7
72.24	64.5	0.24	3.3	7.15	11.1
91.42	77.8	0.28	4	8.19	10.5
2.5	34	0.12	1.8	3.7	10.9

Table B.14 (continued) Duct leakage Testing Data using a calibrated fan

Actual Mass Flow Rates used in experiments (kg/hr/m ²)	Mass Flow Loss Extrapolated (linear)	Extrapolated Percentage of Mass Flow Loss (linear)	Extrapolated Mass Flow Loss (exponential)	Extrapolated Percentage of Mass Flow Loss (exponential)
50	5.4285	10.9	5.705175135	11.4
75	8.111	10.8	8.002297158	10.7
100	10.7935	10.8	9.632131172	9.6
125	13.476	10.8	10.89632865	8.7
150	16.1585	10.8	11.9292532	8.0

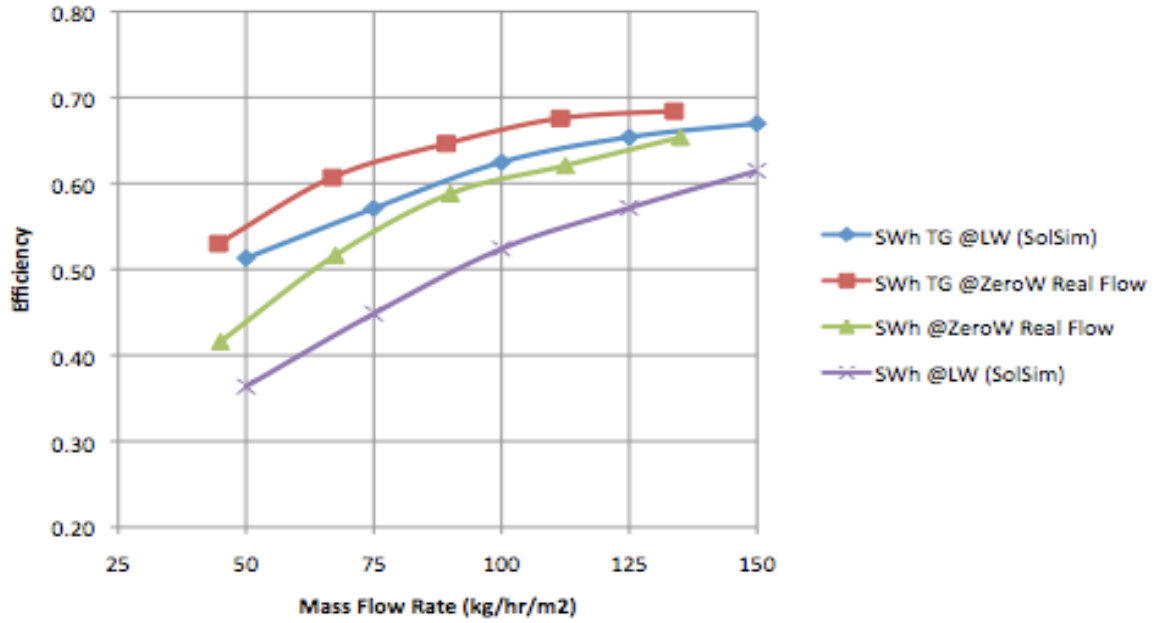


Figure B.12 Duct Air Leakage Correction Results for Collector B4 (SWh) and B5 (SWh+TG)

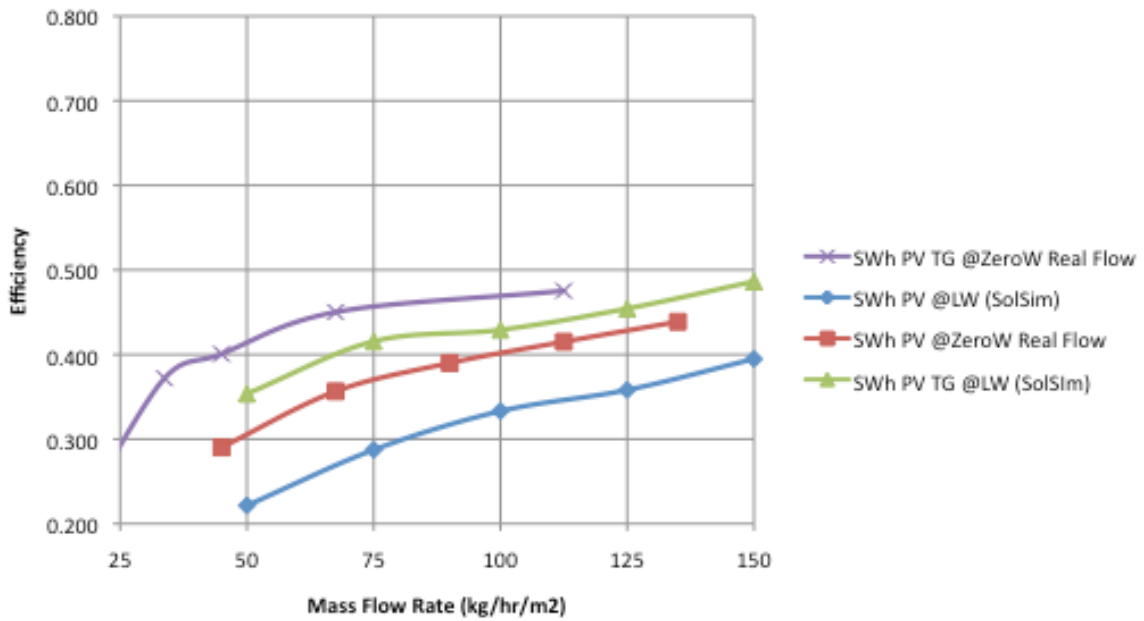


Figure B.13 Duct Air Leakage Correction Results for Collector C1 (SWh+PV) and C2 (SWh+PV+TG)

Appendix C. Uncertainty Analysis

Table C.1 Example values of the measured variables used in this uncertainty analysis

Measured Value	Measured Value	Variable	Measured Value
T_{amb}	20°C	T_{outlet}	35°C
Length and Width	1465mm	MFR	150 kg/hr/m ²
ρ_{air} air density	1.14 kg/m ³	Q_U Useful Heat	600W

Below are examples of uncertainty analysis for all calculated variables.

C.1 Uncertainty of collector outlet temperature rise: $\Delta T = (T_{outlet} - T_{amb})$

Firstly, since collector outlet temperature is the average of two thermocouples at the duct outlet of $\pm 0.5^\circ\text{C}$:

$$\delta T_{outlet} = \pm \sqrt{0.5^2 + 0.5^2} = 0.707$$

The ambient temperature is taken as the average value of four thermocouples mounted above the collector surface:

$$\delta T_{amb} = \pm \sqrt{0.5^2 + 0.5^2 + 0.5^2 + 0.5^2} = 1$$

Therefore, the uncertainty of collector outlet temperature rise is given by:

$$\frac{\delta \Delta T}{\Delta T} = \pm \sqrt{\left(\frac{\delta T_{outlet}}{T_{outlet}}\right)^2 + \left(\frac{\delta T_{amb}}{T_{amb}}\right)^2} = \pm \sqrt{\left(\frac{0.707}{35}\right)^2 + \left(\frac{1}{20}\right)^2} = \pm 0.01865$$

$$\delta \Delta T = 0.01865 \cdot 15(^{\circ}\text{C}) = 1.224^{\circ}\text{C}$$

C.2 Uncertainty of Irradiance: I

From calibration certificate of CMP 21 manufactured by Kipps and Zonen, uncertainty is given by the World Radiation Center in Davos as $\pm 0.11/8.75=1.26\%$ from temperature -50°C to 20°C

C.3 Uncertainty of Collector Area: $A=L*W$

$$\frac{\delta A}{A} = \pm \sqrt{\left(\frac{\delta L}{L}\right)^2 + \left(\frac{\delta W}{W}\right)^2} = \pm \sqrt{\left(\frac{1}{1465}\right)^2 + \left(\frac{1}{1465}\right)^2} = \pm 0.00965$$

$$\delta A = 0.00965 \cdot (1465 \times 1465)(\text{mm}^2) = 2071\text{mm}^2$$

C.4 Uncertainty of Mass Flow Rate: MFR

The overall mass flow rate measured in the air duct is calculated by ISO5167 standard using the general equation for mass flow rate:

$$Q_M = MFR \cdot A = \frac{C}{\sqrt{1-\beta^2}} \cdot \frac{\pi}{4} \cdot d \cdot \sqrt{2 \cdot \Delta P \cdot \rho_{air}}$$

where β is the diameter ratio and C is the discharge coefficient as a function of β ; without getting into details about β and d (which are geometric values with very small uncertainty), the terms inside the square root will dominate the uncertainty of Q_M .

Therefore, the uncertainty of MFR can be calculated by:

$$\frac{\delta Q_M}{Q_M} = \pm \frac{1}{2} \sqrt{\left(\frac{\delta \Delta P}{\Delta P}\right)^2 + \left(\frac{\delta \rho_{air}}{\rho_{air}}\right)^2} = \pm \sqrt{(0.07)^2 + (0.006)^2} = \pm 0.03513$$

$$\frac{\delta MFR}{MFR} = \pm \sqrt{\left(\frac{\delta Q_M}{Q_M}\right)^2 + \left(-\frac{\delta A}{A}\right)^2} = \pm \sqrt{(0.03513)^2 + (0.006)^2} = \pm 0.03514$$

$$\delta MFR = 0.03514 \cdot (150)(kg / hr / m^2) = 5.271 kg / hr / m^2$$

C.5 Uncertainty of useful heat captured: Qu

The useful heat captured by the solar heated air is calculated as:

$$Q_U = (MFR \cdot A) \cdot c_p \cdot \Delta T$$

Since c_p is constant, the uncertainty of Q_U is calculated by:

$$\frac{\delta Q_U}{Q_U} = \pm \sqrt{\left(\frac{\delta Q_M}{Q_M}\right)^2 + \left(-\frac{\delta \Delta T}{\Delta T}\right)^2} = \pm \sqrt{(0.03513)^2 + (0.01865)^2} = \pm 0.08889$$

$$\delta Q_U = 0.08889 \cdot (600)(W) = 53.33W$$

C.6 Uncertainty of efficiency: $\eta = Q_U / (I \cdot A)$

$$\frac{\delta \eta}{\eta} = \pm \sqrt{\left(\frac{\delta Q_U}{Q_U}\right)^2 + \left(-\frac{\delta I}{I}\right)^2 + \left(-\frac{\delta A}{A}\right)^2} = \pm \sqrt{(0.08889)^2 + (-0.0126)^2 + (-0.00965)^2} = \pm 0.0911$$

Appendix D. Steady-State Simulation and Results

D.1 Sample MathCAD output for Simple PV/T model at steady-state

Steady-State PVT model

Given constants:

$$\begin{aligned} L &:= 0.05\text{m} & w &:= 1.46\text{m} & h &:= 0.36\text{m} & v &:= 0.1051 \frac{\text{m}}{\text{s}} & \text{degC} &:= 1 \\ V_w &:= 0.86 \frac{\text{m}}{\text{s}} \dots \text{Wind speed} & \text{hour} &:= 3600\text{s} \end{aligned}$$

Temperature corrected air properties (based on 20degC):

$T_{\text{air}} := 34.8\text{degC}$.. Assumed temperature in the air cavity

$$\rho := 1.2 \frac{\text{kg}}{\text{m}^3} \cdot \frac{293.15}{T_{\text{air}} + 273.15} \quad \dots \text{Density of air}$$

$$c_p := 1000 \frac{\text{J}}{\text{kg}\cdot\text{K}} \quad \dots \text{Specific heat of air (assume constant)}$$

$$\mu := \left(15.11 \cdot 10^{-6} \cdot \frac{\text{m}^2}{\text{s}} \cdot \rho \right) \cdot \frac{(293.15 + 120)}{(T_{\text{air}} + 273.15 + 120)} \cdot \left(\frac{293.15}{T_{\text{air}} + 273.15} \right)^{1.5} \quad \dots \text{Dynamic viscosity of air}$$

$$k := \left[0.0243 + (0.0257 - 0.0243) \cdot \frac{(T_{\text{air}})}{20\text{degC}} \right] \frac{\text{watt}}{\text{m}\cdot\text{K}} \quad \dots \text{Thermal conductivity of air (assume linearly varying between 0degC to 20degC)}$$

$$Re := \frac{\rho \cdot v \cdot 2L}{\mu} = 775.727 \quad \dots \text{Reynolds number}$$

$y := 0, 0.05, \dots, 0.35$.. Distance from inlet

$$H(y) := \frac{y \cdot \text{m}}{L} \quad \dots \text{Dimensionless channel height}$$

Find convective heat transfer coefficient hc (Liao and Athienitis, 200?):

On the PV side ($hc1$), Nusselt number is:

$$Nu1(y) := (0.011 \cdot Re + 62.856) \cdot e^{-0.475 \cdot H(y)} + 2.766 \cdot 10^{-3} \cdot Re + 5.58$$

$$hc1(y) := \frac{Nu1(y) \cdot k}{L}$$

On the insulation side ($hc2$), Nusselt number is:

$$Nu2(y) := (0.109 \cdot Re - 124.344) \cdot e^{(-1.635 \cdot 10^{-5} \cdot Re - 0.593) \cdot H(y)} + 4.098 \cdot 10^{-3} \cdot Re + 3.896$$

$$hc2(y) := \frac{Nu2(y) \cdot k}{L}$$

At half of the plate height:

$$hc1(0.3) = 6.339 \cdot \frac{\text{watt}}{\text{m}^2\text{K}} \quad hc2(0.3) = 3.221 \cdot \frac{\text{watt}}{\text{m}^2\text{K}}$$

Average hc on both sides of the plate:

$$hc1_{avg} := \frac{hc1(0) + hc1(0.05) + hc1(0.1) + hc1(0.15) + hc1(0.2) + hc1(0.25) + hc1(0.3) + hc1(0.35)}{8} =$$

$$hc2_{avg} := \frac{hc2(0) + hc2(0.05) + hc2(0.1) + hc2(0.15) + hc2(0.2) + hc2(0.25) + hc2(0.3) + hc2(0.35)}{8} =$$

Properties of the PV:

$$\epsilon_{pv} := 0.9 \quad \epsilon_{pv_b} := 0.8 \quad \text{.. Emissivity of PV (front and back)}$$

$$\alpha_{pv} := 0.925 \quad \text{.. Absorptance of PV}$$

Assume PV thermal resistance negligible: no Rpv

PVT

$$T_o := 22.141K + 273.15K \quad T_r := 293.15K \quad \text{Unit area: } \underline{\underline{A}} := 1m^2$$

$$hw := \left(14.5 \cdot V_w \cdot \frac{s}{m} + 6.603 \right) \frac{\text{watt}}{m^2 \cdot K} \quad \text{.. Experimental Wind loss}$$

$$h_o := 5.771 \frac{\text{watt}}{m^2 \cdot K} + hw \quad \text{.. Outdoor film coefficient} \quad U_o := h_o \cdot A$$

$$\sigma := 5.67 \cdot 10^{-8} \frac{\text{watt}}{m^2 \cdot K^4} \quad \text{.. Stephan Boltzman constant}$$

$$Spv := 838 \frac{\text{watt}}{m^2}$$

$$\epsilon_{wall} := 0.9 \quad \text{.. emissivity of the wall}$$

$$U_{ins} := \frac{A}{1.32} \frac{\text{watt}}{m^2 \cdot K} + 0.12 \frac{\text{watt}}{K} \quad \text{.. Insulation RSI1.32}$$

$$\text{Time step: } p := 0, 1 \dots 100$$

Assume air mass flow rate here:

$$M_{air} := v \cdot \left(\frac{L}{h} \right) \cdot \rho = 60.029 \cdot \frac{\text{kg}}{\text{hour} \cdot m^2}$$

Initial Conditions:

$$\begin{pmatrix} T_{pv_0} \\ T_{b_0} \\ T_{ma_0} \\ Qu_0 \\ \underline{\underline{hr}}_0 \\ \underline{\underline{F}}_0 \\ FR_0 \\ \eta_{pv_0} \\ T_{out_0} \\ \underline{\underline{T}}_{air} \end{pmatrix} := \begin{pmatrix} 290K \\ 290K \\ 290K \\ 100\text{watt} \\ 1 \frac{\text{watt}}{m^2 \cdot K} \\ 0.2 \\ 0.2 \\ 0.15 \\ 290K \\ 290K \end{pmatrix}$$

Assume inlet temp is same with outdoor air temp:

$$T_{in} := T_o$$

$$U_a(y) := A \cdot hc1(y) \quad U_b(y) := A \cdot hc2(y)$$

$$uL := h_o + \frac{U_{ins}}{A} = 25.722 \cdot \frac{\text{watt}}{\text{m}^2 \text{K}}$$

$$U_a(0.06) = 25.719 \frac{\text{m}^2 \cdot \text{kg}}{\text{K} \cdot \text{s}^3}$$

Energy balance at each node:

$$\begin{pmatrix} T_{pv_{p+1}} \\ T_{b_{p+1}} \\ T_{ma_{p+1}} \\ Q_{u_{p+1}} \\ h_{r_{p+1}} \\ F_{p+1} \\ FR_{p+1} \\ T_{out_{p+1}} \\ T_{air_{p+1}} \end{pmatrix} := \left[\frac{\alpha_{pv} \cdot Spv \cdot A - \eta_{pv} \cdot \alpha_{pv} \cdot Spv \cdot A + h_o \cdot A \cdot T_o + h_r \cdot A \cdot T_{b_p} + hc1_{avg} \cdot A \cdot T_{ma_p}}{h_o \cdot A + h_r \cdot A + hc1_{avg} \cdot A} \right. \\ \left. \frac{U_{ins} \cdot (Tr) + hc2_{avg} \cdot A \cdot (T_{ma_p}) + h_r \cdot A \cdot (T_{pv_p})}{U_{ins} + hc2_{avg} \cdot A + h_r \cdot A} \right. \\ \left. \frac{hc1_{avg} \cdot A \cdot (T_{pv_p}) + hc2_{avg} \cdot A \cdot (T_{b_p}) - Q_{u_p}}{hc1_{avg} \cdot A + hc2_{avg} \cdot A} \right. \\ \left. FR_p \cdot A \cdot \left[\alpha_{pv} \cdot Spv - uL (T_{air_p} - T_o) \right] \right. \\ \left. \frac{4 \cdot \sigma \cdot \left[\left(\frac{T_{pv_p} + T_{b_p}}{2} \right)^3 \right]}{\left(\frac{1}{\epsilon_{pv_b}} + \frac{1}{\epsilon_{wall}} - 1 \right)} \right. \\ \left. \frac{1}{1 + \frac{uL}{hc1_{avg} + \frac{1}{\frac{1}{hc2_{avg}} + \frac{1}{hr_p}}}} \right. \\ \left. Mair \cdot A \cdot \frac{c_p}{A \cdot uL} \left(1 - e^{\frac{-A \cdot uL \cdot F_p}{Mair \cdot A \cdot c_p}} \right) \right. \\ \left. \frac{(T_{pv_p} - T_{air_p}) hc1_{avg} + (T_{b_p} - T_{air_p}) hc2_{avg}}{Mair \cdot c_p} + T_{in} \right. \\ \left. \frac{T_{in} + T_{out_p}}{2} \right]$$

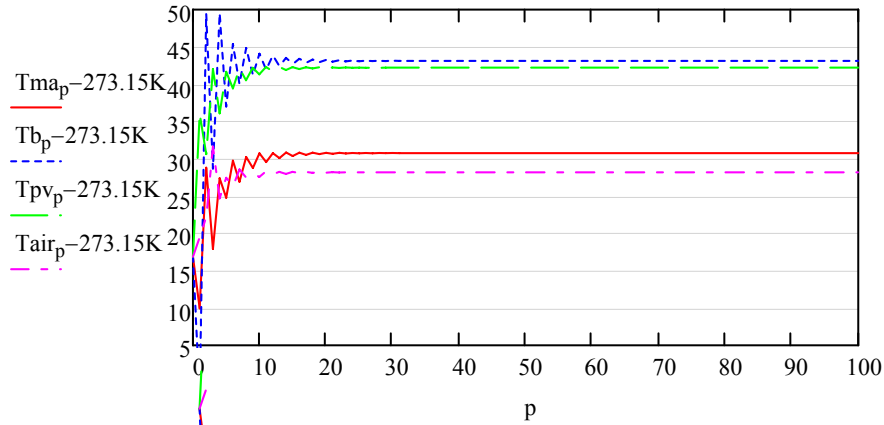


Figure D.1 Results of finite element analysis after all results converge

$$T_{\text{airstream}_0} := \frac{T_{\text{air}_{60}} - 273.15\text{K}}{\text{K}} = 28.163 \cdot \text{degC} \quad \text{.. Changes the original Tair to re-evaluate air properties in the cavity until the two value converges.}$$

$$T_{\text{outlet}_0} := T_{\text{out}_{60}} - 273.15\text{K} = 34.186 \text{ K}$$

$$T_{\text{midair}_0} := T_{\text{ma}_{60}} - 273.15\text{K} = 30.741 \text{ K}$$

$$T_{\text{surf pv}_0} := T_{\text{pv}_{60}} - 273.15\text{K} = 42.196 \text{ K}$$

$$T_{\text{back}_0} := T_{\text{b}_{60}} - 273.15\text{K} = 43.103 \text{ K}$$

$$Q_{U_0} := Q_{u_{60}} = 163.609 \text{ W} \quad \text{... e.g. after 60 iterations the calculated values are constant}$$

$$Q_{u_pv} := M_{\text{air}} \cdot (T_{\text{out}_{60}} - T_o) c_p = 200.843 \frac{1}{\text{m}} \cdot \text{watt}$$

$$\eta_{\text{pv_th}} := \frac{Q_{u_pv}}{S_{\text{pv}}} = 0.24$$

D.2 MATLAB/Simulink interface for SW and SW+TG models:

The thermal network models of SW and SW+TG discussed in Section 5.1 are configured in the MATLAB/Simulink platform. Figure D.2 shows the primary interface of steady state simulations matching the conditions of the Solar simulator experiments. Note that each blue block is an independent model at one specific flow rate and under a set of environmental conditions.

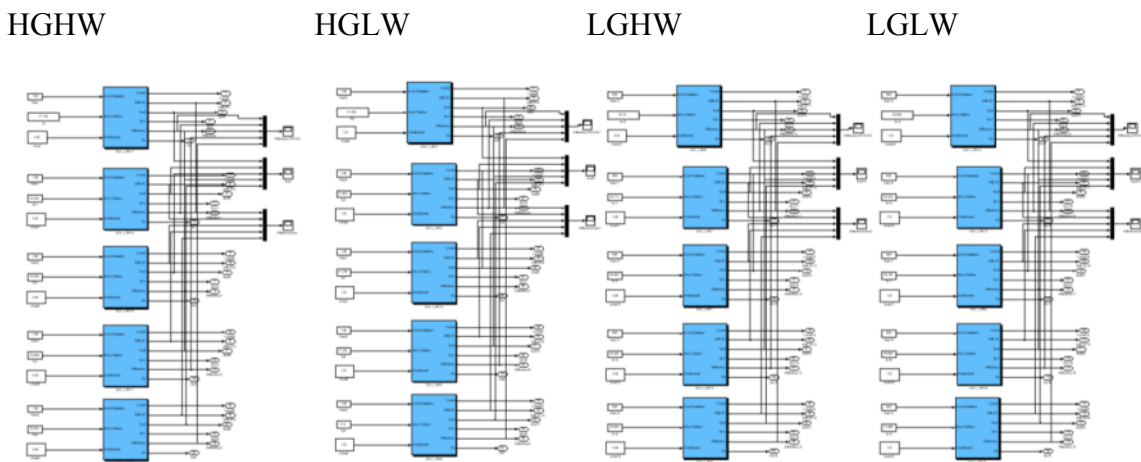


Figure D.2 Level-1 Block diagram of SW or SW+TG models: climatic loads matching 4 sets of experimental tests (HGHW, HGLW, LGHW, LGLW) at five mass flow rates; e.g. Each blue block contains one flow rate at one set of environmental conditions.

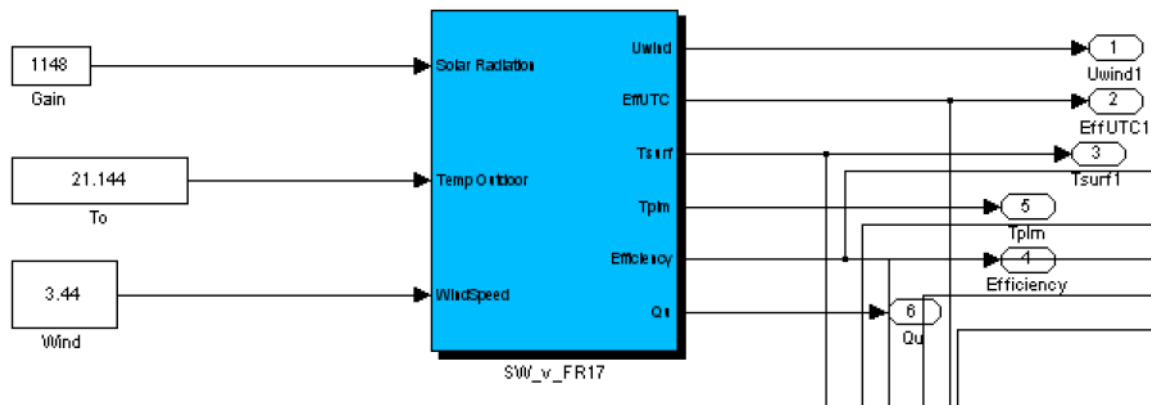


Figure D.3 Close up section of one SW or SW+TG model, showing input and output variables for one flow rate and one set of environmental conditions.

Discrete inputs include steady state environmental conditions such as ambient temperature, irradiance and wind speed; Output variables include convective wind loss coefficient, collector effectiveness, surface temperature, outlet temperature, collector efficiency, and useful heat captured (Figure D.3).

Figure D.4 shows the logic inside each blue block, three modular components are calculated simultaneously and some outputs are looped back into the following time step.

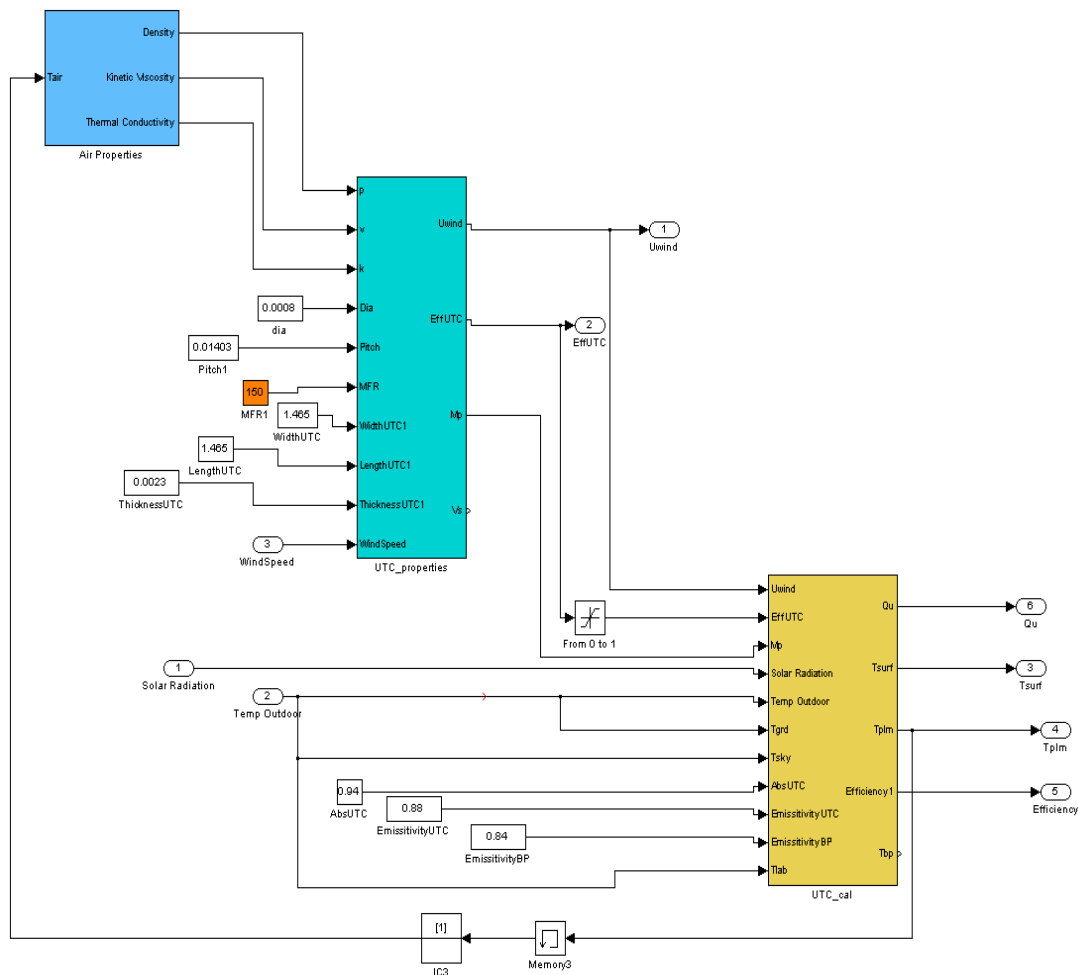


Figure D.4 Thermal network Model detail (inside each blue block): Complete View

Figure D.5, D.6 and D.7 expand the details inside the three blocks illustrated in Figure D.4. The “Air Properties” Block outputs all the necessary air properties (Figure D.5). The D.6 “UTC Properties” block computes important variables such as collector effectiveness and convective wind loss coefficient, leading up to main calculation block of “UTC cal” in Figure D.7.

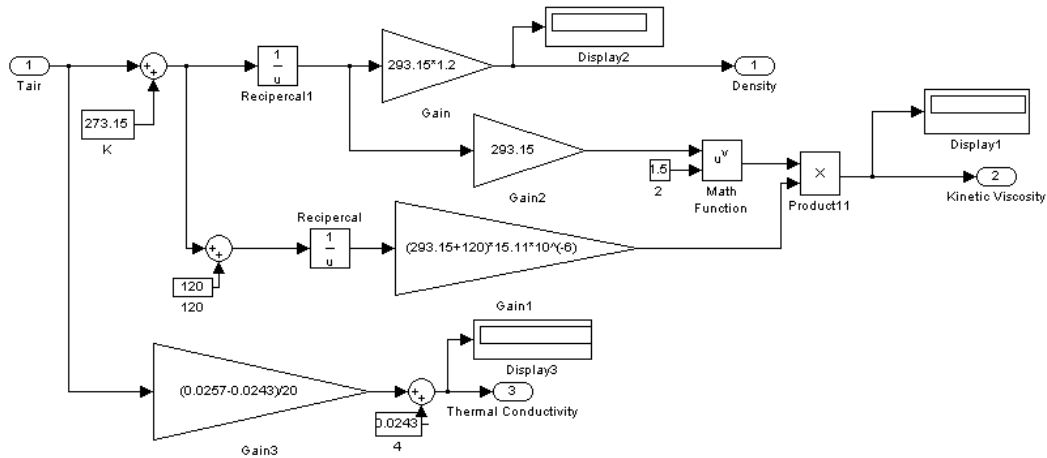


Figure D.5 Details of the “Air Properties” Block for appropriate air properties

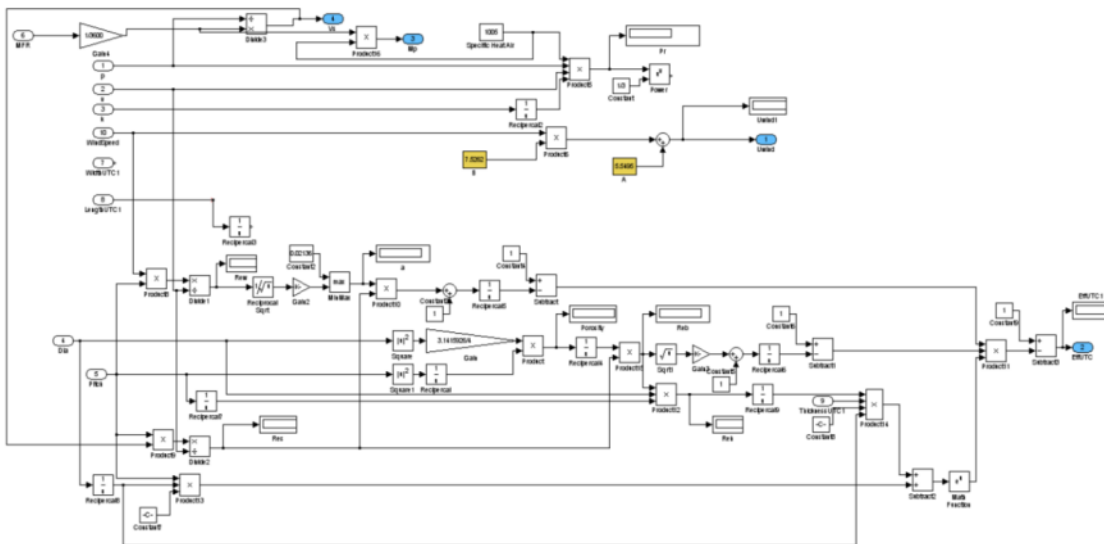


Figure D.6 Details of the “UTC Properties” block: preparation block for performance calculation of a transpired collector (SW or SW+TG);

collector, especially at low wind conditions (Figure D.9). Additionally, the slope and intercept of the linear approximation is dissimilar between low and high wind conditions, resulting in difficulty to fit a universal approximation that works for all MFR and at all wind speeds between 0.9m/s to 3.5m/s. In conclusion, the approximation method presented in equation 5.11 (Section 5.4.4) is used for final simulation.

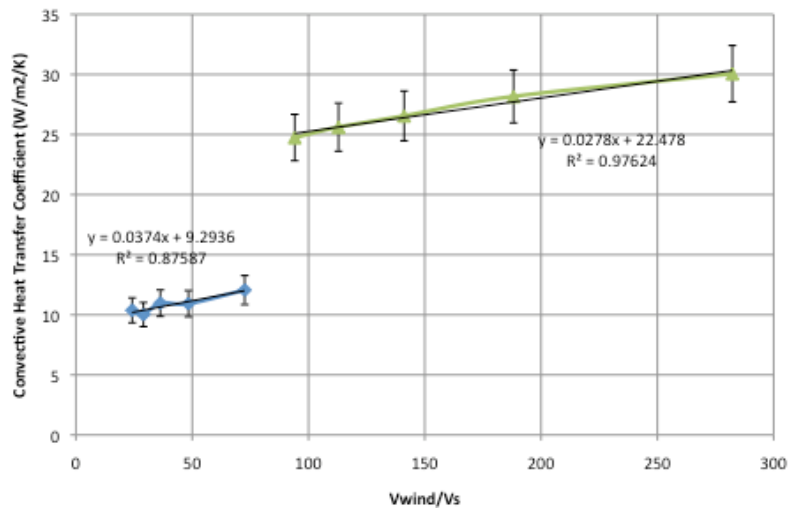


Figure D.8 Convective heat loss coefficients in relation with V_{wind}/V_s ratio, for Collector B4 (SWv)

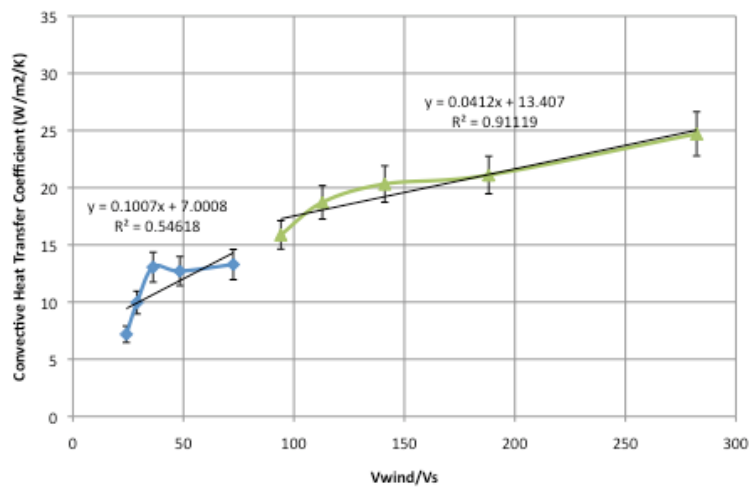
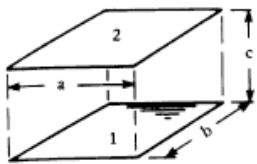


Figure D.9 Convective heat loss coefficients in relation with V_{wind}/V_s ratio, for collector B5 (SW+TG)

**D.4 Test Results from Environmental Chamber compared to Solar Simulator:
Radiant Gain Correction**

Table D.1 View Factor for two parallel finite surfaces

Configuration	Equation
1. 	Let $X = a/c$ and $Y = b/c$. Then: $F_{1-2} = \frac{2}{\pi XY} \left\{ \ln \left[\frac{(1 + X^2)(1 + Y^2)}{1 + X^2 + Y^2} \right]^{1/2} - X \tan^{-1} X - Y \tan^{-1} Y + X\sqrt{1 + Y^2} \tan^{-1} \frac{X}{\sqrt{1 + Y^2}} + Y\sqrt{1 + X^2} \tan^{-1} \frac{Y}{\sqrt{1 + X^2}} \right\}$

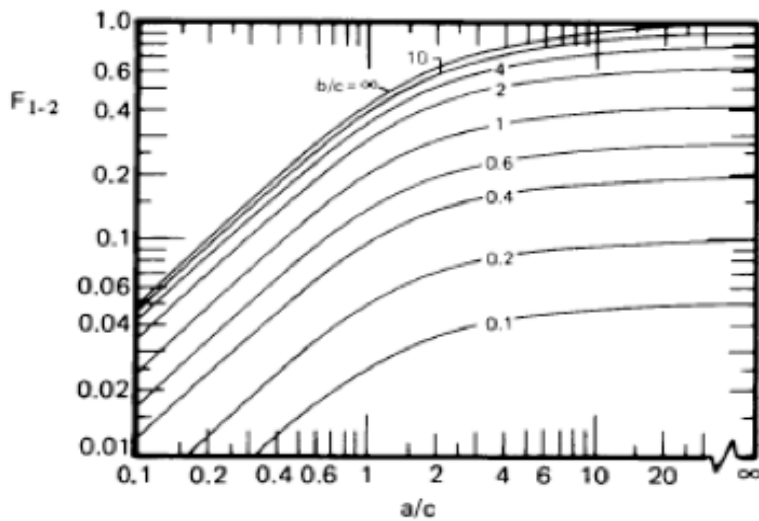


Figure D.10 View Factor for two parallel finite surfaces

For geometry of the collector surface and the chamber façade, $a=b=1.5\text{m}$, $c=0.77\text{m}$. Calculated from Table D.1 and Figure D.10, the view factor from Chamber façade to collector surface ($F_{\text{façade-surface}}$) equals to 0.5.

To supplement the radiant gain results for collectors B4 and B5 in Section 5.4.2, radiant gain correction for the performance of C1 and C2 are shown in Figure D.11.

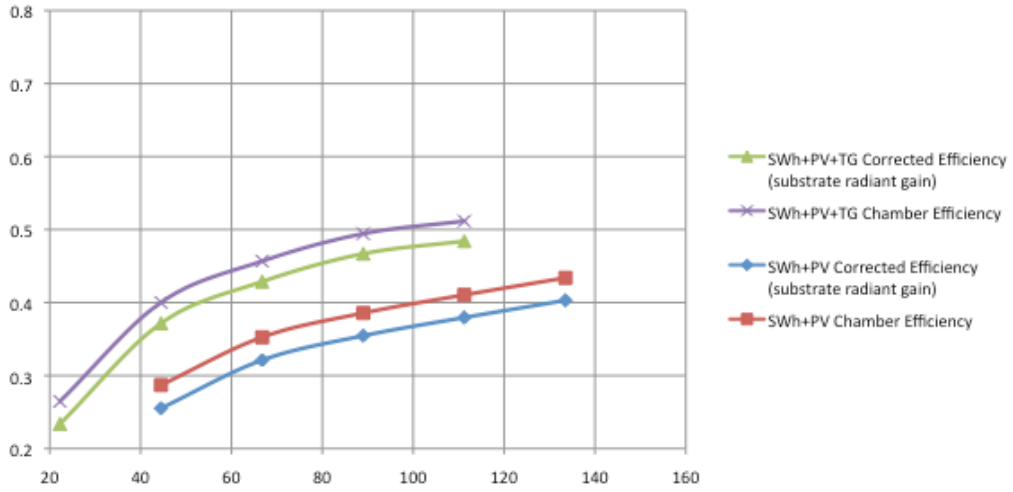


Figure D.11 Collector SWh+PV and SWh+PV+TG: Efficiency in Chamber corrected for radiant gain to account for heated Chamber façade surface due to lack of artificial sky.

Appendix E. Annual Results

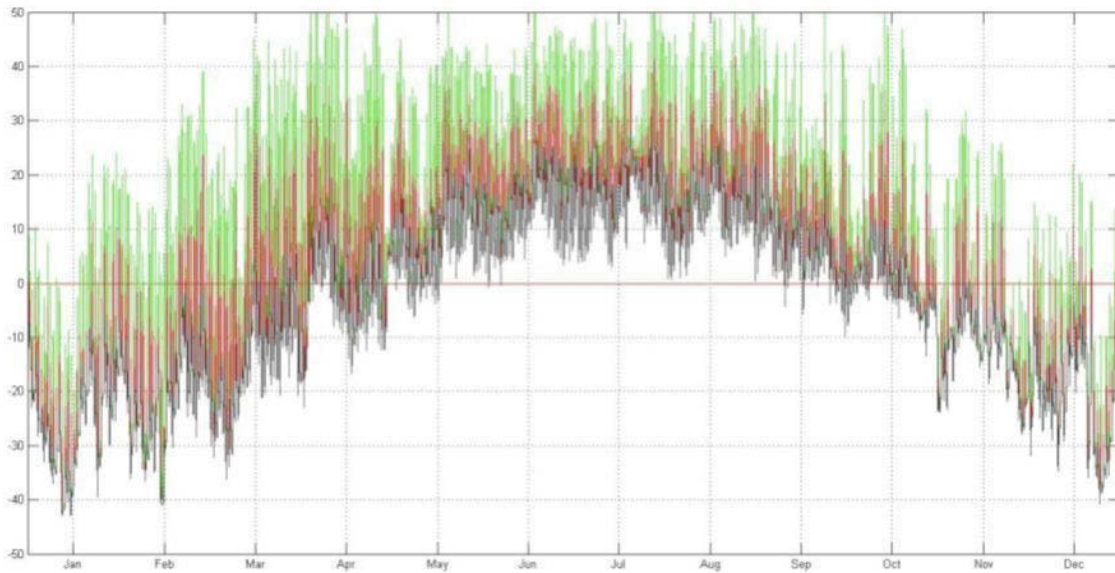


Figure E.1 Collector Outlet temperatures of SW+TG (green), and SW+PV (red), and outdoor temperature (black). MFR=50kg/hr/m²; **Fort Smith**;

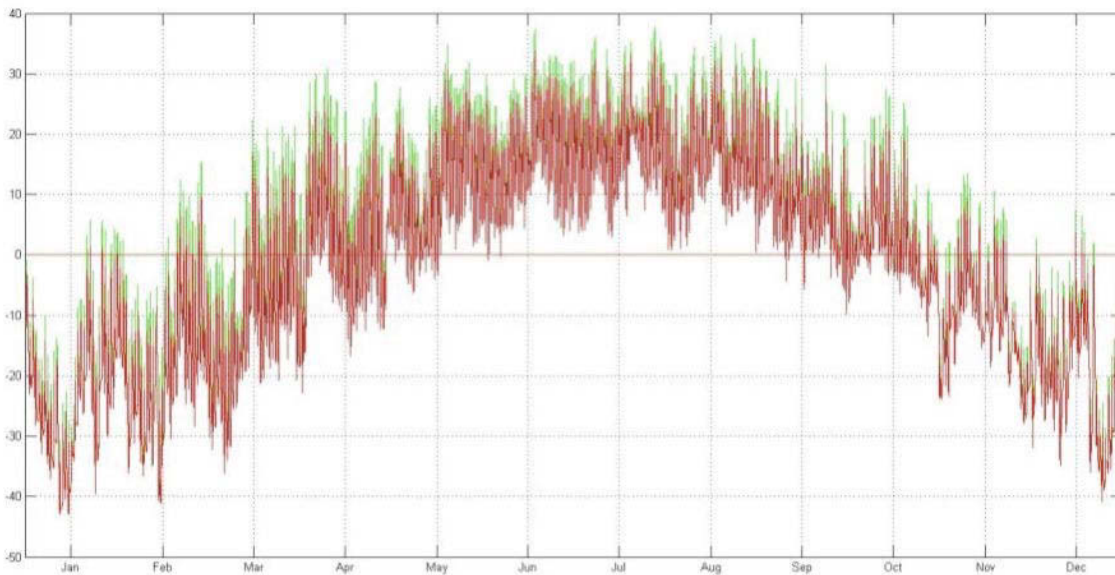


Figure E.2 Collector Outlet temperatures of SW+TG (green), and SW+PV (red), and outdoor temperature (black). MFR=150kg/hr/m²; **Fort Smith**;

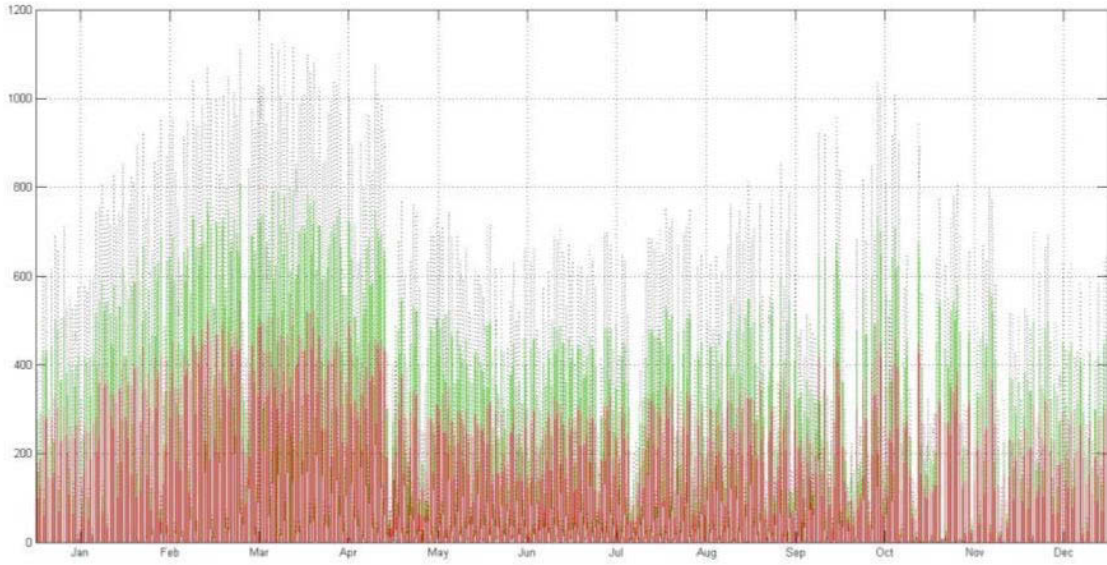


Figure E.3 Useful power (W/m^2) collected by SW+TG (green), and SW+PV (red), and total irradiance on Facade (black). MFR= $150\text{kg}/\text{hr}/\text{m}^2$; **Fort Smith**;

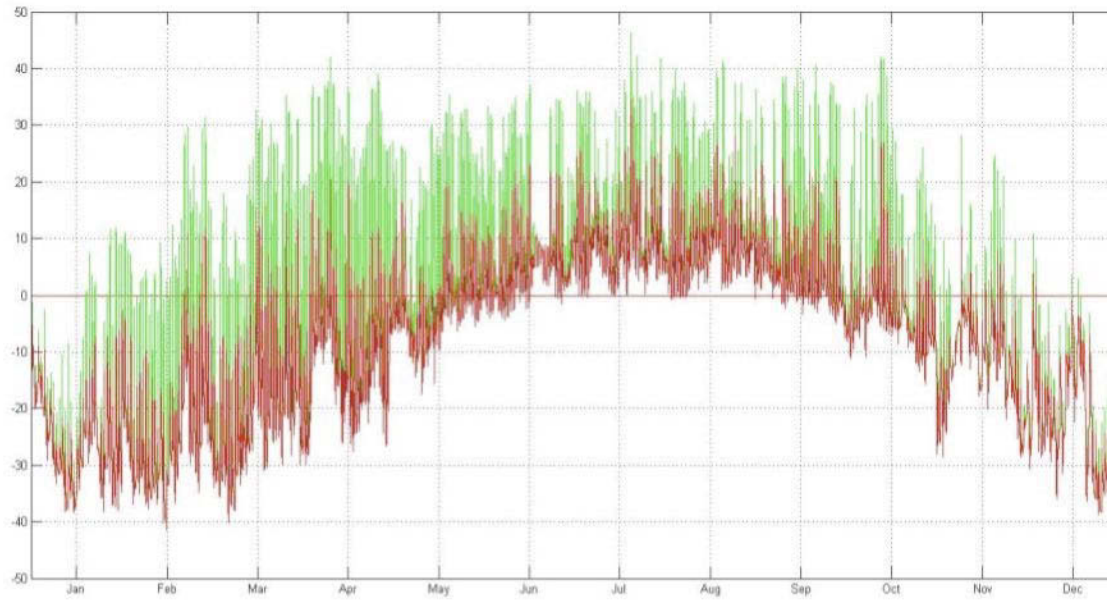


Figure E.4 Useful power (W/m^2) collected by SW+TG (green), and SW+PV (red), and total irradiance on Facade (black). MFR= $50\text{kg}/\text{hr}/\text{m}^2$; **Iqaluit**;

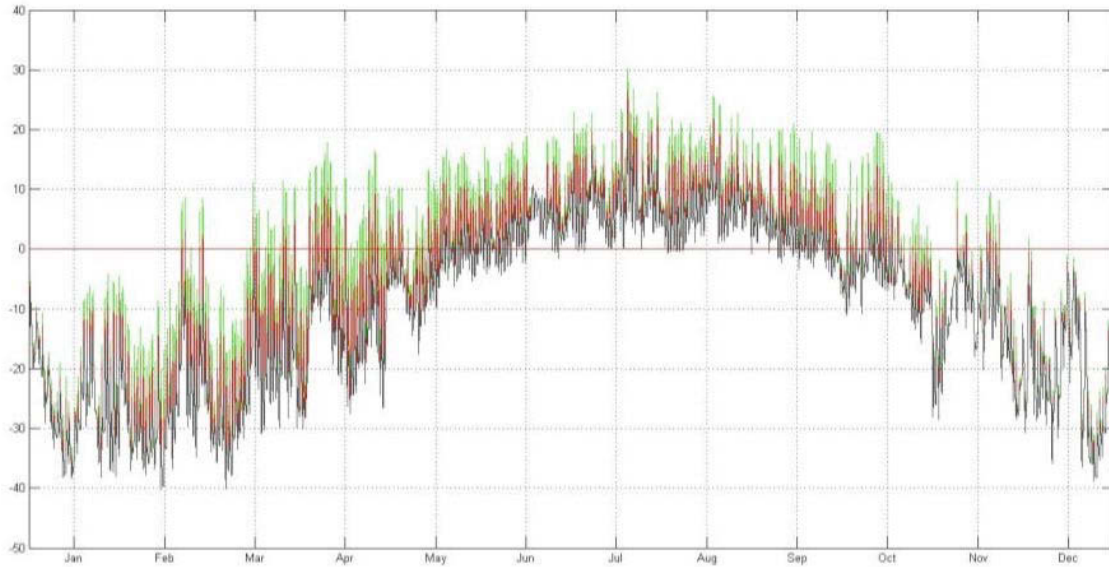


Figure E.5 Useful power (W/m^2) collected by SW+TG (green), and SW+PV (red), and total irradiance on Facade (black). MFR=150kg/hr/m²; **Iqaluit**;

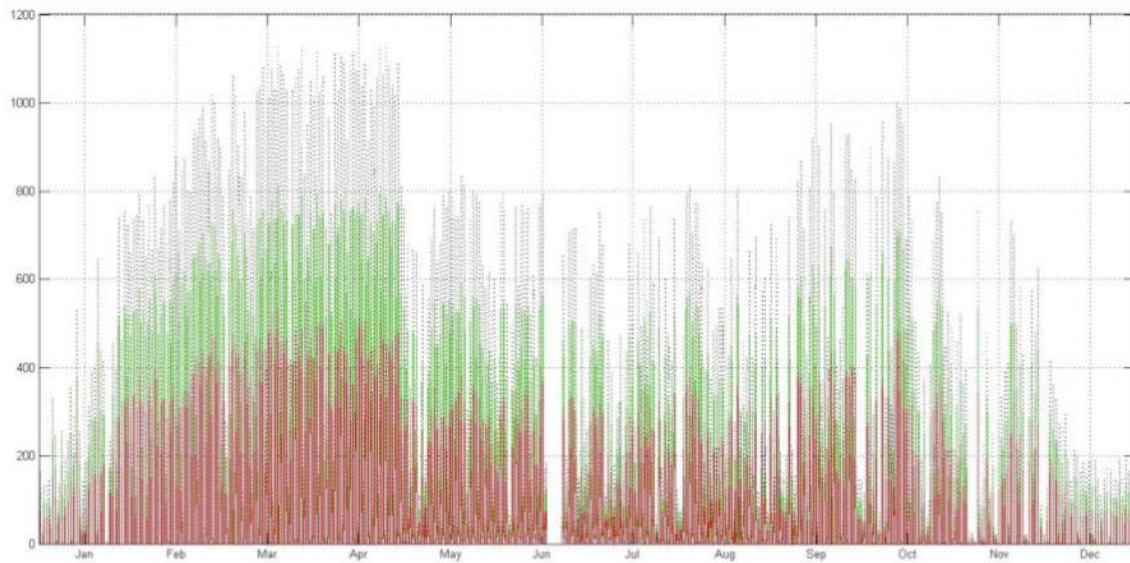


Figure E.6 Useful power (W/m^2) collected by SW+TG (green), and SW+PV (red), and total irradiance on Facade (black). MFR=150kg/hr/m²; **Iqaluit**;

Appendix F. Field Evaluation of PV Façade at Nunavut Arctic College, Iqaluit

F.1 Project Description

In 1995, a 3.2kWp grid-connected photovoltaic (PV) system was installed on the facade Nunavut Arctic College, Nunatta Campus in Iqaluit (Figure F.1). Since then, the façade integrated PV system has been delivering electricity to the grid with no interruption, confirmed by monitoring data until 2005. However, the monitoring systems stopped functioning in 2006. While it is entirely possible that PV is still producing electricity and feeding into the grid, there was no way of knowing for sure.



Figure F.1 Façade PV system, Iqaluit. Left: Picture 1995 (Sunny day); Right: Picture 2012 (Snowy day);

Therefore, the proposed fieldwork took place in Iqaluit, from April 22nd to 25th 2012, to determine quantitatively whether the PV is currently in working order. An I-V tracer was brought up to quantify the PV characteristics, and the Eppley pyranometer from the original data acquisition systems is used to measure the local solar radiation level. The data gathered from the fieldwork are documented in this report.

F.2 Testing Protocol

F.2.1 Technical Information of PV systems

The PV façade installation was initiated and supported by Natural Resource Canada (NRCan) in 1995. Oriented at 30° West of South, there are sixty PV panels mounted vertically totaling 25.62 m² of module area. The array is composed of 5 parallel groups of 12 modules in series, three groups of which are 36 single crystalline silicon Siemens M55 modules and the remaining two groups are 24 single crystalline Solec S-53 modules (Poissant et al., 2004). The details of manufacturer's specifications for the two types of modules are listed in Table F.1 below.

Table F.1 Specifications of the two types of PV modules used in the original installation

Model Name	Area (m ²)	Rated Power	Rated Efficiency	V _{oc}	I _{sc}	V _{mpp}	I _{mpp}
Siemens M55	0.4254	55 watt	12.9%	21.7 V	3.45 A	17.4 V	3.15 A
Solec S53	0.4294	53 watt	12.3%	20.3 V	3.4 A	17.1 V	3.1 A

The array output is rated at 220VDC at 25°C, and connected to a Prosine 5000 GT 3kW inverter, which produces 208VAC and directly feeds for building electricity usage. The PV-generated electricity is used as it is produced, all the while displacing the diesel power generation.

F.2.2 Testing Procedures

Though the monitoring system is no longer sending data to the computer, the Eppley pyranometer from the original data acquisition system is still functioning to this date. The output voltage is manually read by a multi-meter, quantifying the value of solar irradiance on the PV façade (Figure F.2). Unlike the Li-Cor pyranometer, which has

drifted significantly since the time of installation in 1996 due to increased spectral effects in high latitude, the measurements from the Eppley pyranometer remained comparatively reliable over time.



Figure F.2 Eppley pyranometer used for measuring solar irradiance

A DS-100C I-V Curve Tracer is used to determine if the PV system is still in operation and to evaluate the characteristic performance of the PV array. Testing was done on two dates, a sunny day on April 23rd and a snowy day on April 25th. In addition to the PV array itself (60 modules), there are also 9 experimental PV panels available for testing, installed at roughly the same time but unwired to the array.

F.2.3 Limitations

The nature of the I-V tracer allows only for momentary results of the PV performance. A new monitoring system will be needed to obtain continuous data and yearly kWh output. During the field tests, the reading from Eppley is manually taken from the multi-meter, therefore a few minutes lagging from the actual I-V curves. The error may be minimal on a sunny day when the solar radiation is relatively constant,

however, on a snowy day, the irradiance on the surface could change from second to second due to snow obstruction, causing significant errors.

In addition, the systematic drift of the Eppley pyranometer is not corrected due to the lack of the calibration device in the field. Since the testing were conducted in April 2012, the spectral effect that causes the pyranometer drift is minimal compared to winter months (Thevenard 2005; Thevenard 2006).

Lastly, no tests were done regarding the current efficiency of the Prosine 3kW inverter. Though the inverter is operational (with hot air rejected from the back of the inverter) at the time of inspection, its efficiency drop since 1995 is unknown.

F.3 Results and Discussion

F.3.1 Results of Solar Radiation data from the Existing Eppley Pyranometer

The Eppley Precision Spectral Pyranometer (PSP) outputs a low level voltage ranging from 0 to ~25 mV, which is amplified to a 0-5 Volts range. The calibration sheet for the PSP lists the following: Sensor calibration = $8.61 \mu\text{V W}^{-1} \text{m}^2$.

Since $\mu\text{V W}^{-1}\text{m}^2 = \text{mV kW}^{-1}\text{m}^2$, the estimate for the output voltage of 2.66Volts is:
 $\text{Irradiance} = 2.66\text{V}/5\text{V} * 25\text{mV}/(8.61 \text{mV kW}^{-1} \text{m}^2) * 1000 = 1544.7 \text{W}/\text{m}^2$.

Sample readings of the pyranometer are listed and interpreted in Table F.2 below.

Table F.2 Eppley PSP Readings

Sunny day: Monday April 23rd, 2012 at 3:00-3:15pm

Eppley Reading (V)	Total range (mV)	Amplified range (V)	Irradiance (watt/m ²)	Insolation on ONE panel (watt)	Total Insolation on façade (watt)
2.600	25.0	5.0	1509.9	642.3	38682.9
1.950	25.0	5.0	1132.4	481.7	29012.2
Average			1321.1	562.0	33847.6

Snowy day: Wednesday April 25th, 2012 at 10:30-11:30am

Eppley Reading (V)	Total range (mV)	Amplified range (V)	Irradiance (watt/m ²)	Insolation on ONE panel (watt)	Solar radiation on façade (watt)
0.479	25.0	5.0	278.2	118.3	7126.6
0.372	25.0	5.0	216.0	91.9	5534.6
0.540	25.0	5.0	313.6	133.4	8034.1
0.442	25.0	5.0	256.7	109.2	6576.1
Average			266.1	113.2	6817.9

F.3.2 Results from Nine Experimental PV Modules

Five Siemens modules and four Solec modules, a total of nine experimental PV modules were tested individually, as shown in Figure F.3. The monitor room in the Arctic College is designed to provide easy access to the unwired experimental PV modules for education purpose.

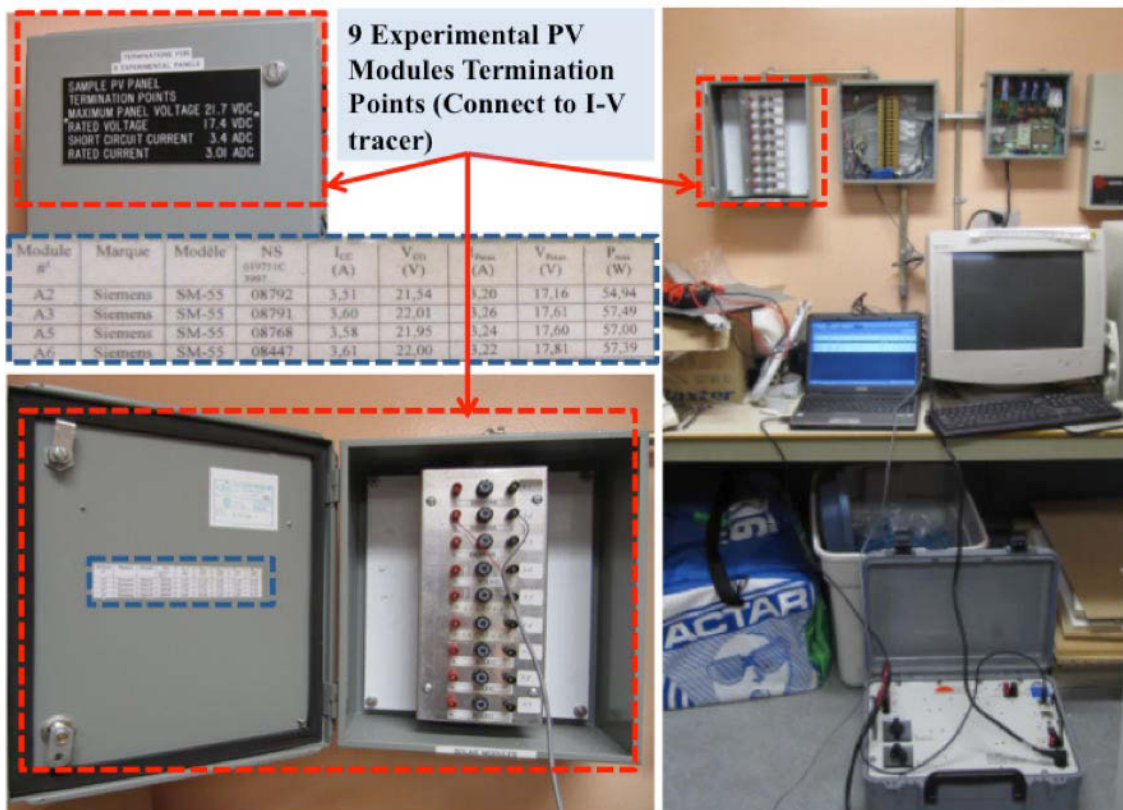


Figure F.3 Experimental PV Module Testing

For each experimental module, two characteristic I-V curves were swept and the results were in good agreement with each other. The results from the nine experimental modules are representative of the Siemens and Solec PV quality, as the nine modules and the PV array were installed at the same time and exposed to the same weather conditions.

All the Siemens panels are currently functioning, while two out of four Solec panels are not in working order (no voltage readings) and probably reached its end-of-life. It is a good indicator of how many PV panels of each module type that may be currently non-functional in the solar array. Measured output of the functioning experimental PV modules shown significant efficiency drop from the original rated power. The results of the nine experimental modules are summarized in Table F.3, allowing relevant insights into the current array performance.

Table F.3 Experimental PV modules Testing Results

Experimental Module	Individually Rated Efficiency (% at STC in 1995)	Actual Efficiency (%) on a Sunny day	Actual Efficiency (%) on a Snowy day	Actual output (watt) on a Sunny day	Actual output (watt) on a Snowy day
A1 (Siemens)	Unknown	6.5	9.4	41.85	11.15
A2 (Siemens)	12.9	7.0	10.5	44.7	12.4
A3 (Siemens)	13.5	7.2	10.6	46.4	12.5
A4 (Solec)	Unknown	5.6	8.0	36.4	9.6
A5 (Siemens)	13.4	6.6	11.4	42.5	13.5
A6 (Siemens)	13.5	6.8	11.7	43.9	13.8
A7 (Solec)	Unknown	Non-functional	Non-functional	/	/
A8 (Solec)	Unknown	Non-functional	Non-functional	/	/
A9 (Solec)	Unknown	6.4	6.7	41.5	8

Though the results may have been tempered with systematic errors due to pyranometer drift as well as the time lag between irradiance reading and I-V curve sweeping, the data are consistent with each other on the same day. Figure F.4 below

illustrates the different I-V curves of the same experimental modules (A1 Siemens and A4 Solec) on a sunny and a snowy day.

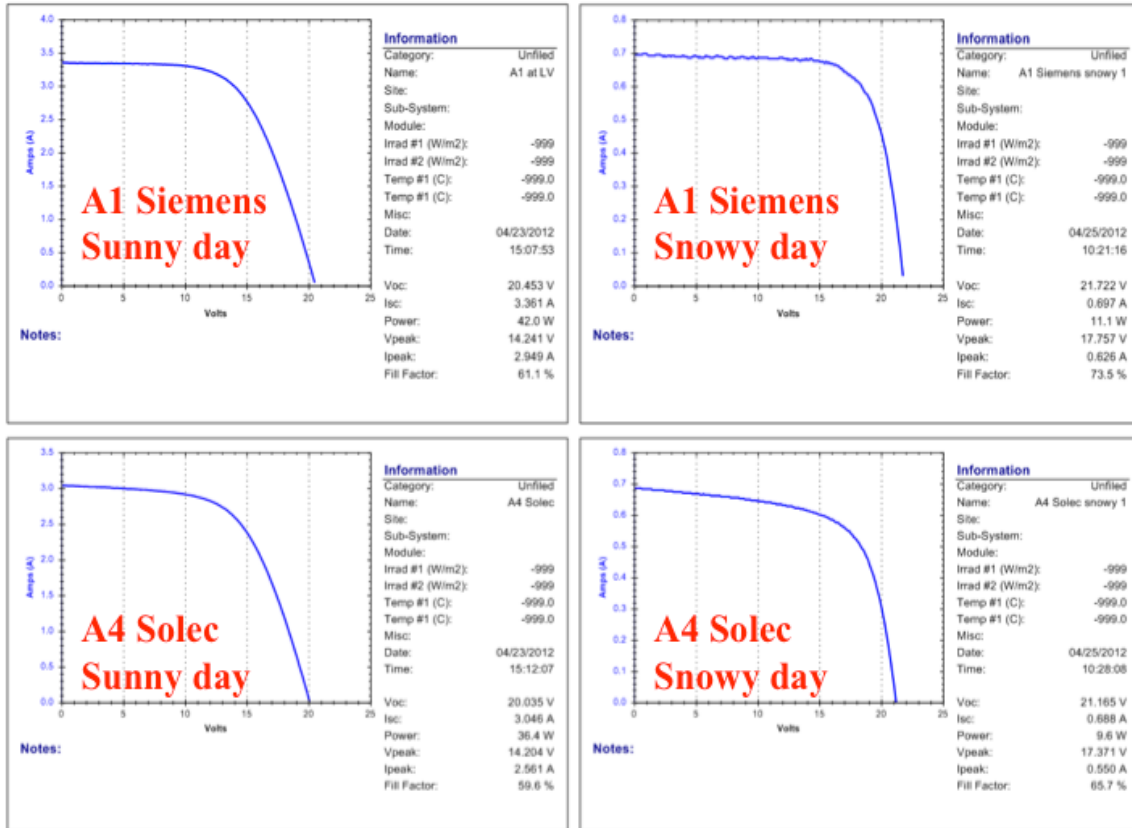


Figure F.4 I-V curves of sample experimental modules under Sunny and Snowy weather

As can be seen on Figure F.4, the falling snow sometimes causes zigzags on the curve (A1 Siemens Snowy day). Interestingly, the fill factor, as well as PV efficiency on a snowy day is better on the snowy day than it is on the sunny day, for both Siemes and Solec modules.

F.3.3 Results from the Total PV Array

The open-circuit voltage of the whole array is measured on both the sunny and snowy days. The rated open-circuit voltage of the array is 220VDC at 25°C, using the

manufacturer's Voc temperature coefficient of $-0.34\%/^{\circ}\text{C}$, the open-circuit voltage values were calculated and compared to measured values, listed in Table F.4.

Table F.4 Open-circuit Voltage of PV Array on April 23rd (sunny) and 25th(snowy), 2012

	Temperature daily mean	Temperature daytime	Measured Array Voc	Calculated Voc from rated Voc at 25°C
Sunny day	-12.6°C	-10°C	250Vdc	246.2Vdc
Snowy day	-10.7°C	-6.6°C	231Vdc	243.6Vdc

The solar array is composed of three parallel groups of Siemens modules (L1, 36 modules total) and two parallel group of Solec modules (L2, 24 modules total). The I-V curve tracing was done only for snowy day, details of the wiring and connections are shown in Figure F.5.

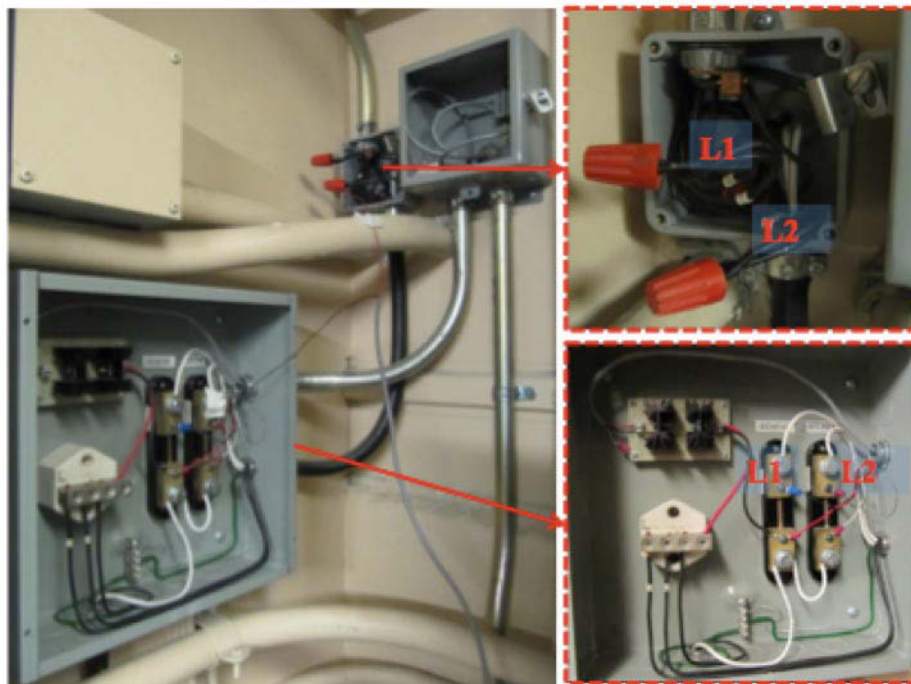


Figure F.5 Solar Array Testing: DC wiring in mechanical room for Siemens (L1) and Solec (L2) array

The results of the PV array performance are summarized in Table F.5 below. Three separate tests (I-V curve and Eppley measurements) were conducted for each array (L1 and L2) on April 25th (snowy) from 10:30 to 11:30am.

Table F.5 Results of Solar Array Performance (snowy day)

	Test 1 (watt)	Test 2 (watt)	Test 3 (watt)		
L1 (36 Siemens Modules)	369.8	380.5	403.4		
L2 (24 Solec Modules)	156.8	179.6	180.3		
				Original Rated Efficiency in 1995 (%)	Average Efficiency Reduction since 1995 (%)
L1 Siemens Efficiency (%)	9.4	8.9	9.5	12.9	28.1
L2 Solec Efficiency (%)	5.9	6.3	6.3	12.3	49.9
Overall Efficiency (%)	8.0	7.9	8.2		

The efficiency reduction of **Solec** modules has dropped by **50%** since 1995 installation, while the efficiency drop of **Siemens** modules is only around **30%**. Considering the findings from the 9 experimental panels, half of Solec experimental panels stopped functioning while all of the Siemens panels are still in operation. The significant efficiency reduction of Solec array can be attributed to the performance drop of each individual Solec panel, as well as due to the dead modules that adversely affect the entire string.

Figure F.6 illustrates the characteristic performance of the two PV types (L1 and L2), at an irradiance of 257 watt/m². Siemens (L1) offers a much better fill factor and efficiency, compared to Solec (L2) modules. It is strongly suspected that some of the Solec modules in the strings are no longer functional, bringing down the efficiency of the entire L2 array.

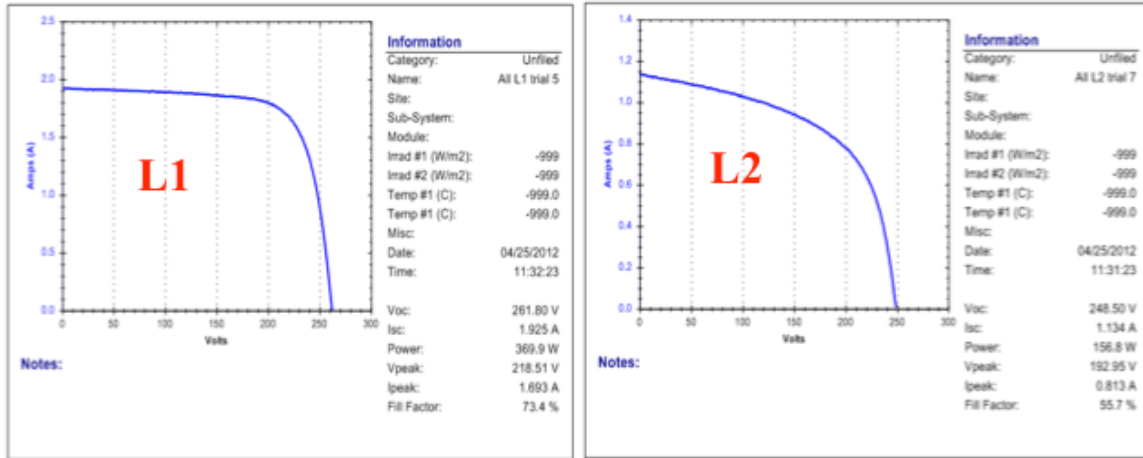


Figure F.6 I-V curves of the Solar Array (L1 Siemens, L2 Solec), snowy day

F.4 Conclusions

This fieldwork provided the most recent updates of the Nunavut Arctic College PV façade project in April 2012. The entire photovoltaic array is in working order to this date, at 8% overall electric efficiency. The Prosine 5000 GT 3-kW inverter is also fully functional, feeding AC electricity to the school for the past 17 years.

The monitoring systems stopped feeding data since 2006, though some of the instruments are still capable of reading measurements, such as the Eppley pyranometer. Calibration of the pyranometer is much needed and future monitoring projects should take into consideration the long-term pyranometer drift in high latitude locations.

Two types of single crystalline silicon PV panels were evaluated, Siemens M55 and Solec S53. The current output (on a snowy day) of the Siemens array is at 9.3% overall, 28% less than its original rated efficiency. However, the Solec array is producing only at 6.2% overall, 50% less than its original rated efficiency.

Moreover, among the nine experimental modules tested, all of the Siemens experimental modules are functional while two out of four Solec modules output no voltage. This finding indicates that some of the Solec panels in the array have also reached their end-of-life, contributing to the significant Solec array efficiency drop. In summary, though the initial rated output of the two PV types are very similar, in a long run, Siemens panels are performing more reliably than Solec modules.

It is also important to recognize limitations of the field tests conducted. Only momentary results of PV performance are evaluated using I-V curve tracing, and the efficiency of PV modules may be systematically overestimated due to pyranometer drift.

The fact that the Nunavut Arctic College photovoltaic façade is outputting AC electricity to this date is encouraging. Photovoltaic has been proven to be a reliable technology for the far North at its current life span of 17 years (1995-2012). Since its operation in 1995, the PV façade and the inverter have outlasted two installations of monitoring systems, even under the harsh weather of Iqaluit.

It is extremely rare to find such existing full-scale photovoltaic installations of similar service life span that are still functioning, especially for high latitude locations. Depending on the availability of funding and technical support, it may be worthwhile to install new monitoring systems to provide annual data on PV performance. Calibration of the existing Eppley pyranometer should be performed, and may be expanded to a research project studying the long-term spectral effects on pyranometer drifts. The current inverter efficiency could be monitored as well, to quantify efficiency drop and to address the aging effects of solar inverters.

Appendix G. Field Survey of Façade Integrated Unglazed Transpired Collectors in the Northwest Territories

G.1 Project Description

This research project took place between May 7th and May 26th, 2012, at locations in the Northwest Territories (NWT) where full-scale façade integrated solar transpired collectors were installed. The fieldwork is collaborated between *Arctic Energy Alliance* and *Concordia University*, with financial support from the *Concordia Graduate Student Mobility Award* to the author.

The existing solar transpired collector (UTC) installations in NWT go by the product name of “SolarWall”, commonly a dark metal cladding on the exterior wall perforated with small and distributed holes. It is a well-researched and widely implemented façade-integrated solar thermal technology in Canada’s North.

From past experience, the existing installations of SolarWall do not function very well under the harsh Northern climate. This research project is initiated in an effort to evaluate the current performance of SolarWall and to investigate the underlying causes of common operational problems.

In addition to field inspections and on-site visits, the project also implemented or proposed monitoring systems for selected SolarWall installations. A scientific protocol is established regarding parameters of interest, while keeping cost-effectiveness of the monitoring systems in mind. There are also long-term plans for logging and servicing the

monitoring data (1-year minimum) to facilitate future assessment and improvements of the solar transpired installations in Northern Canada.

G.2 Inventory of SolarWall installations in NWT

G.2.1 Overview

There are a total of six known SolarWall (unglazed transpired collector) installations in the NWT, shown in Table G.1 and G.2. Due to time and budget constraints, the author was able to travel to Yellowknife and Inuvik for on-site inspection for five out of six SolarWall projects (except for the Fort Smith installation).

Table G.1 Inventory of SolarWall projects in NWT

Location	Facility	Currently Operation Status	Time of Installation	Original or Retrofit	SolarWall Size	Façade Orientation	Usage for SolarWall Heated air
Yellowknife	Welehdeh Catholic School	Functioning	1998	Original	200m ²	15° west of south	Pre-Heat Ventilation air
Yellowknife	Geoscience Building	Unknown	2003	Retrofit	53m ²	South	Ventilation, space heating, heat exchanger to hydronic heating to preheat glycos
Yellowknife	Private House	Not Functioning (Electrical fan control issue)	2009	Retrofit	~30m ²	SouthWest	Offset HRV and offset space heating
Fort Smith	Recreation Center	Unknown	2000	Original	150m ²	Southwest	Preheat air for HRV
Inuvik	Inuvik Correctional Center	Building unoccupied starting March 2011, SolarWall system maybe functional	May, 2005	Original	75m ²	Southwest	Preheat HRV fresh air, also sent to heat exchanger for in-floor heating
Inuvik	Aurora Research Institute	Functioning	2011	Original	~26m ²	35° west of south, Corrugation Horizontal	Fresh air preheat

The diversity exhibited by the SolarWall projects in NWT is helpful for comparing system performance and operational issues. As shown in Table G.1, SolarWall sizes

range from 26 m² to 200 m² and their installation times vary from 1998 to 2011. Four out of six systems were implemented at or near the time of building construction (Original systems), while the other two systems were add-ons after the buildings were completed and occupied (Retrofit systems).

Some of the operational or design problems may be local to a certain installation, while others are shared between several installations, as summarized in Table G.2. Note that the site inspection was conducted in the spring/summer time (May 2012), and winter issues such as icing and reduced efficiency cannot be confirmed by this project alone.

Table G.2 Summary of operational details for SolarWall installations in NWT

Location	Facility	Existing Monitoring System	Operational Problems	Other issues	Owner	Operating party (maintenance)
Yellowknife	Welehdeh Catholic School	No; Honeywell control system	No issues; fan belt worn out and was fixed in May 2012;	Shaded partially	Yellowknife Catholic School Board	
Yellowknife	Geoscience Building	No; Control system unknown	Vegetation obstructions, fan not on, lack of information	Located in the lower field, retrofit on old building	Ministry of Indian and Northern Affairs Canada (INAC)	Public works Federal
Yellowknife	Private House	No	Electric wiring of fan, control issue	Lack of skilled contractor	Pete Mount	
Fort Smith	Recreation Center	Yes, by Enermodal, until 2002	Unknown	Unknown	Town of Fort Smith	
Inuvik	Inuvik Correctional Center	No; Honeywell control system	No problems with SolarWall itself;	Serious foundation problems, building unlikely to be occupied again	Public works GNWT	Public works GNWT
Inuvik	Aurora Research Institute	No; Siemens Control system	No issues so far;	Occupants and Maintenance party are different groups	ARI	Public works GNWT

The site visits concluded that two out of six SolarWall installations are currently functioning, while two systems are definitely not operational, and the state of the remaining two systems is unknown. Only one system (Fort Smith) was monitored from

2000 to 2002 by Enermodal Engineering as part of the follow-up mandates. The rest of the systems have no monitoring equipment to keep track of the energy saving or to detect potential operational problems. Section G.3 will go into details about implementing new monitoring systems for some of the existing SolarWall installations.

G.2.2 Individual Systems

The individual systems listed in Table G.1 and G.2 are shown in Figure G.1 to G.4, except for the projects at Weledeh Catholic School (Yellowknife) and at Aurora Research Institute (Inuvik), which will be discussed in detail in Section G.3 as candidates for adding new monitoring equipment. All the pictures in Figure G.1 to G.8 are taken by the author, with the exception of Figure G.3 (Conserval Engineering, 2010c).

Figure G.1 shows the SolarWall at the Yellowknife GeoScience building from afar (left) and close-up (right). It is clear that vegetation in front of the solar collector has grown out of the control since the installation in 2003. As the building is located at the bottom of a small hill, the low altitude further aggravated the vegetation shading on the SolarWall surface, showing lack of considerations from the design phase.

Furthermore, the building occupants and owner are separate parties that only communicate with each other when there is a maintenance work order. Despite our best efforts and repeated site visits, the building owner was not able to provide with technical information concerning the current state of the SolarWall operation. The occupants expressed interests in learning more about the active solar system in their own building. However, little information was available due to staff turnover and the segregation between occupants and owner. Though the status of operation is shown as ‘unknown’ in

Table G.1, we concluded that it is most likely that this SolarWall installation is not functioning at the moment.



Figure G.1 SolarWall at the GeoScience Building, Yellowknife, 62.4°N

The next system in Yellowknife is also the only residential installation in this survey. The SolarWall system occupied the entire west façade of a private house in Yellowknife, while solar hot water collectors and photovoltaic panels are mounted on its east roof (Figure G.2, left). The SolarWall is designed to pre-heat air for the HRV system in the basement (Figure G.2, right) or to directly offset space heating load.

According to the owner, the SolarWall hasn't worked at all since its installation in 2009. Though all the mechanical components are in working order, there is an electric wiring issue with the fan that draws the pre-heated air. Since it is a residential project, no commercial building control company was involved and the work quality relied upon the skills of private contractors. The cost of hiring a qualified electrician to fix the fan wiring is prohibitive at the moment.



Figure G.2 SolarWall façade on a private house, Yellowknife, 62.4°N

The investigation of the Fort Smith project (Figure G.3) is solely based upon literature, as no site visits were conducted. Monitoring reports by Enermodal Engineering (2001, 2002 and 2005) shown that the combination of SolarWall and HRV contribute to 78% of total energy needed for ventilation air heating, 60% of which attributes to HRV alone while SolarWall is responsible for only the remaining 18%.

At a considerable added cost, this particular solar installation is not very effective in improving the building energy efficiency for several reasons. Firstly, the wall is oriented significantly off south at an azimuth of 55° West, a permanent handicap from design. During operation, the controls of drawing solar heated air is often in ‘Manuel Operation’, while the system would perform more effectively if thermostatically controlled. In fact, in email communication records (McCluskey, 2001), expert from Arctic Energy Alliance has mentioned that *“We won’t be marketing many Walls (SolarWall) north of 60 degrees based on the returns of the Ft. Smith Wall”*.



Figure G.3 SolarWall at Fort Smith Recreation Center, Fort Smith 60°N, Picture from Conservall Engineering (2010c)

Figure G.4 shows another SolarWall installation at the former Young Offenders Correctional Facility in Inuvik. Though there are no reported issues on the SolarWall itself, the system is not in operation as the building is currently unoccupied and unlikely to become habitable due to serious structural and foundation failure.



Figure G.4 Left: SolarWall at Female Young Offenders Correctional Facility, Inuvik 68°N; Right: Honeywell Building Control System Interface showing SolarWall controls

As shown in Figure G.5, there are countless growing cracks on the drywall, window/door frames, and floors across this large institutional building. Quick inspection of the building perimeter and architectural drawings revealed that its design is seriously flawed. The building is constructed on a pad foundation, which relies completely on the flatness of the ground and the rigidity of the permanent frost. Six large thermo siphons (Figure G.4, left) are constructed to prevent the permanent frost from melting. However, the mechanical engineers designed in-floor radiant heating on the ground floor, with only 4” of insulation beneath the concrete floor slab. The permanent frost is essentially heated continuously throughout the winters, tearing apart the building as it slowly sinks into the melting ground since its completion in 2005.



Figure G.5 Interior Structural Failures at Female Young Offenders Correctional Facility

G.3 Monitoring Projects

G.3.1 Selection of Candidates for Future Monitoring

There is a general lack of effort in monitoring solar installations after construction. The only monitored SolarWall system in NWT, the Fort Smith system, produced data from 2000 to 2002 with no updates since then. This research project concluded that continuous monitoring plans are essential to truly quantify the suitability and durability of solar installations in the North. Two NWT SolarWall installations, at the Weledeh Catholic School in Yellowknife and at the Aurora Research Institute (ARI) in Inuvik, were selected as monitoring candidates for the following reasons:

- Both systems are currently functional with no known operational issues;
- Owners and facility managers of the buildings are very enthusiastic and cooperative about the monitoring project;
- They are the **oldest** and the **newest** SolarWall in NWT (Weledeh system is completed in 1998 while the ARI system in 2011);
- They are the **largest** and the **smallest** SolarWall collectors in NWT (Weledeh system is 200 m² while ARI system is 26 m²);
- They are located in **two different cities** and each building employs a **different control company** (Weledeh system uses Honeywell while ARI system uses Siemens control);

To obtain the energy output and solar fraction of the SolarWall systems, it is necessary to obtain monitoring values for parameters of interest, such as air mass flow rate, exterior temperature, air temperature and relative humidity at collector outlet, etc.

Fortunately, some of those sensors are already implemented by the building control company (Honeywell or Siemens), to execute the thermostatic control algorithms. Though past data were stored in temporary memory and cannot be recovered, the existing infrastructure is able to log future sensor data simply by asking the software to trend and store sensor values.

By using existing sensors, the cost of implementing new monitoring systems can be reduced. With reasonable redundancy in sensor selections, the project proposals (Section G.3.2 and G.3.3) aim to build solar monitoring capacity in NWT in an efficient and cost-effective manner.

G.3.2 Monitoring Project 1: Weledeh Catholic School, Yellowknife

The monitoring project for the SolarWall installation at the Weledeh Catholic School took place during the site visits in May 2012 (Figure G.6). The project was made possible with the help of the building facility manager and maintenance staff at the Weledeh school.



Figure G.6 Left: SolarWall at Weledeh Catholic School, Yellowknife 62.4°N; Right: Honeywell Building Control System Interface showing SolarWall controls

Data from some of the existing sensors, such as the exterior temperature, SolarWall outlet temperature, damper and fan status, are logged since June 2012 with the help of Honeywell technicians.

The new sensors and data acquisition system were purchased or donated by the Arctic Energy Alliance and the NSERC Smart Net-zero Energy Buildings Strategic Research Network. New sensors for temperature (exterior and in-duct), relative humidity, solar radiation have been installed by the author (Figure G.7). The data points are logged every 15 minutes by an Agilent system and fed into a local laptop for storage. All the parameters necessary to calculate the total amount of solar thermal energy captured by this façade solar installation are currently monitored.

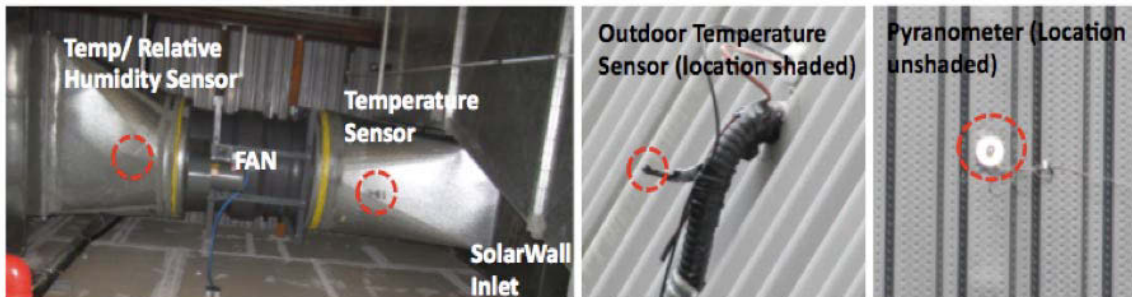


Figure G.7 Locations of New Sensors implemented for the Weledeh SolarWall system

There are still a few tasks left as part of the monitoring efforts. The data logged from the Honeywell interface need to be transferred to a secure server that can be accessed remotely via Internet. The local laptop storing data from new sensors also needs to connect to the Internet to allow for Remote Desktop connection. The Agilent system is currently set to work until August 17th and its scan rate needs to be reset before then to accommodate long-term monitoring. Finally, the Arctic Energy Alliance is responsible for servicing and analyzing the monitoring data throughout the year. The ultimate goal is

to monitor and evaluate the performance of this 14-year old SolarWall system in Yellowknife.

G.3.3 Monitoring Project 2: Aurora Research Institute, Inuvik

The Aurora Research Institute (ARI) has recently completed three renewable installations including a wind turbine, a photovoltaic system (solar electric), and a SolarWall façade (solar thermal). For education and demonstration purposes, the ARI plans to monitor all three renewable systems and enable real-time online display of the renewable energy generation. The objective of this project is to monitor one of the renewable systems, the SolarWall façade located on the penthouse at the back of the ARI building (Figure G.8, left).



Figure G.8 Aurora Research Institute, Inuvik 68°N; Left: Back of building with SolarWall on the Penthouse; Right: Front of building;

Unlike the Weledeh monitoring project that is close to completion, the monitoring project for the ARI SolarWall is still at the proposal stage. Contacts were made during site visits in Inuvik, and the ARI is very supportive of the initiative. It would be extremely interesting to compare the SolarWall performance at ARI (installed in 2011)

with the SolarWall at Weledeh (installed in 1998) to determine the durability such solar thermal systems at high latitudes.

The ARI building uses Siemens building control system, the algorithm of which also includes the control of SolarWall operation for fresh air pre-heating. Data from existing sensors, including exterior temperature, SolarWall outlet temperature/humidity, damper and fan status, can be logged using the Siemens interface.

Several new sensors are needed to fully monitor the SolarWall energy output as well as the system's efficiency. Inside the mechanical room, one Relative Humidity sensor and two air velocity probes will be positioned at the SolarWall air intake duct to measure the incoming mass flow rate (Figure G.9). At the exterior, a pyranometer and a temperature sensor will be mounted to measure solar radiation and outdoor temperature.

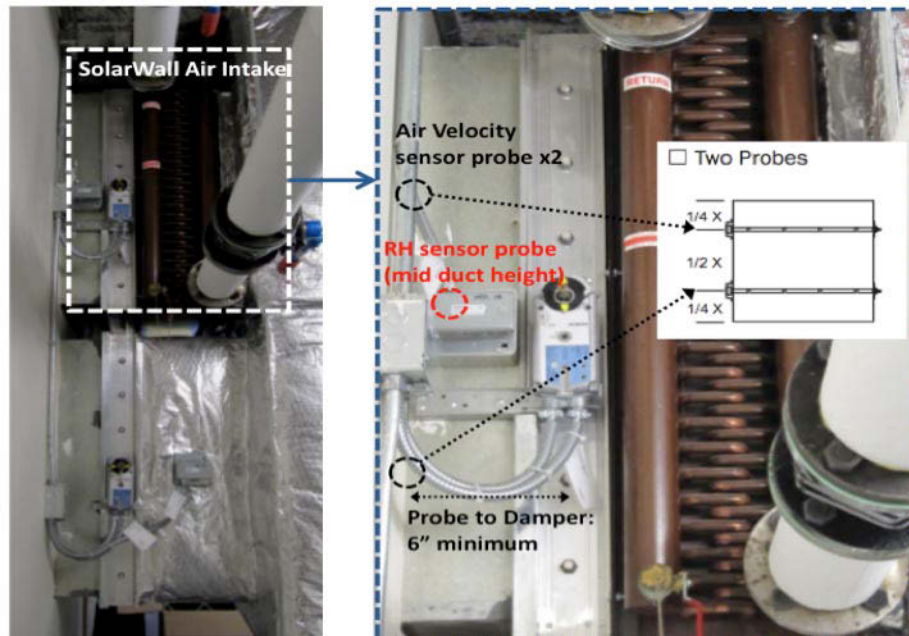


Figure G.9 Sensors Installation, at SolarWall air intake inside the mechanical room

All the new sensors can be configured to generate analog output of 0-5mV or 4-20mA, which will be wired to feed into the Siemens data acquisition and displayed by the Siemens Insight interface on the local desktop. Internet connection is needed on this desktop to upload offline data to online servers for safekeeping and real-time display.

This monitoring project incurs two-part costs, including:

1. Hardware cost of new sensors and accessories, plus shipping and taxes;
2. Labor and work order cost from Public Works and Siemens to install, wire and program the new sensors, as well as to set up desktop internet connection, retrieve data points and to maintain the server.

G.4 Conclusions

The SolarWall collector developed by Conserval Engineering is a proven solar thermal system that has worked well in populated areas. Natural Resources Canada has commissioned multiple reports to study the technical and economic feasibility of SolarWall system in northern remote communities, including monitoring reports on the Fort Smith installation (Enermodal Engineering, 2001, 2002 and 2005).

Based on findings from this applied research project, the SolarWall installations in Canada's North are experiencing some design and operation challenges. Firstly, most SolarWall installations in NWT are oriented off south to different extents, due to site restriction or lack of design efforts. The non-optimal orientation contributes to significant annual loss and prolonged payback time. For Northern applications where energy is expensive, it is vital that solar installations are oriented as south facing as possible.

Secondly, there is ongoing segregation and communication disconnect between the building owner and occupants in commercial buildings, leading to gaps in knowledge transfer of building systems, especially for innovative systems like the SolarWall.

Despite the local financial incentives, little technical support is present for residential solar projects. The work quality relies completely on the competence of individual contractors who are called in to do the installation. The arising issues with renewable energy systems in the North are often more human than it is technical,

Energy cost evaluation is extremely complex in Canada's North, as infrastructure costs for fossil fuel (e.g. tanks and pipeline) are not included in the actual energy price (Enermodal Engineering, 1997b). With additional government subsidy injected to the energy sector, calculation of payback time for solar installations is conducted on unlevel playing fields when compared with traditional fossil fuel prices.

Therefore, financial incentives and technical support for adopting renewable energy are necessary in the North. To avoid the mentality of 'build and forget', the incentive programs for SolarWall and other renewable systems should make ongoing monitoring mandatory for all new installations. The monitoring data obtained from this research project will offer insights to the suitability and durability of solar transpired collectors in the North. Only by quantifying the performance and learning from the past mistakes, can we improve the current state of building-integrated solar systems at high latitude locations.